New approaches to studying liquid structure and Lewis acidity

By

Anne McGrogan, MSci

Presented to the School of Chemistry and Chemical Engineering

Queen's University, Belfast

in fulfilment of the requirements for the degree of

Doctor of Philosophy

Queen's University, Belfast

December 2023

Acknowledgements

I would like to express my deepest gratitude to all those who helped me along in my PhD journey. To Professor Gosia Swadźba-Kwaśny, thank you for the opportunity to pursue this research, for your invaluable advice and challenging me to grow as a scientist. I am grateful for your mentorship, patience and support. Thank you for the many opportunities you have encouraged me to take. I would also like to thank Professor John Holbrey for his time, support, and guidance. Thank you for always having your office door open to me and for all the interesting discussions.

To the research group – there are so many people to thank but I especially want to mention Sam, Mark, Dominic, Emily, Beth, Shannon, Haris and Yoan. I couldn't have asked for a better bunch of people to go through this journey with. Thank you for help in the lab as well as all the laughs, chats and coffee breaks. I would also like to thank Dr Nimal Gunaratne, for his advice and insightful comments about my work. I am grateful to the admin and technical staff at QUILL and QUB in supporting my research and a special thanks must go to Deborah Poland. Thank you to my industrial mentor, Dr Peter Klusener for his advice and guidance throughout the past four years.

Without funding this PhD would not have been possible and for that I would like to thank the Engineering & Physical Sciences Research Council (EPSRC).

I would like to express my appreciation to my parents for their constant support throughout my studies. I am also grateful to my friends, Sara, Heidi, Ruth and Alison, thank you for always believing in me and for being my biggest supporters. Finally, thank you Seb for all of your help during this time and for always being so supportive and encouraging.

Abstract

Ionic liquids (ILs) are characterised by complex intermolecular interactions through Coulombic and van der Waals forces, as well as the rich network of hydrogen bonds. Elucidation of the liquid structure gives an important indication as to which of these interactions dominate in each IL, which in turn sheds light on the origin of their physicochemical properties. In this work, the structure of both protic and aprotic ILs has been studied using neutron scattering. Data-driven simulations were carried out using Empirical Potential Structure Refinement (EPSR), using EPSR25 and Dissolve.

Chapter 2 reports on the structure of protic ILs based on sulfuric acid, doped either with excess acid or water. These ILs were successfully used in industrially relevant processes, chiefly Fischer esterification reactions and biomass pre-treatment, and in both demonstrated beneficial phase behaviour compared to neat sulfuric acid. Enhanced phase separation of the ester product was observed in Fischer esterification, and the water-doped IL had a higher propensity to dissolve lignin in biomass fractionation. The rationale behind this behaviour was unknown, which motivated the liquid structure study of these systems. This led to a key finding that, in addition to the typical cation-anion interactions of ILs, they also have a persistent sulfate/sulfuric acid/water network structure, which is retained even in the presence of 2 moles (∼17wt%) of water. Hydrogen sulfate PILs have been shown to incorporate water into hydrogen-bonded anionic chains and it is the properties of this hydrated PIL that explains their excellent performance in these industrial processes. In esterification reactions, the IL gradually binds the water that is generated upon the formation of an ester, and the resulting hydrated IL phase separates from the weakly hydrophilic ester product. In contrast, such hydrated IL is excellent in hydrogen bonding to lignin and dissolving it.

The presence of long alkyl chains in ILs induces microsegregation into polar and non-polar domains, which translates to differences in physicochemical properties. Chapter 3 details an experimental, neutron scattering study of the liquid structure of three common ILs, all based on the bis(trifluoromethanesulfonyl)imide anion, abbreviated in the literature as $[NTf_2]^-$ or $[TFSI]^-$, and on the following cations: 1-ethyl-3-methylimidazolium, $[C_2mim]^+$, 1-decyl-3-methylimidazolium, $[C_{10}mim]^+$, and trihexyl(tetradecyl)phosphonium, $[P_{666,14}]^+$. This study adds fundamental understanding to structure-property relationships. Until recently, such studies were inhibited due to the paucity of suitable software. In contrast to EPSR, Dissolve has enabled robust modelling of long alkyl chains, therefore neutron scattering-derived structures of $[C_{10}mim]^+$ and $[P_{666,14}]^+$ could be elucidated for the first time. Along with demonstrating the suitability of the Dissolve methodology for the analysis of IL data, a detailed procedure for the synthesis of fully deuteriated D_{68}-$[P_{666,14}][NTf_2]$ is also reported. This study could pave way to a new strand of neutron scattering studies, involving ionic liquids with long alkyl chains.

Chapter 4 was motivated by, and is a continuation of, previous work in the Swadźba-Kwaśny group. The group reported the first direct experimental evidence for the formation of the encounter complex of the frustrated Lewis pair (FLP), tris(pentafluoro)phenyl borane (BCF) and tris(*tert*-butyl) phosphine (P^tBu_3), in benzene by neutron scattering, and in an ionic liquid, $[C_{10}mim][NTf_2]$, by NMR spectroscopy. This work confirmed that neutron scattering can be used for the direct observation of FLP encounter complexes. In this thesis, the focus was on modelling and interpretation of neutron scattering data for the FLP in $[C_2mim][NTf_2]$ and $[C_{10}mim][NTf_2]$, the latter enabled by the Dissolve software.

Finally, the work in Chapter 5 was inspired by the earlier work in the Swadźba-Kwaśny group on Lewis acidity and Lewis acidic ionic liquids. The motivation was the desire to develop a Lewis acidity scale which was not dependent on a reference base. A new probe-free approach to studying Lewis acidity of boron compounds is described using B 1s X-ray absorption spectroscopy (XAS). Preliminary results validated this new approach as a mean of getting insight into Lewis acidity of tricoordinate compounds of boron. This work was intended to progress to measuring Lewis acidity of ionic liquids, and was the original focus of my PhD studies. However, with the emergence of COVID-19, visits to synchrotron facilities to carry out this work was not possible, and laboratory work had been disrupted for several months. Therefore, the focus of this PhD work shifted to neutron scattering studies, working with data collected just before the COVID-19 outbreak. The work in Chapter 5 has discussed the problem of quantifying Lewis acidity and has highlighted the many different factors which can affect Lewis acidity. It has generated preliminary data and opened up a new strand of research in the group, now taken over by a new PhD student, who is jointly supervised by Diamond and ISIS scientists.

Publications

1) L. C. Brown, A. McGrogan, Y. Delavoux, J. M. Hogg, J. D. Holbrey, H. Q. N. Gunaratne, M. Swadźba-Kwaśny, J. P. Tellam and S. E. Youngs, The synthesis of deuteriated tri-tert-butyl phosphine, *J. Label. Compd. Radiopharm.,* 2022, **65**, 338-342

2) Z. Wojnarowska, S. Cheng, B. Yao, M. Swadzba-Kwasny, S. McLaughlin, A. McGrogan, Y. Delavoux and M. Paluch, Pressure-induced liquid-liquid transition in a family of ionic materials, *Nat. Commun.*, 2022, **13**, 1–10.

3) A. McGrogan, E. L. Byrne, T. G. A. Youngs, A. Chrobok, R. Guiney, T. F. Headen and J. D. Holbrey, The structure of protic ionic liquids based on sulfuric acid, doped with excess of sulfuric acid or with water, *Phys. Chem. Chem. Phys.,* 2023, **25**, 9785–9795. ***Cover paper and selected for 2023 PCCP HOT articles.***

4) B. Yao, M. Paluch, M. Dulski, C. Quinn, S. McLaughlin, A. McGrogan, M. Swadzba-Kwasny and Z. Wojnarowska, Tailoring Phosphonium Ionic Liquids for a Liquid-Liquid Phase Transition, *J. Phys. Chem. Lett.*, 2023, **14**, 2958–2964.

5) B. Yao, M. Paluch, J. Paturej, S. Mclaughlin, A. McGrogan, M. Swadzba-Kwasny, J. Shen, B. Ruta, M. Rosenthal, J. Liu, D. Kruk and Z. Wojnarowska, Self-assembled nanostructures in aprotic ionic liquids facilitate charge transport at elevated pressure, *ACS Appl. Mater. Interfaces*, 2023, **15**, 39417−39425

6) A. McGrogan, J. Lafferty, L. O'Neill, L. Brown, M. Young, P. Goodrich, M. Muldoon, L. Moura, T. Youngs, S. Youngs, T. Hughes, J. D. Holbrey and M. Swadźba-Kwaśny, The liquid structure of ionic liquids with $[NTf_2]^-$ anions from neutron scattering, submitted to *J. Phys. Chem. B*. ***Invited submission to Special Issue - COIL-9: 9th Congress on Ionic Liquids.***

7) A. McGrogan, L. C. Brown, L. R. Marques, R. A. Ando, L. Moura, T. Youngs, S. Youngs, S. Imberti, S. Gärtner, J. D. Holbrey and M. Swadźba-Kwaśny, Experimental evidence for ionic liquids enhancing and fine-tuning the formation of encounter complex in frustrated Lewis pairs, in preparation.

8) F. F. M. Yasin, A. McGrogan, F. Coleman, M. Sateriale, N. Malviya F. Bellino, Y. Delavoux, A. Dolfi, G. Srinivasan and M. Swadźba-Kwaśny, Tribological behaviour of phosphorous- and sulfur-free boron compounds as lubricant additives, *Tribol. Lett.,* 2023, in preparation.

9) J. M. Young, A. McGrogan, T. Hughes, S. Fourmentin, M. Swadźba-Kwaśny, L. Moura, J. D. Holbrey, Cyclodextrin-levulinic acid formulations with water: DES in water or water in DES? - in preparation

Conference presentations

1) *Hydrogen activation using frustrated Lewis pairs*, Shell Energy Transition Campus Amsterdam, Netherlands, June 2023, (oral)

2) *Quantifying acidity of boron Lewis acids,* Ionic Liquids Gordon Research Conference, Maine, U.S, August 2022 (poster)

3) *Borenium ionic liquids and other boron Lewis acids,* 28th EUCHEM Conference on Molten Salts and Ionic Liquids (Euchemsil), Patras, Greece, June 2022 (oral)

4) *The structure of protic ionic liquids based on sulfuric acid, doped with excess of sulfuric acid or with water,* 6th International Conference on Ionic Liquid-Based Materials (ILMAT-VI), Strasbourg, France, November 2021 (oral)

5) *The structure of protic ionic liquids based on sulfuric acid, doped with excess of sulfuric acid or with water,* ISIS student meeting (ISM), Oxfordshire, United Kingdom, October 2021 (oral)

6) *Boron Lewis acids: structure and applications,* 72nd Irish Chemistry Colloquium, MS teams, June 2021 (thesis in three)

7) *Boron Lewis acids: structure and applications,* Dalton - Joint Interest Group Meeting and DYME, MS Teams, June 2021 (poster)

Table of Contents

List of Figures

List of tables

Abbreviations

AN - Acceptor number

BOB - Bis(oxalate)borate

CCR - Closed cycle refrigerator

C_nMIM – 1-alkyl-3-methylimidazolium

COM - Centre of mass

DCM - Dichloromethane

DMSO - Dimethylsulfoxide

DSC - Differential scanning calorimetry

EPR - Electron paramagnetic resonance

EPSR - Electron potential structure refinement

ESI-MS - Electrospray ionisation mass spectrometry

ESP - Electrostatic potential

FIA - Fluoride ion affinity

FLP - Frustrated Lewis pair

GEI - Global electrophilicity index

HIA - Hydride ion affinity

HSAB - Hard soft acid base

IL - Ionic liquid

LLT - Liquid-liquid transition

LUMO - Lowest unoccupied molecular orbital

MD - Molecular dynamics

NIMROD - Near and intermediate range order diffractometer

NMR - Nuclear magnetic resonance

PIL - Protic ionic liquid

pRDF - Partial radial distribution functions

RDF - Radial distribution function

SANDALS - Small angle neutron diffractometer for amorphous and liquid samples

SDF - Spatial distribution function

XAS - X-ray absorption spectroscopy

XPS - X-ray photoelectron spectroscopy

Chapter 1

Introduction

1. Introduction

1.1 Ionic liquids

Ionic liquids (ILs) are arbitrarily defined as molten salts that are liquid below 100 °C.[1] They generally have negligible vapour pressure, high thermal stability and wide liquidus range. The properties of ILs, especially their low melting points are defined by their chemical structure. Typically, the bulky and asymmetric nature of the ions, especially the cation, reduce the columbic interactions between ions and disrupt the lattice packing. The electrostatic forces are reduced due to the larger size of ions, resulting in a greater separation of charged centres. Additionally, dependent on the functional groups present, the charge can be distributed over a large volume. The asymmetry of one or both ions disrupts the lattice packing and destabilises the solid phase. Therefore, the liquid phase is favoured and ILs with low melting points around room temperature can be prepared.[2] By changing the cation or anion of ILs, their physical properties can be modified, and a large library of ILs exist (Figure 1). ILs have been known for a long time, since their first discovery by Paul Walden in 1914, who prepared a molten ethylammonium nitrate salt. However, it has only been in the last three decades that the interest in ionic liquids has grown significantly and ionic liquids have been investigated in a wide range of areas.[2–4]

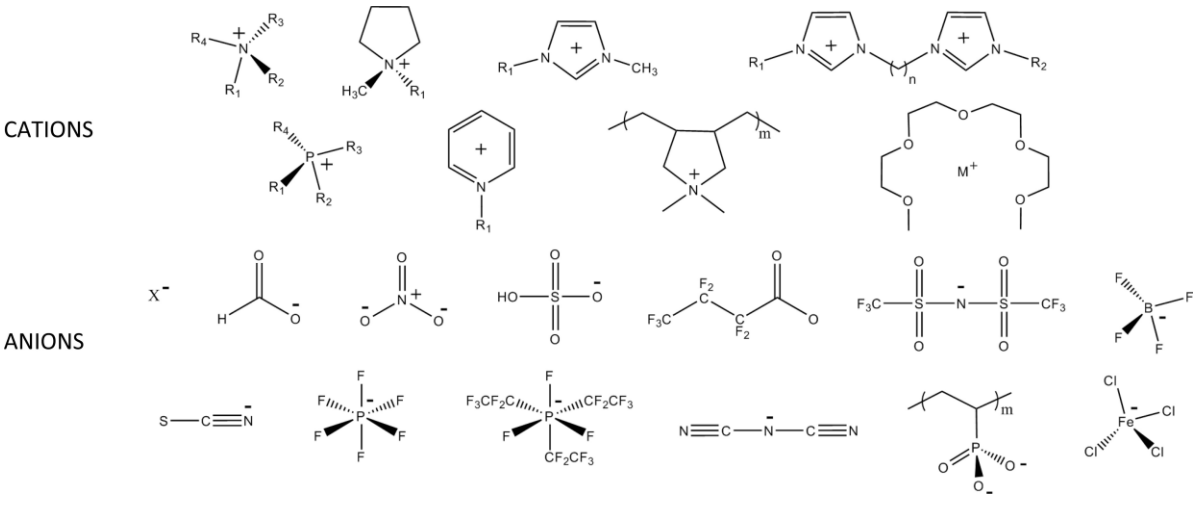

Figure 1. Examples of common cations and anions used to prepare ionic liquids.[2]

The applications and properties of ionic liquids are linked to their structure. The structure of liquids is more challenging to define, than those of gases and solids, mostly due to their disordered and isotropic nature.[5] A

liquid is a fluid of solid-like density and has a gas-like ability to flow. Liquids do not have long-range order which characterises solid crystalline materials, but they are not completely uncorrelated, like a gas. Neutron diffraction and Monte Carlo (MC) simulation methods are effective techniques to help to elucidate the structure of liquids and explain their behaviour.[6,7] Neutron diffraction has been used to determine the structure of many liquid systems, from water[7,8] and organic solvents[9–11] to more complex systems including ionic liquids[12–14] as well as investigating the interactions between ILs and solute molecules.[15]

The basic liquid state structure of ionic liquids is dominated by Coulombic interactions and is comprised of alternating shells of anions and cations.[2,16] Understanding the arrangement of ions in ILs is crucial as many of their properties and applications are directly related to their structure. One of the most important features of ILs is their solvent nanostructure. Most ILs are structurally heterogeneous,[17–22] which is very different to the initial description of liquids as homogenous systems.[23,24] A range of models have been used to describe this structure such as, ion pairs, hydrogen bond networks, ion clusters and self-assembled nanoscale structuring.[2]

1.1.1 Imidazolium based ionic liquids

The most common IL cations are derived from nitrogen or phosphorus bases. 1-alkyl-3-methylimidazolium cations, $[C_n\text{mim}]^+$, have served as workhorse IL cations for decades, since their propensity to give room-temperature molten salts with chloroaluminate anions was reported by Hussey,[25] and then extended to air- and water-stable ionic liquids.[26,27] Early molecular dynamic (MD) simulations showed that the structure of $[C_n\text{mim}]^+$ ILs are characterised by nanostructure formation.[20,21,28,29] At first, this was attributed to the aggregation of alkyl chains of sufficient length, while the polar regions (e.g. imidazolium ring and anions) were distributed homogeneously.[21] However, an atomistic simulation then suggested that there is also aggregation of these polar domains which exists alongside the non-polar domains of the alkyl chains.[22] Increasing the alkyl chain length equal to or above C_4 resulted in increased size of non-polar domains, which became connected in a bicontinuous, sponge-like arrangement (Figure 2). At shorter alkyl lengths of C_2, small globular non-polar domains are observed.

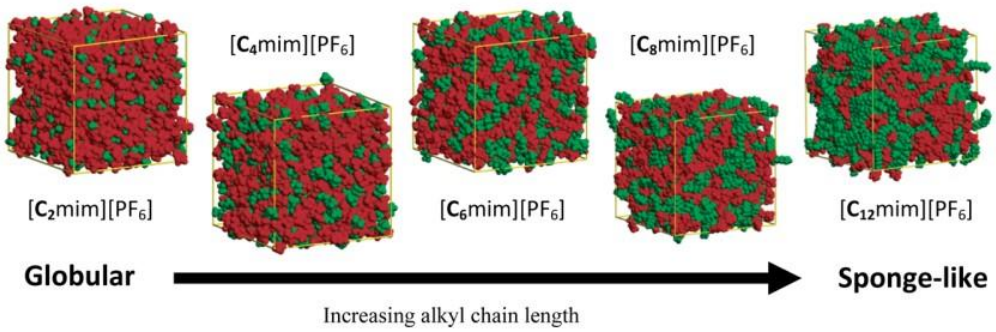

Figure 2. Snapshots of simulation boxes representing the bulk structure of [C$_n$mim][PF$_6$] ILs. Colour coding shows the polar regions (anion and imidazolium ring) in red and non-polar regions (alkyl chain) in green that form.[2]

X-ray diffraction provides strong evidence of this IL self-assembled nanostructure.[19,30–33] A peak at low *q* values (larger distances) in diffraction patterns is indicative of alkyl chain aggregation, that separates the charged networks. Figure 3 shows computationally derived square functions (S(*q*)) for ILs and molecular solvents from X-ray scattering. ILs typically display three peaks in the structure function S(*q*): a peak at larger *q* values (pink area in Figure 3, right) represents correlations between ions of opposite charge; the intermediate peak, which typically appears around 0.85 Å^{-1} (blue area in Figure 3, right) is referred to as the charge alternation peak, as it corresponds to the separation of ions of the same charge; finally, the peak at lowest *q* is related to ion-ion distances that are separated by the non-polar domains (green area in Figure 3, right). This diffraction pattern differs from that of molecular solvents, where only one feature is observed at the largest value of *q,* except for methanol which shows a small peak related to hydrogen bonding (Figure 3, left).[34]

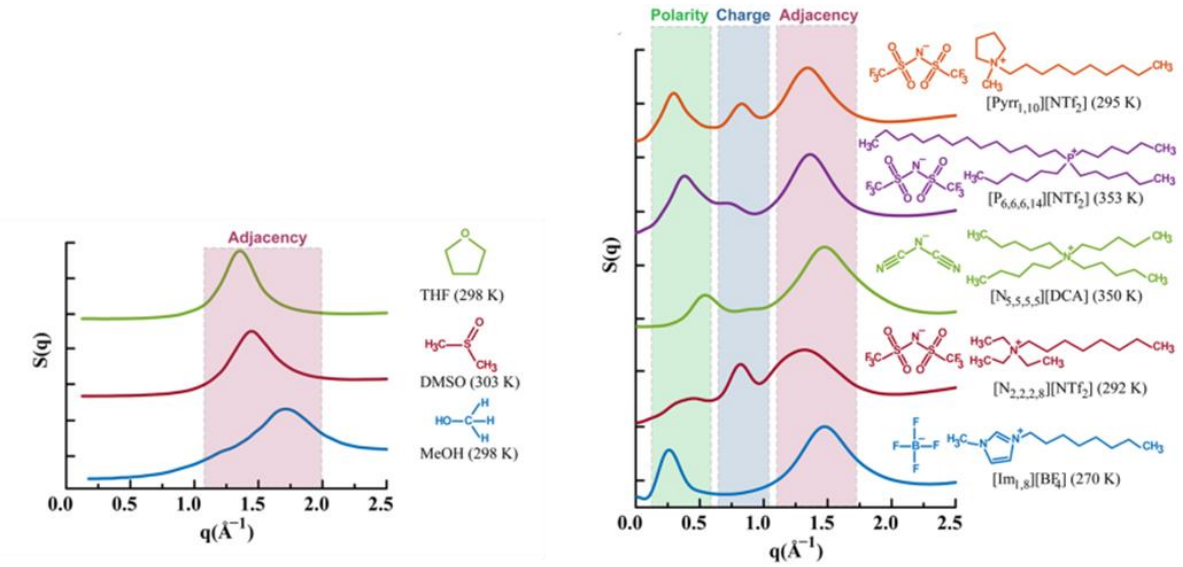

Figure 3. Computationally derived square functions, S(*q*), for molecular solvents (left) and ionic liquids (right) based on data from Kashyap *et al*.[31,35–37] and graph generated by Araque *et. al.*[34]

In some cases, the charge alternation peak (intermediate peak) is not present in the S(*q*), as exemplified by the S(q) plot for $[Im_{1,8}][BF_4]$ in Figure 3. This is due to the cancellation of peaks and anti-peaks at the same *q* value. For example, for the charge alternation peak, one finds an increase in density of charges of the same type (peak), but this means that there is also a decrease of charges of opposite signs (anti-peak). A similar trend is also observed for the peak at the lowest *q* value, typically only observed in ILs with long alkyl chains. This peak corresponds to polar-apolar alternation, where polar-polar and apolar-apolar densities contribute to the pre-peak and polar-apolar densities contribute to the anti-peak.[37] Therefore, the structure of ILs is defined by charge and polar alternation; polar-apolar alternation defines their nanoscale ordering and positive-negative charge alternation defines short length scale order.

The pre-peak, and therefore the existence of nanoscale segregation, was first identified experimentally by Triolo and co-workers in 2007, using X-ray scattering.[19] Subsequent studies[18,32,38,39] by the same group followed, supporting the formation of the sponge-like nanostructure, which exists with alkyl chains equal to a butyl group or longer. It was then identified by many other groups, including Hardacre *et. al*[40] who has published a number of important articles on the structure of aprotic ionic liquids, using neutron scattering.[16,40–42] In this particular paper, they were able to identify the pre-peak by neutron scattering at low *Q* in a series of 1-alkyl-3-methylimidazolium hexafluorophosphate ILs, $[C_n mim][PF_6]$, where $n = 4$, 6, and 8.[37] They investigated the peak position with increasing alkyl chain length and reported that the peak at low *Q* sharpens, increases in intensity, and shifts to longer distances. The longer correlation distance makes sense as the size of the non-polar domain is larger with longer alkyl chains and there is greater separation of the polar components. It

might be expected for the intensity of the peak to decrease as the polar components are further apart and it is a less ordered system.

Hydrogen bonding is an important feature in ionic liquids. A hydrogen bonded network of ions, which is a common characteristic of imidazolium crystals, is retained in the liquid phase.[43] These hydrogen bonds typically form between the anions and the hydrogens of the imidazolium ring as well as through the methyl or methylene groups directly attached to the ring, with each cation typically surrounded by at least three anions. Hardacre and co-workers[41] were the first to study ionic liquids using neutron diffraction. They reported significant charge ordering in the ionic liquid 1,3-dimethylimidazolium chloride and found consistency between the crystal and liquid structures. A higher degree of interaction between the ring of the imidazolium cation and the anion was observed, which did not correlate with previous findings of the system when only using computer simulations. The liquid structure of 1,3-dimethylimidazolium hexafluorophosphate, $[C_1mim][PF_6]$, was then investigated by the same group[42] and compared to the structure for the chloride salt. They reported similar structures between the two systems, which may be surprising due to the difference in hydrogen bonding ability and the size of the anion. A simple expansion of the structure in $[C_1mim][PF_6]$ was reported due to the larger size of the anion. The group then investigated the interactions between ionic liquids and solutes such as benzene[15] and glycerol.[44] Finally, 1-ethyl-3-methylimidazolium acetate, $[C_2mim][OAc]$, was studied by neutron scattering and MD simulations. Acetate, like chloride, is a strong hydrogen bond acceptor, which explains why the greatest area of association of the anions was with the hydrogen atoms of the imidazolium ring (Figure 4).[45]

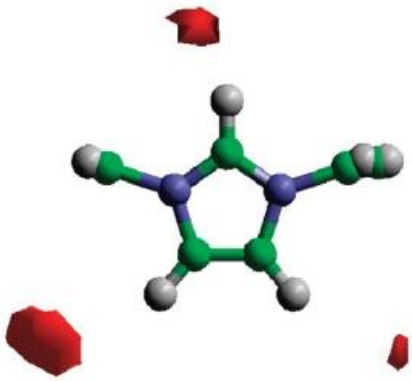

Figure 4. Probability densities of anions (red surfaces) around a central cation in 1-ethyl-3-methylimidazolium acetate at 323 K calculated through MD simulation. Surfaces are drawn to encompass the top 5% of ions within a distance corresponding to the position of the first minimum in the respective radial distribution functions.

Hardacre and co-workers[46] also investigated the structure of $[C_1mim][NTf_2]$ by neutron scattering, and reported significantly smaller charge ordering compared to the chloride and hexafluorophosphate salts,

resulting from larger size and diffuse charge density of the $[NTf_2]^-$ anion. The low hydrogen bonding ability of the anion was evident from spatial distribution functions (SDFs), where there was a larger association of the anion with the π system of the ring, as opposed to the ring hydrogens. The bis(trifluoromethanesulfonyl)amide salt showed little similarity between the liquid and crystal structures, in contrast to the other two salts. This was attributed to the conformational flexibility of the anion, which can adopt both *cis* and *trans* conformers in the liquid state in contrast to fixed conformers in the solid.[47] The group reported that, across the three ILs, each ion was surrounded by around seven counterions of opposite charge.

1.1.2 Phosphonium based ionic liquids

Tetraalkylphosphonium ILs are of interest as they have a wide liquidus range, as well as relatively high thermal and electrochemical stability, making them attractive options for energy storage applications (batteries and supercapacitors)[48–50] and in ammonia generation.[51] They are hydrophobic, which has sparked interest in their use in liquid-liquid separations, from metals to biomass.[52–59] There has been several studies on the structure of ILs based on the $[P_{666,14}]$ cation.[30,31,60–63] Gontrani *et al.*[30] studied the tetradecyltrihexylphosphonium chloride IL using X-ray scattering and MD simulations, and reported that the structure is dominated by strong cation-anion interactions and nanoscale segregation, similar to long-chained imidazolium-based ILs.

Low degree of ionicity can be attributed to ion pairing.[64] The Walden plot for $[P_{666,14}]Cl$ showed conductivity significantly lower than would be expected given the viscosity.[65] This was rationalised by the very small size of Cl^-, which can get close to the positively charged phosphonium center and form strong interactions, while the long cation alkyl chains can effectively align and trap the chloride anion. In such extreme cases, these ILs where described by MacFarlane and co-workers as liquid ion pairs: an interesting intermediate between true molecular solvents and true ionic liquids.[65] Considering bulkier anions, such as bis(trifluoromethylsulfonylimide) in $[P_{666,14}][NTf_2]$, increased anion size and its lower basicity prevent such a close contact; this IL has higher ionicity and does not form liquid ion pairs.[65] X-ray scattering and molecular dynamics simulation studies of this IL have been reported by Liu and co-workers[61] and the Margulis group.[60,31,66] Similarly to many other ILs, three characteristic intermolecular peaks can be detected in the structure function $S(q)$, in the range of 0.3 to 1.5 $Å^{-1}$.[31] It is common in many ILs that the peak at largest value of q (shortest distance) corresponds to interactions between oppositely charged ions. This is the case with $[P_{666,14}][NTf_2]$ but there are also hydrophobic interactions that contribute to this peak because of the long alkyl chains on the cations. A peak at 0.75 $Å^{-1}$ is present, signature of cation-cation and anion-anion interactions. The pre-peak is expected to appear for this system as it is characteristic of systems with long alkyl chains. It was reported that the main contribution to this peak is from the second anion-anion sphere, correlated with

the distribution of the long alkyl chains. These findings also relate to the SDFs which show that the anions surround a cation close to the phosphonium centre and the cations form a ring about the nitrogen atom of the anion.

The Margulis group has particularly focused on this long-range correlation for $[P_{666,14}][NTf_2]$ as well as other anions and investigated the effect of temperature on this pre-peak.[60,66] They showed that a temperature increase consistently results in an increase of intensity of the pre-peak, independent of the anion. This suggests higher intermediate range order at higher temperatures. This was unexpected, and does not correlate with other IL systems.[19,67] Margulis and co-workers have rationalised this finding by analysing the different interactions and their contributions to the pre-peak. They observed that at higher temperatures, there is an increase in order of the polar components and a decrease in order of the non-polar alkyl chains. They state that anions are often most important as reporters of structure,[35] and as anions are polar components of the system, it makes sense that the increased order of the polar components has a larger contribution to the intensity of the pre-peak than the decreased order of the non-polar components, resulting in an increase in pre-peak intensity. Figure 5 shows the S(*q*) of $[P_{666,14}][NTf_2]$ at different temperatures which shows the increase in intensity of the pre-peak at increasing temperature.[66]

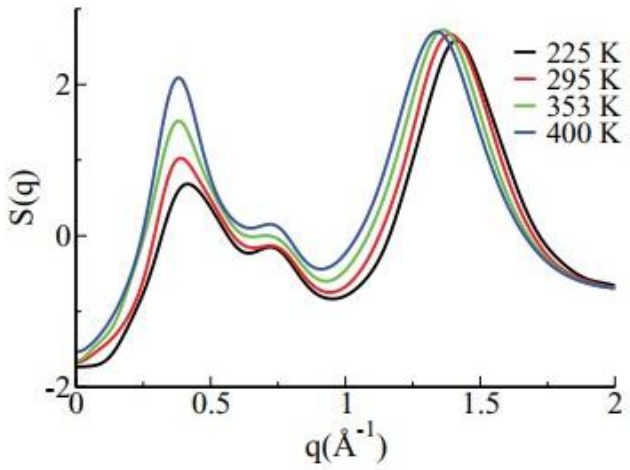

Figure 5. Structure functions S(q) of $[P_{666,14}][NTf_2]$ recorded at different temperatures.[66]

Liu *et. al* also studied the structure of $[P_{666,14}][NTf_2]$ by MD and explored the influence of temperature on the thermodynamic and transport properties.[61] Radial distribution functions (RDFs) of cations and anions were calculated at different temperatures, and analysed to determine the reason for high viscosities. The RDFs showed strong interactions between protons alpha to the phosphorus and the O atoms of the anion, and postulated the formation of hydrogen bonds, P-C-H···O=S. This demonstrates that, although MacFarlane and co-workers[65] did not see significant ion pairing in $[P_{666,14}][NTf_2]$, close contacts between the centres of charges

persist. They reported that three anions surround a cation in the first coordination shell. They also observed that with increasing temperature, the interaction between ions is weakened (Figure 6). This is an expected result and can be used to explain the lower viscosity at higher temperature. The group also examined some transport properties of $[P_{666,14}][NTf_2]$ and reported an increase in self-diffusion coefficients and velocities at higher temperatures. The anion experiences greater diffusivity compared to the cation due to its significantly smaller size. At higher temperatures, a greater increase in diffusion coefficient is observed for the cation compared to the anion. This may be due to the greater flexibility of the alkyl chains with higher temperature.

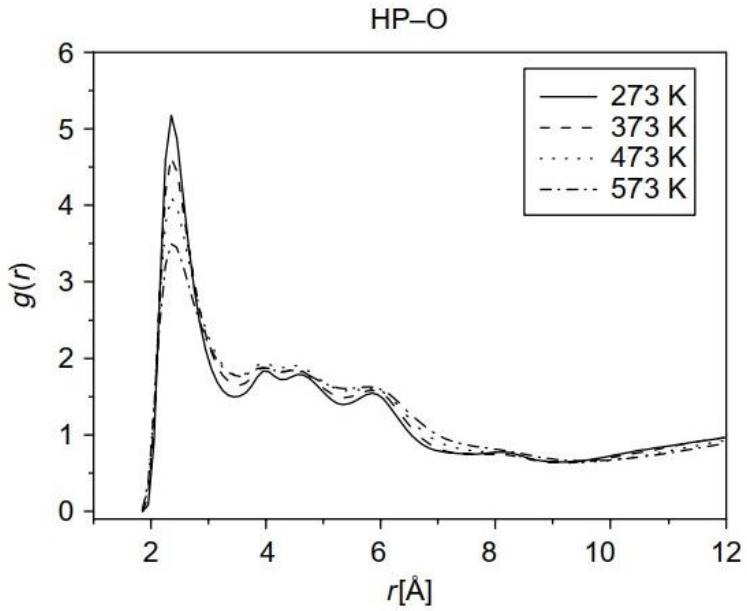

Figure 6. Specific site-site RDFs for $[P_{666,14}][NTf_2]$ between the protons alpha to P atom (HP) and the O atom of the anion, showing that with higher temperature, there are weaker interactions.[61]

1.1.3 Protic ionic liquids

Protic ionic liquids are easily formed *via* proton transfer from a Brønsted acid (HA) to a Brønsted base (HB) as shown in Equation 1. Their speciation is complicated due to equilibria arising from incomplete proton transfer.[68,69]

$$HA + B \rightleftharpoons [HB]^+ + A^-$$

Equation 1

It was suggested that the difference between pK_a (ΔpK_a) of the acid and base could be a reliable indicator of the extent of proton transfer in protic ionic liquids.[70] Angell and co-workers[70] used the relationship between

the observed boiling points and ΔpK_a determined in dilute aqueous solutions and reported that a ΔpK_a of 10 was required to ensure full proton transfer. Watanabe and co-workers[71] then stated that for DBU-based protic ionic liquids, a ΔpKa of 15 was required to achieve full proton transfer. Generally, when considering the same base, both proton transfer and ionicity tend to increase as the pKa of the acid increases. However, the hydrogen-bonding capabilities of the bases play a crucial role. An investigation conducted by Stoimienovski and colleagues[72] involving primary, secondary, and ternary amines combined with acetic acid revealed that a ΔpKa of 4 was adequate to achieve 99% proton transfer when primary amines were used. Conversely, ternary amines with the same ΔpKa value were incapable of forming a homogeneous mixture with acetic acid.

In a recent publication, Mariani, Passerini, and their colleagues[64] emphasise that although ionicity and proton transfer share a connection, they are not synonymous. They refer to MacFarlane and Seddon's[73] definition of PILs as “a salt that melts below 100 °C and contains at least 99% of ions” to describe proton transfer as primarily concerned with the number of ions in the system and points out that it does not equate to ionicity. Ionicity, on the other hand, is concerned with the number of free charge carriers, and will be decreased by factors like close-contact ion pairing.

There has been much deliberation over the speciation of protic ionic liquids, in particular of those with non-stoichiometric composition. In 1981, Arnett and co-workers, conducted thermodynamic studies which led them to suggest that ethylammonium nitrate (EAN) had a 3D hydrogen bonded network complementary to that of water (Figure 7).[2,74] They investigated gas solubilities in EAN as a function of temperature and reported entropy and enthalpy values which when compared to water, were very similar. This 3D network structure was then confirmed by far IR spectroscopy and DFT calculations.[75] Neutron[14,2,17,76,77] and X-ray[78] scattering studies on EAN have also emphasised the importance of hydrogen bonding in elucidating the structure of protic ionic liquids. Due to the extensive hydrogen bonding that occurs, nanostructures form in all protic ionic liquid systems. Atkin and co-workers[14] studied the size, direction, strength, and distribution of hydrogen bonds in several primary ammonium protic ionic liquids consisting of different anions and varying chain length. They showed that there was significant variation in the nature of the hydrogen bonds of the studied ionic liquids which is reflected in their nanostructure and physical properties. Additionally, when water was added to EAN, the liquid structure of this protic ionic liquid changed.[77] Weaker acids add another level of complexity due to incomplete proton transfer; for example, there was little evidence of proton transfer in pyridine and acetic acid mixtures, as shown by neutron scattering, even with an excess of acid. A 3D hydrogen bonded network was observed, but of oligomeric chains of acetic acid with pyridine inclusions.[12]

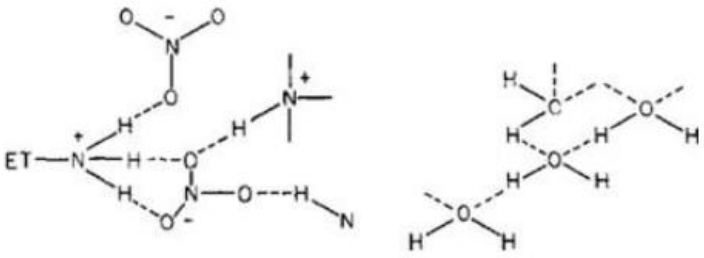

Figure 7. Arnett and co-workers proposed a hydrogen bonded network in ethylammonium nitrate (left) comparable to that of water (right).[74]

There is also an argument for the formation of hydrogen-bonded clusters, for example in protic ionic liquids synthesised from amines and excess of hydrogen halides. These studies where X is a halide ion (X = Cl^-,[79] Br^-[80] or F^-[81–86]) have reported discrete dimeric and oligomeric anionic clusters of $[X\cdots H\cdots X]^-$. In a study of mixtures of amines and trifluoroacetic acid (HTFA), the formation of discrete hydrogen bonded clusters of $[TFA(HTFA)_X]^-$ was suggested when $\chi_{HTFA} > 0.5$.[70] The same conclusions can also be found in the literature for other Brønsted acidic protic ionic liquids, including those based on sulfuric and acetic acid (Figure 8).[63,89]

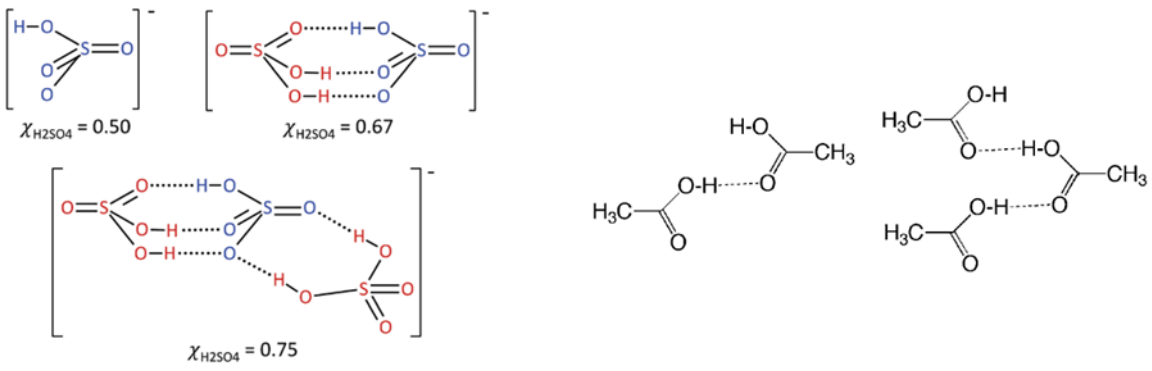

Figure 8. Left: The structure of hydrogen-bonded clusters of hydrogensulfate and sulfuric acid, $[(HSO_4)(H_2SO_4)_x]$, depending on the mole fraction of the acid, χ_{H2SO4}. For ease of comparison, atoms of the hydrogensulfate anion are represented in blue, and those of sulfuric acid are in red.[89] Right: Proposed formation of hydrogen-bonded clusters of acetic acid dimers and oligomers.[87]

1.2 Neutron scattering

1.2.1 Background and principles of neutron scattering

A neutron is a subatomic particle with no net charge and a mass of 1.675×10^{-27} kg, slightly higher than that of a proton. Neutrons have an associated de Broglie wavelength, allowing them to be used as probes in diffraction experiments. Neutrons primarily interact with the nucleus, as opposed to X-rays that interact chiefly with the electron cloud. Therefore, neutrons are more highly penetrating without interaction with the sample, and neutron scattering is a non-destructive technique. Because neutrons interact with the core, not with the electron cloud that accounts for the atom size, neutron scattering is not dependent on the atomic number, which makes it an effective technique for studying systems containing light elements (Figure 9). Furthermore, the neutron scattering power of an atom is isotope-specific, which enables a powerful tool of isotopic substitution experiments. This is a valuable technique to obtain chemically similar datasets, but with different scattering patterns. Hydrogen/deuterium substitution is the most common, using the fact that the scattering lengths between the isotopes are very different (^{1}H, b_H = -3.74 fm and ^{2}D, b_D = 6.67 fm). As a nucleus is very small in size, most neutrons pass through the sample without interacting with it, which means that larger sample sizes/longer acquisition times are required for neutron experiments, when compared to X-rays.

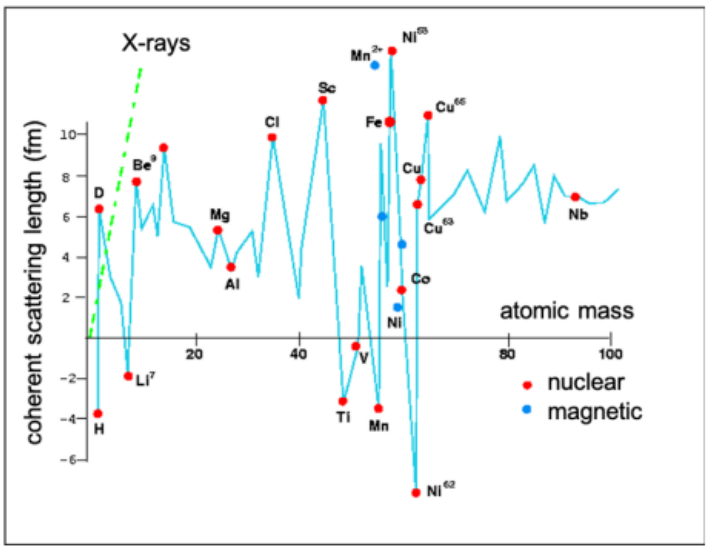

Figure 9. Coherent scattering lengths of isotopes, reproduced from reference [90].

There are two main ways of generating neutrons for scattering experiments: the use of a nuclear reactor or *via* spallation. The first method produces a continuous stream of neutrons using nuclear fission of uranium, and is used at the Institut Laue-Langevin (ILL) in France. These high energy neutrons must subsequently lose sufficient energy, which is achieved using a moderator, to make them useful for scattering applications. The second method uses a more modern and significantly safer spallation source. It produces beams of neutrons that are pulsed, generated when a pulse of high-energy protons strikes a heavy metal target (W, Ta, or U). This method is used at the ISIS Pulsed Neutron and Muon Source and due to the pulsed nature of the beam, the time-of-flight (TOF) method is used to measure the neutron energy. In contrast to nuclear reactor sources, there is no need for a monochromator, increasing the effective number of neutrons that can be used in the experiment.

1.2.2 Theory of neutron scattering

Neutrons have an associated wavelength called de Broglie wavelength. A diffraction pattern is obtained by measuring the intensity of the scattered beam as a function of the scattering vector *Q* (relating to scattering angle 2θ and wavelength λ*)* - Equation 2. *Q* is translated into distances, *d,* by the reciprocal relationship in Equation 3. Low *Q* values correspond to larger *d* spacings, and higher *Q* values - to smaller *d* spacings.

$$Q = \frac{4\pi sin\theta}{\lambda}$$

Equation 2

$$Q = \frac{2\pi}{d}$$

Equation 3

The differential scattering cross-section of the sample is measured which contains the information related to the structure of the sample. It is then subsequently calibrated using a standard, and appropriate corrections and background subtractions for multiple and inelastic scattering are made. This results in the total structure factor, *F(Q*) - Equation 4.

$$F(Q) = \sum_{i,j}(2 - \delta_{ij})c_i c_j b_i b_j S_{ij}(Q)$$

Equation 4

F(Q) is the weighted sum of all the partial structure factors between the different atom types in the system, indicated by *i* and *j*. The c_i, c_j values are the atomic fractions of the different atoms in the sample, b_i, b_j are the atomic scattering lengths and $S_{ij}(Q)$ is the partial structure factor between the different atom types and gives a measure of the structural correlations between the different atomic sites. Finally, the $(2 - \delta_{ij})$ term has been introduced to avoid counting atom pairs twice.

Fourier transform results in the radial distribution functions, $g_{ij}(r)$, which describes statistically the probability of finding an atom at a distance *r* from any other atom. This is expressed in Equation 5 where ρ is the atomic density and G(r) is a weighted sum of the pair distribution functions,[91] whereas the total radial distribution function, G(r), is expressed in Equation 6 ($c_i = p_i/p$ and p_i is the number density of atom type i).

$$G(r) = \frac{1}{(2\pi)^3 p}\int_0^\infty 4\pi Q^2 F(Q)\frac{sinQr}{Qr}dQ$$

Equation 5

$$\mathrm{G}(\boldsymbol{r}) = \sum_i c_i \delta(\boldsymbol{r}) + p\sum_{i,j\geq i}(2 - \delta_{ij})c_i c_j g_{ij}(\boldsymbol{r})$$

Equation 6

Structural information for the entire system is obtained from the radial distribution function. An exemplar RDF for liquid nickel is shown in Figure 10. From this, the probability of locating atoms at a specific distance *r* from the reference point can be calculated. When *r* = 0, the distribution function is zero, as two atoms can't occupy the same space. The peaks represent atoms in consecutive coordination shells. The positive peaks correspond to areas of high atomic density, while the negative peaks or minima immediately following them signify reduced atomic density. Typically, the first peak has the highest intensity, due to the short-range repulsive interactions felt between atoms in the first shell. As the distance from the central atom increases (as indicated by higher *r* values), the correlations with the central atom decrease, leading to a tendency for the spectrum to approach unity.

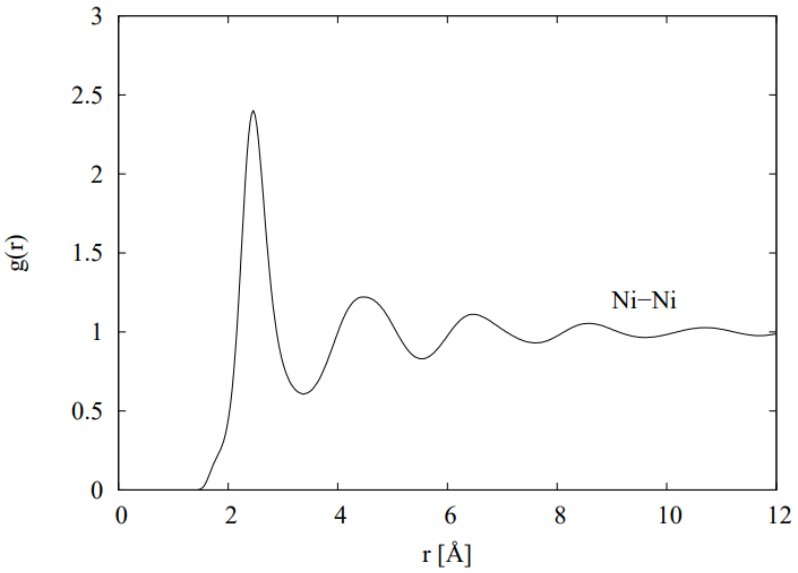

Figure 10. Radial distribution function, *g(r)*, for supercooled liquid nickel reproduced from an open source RAL Technical Report written by Soper.[92]

1.2.3 Data analysis

The Gudrun software[93] package is used for the reduction, correction and processing of neutron scattering data. The software was written by Alan Soper and other members of the Disordered Materials Group at ISIS. The initial correction includes removing instrument and sample backgrounds. Further refinement involves sample attenuation and performing multiple scattering corrections. It also reduces large inelasticity effects, which is common with light elements such as hydrogen. Conversion of the diffraction data onto an absolute length scale is possible by normalising the collected data to a known standard such as vanadium.

EPSR is a computational technique, based on a Monte Carlo simulation approach, for the interpretation of scattering data.[6] EPSR is designed to produce a 3D structure of the system under study, based on known physical and chemical restraints, that is in agreement with a set of experimental data. The foundation of EPSR is then to apply an additional interatomic potential, driving the simulation model towards the experimental data. Once this has been achieved, the structural properties of interest can be extracted from the model. Figure 11 outlines the basis of EPSR.

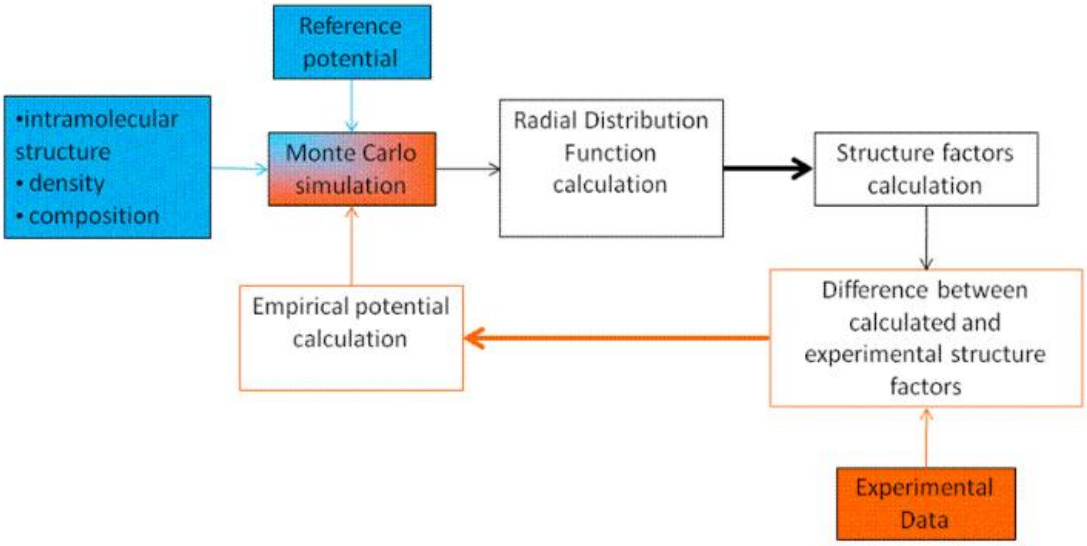

Figure 11. Outline of the steps in an EPSR simulation.

EPSR has become a crucial tool in the analysis and structural characterisation of disordered materials. However, there has been an evolution in the user community towards the study of systems of increasing complexity, demanding a full classical forcefield to better describe molecules. This demand has been addressed by a new code for the simulation of total scattering data, Dissolve, written by Tristan Youngs and his collaborators in the Disordered Materials Group at ISIS.[94] The code is similar to that of EPSR, but it has been built from the ground up with more complex and larger systems in mind. EPSR employs harmonic restraints (bonds, angles and dihedrals), which work well for small to medium molecules, but are insufficient to represent larger molecules, in particular those with greater structural flexibility. In contrast, Dissolve implements a full classical forcefield and addresses some of the major limitations of EPSR, such as simulation size and the introduction of flexibility. The code in EPSR restricts the maximum number of atoms to around 2×10^5, or the maximum number of molecules to around 5×10^4, whereas Dissolve has a million-atom capability. Dissolve also employs a customisable, fully flexible forcefield. Standard forcefields, such as OPLS-AA,[95] are typically used directly as the starting potential, but additional functional forms can be added. This allows for more complex and flexible systems to be treated with a greater level of accuracy. However, in contrast to EPSR, the user must specify a complete forcefield that they wish to use.

As it has been developed, a requirement of Dissolve was that it should implement the core routines within EPSR and demonstrate consistency with EPSR. The generated potentials and fit quality should not be expected to be identical between, as Dissolve uses a different forcefield, but they should be similar. Very recently, this benchmarking has been successfully demonstrated for benchmark systems such as water, benzene and silica,

where both codes showed slight discrepancies in the generated empirical potentials but excellent agreement with the data.[94]

1.3 Liquid-jet X-ray spectroscopy

X-rays, first discovered in 1985 by Wilhelm Conrad Röntgen,[96] are a form of electromagnetic radiation, with photon energies in the range of 0.1-100 keV. One of the most common applications of X-rays is in the characterisation of crystalline materials using X-ray diffraction (XRD). XRD is when X-rays get diffracted by the spacing between atoms in a crystalline material. The interaction of the incident X-rays with the sample results in constructive interference and scatters the X-rays at specific angles from each lattice plane of the crystal. This generates a diffraction pattern which can be analysed using Bragg's law – Equation 7. This law relates the wavelength of the incident radiation to the diffracted angle and the lattice spacing. X-rays are used to generate the diffraction pattern because their wavelength is of the same order as atomic spacings in crystals. Conversion of the diffraction peaks to *d*-spacings enables identification of materials because each material has a set of unique d-spacings.

$$n\lambda = 2d\sin\theta$$

Equation 7

While XRD gives detailed information about the arrangement of atoms in a crystal, X-ray spectroscopy involves a wide range of techniques to investigate the chemical composition and electronic structure of materials. It provides information about the local geometric structures, oxidation states and chemical bonding. Common X-ray spectroscopy techniques include X-ray photoelectron spectroscopy (XPS), X-ray fluorescence (XRF), and X-ray absorption spectroscopy (XAS). These techniques typically involve irradiating a sample with X-rays and measuring the energy of the emitted electrons.

The focus of this work was the use of XPS and XAS to study boron-based Lewis acids, with an outlook to develop a probe of Lewis acidity that is independent of a molecular (spectroscopic) probe. Studying light elements, such as boron, is challenging as the absorption edge is in the soft X-ray regime, requiring a high photon flux and high vacuum environment.

XPS is a powerful tool for probing the electronic structure and it is the X-ray technique most used to study the valence molecular orbitals (MO). It has traditionally been applied to solid samples due to the ultra-high vacuum conditions that are usually required. In XPS, the sample is irradiated with soft X-rays of a known energy

(*hv*) which induces the ejection of an electron from a particular (core or valence) orbital. The kinetic energy, E_K, of the ejected electron is measured to determine the electron binding energy, E_B, of the probed orbital (Equation 8).

$$E_B = hv - E_K$$

Equation 8

An XPS instrument contains an X-ray source, a sample chamber, an electron analyser and detector which are housed in an ultra-high vacuum (UHV) environment (10^{-9} mbar). A schematic diagram of an XPS set up is shown in Figure 12. The main reason for an UHV environment is to prevent the emitted electrons from interacting with any gaseous particles on their way to the detector. In addition, as XPS is a surface sensitive technique, it is important to reduce the possibility of contamination of the sample surface which can be achieved using UHV conditions.

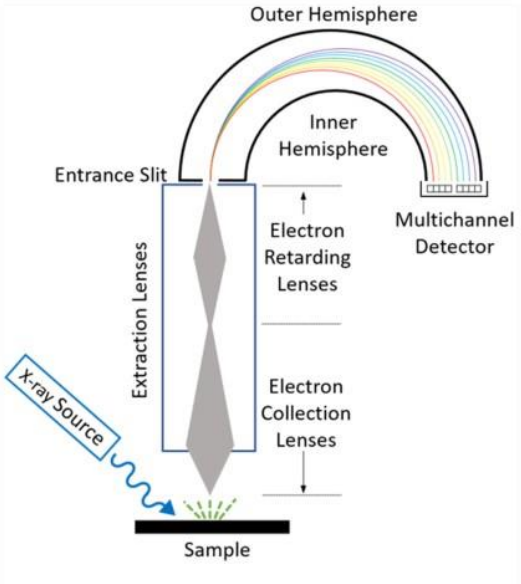

Figure 12. Schematic diagram detailing the major components of an XPS instrument.[97]

A typical spectrum is a plot of the photoelectron count *vs.* binding energy, with binding energy usually expressed in units of electron volts (eV). XPS is element specific, and each element produces a set of characteristic XPS peaks which correspond to the electron configuration of the electrons within the atoms. A characteristic wide scan XPS spectrum is shown in Figure 13 along with the high-resolution N 1s spectrum.

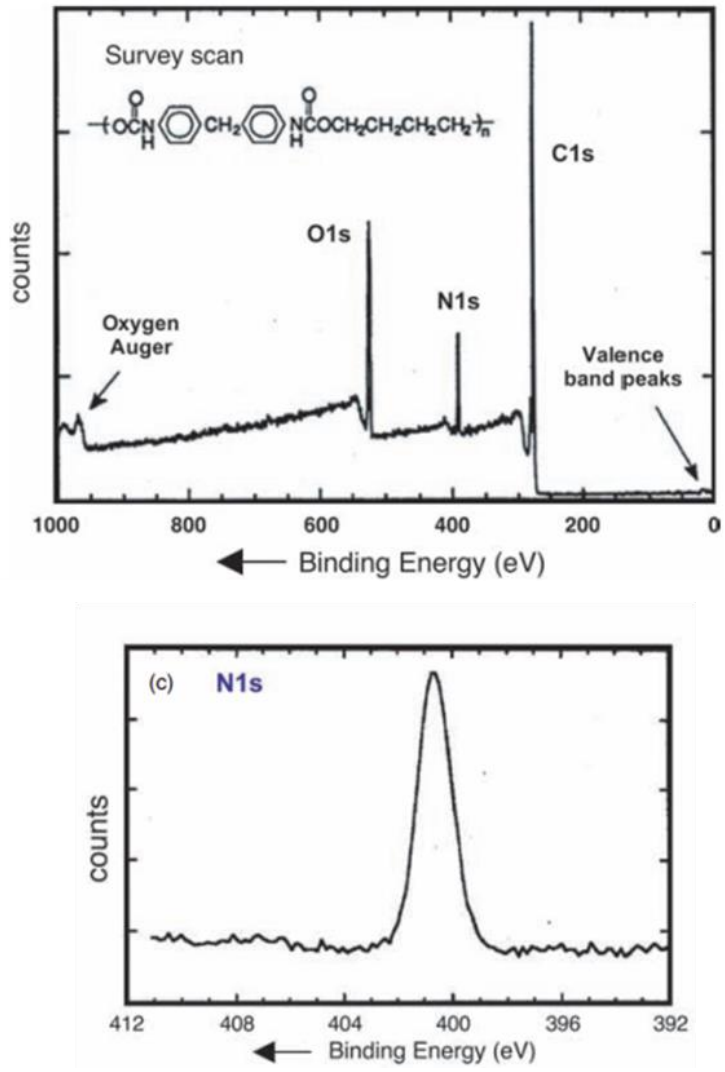

Figure 13. Top: XPS scan of a hard-segment polyurethane and bottom: N 1s high resolution XPS spectrum for the hard-segment polyurethane.[98]

XPS investigation of volatile samples, such as molecular liquids and easily subliming solids, is prohibited by UHV conditions. However, as most chemical reactions occur in solutions, it is of great interest to enable the study of electronic structure in liquid samples. It is only with the introduction of the liquid micro-jet technique, on synchrotron source XPS instruments, that liquid-phase photoelectron spectroscopy has advanced.[99–106]

With the liquid jet sample delivery methodology, pure liquids and solutions are introduced *via* a 5 – 50 µm glass capillary nozzle and typical jet velocities ranging between 30 – 120 ms^{-1} are achieved. The liquid jet's relatively small diameter and high speed enables the study of liquids with high vapor pressure in vacuum conditions necessary for XPS experiments. The distance over which electrons travel is reduced and the effective pressure is reduced by several orders of magnitude over a very short distance. This creates a

millimeter-long laminar-flow of liquid, providing a stable surface from which measurements can be performed. A free-flowing sample at high velocity also enables continuous renewal of the liquid surface.[99] Figure 14 shows a typical set up for a liquid microjet photoemission experiment.

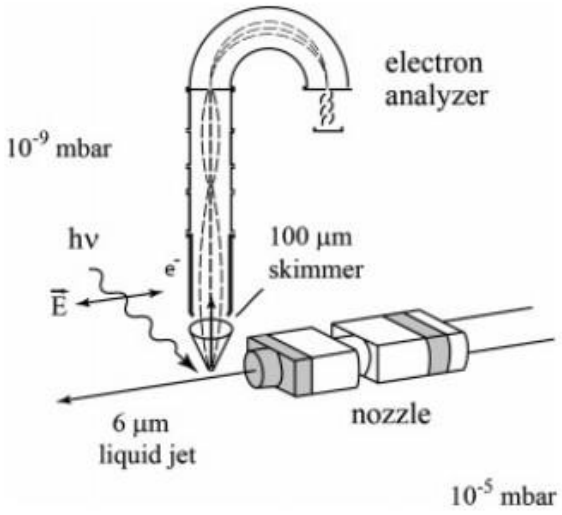

Figure 14. Experimental set-up of the liquid microjet photoemission experiment.[99]

X-ray absorption spectroscopy (XAS) is an inner shell spectroscopy, in which the X-rays interact mainly with deep core electrons (such as the 1s of boron), rather than valence electrons. When the photon energy is larger than the binding energy of a core-level electron, there is a sharp increase in absorption. This happens at specific photon energies which are element specific and are often referred to as the absorption edge. This energy corresponds to the energy required to eject a core electron into the lowest unoccupied molecular orbital (LUMO). Trigonally coordinated boron exhibits a sharp peak around 192-193 eV, which corresponds to the transition of an electron from the B 1s core state to the unoccupied B 2pz orbital (Figure 15).

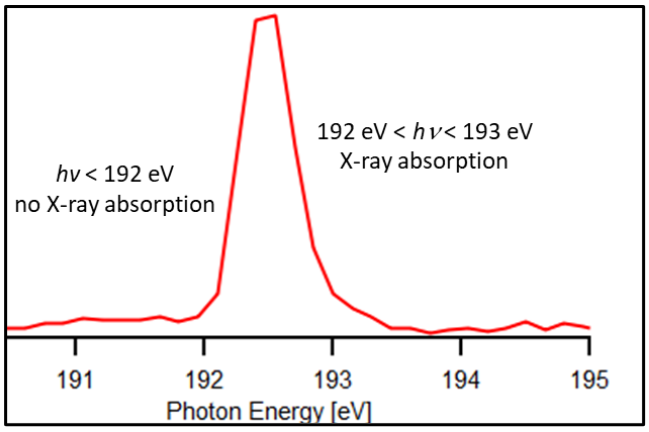

Figure 15. A typical XAS plot of trigonally coordinated boron with a sharp peak around 192-193 eV, corresponding to the transition of an electron from the B 1s core state to the unoccupied B 2pz orbital.

The boron 1s core orbital has an energy of ~200 eV, which is in the soft X-ray range, again necessitating vacuum conditions for any electronic structure measurements, to avoid strong scattering of the emitted electrons by gas molecules under ambient pressures. This means that, to study volatile samples, the liquid microjet technique is the only available – if still underutilised - approach.

The liquid-jet technique has its own limitations, which partially explains its underutilisation. Only very low viscosity solutions can be studied, which excluded neat ionic liquids. There is a limited number of solvents that are acceptable from health and safety viewpoint, which further limits the scope of experiments. Large sample sizes are required as the sample is loaded into coiled tubing and continuously pumped using a high-performance liquid chromatography (HPLC) pump at an appropriate flow rate. It is currently impossible to test samples under inert atmosphere, which prevents the study of strong Lewis acids, that tend to react with atmospheric moisture. Finally, maintaining the stability of the liquid jet can be challenging, which can affect the stability of the sample and the quality of the gathered data.

XAS usually involves the excitation of electrons from the 1s or 2p shell, so the energies are on the order of thousands of electron volts. XAS therefore requires high-energy X-ray excitation, which occurs at synchrotron facilities. They also provide tuneable X-ray energies over a wide range which is crucial for selecting the optimal X-ray energy to probe specific absorption edges.

1.4 Motivation for this work

The focus of this thesis is the structure of ionic liquids, with the aim to a) further understand structure-property relationships in industrially relevant systems and better tailor these systems for their industrial applications (neat and molecular solvent doped Brønsted acidic protic ILs based on sulfuric acid), b) test new neutron scattering analysis software, Dissolve, and pave way to a new strand of neutron scattering studies, involving ionic liquids with long alkyl chains and c) investigate the behaviour of frustrated Lewis pairs in conventional ionic liquids.

The final chapter of the thesis focuses on the study of Lewis acidity and describes the problem of quantifying Lewis acidity and the need for greater understanding of the different factors that influence Lewis acidity. The development of a new Lewis acidity scale for boron compounds using B 1s X-ray absorption spectroscopy (XAS) is introduced which is not dependent on a reference base. This was the initial focus of my PhD work, however the emergence of COVID-19 meant that visits to synchrotron facilities to carry out this work were not possible, and laboratory work was disrupted for several months. Therefore, the focus of this PhD work shifted to neutron scattering studies, working with data collected just before the COVID-19 outbreak.

Chapter 2

The structure of protic ionic liquids based on sulfuric acid

2. The structure of protic ionic liquids based on sulfuric acid

This chapter describes the investigation of the liquid structure of a Brønsted acidic protic ionic liquid system, formulated from pyridine and sulfuric acid. Neutron scattering data was used to compare the liquid structures of concentrated sulfuric acid and two pyridine/sulfuric acid protic ionic liquids (PILs) containing either excess of the acid or doped with water. The objective was to elucidate potential relationships between the local liquid structure, the effectiveness of these PILs as catalysts and solvents for esterification reaction and for treatment of lignocellulosic biomass. Neutron scattering data of isotopically substituted samples were measured on the SANDALS diffractometer and modelled using empirical potential structure refinement potential (EPSR). The data was firstly analysed using EPSR[6] (version 25) and then with Dissolve;[94] a new software for the simulation of total scattering data which implements a methodology similar to that in the EPSR code but utilises a full classical forcefield. The consistency between the two codes has been compared. The structures of the individual components used to prepare the PILs for this study are shown in Figure 16.

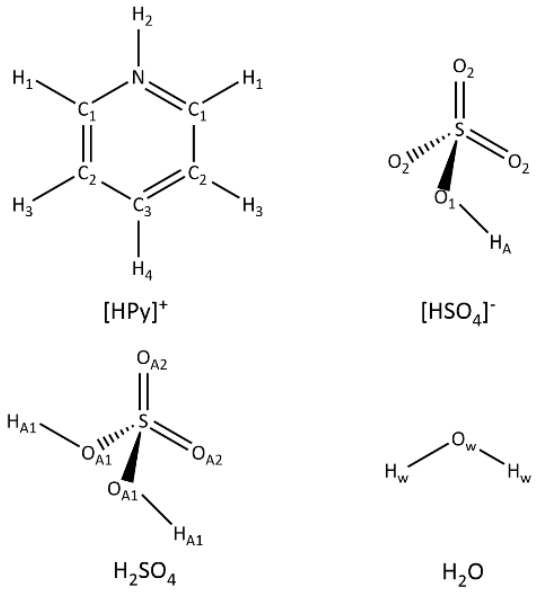

Figure 16. Atom types used in the EPSR simulation models for the pyridinium cation, hydrogen sulfate anion, molecular sulfuric acid and water.

Work reported in this chapter has been published in *Physical Chemistry Chemical Physics* as a cover paper.[107]

2.1 Introduction

2.1.1 Structure of sulfuric acid and its hydrates

In 1986, Andreani *et al.*[108] used X-ray and neutron scattering measurements to report on the ordered arrangement of almost tetrahedral SO_4 groups involved in four hydrogen bonds in liquid sulfuric acid which corresponded to the structure of solid, anhydrous sulfuric acid (Figure 17).[109,110]

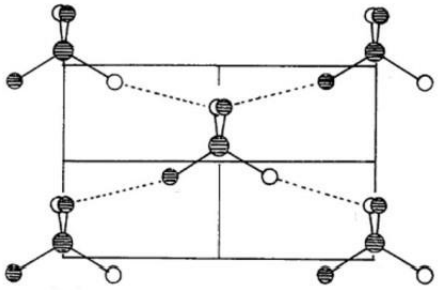

Figure 17. Structure of solid, anhydrous sulfuric acid showing hydrogen bonds arranged tetrahedrally between the sulfate groups (hydrogen atoms have been excluded for clarity).[109]

Aqueous sulfuric acid solutions, $(H_2SO_4)_x(H_2O)_{1-x}$, where x = 0.00, 0.25, 0.5, 0.75 and 0.86, were also studied and again, a strong hydrogen bonded 3D network of tetrahedral {SO_4} groups was observed.[111] However, at low concentrations of sulfuric acid, the structure more closely resembles water, but with approximately 0.2 Å shorter intermolecular $r_{O\cdots O}$ bond distances.

Furthermore, sulfuric acid hydrate liquid structures based on $H_2SO_4{\cdot}nH_2O$, where n is 4, 6½ or 8, were studied with both neutron and X-ray scattering.[112–114] All three systems consist of tetrahedral {SO_4} units surrounded by a water layer, with differing hydrogen bond networks and contains either neutral water molecules (H_2O) and/or charged species (H_3O^+ or $H_5O_2^+$). These differences in the liquid structure persisted through the phase change and were reflected in the hydrates having different lattice types and space groups in their crystalline state.

In conclusion, the most prominent structural feature in sulfuric acid and its hydrates is the formation of hydrogen bonded networks, which can differ significantly with acid-to-water ratio. No X-ray or neutron scattering work on sulfuric acid-based protic ionic liquids has been reported prior to this study; however, older papers from our group postulated the existence of clusters rather than a network (Figure 8),[89] in analogy to clustered structure suggested for acid-rich acetate ionic liquids.[87]

2.1.2 Applications

Protic ionic liquids (PILs) have been known for over 100 years, but only recently PILs based on sulfuric acid gained interest as low-cost functional solvents. With careful selection of base, PILs can be produced in the range of just US$0.78 kg^{-1}, as exemplified by triethylammonium hydrogensulfate, $[HN_{222}][HSO_4]$.[115–118] Ionic liquids formed from di- and triamines with excess of sulfuric acid, were postulated to be even cheaper.[119] This means that the cost of such PILs can be compared to the price of some common organic solvents such as acetone (US$1.30-1.40 kg^{-1}), and is significantly less expensive than typical aprotic ionic liquids, such as $[C_2mim][OAc]$ (US$ 20-101 kg^{-1}).[120] The low price arises from the combination of simple preparation (one-step acid-base neutralisation reaction), and inexpensive starting materials (commodity chemicals such as sulfuric acid). It is unsurprising, with their low cost and interesting properties, that processes utilising sulfuric acid-based PILs have sparked the interest of the industrial sector.

PILs based on sulfuric acid have shown excellent performance as acidic catalysts,[89,121–123] particularly in esterifications, where reaction equilibria was strongly shifted towards the products, much more favourably than when using concentrated sulfuric acid. This was explained by improved phase separation of the ester from the acidic PIL, compared to is separation from concentrated sulfuric acid.[89] PILs prepared from equimolar quantities of amines and sulfuric acid, but with the addition of *ca.* 10-40 wt% water, were found to be excellent solvents for biomass pre-treatment, improving the fractionation of cellulose, lignin and hemicellulose, leading to higher yields in the saccharification step.[124–126] In both applications, the enhanced performance stems from the doping of simple, stoichiometric hydrogen sulfate salts, $[HB][HSO_4]$, either with excess of an acid, or with water.

The concept of doping ionic liquids with molecular solvents (and other small molecules) has been branded the 4th evolution of ILs by MacFarlane and co-workers.[127] The approach has attracted a great attention, as a route to modify important properties of ionic liquids without extensive synthetic effort. It been used in a wide range of applications, from hybrid electrolytes[128] to stabilising protein structure.[129] Doping PILs with charge-neutral molecules, although technically simple to perform, adds another level of complexity when the liquid structure is concerned. The effect that this has on hydrogen bonding and proton transfer must be carefully considered as this influences their chemistry. For example, a change in the liquid structure upon doping with water of the archetypal IL, ethylammonium nitrate, was observed by neutron scattering. The addition of water did not, simply result in a dilution effect, or swelling of the polar domains of the existing IL nanostructure, but it indicated a change in the nanostructure of the liquid. Separate ethylammonium nitrate and water regions were evident, with interactions between water and the charged groups of the IL resulting in a higher curvature network structure. It is interesting that even with the addition of up to six moles of water, the structure of the

hydrated protic IL still remained ionic-liquid like.[77] This observation correlates with water-in-salt solvents, defined in analogy to water-in-salt electrolytes, where the macroscopic properties and the liquid structures of hydrated PILs are distinct from both the parent PIL and the aqueous solution.[130,131] Understanding how this change in structure affects properties of the IL is important to enable the future design of PILs for specific applications *via* doping. In this work, molecular dopants are incorporated into the IL matrix, at quantities that maintain the crucial properties of the IL (that is, without turning it into a concentrated solution of ions), but may improve specific physicochemical characteristics, for example increased acidity, lowered viscosity or advantageously alter the phase behaviour.

The Hallett group have intensively researched lignocellulosic biomass pre-treatment with ILs, in particular PILs doped with molecular solvents.[115,118,137–143,120,124,125,132–136] The ionoSolv process is one of the most promising biomass pretreatment methods, which uses water-doped protic $[HSO_4]^-$-based ILs, such as triethylammonium hydrogen sulfate, $[HN_{222}][HSO_4]$ and dimethylbutylammonium hydrogen sulfate, [DMBA][HSO_4].[118,125] Lignin and hemicellulose are dissolved in the water-doped IL, leaving behind a cellulose rich solid residue. Lignin can be recovered from the IL with addition of water. The IL can be recycled several times and does not result in a reduction in the pre-treatment efficiency with further cycles. It has been noted that the addition of 10–40% water to the ILs is needed for optimal fractionation to occur.[120,124] The beneficial role of water in this process is interesting, however its role wasn't very well understood until a study from Hallett and co-workers in 2021.[139] They explained the dual role of water in this process, acting as both an antisolvent and a cosolvent as shown in Figure 18.

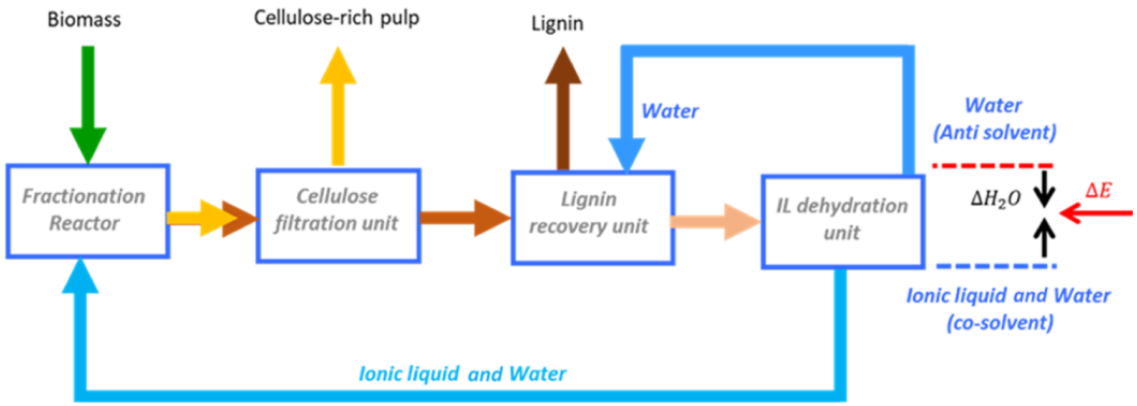

Figure 18. Process flow diagram showing the stages in the ionoSolv biomass fractionation process. Hemicellulose and lignin are dissolved into the water-doped IL, while the cellulose-rich pulp is filtered off. Lignin is then recovered with water addition and the removal of water recovers the IL, reducing operating costs.[139]

As a cosolvent, it has been shown that water plays an important role in lignin depolymerisation through hydrolysis of the ether bonds in lignin and through dehydration reactions.[126] It has been widely accepted in literature for $[HSO_4]^-$ based PILs that about 20 wt% water is an optimal amount for biomass fractionation.[120,124] By adding water as a cosolvent, Hallett and co-workers showed that they could reduce the amount of IL used, which reduced operating expenses but without compromising on the effectiveness of biomass fractionation.[139] Water is also used as an anti-solvent to precipitate the lignin from the IL. This is an important step to be able to recover and recycle the IL. The IL also needs to be dried before the next fractionation cycle which is the most energy intensive step of the whole process. The ability to recycle the IL is crucial to the success of large-scale operations.[144] The IL dehydration step has been recognised as a major challenge in other IL-based processes such as sugar valorisation and biomass dissolution.[120,145,146] Hallett and co-workers showed that that they could reduce the quantity of water used to precipitate the lignin without affecting the yield of lignin or its properties. This meant that the IL dehydration stage required less energy as there was less water input and reduced the energy consumption up to 65%.[139] Protic ILs with an excess of acid $[HB][HSO_4]\cdot(n\text{-}1)H_2SO_4$ were active catalysts for industrially important reactions of Fischer esterification[89,122] and Beckmann rearrangement.[123] Esterification of acetic acid with 1-butanol (Scheme 1) is an equilibrium reaction. Without catalyst, the maximum yield of butyl acetate was limited to 67%. When the reaction was catalysed by sulfuric acid, the equilibrium was shifted further to the right and 78% conversion was achieved.[89] However, using $[HN_{222}][HSO_4]\cdot 2H_2SO_4$ protic ionic liquid, yields of butyl acetate >95%. This was achieved by driving the reaction equilibrium to the right-hand side *via* the formation of a liquid biphasic system that formed gradually with the formation of the ester product (Figure 19). The IL could then be easily separated and reused without any significant loss in activity.[89]

Scheme 1. Model esterification between acetic acid and 1-butanol.

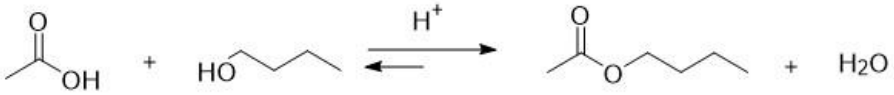

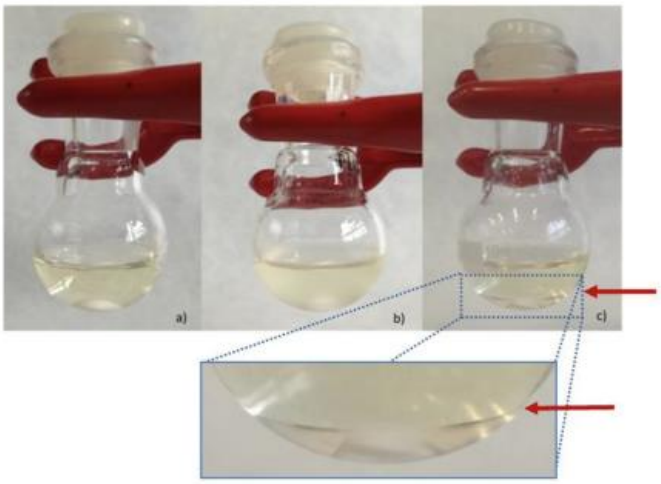

Figure 19. Left: Formation of a biphasic system at ambient temperature as Fischer esterification progressed and the ester product was formed. (a) monophasic, 5 min (b) turbid, 3 h (c) biphasic, 5 h. 12 mol% [Hmim][HSO_4]·$2H_2SO_4$ as a solvent and catalyst. Reported by Gillner and co-workers.[122]

The main goals of this work were to: understand the effect of water addition to ILs and how it increased efficiency of biomass fractionation, and to understand the structure of sulfuric acid-rich PIL compared to sulfuric acid, and how it enabled better phase separation in the esterification process. Conclusions drawn from structural insights were expected to aid in optimised design of these Brønsted acidic systems. Seeking to close these gaps in the knowledge led to the investigation of the liquid structure of these protic liquids when doped with water or excess acid by neutron scattering.

2.2 Experimental

2.2.1 Neutron scattering

Neutron scattering data were collected from three samples: concentrated sulfuric acid, a Brønsted-acidic PIL formed from sulfuric acid and pyridine in 2:1 molar ratio, [Hpy][HSO_4]·H_2SO_4, and a hydrated PIL, formed from concentrated sulfuric acid, pyridine and water in 1:1:2 molar ratio, [Hpy][HSO_4]·$2H_2O$. For each composition, isotopologues containing protiated (H), deuteriated (D) or equimolar mixture of protiated and deuteriated components (H/D) were prepared (Table 1). Robert Guiney and Emily Byrne made the samples.

Table 1. Mixtures of sulfuric acid:pyridine:water, their compositions and corresponding levels of protiation and/or deuteriation.

Sample number	Theoretical formula (actual H_2SO_4:py:H_2O)	sulfuric acid	py	water
1	Concentrated sulfuric acid	H		H
2	H_2SO_4	H/D		H/D
3	(1:0:0.2)	D		D
4	Brønsted acidic PIL	H	D	H
5	$[Hpy][HSO_4]\cdot H_2SO_4$	H/D	D	H/D
6	(2:1:0.4)	D	D	D
7		D	H	D
8		D	H/D	D
9		H	H	H
10		H	H/D	H
11	Hydrated PIL	H	D	H
12	$[Hpy][HSO_4]\cdot 2H_2O$	H/D	D	H/D
13	(1:1:2.2)	D	D	D
14		D	H	D
15		D	H/D	D
16		H	H	H
17		H	H/D	H

The neutron scattering data for the seventeen samples were recorded using the SANDALS spectrometer at the ISIS Pulsed Neutron and Muon Source at Rutherford Appleton Laboratory, Oxfordshire, UK. The instrument uses neutrons over a wavelength range 0.05–4.5 Å, giving an accessible Q range of 0.1–50 $Å^{-1}$. All samples were measured in quartz cells with 30 x 30 mm flat-plate geometry and with a path length of either 1 or 2 mm. The 2 mm cells were used for samples with high deuteriation levels (samples 2, 3, 5, 6, 8, 12–15 – Table 1) and 1 mm cells were employed for the more hydrogenous samples (samples 1, 4, 7, 9, 10, 11, 16, 17 – Table 1) in order to avoid high levels of beam attenuation and multiple scattering. At least 1000 μA of data were collected on each sample. Prior to data collection, quartz cells filled with sample were weighed, placed in a Thermo Scientific vacuum oven (25 °C, $<1 \times 10^{-2}$ mbar, 20 min), and weighed again, to ensure tightness of the seal against leakage in the instrument vacuum. Data were collected at 25 °C, with the temperature maintained using an FP50 Julabo heating circulator.

Total scattering data were reduced into a differential scattering cross section using the GUDRUN package.[92] Data collected on a 3.1 mm vanadium niobium alloy plate standard were used for calibration, data recorded on the empty SANDALS instrument and an empty 1 mm quartz cell were used for background subtraction.[12]

For each mixture, simulations were equilibrated over *ca.* 2000-3000 cycles before accumulating and averaging data. The EPSR refinements, in each case, were initialised using an equilibrated Monte Carlo simulation containing 500 or 1000 molecular moieties (pyridine, hydrogen sulfate, molecular sulfuric acid and water, with atomic sites labelled as shown in Figure 16) depending on the sample. The simulation box sizes and the corresponding experimentally determined molecular densities of the mixtures are shown in

Table **2**. Equation 9 represents the non-bonded interactions, based on the Lennard Jones 12-6 potential with addition of terms to account for Coulombic interactions. The Lennard-Jones well-depth is represented as ε, σ is the distance between particles at which the potential is zero and q is the charge of an atom, as outlined in Table 3. Charges were scaled to ± 0.8 e, in line with results from neutron diffraction and MD simulations of ILs.[147] Here reduced charges have been shown to reproduce experimental data more effectively. This better simulates effects of electronic polarisability captured when using more expensive polarisable force fields.[148]

Table 2. Simulation box size parameters.

Acid:pyridine:H_2O	***N_i*** [a]	**Box size, *n* / Å**	**Number density / atoms Å^{-3}**
1:0:0.2	600 (500:0:100)	36.41	0.0787
2:1:0.4	1700 (1000:500:200)	53.43	0.0859
1:1:2.2	2100 (500:500:1100)	50.61	0.0949

$$E_{nonbond} = \sum_{i} \sum_{j>i} \left\{ \frac{q_i q_j e^2}{r_{ij}} + 4\varepsilon_{ij} \left[\left(\frac{\sigma_{ij}}{r_{ij}} \right)^{12} - \left(\frac{\sigma_{ij}}{r_{ij}} \right)^{6} \right] \right\}$$

Equation 9

Table 3. Lennard-Jones parameters, including the charges and masses used for reference potential of the EPSR refinement model.

Atom type	ε / kJ mol^{-1}	σ / Å	q / e
Pyridinium			
N	0.5	3.2	0.1500
H_2	0.0	0.0	0.2820
H_1	0.2	2.4	0.0800
C_1	0.5	3.5	0.0736
H_3	0.2	2.4	0.0512
C_2	0.5	3.5	-0.024
C_3	0.5	3.5	-0.0448
H_4	0.2	2.4	0.0512
Hydrogen sulfate[a]			
S_1	1.046	3.55	0.944
O_1	0.837	3.15	-0.544
O_2	0.837	3.15	-0.544
H_A	0.0	0.0	0.432
Water			
O_w	0.65	3.1	-0.667
H_w	0.0	0.0	0.336

[a] The parameters for hydrogen sulfate and sulfuric acid are the same, except that both hydrogens in sulfuric acid have q = 0.616 e.

2.3 Results and discussion

2.3.1 Sample selection

The experimental design included the study of concentrated sulfuric acid, a Brønsted acidic PIL formulated with two moles of H_2SO_4 per one mol of pyridine, [Hpy][HSO_4]·H_2SO_4 and a hydrated ionic liquid, [Hpy][HSO_4]·2H_2O.

The structure of concentrated sulfuric acid was used as a baseline to compare with the structures of both PILs. The composition of the Brønsted acidic PIL, [Hpy][HSO_4]·H_2SO_4, was one of the two standard acidic compositions used in earlier catalytic studies by the group.[119,149,122,123,89] The aim of this work was to elucidate its structure (3D network *vs*. discrete anionic clusters) and understand how differences in the liquid structure

of this PIL and sulfuric acid account for their different miscibilities with the ester product. Finally, the hydrated PIL, [Hpy][HSO_4]·$2H_2O$, with a 1:1:2 acid:pyridine:water ratio (*ca.* 17 wt% of water), was close in composition to the 20 wt% water content, cited as the optimum composition for delignification of cellulosic biomass.[118,124–126,150] It was anticipated that particularly efficient biomass fractionation reported for this aqueous PIL composition could be tied to the speciation of water in the 1:1:2 mixture.

2.3.2 EPSR modelling

2.3.2.1 Free proton model

Neutron scattering data of acids are usually modelled as molecular (undissociated) descriptions in the EPSR model. However, previous work by the group applied the 'free proton model' methodology to study pyridine:acetic acid mixtures were acetic acid was described as an acetate and an unconstrained proton.[12] This meant that the acidic hydrogen was incorporated as a 'free proton' with no defined connectivity and could locate within the simulation model at positions driven by the iterative fit to the experimental data. This approach was chosen to permit the simulation to respond to potential ionisation of acids and report directly on the degree of proton transfer and resulting speciation.

The same approach was initially applied to this data for the 1:2 pyridine:sulfuric acid mixture, with pyridine modelled using a simple molecular description while sulfuric acid was described using the 'free proton' description: as hydrogen sulfate anion, $[HSO_4]^-$, and unconstrained proton, H^+. The free proton was assigned initial parameters of ε = 0.100 kJ mol^{-1} and σ = 0.60 Å. It was anticipated that the 'free proton' modelling of the pyridine:sulfuric acid mixture would report the formation of pyridinium ions representing a protonated ionic liquid in contrast to pyridine:acetic acid mixtures that were previously studied.[12] Especially as pyridine in the presence of sulfuric acid can be considered fully protonated, based on both FT-IR spectroscopy[151] and crystallographic data for pyridinium hydrogen sulfate.[152]

This was confirmed in the model, which showed a substantial degree of protonation of the pyridine rings in the simulation. However, the 'free-proton' model tends to significantly underestimate the degree of pyridine protonation and overestimates the average distance for the correlation. This was reflected in the data with an average N···H_F coordination number (CN) of only 0.2±0.4 and with the maximum in the N···H_F correlation (corresponding to N-H bonds in pyridinium cations) overestimated at 1.6 Å. Nevertheless, it does confirm protonation with this initial model confidently predicting protonated pyridinium cations, hydrogen sulfate anions and sulfuric acid molecules. This contrasts with results from pyridine:acetic acid mixtures,[12] indicating

that the EPSR simulation is sensitive to individual site isotopic substitution in the molecules. The spatial distribution function (SDF) in Figure 20 shows that the highest probability for locating the H_F around a central pyridine is just above the nitrogen atom.

Figure 20. Spatial distribution function (SDF) illustrating the correlation of the H_F with the nitrogen of the pyridine (2.0–4.0 Å, 20% probability).

Having established from the free proton model that pyridine was – unsurprisingly - protonated in these systems, subsequent modelling was undertaken using a defined $[Py\text{-}H]^+$ cation. To remain consistent within the mixtures, a common $\{SO_4\}$ core was present in both systems. The 2:1 sulfuric acid:pyridine sample was modelled as $[Py\text{-}H]^+$, $[HSO_4]^-$ and H_2SO_4, and the 1:1:2 sulfuric acid:pyridine:water sample was modelled as $[Py\text{-}H]^+$, $[HSO_4]^-$ and two H_2O molecules, fitting to the neutron scattering data collected from the isotopomeric samples.

To validate that the sulfuric acid free proton model, $H^+/[HSO_4]^-$, gave a reliable description of the system, the data was also modelled as a molecular acid, mimicking MD simulations from Guàrdia *et al.*,[153] and consistent with analysis of other neat acids, small molecules and mixtures.[9–11,124,154–158] This was done to confirm that using the $H^+/[HSO_4]^-$ pair did not lead to conflicting results, and to verify that retaining the common $[HSO_4]^-$ anion moiety across the three systems was valid. This ensured that a self-consistent set of models was used across the three systems.

Comparisons of experimental and simulated *S(Q)* data and the corresponding Fourier transforms to real space *g(r)* for each of the isotopically distinct experimental mixtures show the quality of fit to the experimental data. In each case, obtained simulation models were refined to a self-consistent fit to the multiple scattering sets. The *S(Q)* and *g(r)* data for both ionised sulfuric acid (free proton model, Figure 21) and molecular sulfuric acid (Figure 22) show generally good fits between the experimental and EPSR simulated structure factors. The primary source of inconsistency occurred in the region affected by the inelastic scattering of light hydrogen, at $Q \leq 2$ Å^{-1}. Inelasticity effects occur widely in neutron scattering experiments, especially for light atoms such

as hydrogen, where their mass equivalence leads to a large exchange of energy during the scattering process. This effect has been studied extensively, yet there does not exist a perfect correction for the inelastic scattering of light atoms.[159,160]

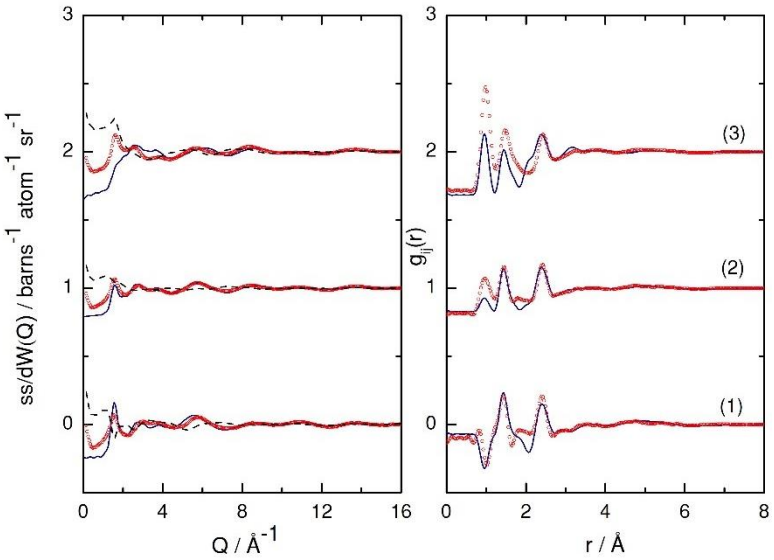

Figure 21. Comparison between simulated and experimental, S(Q), data (left) and Fourier transform to real, $g_{ij}(r)$, space (right) showing experimental data (red symbols) and EPSR modelled (blue solid line) for sulfuric acid modelled using the free proton model with $[HSO_4]^-$ and H^+ descriptions. Labels represent the experimental compositions shown in Table 1 and the curves have been offset for clarity.

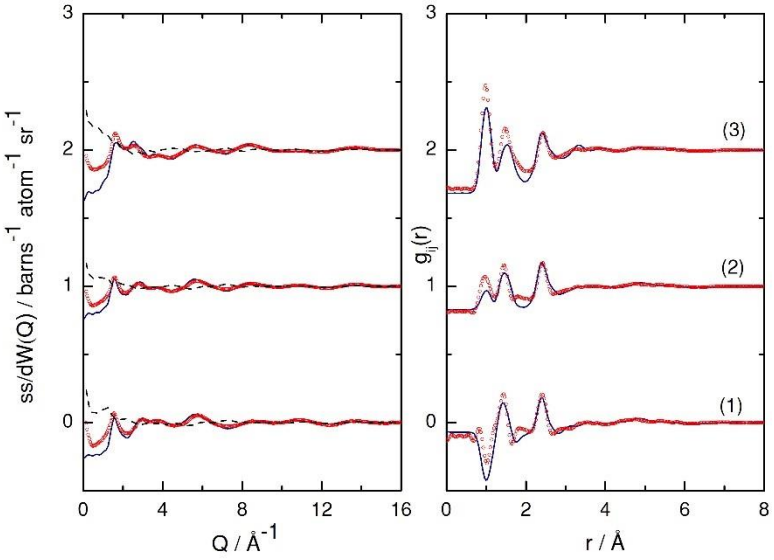

Figure 22. Comparison between simulated and experimental, S(Q), data (left) and Fourier transform to real, $g_{ij}(r)$, space (right) showing experimental data (red symbols) and EPSR modelled (blue solid line) for sulfuric acid modelled using a molecular H_2SO_4 description. Labels represent the experimental compositions shown in Table 1.

The bond distances and coordination numbers of both models are shown in Table 4. Similar results were reported in O···O and S···S descriptions of the $\{SO_4\}\cdots\{SO_4\}$ environment and were comparable with values found in the literature.[161,153] The O···O bond distances in this work (Table 4) are intermediate between a short O···O distance (2.42 Å) inferred from neutron scattering data subjected to direct Fourier transform, without iterative Monte Carlo data fitting,[161] and a longer O···O distance (3.1 Å), derived from MD simulations.[153] Furthermore, the formation of an extended, hydrogen bonded $\{SO_4\}$ network was confirmed, as each $\{SO_4\}$ moiety was surrounded by 11 neighbour $\{SO_4\}$ moieties ($S\cdots S\ CN_{lit} = 12$).[161,153,108] From this, it was concluded that anionic $\{SO_4\}$ environments could be confidently described as an ionic hydrogen sulfate, $[HSO_4]^-$, also in subsequent, more complex systems.

Table 4. Radial distribution function (RDF) intermolecular distances between atom types for sulfuric acid modelled using both a molecular and free proton approaches. The relative coordination numbers (CN) and errors associated with the CN are also listed.

Interaction	RDF distances / Å		CN			
	H_F	Molecular	H_F	±	Molecular	±
$O_{A2}\cdots O_{A2}$	2.9	2.7	8.5	1.4	5.3	1.1
$O_{A1}\cdots O_{A1}$	3.4	3.2	2.3	1.2	4.6	1.3
$O_{A2}\cdots O_{A1}$	2.6	2.6	3.1	1.1	6.7	1.2
$O_{A1}\cdots O_{A2}$	2.6	2.6	9.4	1.4	6.6	1.1
$H_F\cdots O_{A1}$	2.1	-	0.5	0.7	-	-
$H_A\cdots O_{A1}$	-	1.7	-	-	0.8	0.7
$H_A\cdots O_{A2}$	1.6	1.7	0.9	0.5	1.0	0.5

Although the free proton model described the sulfate environment well, it did not sufficiently describe the behaviour of the unconstrained proton. The O···H correlations in sulfuric acid described as H_2SO_4 occurred at 1.7 Å, which is in agreement with strongly hydrogen bonded units.[152] In contrast, the free proton model suggested a much more diffuse proton behaviour, overestimating the O···H correlation distance (O···H = 2.1-2.2 Å). It is probably an artefact of the Monte Carlo methodology, however, these results confirmed that confining the proton to one position by using the molecular descriptor method was a more effective way to describe its behaviour in the system. Consequently, subsequent models were based on a combined ionic/molecular approach.

Comparisons of experimental and simulated total structure factors, *F(R),* and the corresponding Fourier transforms to real space *G(r)* for the 2:1:0 sulfuric acid:pyridine mixture and 1:1:2 sulfuric acid:pyridine:water mixture is shown in Figure 23. The fits are generally good, except for the region at $Q \leq 1$ Å^{-1}, which is most susceptible to inconsistencies due to inelastic scattering contributions from hydrogen in the data. There is also

a mismatch in some of the peaks, notably in sample 12 and 8. Mismatch of *f(r)* at low *r* indicates that the level of deuteriation is either wrong for the sample, or in the simulation in the weights file. In this case, the experiment appeared to contain more deuterium than the simulation. The overall poorer fits are likely to be a result of the water content in sulfuric acid which hasn't been accounted for.

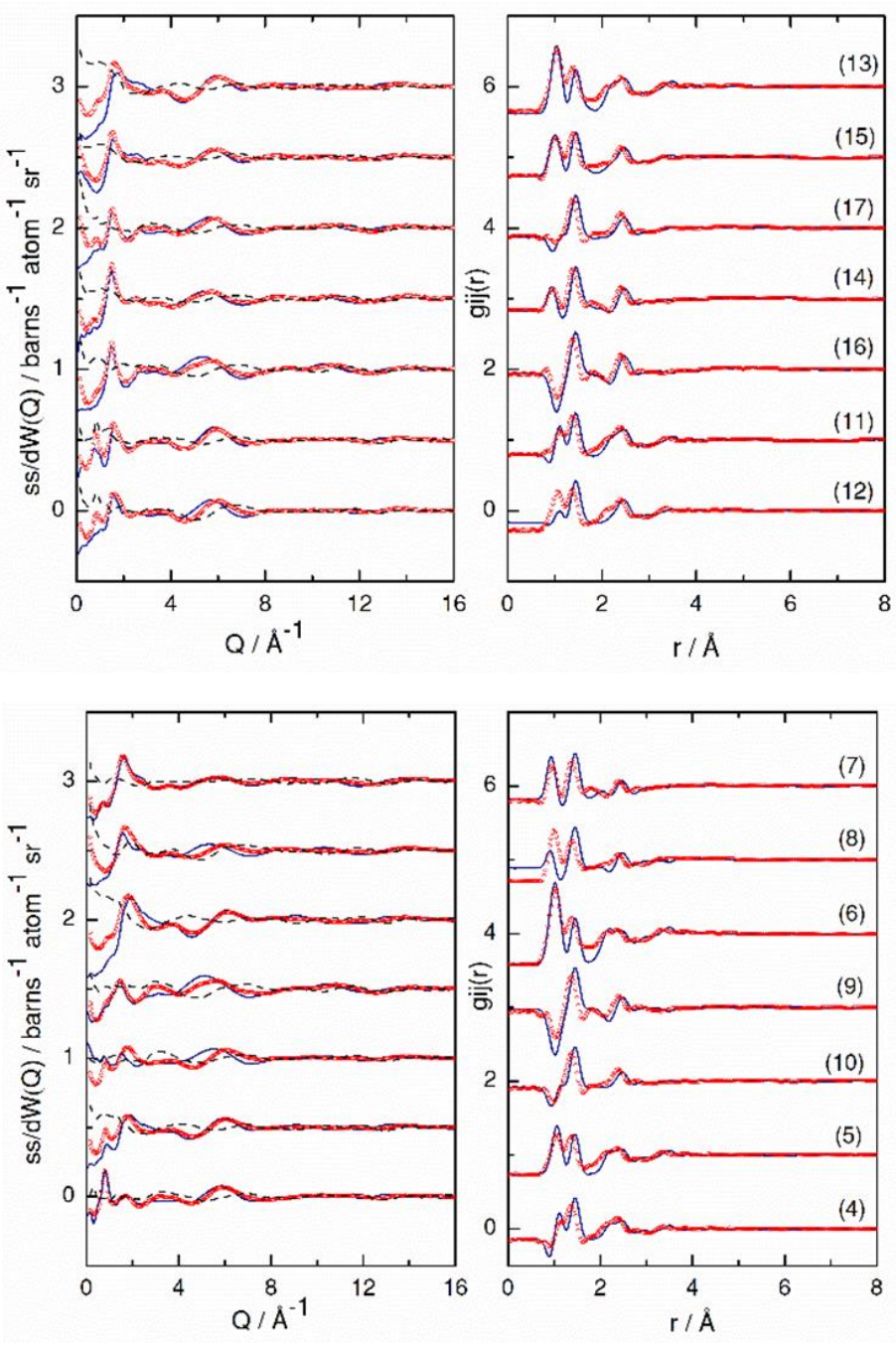

Figure 23. Total structure factors F(Q) (left), and the corresponding Fourier transform to real space G(r) radial distribution functions (right) showing experimental data (red symbols) and EPSR modelled (blue solid line) for top: Brønsted acidic PIL (H_2SO_4 : py 2 : 1) and bottom: hydrated PIL (H_2SO_4 : py : H_2O 1 : 1 : 2). Labels represent the experimental compositions shown in Table 1.

After reviewing the data again and investigating more closely, it was decided that the compositions for the three mixtures should be adjusted to account for the concentration of H_2O (in H_2SO_4) or D_2O (in D_2SO_4). Therefore, adjusting for actual water content from these idealised compositions, concentrated sulfuric acid (98%) was assumed to contain 0.2 M of either H_2O (in H_2SO_4) or D_2O (in D_2SO_4). The levels were then adjusted in the models for each mixture and the measured neutron scattering levels improved significantly. As such, actual compositions of the examined samples used to model the neutron scattering data were: concentrated sulfuric acid (1:0.2, acid:water), Brønsted acidic PIL (2:1:0.4, acid:pyridine:water) and hydrated PIL (1:1:2.2, acid:pyridine:water), as summarised in Table 1.

2.3.2.2 Water in PIL systems

The data from sulfuric acid (samples 1-3) was modelled using molecular descriptions of the species present (H_2SO_4 and H_2O in a 1:0.2 molar ratio) – see Figure 16. Although several more complex water species (H_3O^+, $H_5O_2^+$) have been reported as constituents of sulfuric acid hydrates,[112–114,162,163] descriptors were limited to the main moieties, enabling the examination of key associations in these already complex mixtures. This approach is aligned with EPSR analysis of neutron scattering data recorded for other 'neat' acids (acetic acid, formic acid),[10] in which molecular (undissociated) descriptions were used. The same strategy has been used in MD simulations of sulfuric acid:water mixtures[153] and other 'neat' acids, small molecules and mixtures.[124,101,109,11,155–158]

Brønsted acidic PIL (samples 4-10) and hydrated PIL (samples 11-17) were modelled using fully protonated pyridinium cation $[Py\text{-}H]^+$, anionic $[HSO_4]^-$ and molecular H_2O. Additionally, the model of samples 4-10 contained molecular H_2SO_4.

Comparisons of experimental and simulated total structure factors, *F(R)*, and the corresponding Fourier transforms to real space *G(r)* for each of the isotopically distinct experimental mixtures (Figure 24) show the quality of fit to the experimental data. Except the $Q \leq 1$ Å^{-1} region, the fitted data aligns well with experiment. For the neat sulfuric acid systems (1-3, Table 1), a larger degree of scattering at low Q is present in the experimental data than is captured within the EPSR model which may reflect either incomplete subtraction of the inelastic hydrogen background from the data or additional long range order. Similar profiles are also apparent for the fully deuteriated PILs (samples 6 and 13), suggesting the presence of some hydrogen-generating inelastic scattering from the sample in this region.

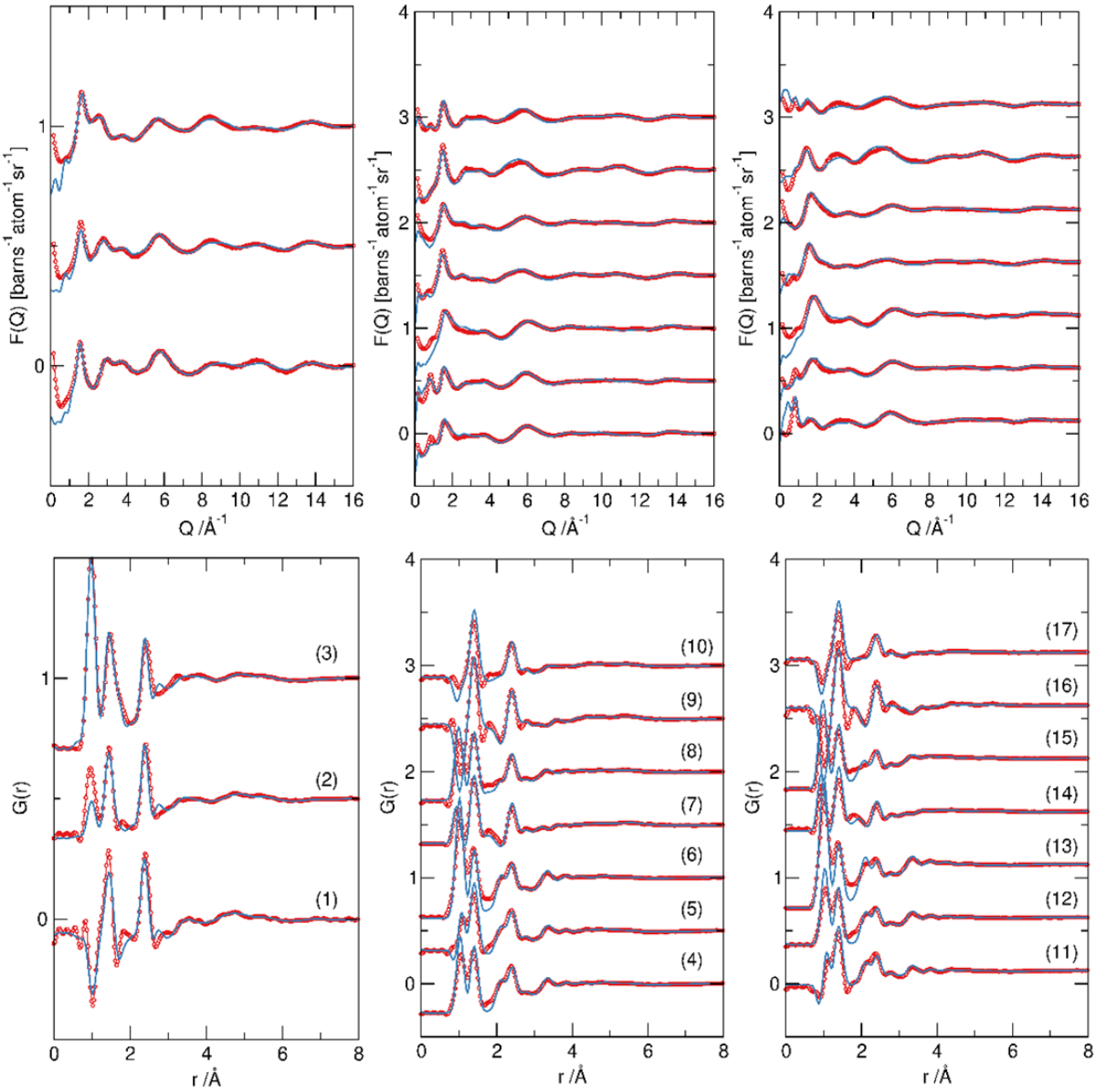

Figure 24. Total structure factors F(Q) (top), and the corresponding Fourier transform to real space G(r) radial distribution functions (bottom) showing experimental data (red symbols) and EPSR modelled (blue solid line) for left: sulfuric acid (H_2SO_4:H_2O 1:0.2); middle: Brønsted acidic PIL (H_2SO_4:py:H_2O 2:1:0.4) and right: hydrated PIL (H_2SO_4:py:H_2O 1:1:2.2).

2.3.2.3 Centre of mass radial distribution functions

Centre of mass (COM) radial distribution functions (RDFs) were calculated using the SHARM routines within EPSR, for each of the components in the three systems (Figure 25). The RDFs reveal a remarkable persistence of structure, similar between the three systems: H_2SO_4, [Hpy][HSO_4]·H_2SO_4 and [Hpy][HSO_4]·2H_2O.

In concentrated sulfuric acid, the $\{SO_4\}$-$\{SO_4\}$ RDF shows a first shell correlation with a maximum at *ca*. 4.6 Å, with a broad second shell correlation between 6.6-11.5 Å (Figure 25 left, blue dotted line). The corresponding water-$\{SO_4\}$ first shell correlation (Figure 25, right, blue dotted line) is centred around 4 Å (minimum 5.5 Å), and the water-water RDF correlation (Figure 25, right, dotted green) at 3.2 Å. This is significantly longer than water-water distances in bulk water (2.6 Å), confirming that water molecules are confined within sulfuric acid as hydrates. Further supporting this conclusion, the water-water RDF lacks a second shell peak between 4-6 Å, that would have been indicative of 'free' water.

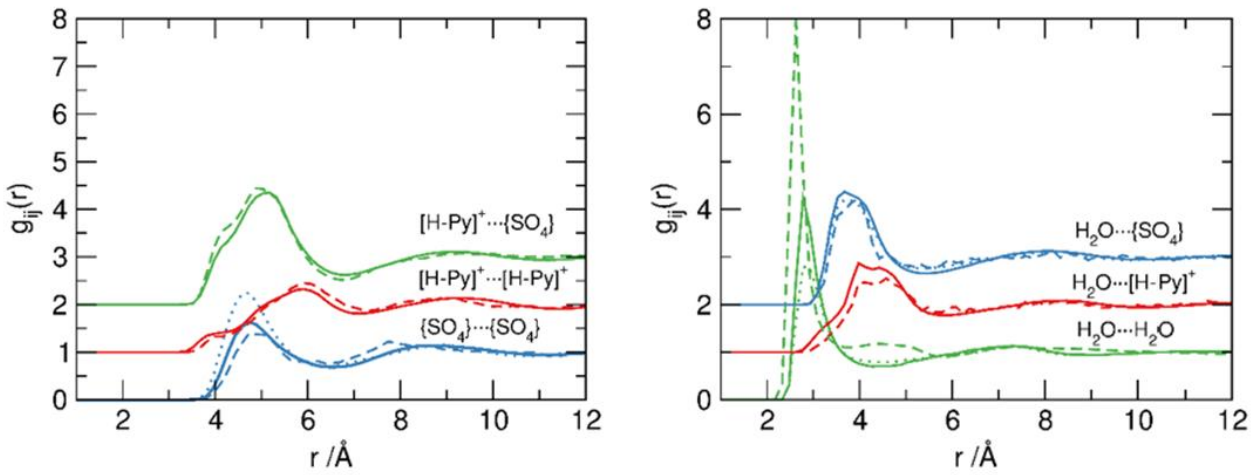

Figure 25. COM RDFs between $[H\text{-}Py]^+$ and $\{SO_4\}$ (left) and between H_2O and $[H\text{-}Py]^+$ or $\{SO_4\}$ units (right) in: concentrated sulfuric acid (dotted lines), Brønsted acidic PIL (solid lines) and hydrated PIL (dashed lines), from the EPSR simulations.

In both PIL systems, the cation-$\{SO_4\}$ RDFs are characteristic of strong cation-anion association, typical of ILs.[16] The cation-anion RDFs (Figure 25, left, green curves) exhibit a first correlation peak at 5.0-5.2 Å with a shoulder at 4.2 Å, and a second broader correlation peak, indicative of the second shell, at *ca*. 9 Å. The shoulder at 4.2 Å reflects the oblate topology of the pyridinium cations (Figure 26), allowing two distinct routes to approach its centre of mass. The cation-cation first correlations (Figure 25, left, red curves) are present at a larger separation (maxima at ~6 Å), followed by a second shell at 9-10 Å, overlapping with the second shell of cation-anion correlations. Again, a small shoulder at *ca*. 4 Å in the cation-cation RDFs may be due to a small number of face-to-face correlations, typical of the π-π interactions observed in liquid pyridine at distances below 5 Å (Figure 26).[164] The larger separation at *ca*. 6 Å is due to the edge-to-face Y-interactions of the pyridine rings (Figure 26). Similar features are observed in aprotic ILs containing N-alkylpyridinium cations, arising from anions associating equatorially around pyridinium cations.[13,165,166]

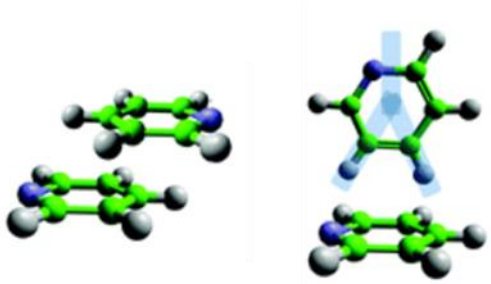

Figure 26. Typical intermolecular interactions between nearest neighbour pyridine molecules. Left: face-face configuration and right: edge-to-face Y-interactions.[164]

Contrasting with typical IL structures, there is very close anion-anion interaction in both PILs. The corresponding {SO_4}-{SO_4} associations (Figure 25, left, blue dashed and solid curves) closely resemble sulfate associations in 'neat' sulfuric acid (first shell at 4.6 Å, second one at 6.6-11 Å). In PILs, the first correlation lengthens slightly (4.8 Å), which can be attributed to the decreasing number of acidic hydrogens in the H_2SO_4/$[HSO_4]^-$ components, therefore reducing the number of available S-O-H···O=S hydrogen bonding motifs: from 2 per {SO_4} unit in H_2SO_4, through 1.5 per {SO_4} unit in [Hpy][HSO_4]·H_2SO_4, to 1 per {SO_4} unit in [Hpy][HSO_4]·2H_2O.

This close anion-anion interaction in both PILs results in the unusual presence of both cations and anions in the first coordination shell of {SO_4}. Their liquid structure combines characteristics of ionic liquid (close cation-anion correlations) and of the parent sulfuric acid (sulfate-sulfate organisation).

The water···{SO_4} and water···$[H\text{-}Py]^+$ RDFs (Figure 25, right, blue and red lines, respectively) have their corresponding first peak correlations of 4.0 and 4.8 Å respectively. There is no significant difference in the water association with either {SO_4} or $[H\text{-}Py]^+$ on changing the water content of the PILs.

In contrast, water-water RDFs show a marked difference. In H_2SO_4 and in [Hpy][HSO_4]·H_2SO_4, that is with low water content, $H_2O\cdots H_2O$ correlation is found at 3.2 Å, slightly more intense in [Hpy][HSO_4]·H_2SO_4. In [Hpy][HSO_4]·2H_2O, this distance decreases to 2.7 Å, showing both greater self-association of water molecules and a larger number of correlations, as indicated by the increase in intensity. This distance is close to $H_2O\cdots H_2O$ correlation in bulk water (2.6 Å). However, lack of significant second shell correlation (4-6 Å) indicates that there are no large-size water clusters and [Hpy][HSO_4]·2H_2O retains water-in-IL rather than IL-in-water characteristics.

The similarity of RDF correlation profiles (Figure 25), aside from the water-water correlation, suggests essentially similar liquid structure and character of both PILs, and that the presence of the water (up to 2 moles, *ca.* 17 wt%) does not perturb the ion-ion structure significantly. Moreover, the hydrogen-bonding

network of sulfuric acid appears to be retained as a core structural motif in the PILs, in addition to the typical Coulombic charge screening structure usually observed in ILs.

In the context of applications of Brønsted acidic PILs in esterification, it was initially assumed that phase-separation of the organic phase, that is much more efficient in Brønsted acidic PILs than in concentrated sulfuric acid, may be related to marked differences between the structures of the two liquids: H_2SO_4 *vs*. $[Hpy][HSO_4]\cdot H_2SO_4$. However, the results here suggest that there are greater similarities between the structure-defining associations within these liquids rather than significant differences that would explain the distinctly different phase behaviours of H_2SO_4 and PILs in esterification reactions.

In contrast, the water-in-salt structure of the hydrated PIL, $[Hpy][HSO_4]\cdot 2H_2O$, with negatively-charged hydrogen-bonded network of hydrogen sulfate and water (with or without H_2SO_4 present) can be expected to have distinctly different properties when compared to anhydrous $[Hpy][HSO_4]$, as described in the literature.[124,139,167] Furthermore, in esterification reactions, where water and ester are generated, the Brønsted acidic PIL can be envisaged to gradually bind water to form a similar hydrogen sulfate – sulfuric acid – water anionic network, in which water is bound as a hydrate and less likely to hydrolyse the ester product.

Detailed, comparative structural analysis of the three liquid systems studied in this work is provided below.

2.3.2.4 Correlation and association around {SO_4} groups

Site-site analysis of contributions to the scattering were made. The positions of first peaks within the partial radial distribution functions (pRDFs) of selected site-site correlations and corresponding coordination numbers, calculated to the first minima after the peak, are included in Table 5 for concentrated sulfuric acid (H_2SO_4:H_2O 1:0.2), Table 6 for 'anhydrous' acidic PIL (2:1:0.4), and in Table 7 for the sulfuric acid:pyridine:water system (1:1:2.2).

Table 5. Interatomic distances (taken from the first peak maximum in the site-site radial distribution functions) and relative coordination numbers (CN), calculated to the minimum after the first peak in the radial distribution functions) between different atom types in concentrated sulfuric acid (H_2SO_4:H_2O 1:0.2).

Interaction	Peak (minima)	CN
S···S	4.6 (6.4)	11.0±1.3
OA2···OA2	3.1 (4.0)	4.2±1.3
OA2···OA1	2.6 (3.0)	5.7±1.3
OA1···OA1	3.1 (3.8)	4.0±1.3
OA1···Ow	2.6 (4.0)	0.5±0.7
OA2···Ow	2.9 (4.0)	0.5±0.7
Ow···Ow	2.8 (4.0)	0.6±0.7
Hw···Ow	3.2 (4.8)	0.4±0.5
Hw···OA1	3.2 (4.6)	8.3±1.6
Hw···OA2	1.9 (2.3)	0.4±0.5
HA···OA2	1.6 (2.3)	0.8±0.5
HA···OA1	3.8 (4.6)	8.0±1.6
HA···Ow	1.6 (2.3)	0.1±0.3
Ow···HA	1.6 (2.3)	0.9±0.6
OA2···HA	1.6 (2.3)	0.8±0.6
OA1···HA	3.8 (4.6)	8.1±1.5

Table 6. Interatomic distances (taken from the first peak maximum in the site-site radial distribution functions) and relative coordination numbers (CN, calculated to the minimum after the first peak in the radial distribution functions between different {SO_4} oxygen sites in the 2:1:0.4 'anhydrous' acidic PIL. Half the {SO_4} units in the system were described as H_2SO_4 and half as $[HSO_4]^-$ giving rise to the apparent duplication of correlations.

Interaction	Peak (minimum) / Å	CN	Interaction	Peak (minimum) / Å	CN
S···S			**S=O···O=S**		
SA1···SA1	4.7 (6.3)	3.4±1.6	OA1···OA1	3.2s (4.0)	2.0±1.0
SA1···S1	4.7 (6.3)	3.5±1.5	OA1···O2	3.2 (4.0)	1.4±1.1
S1···S1	4.7 (6.4)	2.9±1.2	O2···OA1	3.2 (4.0)	0.9±0.9
S-OH···Ow			O2···O2	3.2 (4.0)	3.1±1.0
OA2···Ow	2.8 (4.0)	0.3±0.6	**S=O···HO-S**		
O1···Ow	2.8 (3.9)	0.3±0.5	OA2···OA1	2.6 (3.9)	3.1±1.0
Ow···OA2	2.8 (4.0)	1.7±1.4	OA2···O2	2.6 (2.9)	0.6±0.6
Ow···O1	2.8 (3.9)	0.8±0.8	O1···OA1	2.8 (3.8)	0.8±0.9
S=O···Ow			O1···O2	2.7 (3.7)	4.0±0.9
OA1···Ow	2.8 (3.9)	0.3±0.6	OA1···OA2	2.6 (3.9)	3.2±1.1
O2···Ow	2.8 (4.0)	0.3±0.6	OA1···O1	2.8 (3.8)	0.4±0.6
Ow···OA1	2.8 (3.9)	1.6±1.3	O2···OA2	2.6 (2.9)	0.4±0.6
Ow···O2	2.8 (4.0)	2.5±1.4	O2···O1	2.7 (3.7)	1.3±0.6
{SO_4}···Hw			**S-OH···HO-S**		
OA1···Hw	1.8 (2.4)	0.1±0.3	OA2···OA2	3.0 (4.0)^{sh}	1.9±1.0
O2···Hw	1.9 (2.3)	0.1±0.3	O1···O1	2.9 (3.9)	0.4±0.6
O1···Hw	1.8-3.5^{br}	0.4±0.8	OA2···O1	3.0 (4.0)^{sh}	0.4±0.6
OA2···Hw	1.7-3.2^{br}	0.4±0.8	O1···OA2	3.0 (4.0)^{sh}	1.0±1.0
Ow···Ow	2.8 (4.4)	0.5±0.7	HA1···O2	1.7 (2.2)	0.6±0.5
Hw···Ow	1.8 (2.3)	0.4±0.6	HA1···Ow	1.6 (2.2)	0.1±0.2
OA1···HA1	1.6 (2.2)	0.3±0.5	HA1···Hw	2.2 (2.7)	0.2±0.5
OA1···HA	1.8 (2.4)	0.2±0.4	O2···HA	1.8 (2.4)	0.2±0.4

^{sh} shoulder, ^{br} broad

Table 7. Interatomic distances (taken from the first peak maximum in the site-site radial distribution functions) and relative coordination numbers (CN , calculated to the minimum after the first peak (as indicated in the table) in the radial distribution functions between different {SO_4} oxygen sites in the 1:1:2.2 sulfuric acid:pyridine:water system.

Interaction	RDF distance and minima / Å	CN
S···S	4.8 (6.0)	2.5±1.1
O1···O1	3.0 (4.0)[sh]	0.5±0.7
O1···O2	2.8 (3.9)	4.5±1.0
O1···Ow	2.7 (4.0)[sh]	1.6±1.5
O1···Hw	3.1 (4.5)[sh]	5.9±4.2
O1···HA	3.1 (4.5)[sh]	1.6±1.1
O2···O1	2.8 (3.9)	1.5±0.6
O2···O2	3.7 (4.0)[sh]	3.0±0.9
O2···Ow	2.7 (3.2)	0.8±0.9
O2···Hw	1.8 (2.4)	0.6±0.7
O2···HA	1.8 (2.5)	0.3±0.5
Ow···O1	2.7 (4.0)[sh]	0.7±0.7
Ow···O2	2.7 (3.2)	1.1±0.9
Ow···Ow	2.7 (4.0)	4.1±2.0
Ow···Hw	1.7 (2.5)	2.2±1.3
Ow···HA	1.8 (2.4)	0.1±0.3
Hw···O1	3.1 (4.5)[sh]	1.3±0.9
Hw···O2	1.8 (2.4)	0.4±0.5
Hw···Ow	1.7 (2.5)	1.1±0.9
HA···O1	3.2sh (4.0)	1.2±0.9
HA···O2	1.8 (2.5)	1.0±0.7
HA···Ow	1.8 (2.4)	0.3±0.5

[sh] shoulder

Figure 27 shows oxygen···oxygen correlations between {SO_4} groups, originating both from $[HSO_4]^-$ and H_2SO_4. These were determined from the first peak in the site-site pRDFs. In all three systems, the 'hetero' S-OH···O=S mode of correlation is dominant, appearing as a strongly defined peak in the RDF at 2.6-2.7 Å (Figure 27, green line). In contrast, first contact correlations of S-OH···HO-S and S=O···O=S only occur around 3.0 Å. The peak at *ca*. 5 Å corresponds to the second shell correlations to the remaining oxygens on {SO_4}. It is therefore evident that the primary mode of association between {SO_4} groups is S-OH···O=S hydrogen bonding, retained from sulfuric acid in both PILs.

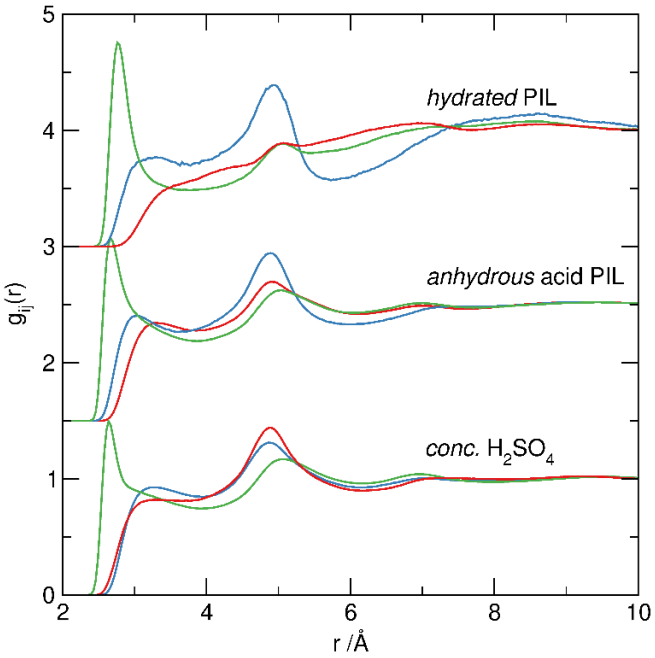

Figure 27. O···O correlations; S=O···O=S (red), S-OH···HO-S (blue) and S=O···HO-S (green) in conc. H_2SO_4 (1:0:0.2), 'anhydrous' acid PIL (2:1:0.4), and 'hydrated' PIL (1:1:2.2) systems showing the strong hydrogen-bonding correlation with a sharp first peak at 2.6 Å between S-OH and O=S oxygen centres and broader less defined correlations at longer distances of 3.0 Å and 3.3 Å for correlations between S-OH oxygens and S=O contact-pairs.

Correlation distances for concentrated H_2SO_4 are broadly consistent with the literature.[108,111,153] Andreani *et al*. first reported data derived from direct Fourier transform of experimental X-ray and neutron scattering data,[108] with S···S and O···O separation distances of 5.3 Å and 2.42 Å. However, the S···S separation, inferred from the summation of intermolecular S-O and intramolecular O-O distances, appears to be over-estimated. Kameda *et al*.[111] subsequently reported a shorter S···S correlation of 4.8 Å, which is more consistent with simulation between contact pairs in concentrated H_2SO_4/H_2O (4.6 ± 0.1 Å),[168] and small clusters of bulk H_2SO_4 (4.8 Å),[155] where an O···O distance of 3.1 Å was also reported. Here, the first shell S···S separation distance

was determined as 4.6 Å, with O···O correlations between OA1 and OA2 sites (S-OH···O=S) at 2.6 Å, and minima after this first correlation peak at 3 Å. The $\{SO_4\}\cdots\{SO_4\}$ coordination number (CN = 11 ± 1) between neighbouring moieties is also in agreement with the literature (CN = 12), and confirms the formation of an extended, tetrahedral hydrogen bonded network linked through S-OH···O=S interactions.[169]

In both PILs, interatomic distances for the first shell O···O correlations, as well as corresponding CN values, are very similar to sulfuric acid, suggesting hydrogen bonding of similar strength across the three systems. However, the $\{SO_4\}\cdots\{SO_4\}$ first shell coordination environment (determined from S···S correlations) decreases: from 11 in H_2SO_4, to 7.5 in $[Hpy][HSO_4]\cdot H_2SO_4$, and to 4.8 in $[Hpy][HSO_4]\cdot 2H_2O$, commensurate with the reduction in the number of available S-OH groups to act as hydrogen-bond donors.

Site-site RDFs between the water molecules (Ow/Hw) and the sulfate units are shown in Figure 28. For the concentrated acid and anhydrous acidic PIL, the presence of *ca*. 0.2 mole fraction of water leads to a broad peak in the Ow···O1/O2 RDFs between ~2.6-3.0 Å (Figure 28, dashed lines). The Hw···O=S correlation at 1.8 Å (Figure 28, solid blue lines) indicates directional hydrogen-bonding retained between the acid and PILs.

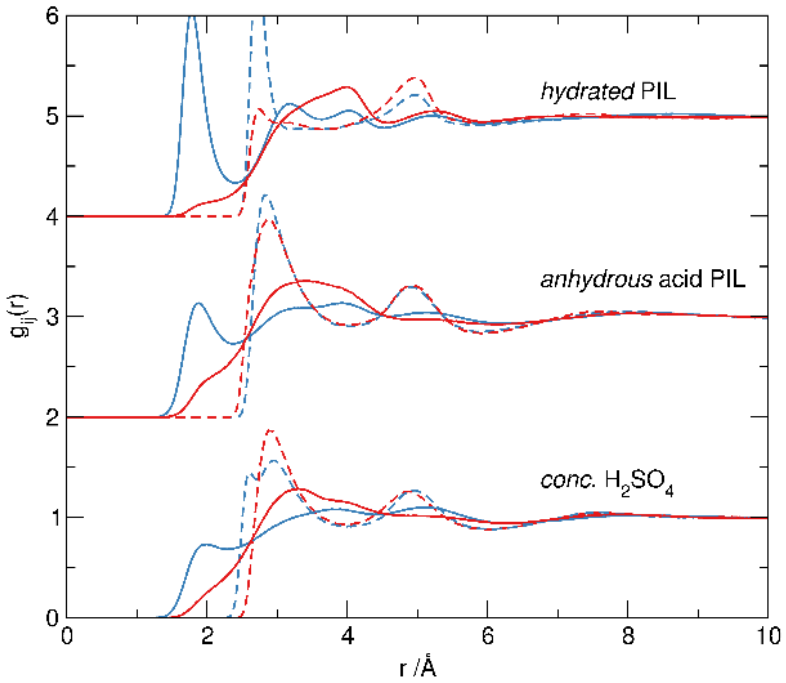

Figure 28. Site-site pRDFs between water Hw (solid line) and Ow (dashed line) and sulfate S=O (blue) and S-OH (red) oxygens in the three systems showing hydrogen-bond donation from the water Hw to the S=O2 oxygen (1.8 Å) and hydrogen-bond acceptance at Ow from S-OH (2.8 Å).

In the hydrated PIL, [Hpy][HSO_4]·2H_2O, the magnitude of these correlations increases, as there is more water molecules available, and less S-OH sites. Associated Ow···O=S correlation at 2.8 Å (Figure 28, dashed blue line) also becomes sharper. Interestingly, the corresponding Ow···O(H)-S correlation at 2.8 Å (Figure 28, dashed red line) is dramatically decreased. This indicates that the remaining available S-OH sites hydrogen bond preferentially to O=S, rather than water. In short, water in [Hpy][HSO_4]·2H_2O (absence of strong Brønsted acid) binds preferentially as Hw···O=S, not as Ow···HO-S, acting as hydrogen bond donor, rather than hydrogen bond acceptor.

2.3.2.5 Water-water association

In the low-water samples, H_2SO_4 and [Hpy][HSO_4]·H_2SO_4, the Ow···Ow distance is longer than in 'bulk' water, and the corresponding coordination number is low (CN ≈ 0.5), which is indicative of isolated water molecules, strongly associated with the sulfate structure. In contrast, the Ow···Ow correlation in [Hpy][HSO_4]·2H_2O (Figure 29, green line) has a first peak at 2.8 Å, comparable to that in pure water, and the coordination number (CN = 4.1 ± 2) slightly lower than that of bulk water (CN = 4.7).[159] However, the O_w···O_w RDF does not have the distinctive second peak around 4.5 Å, which would have been indicative of a long-range tetrahedral order seen in bulk water, or its larger clusters.

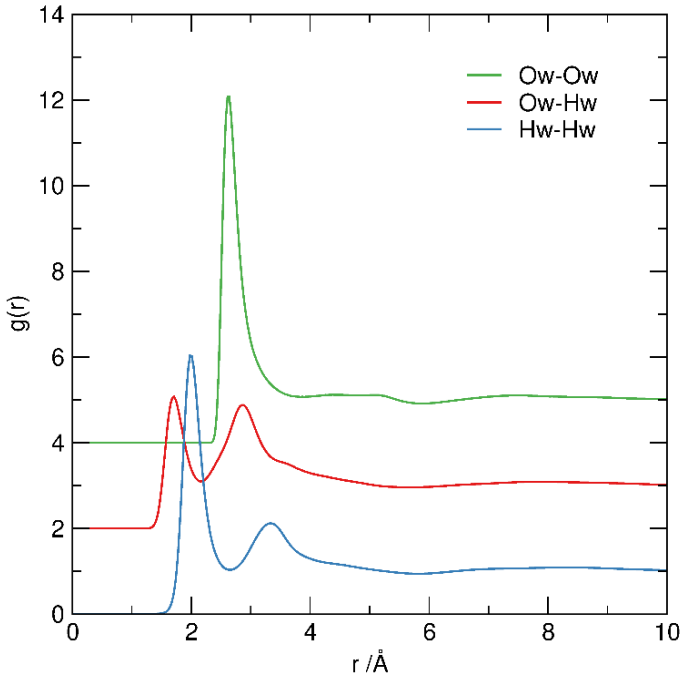

Figure 29. Site-site pRDFs between Hw and Ow for water molecules in [Hpy][HSO_4]·2H_2O.

The combination of water-like first shell and unlike-water second shell has been reported for 'bound' water in inorganic molten salt hydrates, and is consistent with the $[Hpy][HSO_4]\cdot 2H_2O$ PIL having a water-in-ionic liquid structure,[131] but approaching the transition to a concentrated salt solution.

2.3.2.6 Correlation and association around $[H\text{-}Py]^+$

RDF between $[H\text{-}Py]^+$ and $\{SO_4\}$, and between $[H\text{-}Py]^+$ and water Ow, are shown in Figure 30. In both PILs, the hydrogen-bond donating N-H site of $[H\text{-}Py]^+$ has equally close contact with hydrogen bond-accepting sites in $\{SO_4\}$ and in water. The N1···O2 and N1···Ow correlations occur at 2.7 Å in $[Hpy][HSO_4]\cdot H_2SO_4$ (Figure 30, black solid lines) and at 2.8 Å in $[Hpy][HSO_4]\cdot 2H_2O$ (Figure 30, black dashed lines). Carbon atoms of pyridine are separated by 3.4-3.6 Å from both O=S and Ow sites; these are consistent with weak contacts at the van der Waals separation distances.

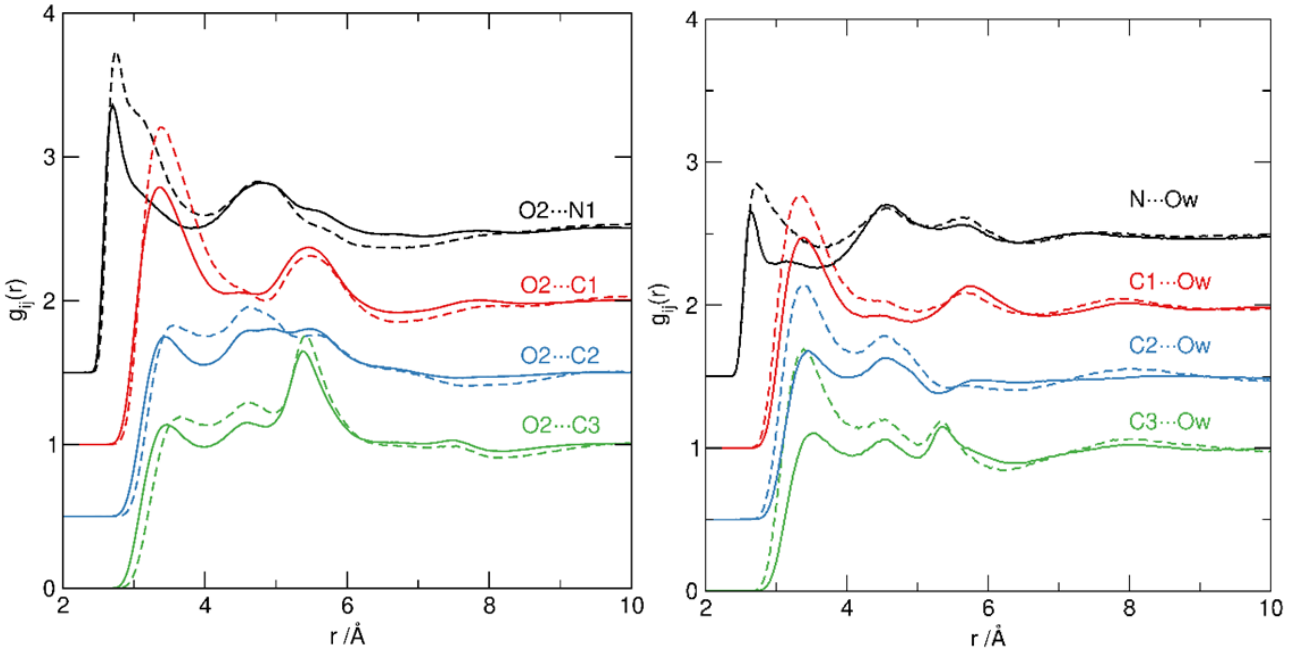

Figure 30. Site-site RDFs from pyridinium N (black) and C1 (red), C2 (blue) and C3 (green) sites to O2 oxygen atoms of the $\{SO_4\}$ units to hydrogensulfate (left) and Ow sites in water (right) for $[Hpy][HSO_4]\cdot H_2SO_4$ (solid lines) and $[Hpy][HSO_4]\cdot 2H_2O$ (dashed). Each set of correlations is displaced by 0.5 in the y-axis for clarity.

Hydrogen bond donation from S-OH sites (O1/OA1) to the pyridinium cation is not observed. Consequently, water molecules act as hydrogen-bond donors to $[HSO_4]^-$ anions through Hw···O=S interaction, and as

hydrogen-bond acceptors from $[H\text{-}Py]^+$, Ow···H-Py. The presence and directionality of water molecules within the first shells of both $\{SO_4\}$ and $[H\text{-}Py]^+$ species demonstrates the structure-forming nature of water molecules, which contributes to the overall hydrogen bond network, reinforcing the sulfate/sulfuric acid network and bridging cations and anions.[131,170]

2.3.2.7 Spatial Associations

There is a remarkable retention of correlation patterns across the three examined systems, as evidenced in the pRDFs. It is interesting to explore whether this translates to the retention of the network structure present in sulfuric acid to PILs, despite the reduced number of acidic S-OH sites and the introduction of $[H\text{-}Py]^+$ cations. SDFs in Figure 31 are plotted to the top 15% probability for correlations within the first coordination shell.

For sulfuric acid, the $\{SO_4\}$···$\{SO_4\}$ correlations (Figure 31 top, yellow surface) show a pronounced tetrahedral symmetry with four high probability nodes, each sitting over a triangular face of the $\{SO_4\}$ tetrahedron, bridged by six bands bisecting O-S-O edges. The SDF map shows holes around each oxygen atom, presumably occupied by hydrogen atoms participating in S-OH···O=S bonding from adjacent acids in the first coordination shell. The weakly correlated association of water molecules with sulfuric acid, shown in Figure 28 RDFs, is also evident in the SDF, (Figure 31, top, green surface), lacking a distinct spatial ordering.

Structure refinement for $[Hpy][HSO_4]\cdot H_2SO_4$ was made with two different $\{SO_4\}$ moieties: $[HSO_4]^-$ and $[H_2SO_4]$. Comparable distributions for both species, centred around a reference $[HSO_4]^-$ was observed, and are plotted as averaged functions, forming the same sulfuric acid-like tetrahedral distribution (Figure 31, middle left, yellow surface). Compared to H_2SO_4, the symmetry of the distribution of $\{SO_4\}$···$\{SO_4\}$ association was somewhat reduced, with the S-OH site in $[HSO_4]^-$ showing a greater probability density than the corresponding S-O oxygens. This results from altered ratio of S-OH and O=S oxygens in the system, from 1:1 to 3:4, reducing the relative proportion of hydrogen bond donor to hydrogen bond acceptor sites. In contrast, distribution of H_2O molecules around $[HSO_4]^-$ (Figure 31, middle left, green surface) was more structured in $[Hpy][HSO_4]\cdot H_2SO_4$ than it was in H_2SO_4, tracking to the positions of $\{SO_4\}$ moieties in the first shell, through Hw···O=S interaction.

Likewise, $[H\text{-}Py]^+$ cations (Figure 31, middle left, blue surface) show correlations in these positions, in an approximately tetrahedral distribution with maxima associated with each triangular face of $\{SO_4\}$ reflecting the association through hydrogen-bond donation from $[H\text{-}Py]^+$ cations to O=S sites (see Figure 30). Both the water and $[H\text{-}Py]^+$ SDFs around $[HSO_4]^-$ are truncated over the acidic S-OH group, as a result of the

predominance of this site as a hydrogen-bond donor to other $\{SO_4\}$ units, rather than a hydrogen-bond acceptor.

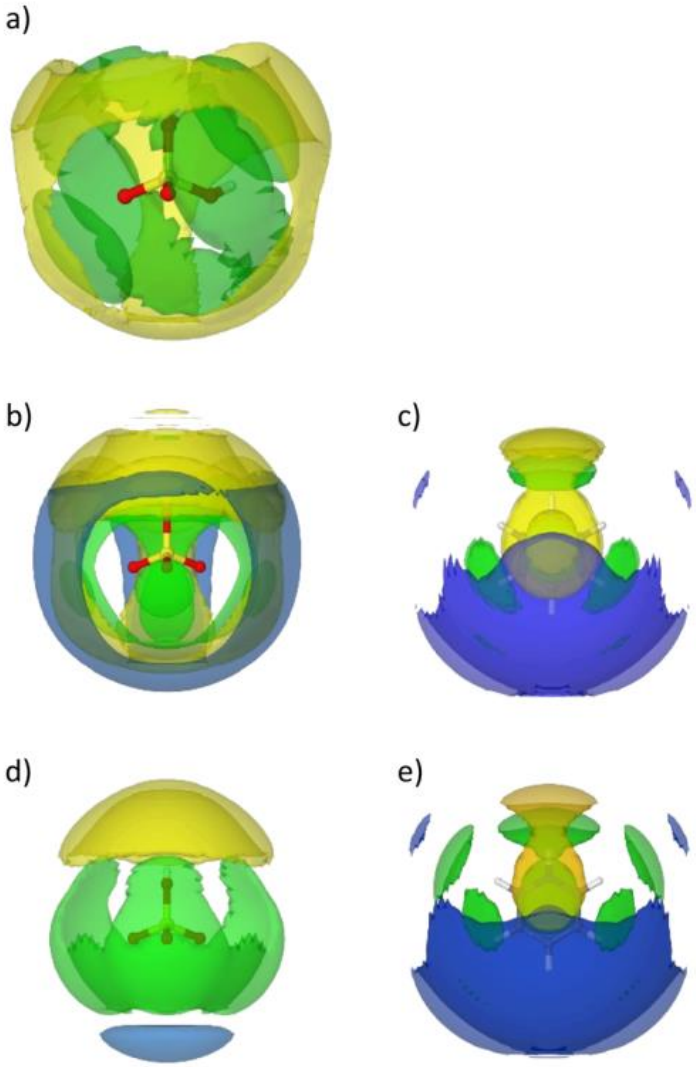

Figure 31. Spatial distribution functions (SDFs) showing the first shell environments around H_2SO_4 (a), $[Hpy][HSO_4]H_2SO_4$ (b) and (c), and $[Hpy][HSO_4]2H_2O$ (d) and (e), presenting the $\{SO_4\}$ (a), (b), (d) and $[HPy]^+$ (c), (e) environments, with the nitrogen-site of $[H\text{-}Py]^+$ pointing up. All SDFs are plotted to show the top 15% probability for correlation within the first shell, determined from the first minimum in the corresponding COM RDFs (Figure 25). The $[HSO_4]/H_2SO_4$ moieties are shown in yellow, H_2O in green and $[H\text{-}Py]^+$ in blue.

In the hydrated PIL, $[Hpy][HSO_4]\cdot 2H_2O$, the S-OH to O=S ratio is reduced to 1:3, which results in closer $\{SO_4\}\cdots\{SO_4\}$ association through the remaining S-OH site in $[HSO_4]^-$ (Figure 31, bottom left, yellow surface). The reduced number of the S-OH hydrogen bond donors leads to increased correlation of water with the O=S

sites (Figure 31, bottom left, green surface), consistent with the increased magnitude and definition of the Hw···O2 pRDF (Figure 28).

Solvation environments around $[H\text{-}Py]^+$ in both PILs are characterised by very similar spatial distributions of $\{SO_4\}$, in a band above and below the pyridinium ring, straddling the N-H site (Figure 31, right, middle and bottom, yellow surface). Water occupies similar positions, and also arranges more broadly within the equatorial plane of the $[H\text{-}Py]^+$ ring, which is particularly evident in the hydrated PIL (Figure 31, right, middle and bottom, yellow surface). This confirms water acting mainly as a hydrogen bond acceptor *via* Ow···H-N interaction, and to a lesser extent interacting through Ow···H-C motif, with hydrogens of the pyridine ring (Figure 30). Finally, the $[H\text{-}Py]^+\cdots[H\text{-}Py]^+$ SDFs (Figure 31, right, middle and bottom, blue surface) show a broad correlation around the C2/C3 positions of pyridinium rings, that even plotting the top 15% probability is highly diffuse and non-specific.

Overall, from H_2SO_4, through the Brønsted acidic PIL, and to the hydrated PIL, the first shell environment of the $\{SO_4\}$ moiety shows a transition from a highly symmetric tetrahedral distribution of acid $\{SO_4\}$ groups towards an increased probability density for $\{SO_4\}\cdots\{SO_4\}$ association at the S-OH position, as a function of the increase in anionic O=S oxygens relative to S-OH acid groups. This is evident in $[Hpy][HSO_4]\cdot H_2SO_4$ through the larger node at the S-OH site, with water-$\{SO_4\}$ and $[H\text{-}Py]^+\cdots\{SO_4\}$ correlations to sites associated with the O=S oxygens. For $[Hpy][HSO_4]\cdot 2H_2O$, the highest probability SDF correlations between $[HSO_4]^-$ anions are with the S-OH site, with hydrogen-bonding between water and O=S sites becoming more dominant, substituting for S-OH···O=S interactions in the first shell. However, these changes in the first shell correlations around $\{SO_4\}$, induced by the changes in availability of different hydrogen-bond donors, have remarkably little effect on the longer-range order in the liquids. The second shell $\{SO_4\}\cdots\{SO_4\}$ correlations between $\{SO_4\}$ units in the three systems are shown in Figure 32, plotting the top 15% probability surfaces for the first shell (3-6.5 Å) and second shell (6.5-11 Å). Remarkably, across all three systems a strong tetrahedral structure is retained, irrespective of the changes in relative $\{SO_4\}$ and water distributions in the first correlation shell. All show the same tetrahedral pattern, despite differences in the first shell. This gives strong evidence that water (and to a lesser extent pyridinium cations) act as surrogates for S-OH hydrogen-bond donors retaining the structure of the parent acid within the PILs.

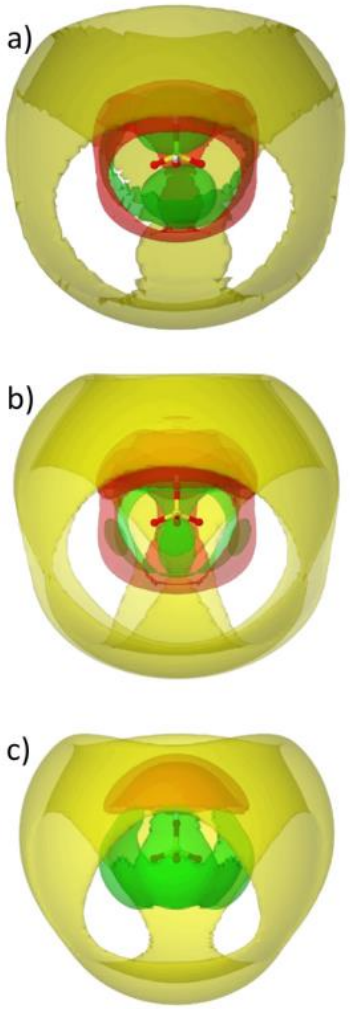

Figure 32. First and second shell correlations around {SO_4} central groups in H_2SO_4 (a); [Hpy][HSO_4]H_2SO_4 (b), and [Hpy][HSO_4]2H_2O (c). The first shell {SO_4}···{SO_4} is in red, the first shell {SO_4} water is in green and the second shell {SO_4}···{SO_4} association (6.5–11 Å) is in yellow.

2.3.2.8 Structure-property relationships

The RDFs indicate that anion-cation correlations between protonated [H-Py]$^+$ cations and [HSO_4]$^-$ anions typical of ionic liquids (and molten salts)[16] are formed in both the 'anhydrous' acidic PIL and 'hydrated' PIL with charge screening between alternate oppositely charged ions. However, in addition to this formation of typical cation-anion IL structure, the overall tetrahedral network structure directed by hydrogen-bonding around the {SO_4} groups in 'neat' sulfuric acid is persistent, retained in the PILs complemented by interactions with the [H-Py]$^+$ cations, as can be seen in the presence of correlations nodes between [H-Py$^+$] and O=S sites in 2:1:0.4 'anhydrous' acidic PIL, and increasingly by replacement of acidic S-OH hydrogen bond donors by

water molecules in the 1:1:2.2 'hydrated' PIL, to retain the supramolecular {SO_4}-network present in the parent sulfuric acid.

As such, it is clear that the 'anhydrous' acidic 2:1:0.2 PIL retains many features of concentrated sulfuric acid in terms of both acidity[89] and network structure, while simultaneously adopting the anticipated anion-cation correlation pattern characteristic of ILs. Consequently, the structure of the 'anhydrous' acidic PIL cannot be attributed to the difference in phase behaviour. However, as it undergoes hydration during esterification, the structure is altered, leading to a modified structure with phase behaviour different from that of concentrated sulfuric acid.

The addition of 2 moles of water (*ca.* 17 wt %) provides additional hydrogen bond donation capacity to complement and replace the diminished number of S-OH hydrogen-bond donors present in the parent acid. This results in a change in the nature of the first shell hydrogen-bond donors around $[HSO_4]^-$ anions, but not in the overall pattern of hydrogen bonding. This 'hydrated' sulfuric acid:pyridine:water (1:1:2.2) system has an equivalent water content to that of the aqueous alkylammonium PILs reported by Hallett *et al*.[118,124,125,133,136,137,139,142,171,172] as media for delignification for cellulosic biomass, with *ca.* 15 wt% water in the IL. It is clear that the water molecules here are present as 'bound' water participating in the ionic liquid solvation structure and not as 'free' water. That is, the system can be viewed as one with water-in-IL rather than as a concentrated IL-in-water environment.

This finding allows for certain speculations in terms of phase behaviour. In esterification reactions, where water and ester are generated, the ionic liquid gradually binds water incorporated in the hydrogen sulfate network, without the formation of 'bulk' water that can contribute to the reverse reaction of ester hydrolysis. The resulting hydrated PIL is more hydrophilic which contributes to lower affinity to the ester products and in consequence, enhanced phase separation. Likewise, it appears that the "composite" anionic structure of water-doped PIL has higher propensity to dissolve lignin, its structure being different from that of anhydrous IL, but unlikely to contain "bulk" water at the optimised ratios of 10-40% (1:1:2 composition amounts to *ca*. 20% water by weight).

The literature increasingly demonstrates intentional doping of PILs with water, revealing that water becomes integrated into the IL matrix, altering its properties rather than behaving as bulk water. The interactions between water molecules and PIL components are highly dependent on the nature of the PILs.[173] In an MD study, Kirchner and co-workers[174] investigated the PIL, methylammonium nitrate containing 1.6 wt% water, which showed strong interactions between water molecules and cations (bearing three {N–H} motifs), resulting in a tetrahedral hydrogen-bonding arrangement. It is evident that the addition of water changed the structure of the IL, mainly the anion-anion orientation. Furthermore, the average dipole moment of water was reduced. A similar finding was reported by Atkin and co-workers[175] in their neutron scattering investigation

of ethylammonium nitrate doped with a six-fold excess of water molecules. Water did not simply act as a diluent but rather interacted with all charged components of the PIL, resulting in a change in the nanostructure of the liquid.

2.3.3 Comparing models: EPSR *vs*. Dissolve

A direct comparison between the results obtained from Dissolve and EPSR is not possible since Dissolve uses a different intramolecular forcefield, which will influence the generated potentials. However, it is expected that there should be consistency between the two codes. This has been shown for liquid water, benzene and silica, where the fit quality to the experimental data was similar and the potentials broadly comparable.[94]

As per Section 1.2, EPSR employs harmonic restraints (bonds, angles and dihedrals), while Dissolve implements a fully flexible forcefield. This means that, in addition to providing harmonic bond stretching and angle bending potentials, Dissolve also implements multiple functions for torsional energy terms, as well as Coulomb and Lennard-Jones parameters for non-bonded interactions. This means that standard forcefields, such as OPLS-AA[95] (see Equation 10-Equation 14) can be used directly as the starting potentials. These potential energy functions rely on empirically derived parameters such as force constants k, and equilibrium values, r_0 and θ_0, that describes the interactions between sets of atoms. The potential energy expressions for bond stretching and angle bending are shown in Equation 10 and Equation 11. They are based on harmonic potentials and show that the potential energy increases as the bond length or angle deviates from that of the ideal.

$$E = k_r(r - r_0)^2$$

Equation 10

$$E = k_\theta(\theta - \theta_0)^2$$

Equation 11

The torsional potential describes how the energy changes as a bond rotates and is expressed as a Fourier series (Equation 12). φ_i is the dihedral angle and V_1, V_2, V_3 and V_4 are the Fourier constants.

$$E_{torsion} = \sum_i \left[\frac{1}{2}V_{1,i}(1 + \cos\varphi_i) + \frac{1}{2}V_{2,i}(1 + \cos 2\varphi_i) + \frac{1}{2}V_{3,i}(1 + \cos 3\varphi_i) + \frac{1}{2}V_{4,i}(1 + \cos 4\varphi_i)\right]$$

Equation 12

Improper torsion angles deal with out-of-plane bending modes within molecules. They are needed, for example, to keep carbon rings planar. They can also be described using a simple harmonic expression.

$$E = k\omega\,(\omega - \omega_0)^2$$

Equation 13

Non-bonded interactions describe the forces between atom pairs separated by at least three bonds. These interactions are grouped into electrostatic interactions, described by Coulomb's law, where *q* is the partial atomic charges (Equation 14). The second group is van der Waals interactions, described by the Lennard-Jones potential where the $1/r^{12}$ term describes the shorter-range repulsive forces and the $1/r^6$ term describes the longer-range attractive forces. The Lennard–Jones radii and well depths are represented by σ and ε.

$$E_{nonbond} = \sum_i \sum_{j>i} \left\{\frac{q_i q_j e^2}{r_{ij}} + 4\varepsilon_{ij}\left[\left(\frac{\sigma_{ij}}{r_{ij}}\right)^{12} - \left(\frac{\sigma_{ij}}{r_{ij}}\right)^{6}\right]\right\}$$

Equation 14

Here, EPSR models of concentrated sulfuric acid and the Brønsted acidic PIL, $[Hpy][HSO_4]{\cdot}H_2SO_4$, reported in Section 2.3.2 were compared to the models generated by Dissolve. The same experimental data is used for samples 1-10 (Table 1) and the same simulation box size parameters (

Table **2**). The difference comes from the application of forcefields to describe the molecules in Dissolve. For the description of sulfuric acid, the forcefield was taken from Kulmala *et. al*.[176] The SPC/Fw forcefield was used to describe water.[177] A forcefield definition based on the OPLS-AA parameter set was created using the LigParGen service offered by the Jorgensen group for the descriptions of hydrogen sulfate and pyridinium.[178–180]

2.3.3.1 Sulfuric acid (H_2SO_4:H_2O 1:0.2)

Figure 33 shows the comparative fits to the experimental data by EPSR and Dissolve for concentrated sulfuric acid. Aside from some relatively small discrepancies in the fits, the two codes give similar results. There is a slight mis-fit in the peak at Q = 2.4 Å^{-1}, more so for EPSR, where the intensity of the peak is not quite matched and the intensity of the next peak at 2.55 Å^{-1} is slightly higher than of the experimental data. It should be noted that the main source of discrepancies between the experimental and the simulated data occur in the region of Q < 1.5 Å^{-1}, where the inelastic scattering effect is most pronounced.

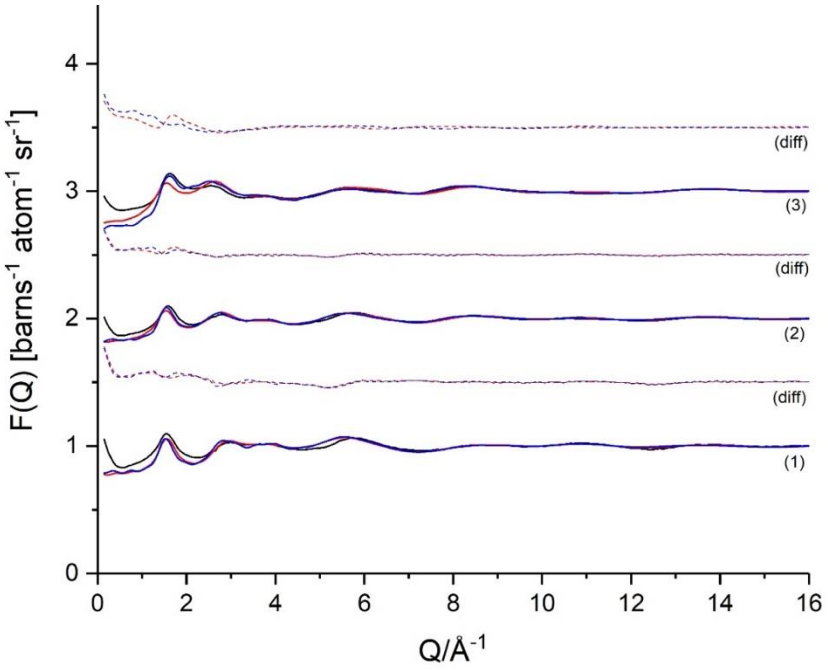

Figure 33. Experimental data (black lines) for sulfuric acid (H_2SO_4:H_2O 1:0.2), with fits (solid lines) and difference functions (dashed lines) as obtained from EPSR (red) and Dissolve (blue).

The positions of first peaks within the partial RDFs obtained for {SO_4}···{SO_4} interactions and corresponding coordination numbers, calculated to the first minima after the peak are compared between EPSR and Dissolve. As can be seen from Figure 34 the COM RDF profiles generated are very similar for both codes. EPSR reported a S···S correlation separation distance of 4.6 Å and Dissolve 4.8 Å, and for both a broad second shell correlation between 6.6-11.5 Å. The intensity of the first and second peak for EPSR does not quite match the intensity of the Dissolve peak; however, the first minimum after the peak is slightly higher in intensity for EPSR and the {SO_4}···{SO_4}. Coordination number of 11 was found by both approaches.

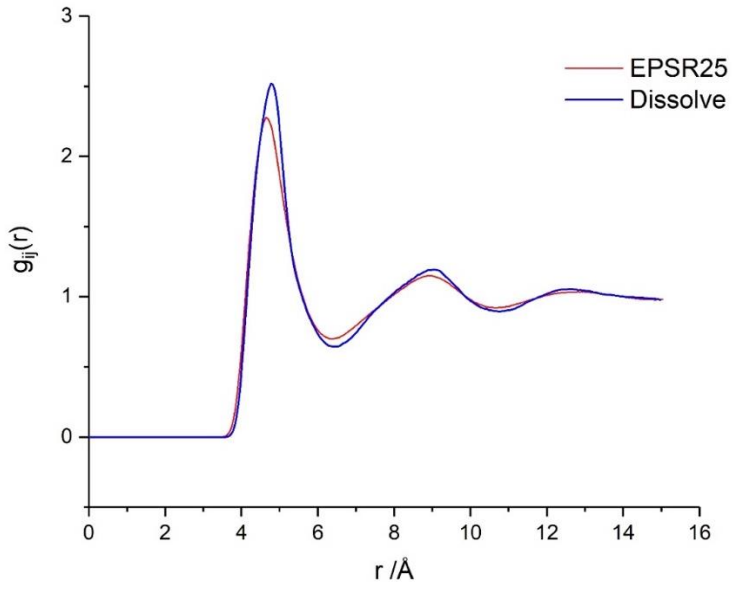

Figure 34. The COM RDFs obtained for $SO_4 \cdots SO_4$ interactions for sulfuric acid (H_2SO_4:H_2O 1:0.2) as obtained from EPSR (red) and Dissolve (blue).

2.3.3.2 Brønsted acidic PIL, $[Hpy][HSO_4]\cdot H_2SO_4$

Figure 35 shows the comparative fits to the experimental data by EPSR and Dissolve for the Brønsted acidic PIL, $[Hpy][HSO_4]\cdot H_2SO_4$. Again, there is only relatively small discrepancies in the fits, with the two codes giving very similar results.

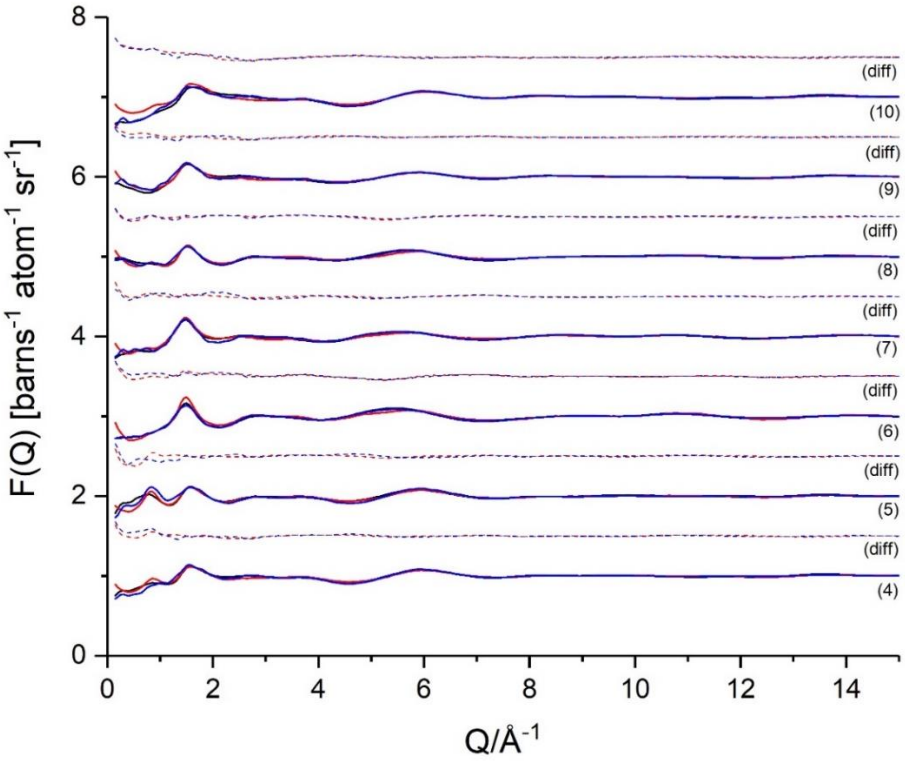

Figure 35. Experimental data (black lines) for Brønsted acidic PIL (H_2SO_4:py:H_2O 2:1:0.4) with fits (solid lines) and difference functions (dashed lines) as obtained from EPSR (red) and Dissolve (blue).

Figure 36 shows a comparison of the COM RDFs generated for EPSR and Dissolve for interactions between {SO_4} units (Figure 36, left) and between [H-Py]$^+$ and {SO_4} (Figure 36, right) for Brønsted acidic PIL (H_2SO_4:py:H_2O 2:1:0.4). Considering that [Hpy][HSO_4]·H_2SO_4 contains both [HSO_4]$^-$ and H_2SO_4 species, which exchange protons, it was challenging to represent the system accurately. To represent {SO_4}···{SO_4} interactions, it was necessary to merge the two components: [HSO_4]$^-$ and H_2SO_4, which introduced a bit of ambiguity. The S-O distance starting potentials of H_2SO_4 and [HSO_4]$^-$ were averaged, which gave a better fit to the experimental data. This was a compromise that had to be made in EPSR to achieve a working model and enable calculating the interactions of the anion as accurately as possible. In Dissolve, the starting potentials from the OPLS-AA forcefield were used to model both H_2SO_4 and [HSO_4]$^-$. Like in EPSR, the RDF profile and the coordination numbers were formulated by averaging the H_2SO_4 and [HSO_4]$^-$ data.

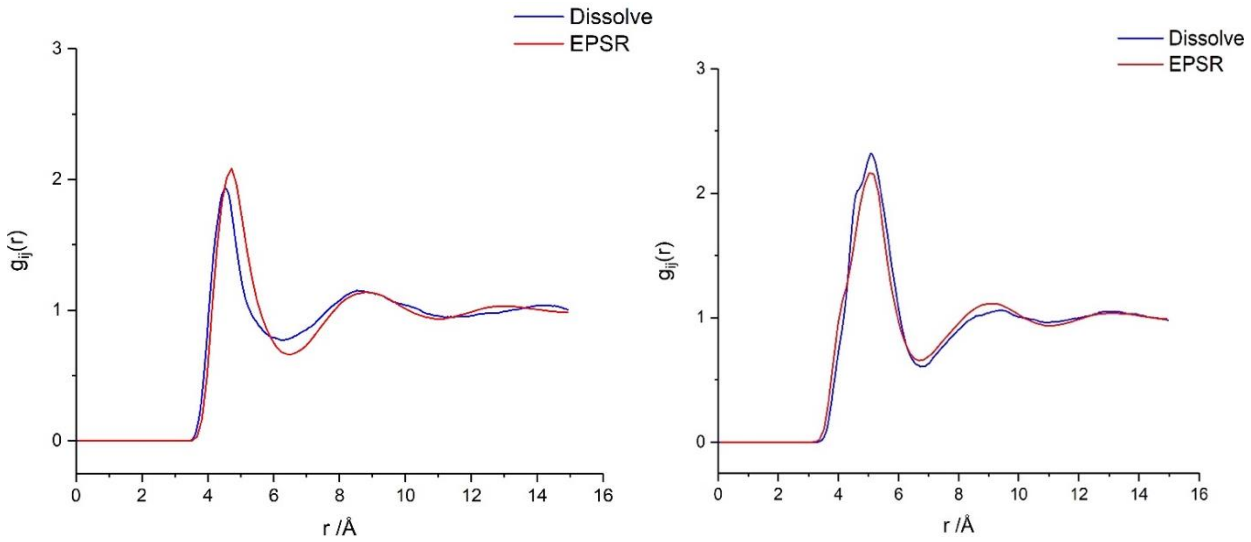

Figure 36. The COM RDFs obtained for interactions between $\{SO_4\}$ units (left) and $[H\text{-}Py]^+$ and $\{SO_4\}$ (right) for Brønsted acidic PIL (H_2SO_4 : py : H_2O 2 : 1 : 0.4) as obtained from EPSR (red) and Dissolve (blue).

The COM RDF profiles were similar for both codes (Figure 36). EPSR reported a S···S separation distance of 4.8 Å and the $\{SO_4\}\cdots\{SO_4\}$ CN of 7.5, which is similar to the separation distance of 4.6 Å and CN of 7.8 reported by Dissolve. The interactions between $[H\text{-}Py]^+$ and $\{SO_4\}$ units were also similar for both codes, reporting CN of 4.

A significant difference between EPSR and Dissolve is their treatment of intramolecular flexibility. In EPSR, intramolecular moves are approached on per-molecule basis, considering only the intramolecular energy. In Dissolve, in contrast, these moves are affected by the field produced by neighbouring molecules. Therefore, while it is expected that the generated interatomic empirical potentials should be similar, it would be unreasonable to assume that they would be identical.

In this work it is evident that the flexibility given to the pyridinium ring can give you different results. Figure 37 shows the RDF profiles between $[H\text{-}Py]^+$ for the Brønsted acidic PIL, $[Hpy][HSO_4]\cdot H_2SO_4$, for three different optimisations of pyridinium: fully flexible, semi-rigid and rigid. It is only the flexible pyridinium ring that gives the prominent pre-peak around 4 Å in the RDF, due to the pyridinium rings interacting with each other. Therefore, it was necessary to increase the value of the force constant given to the improper torsion terms on the pyridinium ring to keep the ring planar and rigid. For semi-rigid and rigid configurations, the peak at 4 Å disappears. The semi-rigid form also gives the better fit to the experimental data and aligns more closely with the EPSR results. However, it is noted that the RDF profile differs between Dissolve and EPSR: with simulations from Dissolve giving more of a shoulder around 4 Å and a slightly more intense second shell correlation peak,

which is offset by the decrease in intensity of the peak at 6 Å. The differences in the correlations of the pyridinium rings between EPSR and Dissolve are ultimately due to the different forcefields used.

EPSR and Dissolve calculate a value indicating the quality of the agreement between the simulated and the experimental F(*Q*), called the *R*-factor, where a low *R*-factor means a better fit (Equation 15).

$$R = \frac{\sum F(Q)_{exp} - F(Q)_{calc}}{\sum F(Q)_{exp}}$$

Equation 15

The calculated *R*-factor when the fully flexible pyridinium ring was used was 1.47×10^{-4} and 1.34×10^{-4} was calculated for the system containing the semi-rigid pyridinium. These low values express a high agreement between the simulated and experimental data.

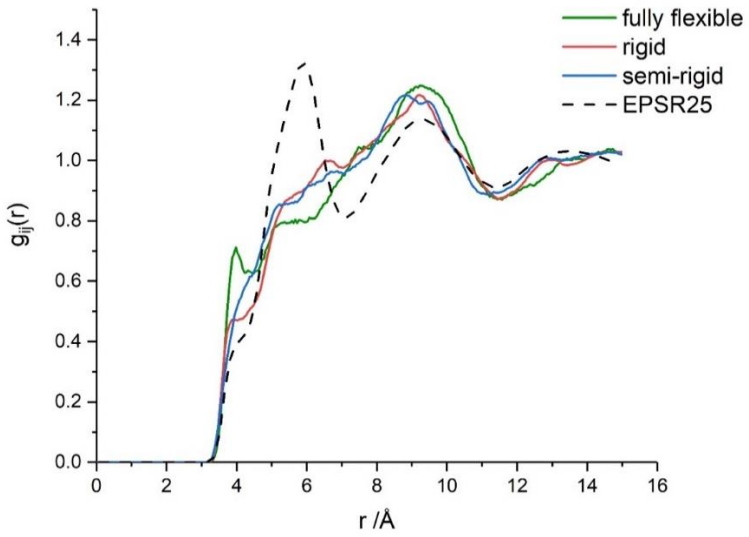

Figure 37. COM RDFs between [H-Py]$^+$ cations for Brønsted acidic PIL, [Hpy][HSO_4]·H_2SO_4, showing the variation in results for three different optimisations of pyridinium: fully flexible, semi-rigid and rigid and comparison to EPSR results.

The comparative study between EPSR and Dissolve for the two systems; sulfuric acid (H_2SO_4:H_2O 1:0.2) and the Brønsted acidic PIL (H_2SO_4:Py:H_2O 2:1:0.4), show that the resulting fits to experimental data are nearly identical between the two codes. The RDFs generated are broadly similar but certainly not identical between EPSR and Dissolve, as expected due to the different starting intramolecular forcefield parameters. It is evident

that the flexibility given to the pyridinium ring, and flexibility in general, can give different results which is an important note for users of Dissolve to keep in mind. With Dissolve, there is more responsibility on the user to supply the correct forcefield and additional functional terms to best describe their system.

2.4 Conclusions and Outlook

The Brønsted acidic protic ILs described in this work have applications in both acid catalysis and biomass pre-treatment. In both cases, the presence of water, either as a product of esterification reactions, or with intentional doping of the IL, has been identified as the key factor altering their properties and contributing to their excellent performance in these particular applications. Neutron scattering results show that in addition to the typical cation-anion interactions of ILs, they have a persistent sulfate/sulfuric acid/water network. Remarkably, this network structure was retained even in the presence of 2 mol (~17 wt%) of water. Hydrogen sulfate PILs have been shown to incorporate water into hydrogen-bonded anionic chains to form essentially a new solvent system, with properties distinctive from both sulfuric acid and the parent IL. This hydrated PIL was understood to be more lipophobic than neat sulfuric acid, thus better phase-separating in esterification and demonstrating favourable solvent/antisolvent behaviour in biomass fractionation.

The neutron scattering data was also analysed by the new total scattering software, Dissolve. Dissolve addresses some of the restrictions of EPSR and enables larger systems to be investigated. This data showed consistency between the two codes, measuring ionic liquids and ionic liquids plus solutes. The differences observed for some of the correlations, reflects the changes in the forcefield parameters.

Given the results from this study, it is evident that water has a beneficial effect on the phase behaviour of these protic ILs due to its incorporation into the $\{SO_4\}$ network. The resulting hydrated PIL is more hydrophilic, which contributes to a lower affinity of weakly hydrogen bonding molecules, such as esters, and in consequence, enhanced phase separation. However, molecules with a high hydrogen bonding ability have greater solubility, aiding fractionation of lignocellulosic biomass. Future work could involve the study of solvation of model compounds such as esters or lignocellulosic biomass in wet and dry PILs by neutron scattering.

Chapter 3

Structure of bistriflimide ionic liquids

3 Structure of bistriflimide ionic liquids

This chapter was inspired by our interest in applications of ionic liquids based on the bis(trifluoromethanesulfonyl)imide anion, abbreviated in the literature as $[NTf_2]^-$ or $[TFSI]^-$. Before moving to more complex problems, the structure of $[NTf_2]^-$ ILs based on three cations: 1-ethyl-3-methylimidazolium, $[C_2mim]^+$, 1-decyl-3-methylimidazolium, $[C_{10}mim]^+$, and trihexyl(tetradecyl)phosphonium, $[P_{666,14}]^+$, were studied using neutron scattering. Data-driven simulations were carried out with a new Dissolve[94] package, which uses methodology similar to the conventional Empirical Potential Structure Refinement (EPSR)[6] code, but enables the inclusion of larger systems. In contrast to EPSR, Dissolve has enabled robust modelling of long alkyl chains, therefore neutron scattering-derived structures of $[C_{10}mim]^+$ and $[P_{666,14}]^+$ could be elucidated for the first time.

Our motivation to study the structure of $[P_{666,14}][NTf_2]$ came from a collaboration with the Wojnarowska group from the University of Silesia, Katowice, published in *Nature Commun,*[181] *J. Phys. Chem. Lett.*, [200] and *ACS Appl. Mater. Interfaces*.[201] Our collaborative work has demonstrated the first evidence of a liquid-liquid transition (LLT) in $[P_{666,14}][NTf_2]$, and other ILs containing the $[P_{666,14}]^+$ cation, combined with anions of different sizes and shapes, thereby providing an insight into the structure-property relationships governing LLT. My involvement in this work was the synthesis of three high-purity ionic liquids: $[P_{666,14}][BH_4]$, $[P_{666,14}][BOB]$ and $[P_{666,14}][NTf_2]$. Our interest in the structure of $[C_{10}mim][NTf_2]$, came from previous work in the group from 2018 by Brown *et. al.*[184] which showed experimental evidence of the encounter complex of the frustrated Lewis pair (FLP), $P(^tBu)_3$/BCF, in $[C_{10}mim][NTf_2]$ by NMR spectroscopy. This is expanded upon in Chapter 4, which combines research strands of FLPs and ionic liquids, where the formation of the encounter complex by neutron scattering in $[C_{10}mim][NTf_2]$ and $[C_2mim][NTf_2]$ is investigated.

The first part of this chapter describes a detailed procedure for the synthesis of perdeuteriated $[P_{666,14}][NTf_2]$. The second part is concerned with the structure of $[P_{666,14}][NTf_2]$, as well as $[C_2mim][NTf_2]$ and $[C_{10}mim][NTf_2]$, with full H/D isotopic substitution, using neutron scattering and the analysis of the results using Dissolve software. This contribution provided an important steppingstone for the neutron scattering study of ionic liquids with long alkyl chains. To demonstrate the robustness of the model, three different sets of cation charges were used for the three ILs and the models were shown to converge on the same outcome. This was a good test for the robustness of the model which will aid in the analysis of results in Chapter 4.

Work reported in this chapter has been submitted to *J. Phys. Chem. B*. *Invited submission to Special Issue - COIL-9: 9th Congress on Ionic Liquids.*

3.1 Introduction

The most common ILs contain cations based on quaternised nitrogen or phosphorus bases, which are the focus of this work. Neutron scattering data of ionic liquids with long alkyl chains, such as $[P_{666,14}][NTf_2]$ and $[C_{10}mim][NTf_2]$, could not be modelled with EPSR[6] due to the long, flexible alkyl chains. This has changed with the release of Dissolve,[94] a new software for total scattering analysis. $[C_{10}mim][NTf_2]$ and $[C_2mim][NTf_2]$ are of interest for FLP chemistry, and a publication by the group showed that the FLP encounter complex could be detected in $[C_{10}mim][NTf_2]$ by NMR spectroscopy.[184] Chapter 4 describes the encounter complex formation by neutron scattering with the FLP dissolved in $[C_{10}mim][NTf_2]$ and $[C_2mim][NTf_2]$.

Tetraalkylphosphonium ILs are of interest as they have a wide liquidus range, relatively high thermal and electrochemical stability, making them attractive options for energy storage applications such as in batteries and supercapacitors.[48–50] MacFarlane and co-workers used a $[P_{666,14}]^+$ IL to generate ammonia from lithium-mediated nitrogen reduction reaction, where the $[P_{666,14}]^+$ cation is the proton carrier in the reaction, through the formation of an ylide.[51] They are also hydrophobic, which has sparked interest in their use in liquid-liquid separations, from metals to biomass.[52–59]

The bis(trifluoromethanesulfonyl)imide anion, $[NTf_2]^-$, imparts a number of beneficial properties to ionic liquids, including, but not limited to: low melting point, relatively low viscosity, wide electrochemical window, hydrophobicity and stability towards hydrolysis. On the molecular level, $[NTf_2]^-$ is characterised by diffuse charge distribution, very weak coordination ability (although it can coordinate to metals and accept hydrogen bonds *via* both N and O atoms) and the ability to adopt two conformations: *cis* and *trans* (Figure 38), all of which contribute to low lattice energy of $[NTf_2]^-$ salts. This combination of properties has inspired a multitude of studies on fundamental properties and applications of $[C_nmim][NTf_2]$[46,185–187] and $[P_{666,14}][NTf_2]$[30,31,60–63,188] ionic liquids. In this work, the ILs are studied by neutron scattering because their liquid structure is vastly different from the solid. This was demonstrated by Deetlefs *et. al*[46] in 2006 who showed that the liquid structure of $[C_1mim][NTf_2]$, obtained from neutron scattering, had little correlation with its crystal structure.[189] This was in contrast to the chloride and hexafluorophosphate salts and the difference was attributed to the conformational flexibility of the $[NTf_2]^-$ anion, which can adopt both *cis* and *trans* conformers in the liquid state, in contrast to fixed conformers in the solid.[47] The C–S–S–C torsional angle within the $[NTf_2]^-$ anion serves as a distinguishing factor between its *cis* and *trans* conformers, spanning from 0° to 180°. This wide range highlights the high flexibility of the system, with higher angles around 180° corresponding to the *trans* conformer and a lower angle around 40° corresponding to *cis* conformer.[190]

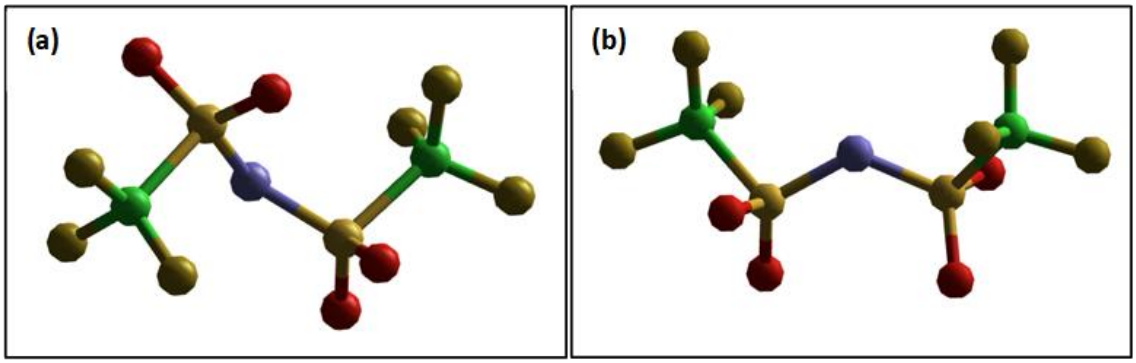

Figure 38. Models showing (a) the *trans* and (b) the *cis* configuration of the bis(trifluoromethanesulfonyl)imide anion, $[NTf_2]^-$.

The main motivation to study $[P_{666,14}][NTf_2]$ came from our collaborative work with the Wojnarowska group,[181,200,201] who studied LLT formation in a series of ILs containing trihexyl(tetradecyl)phosphonium cation $[P_{666,14}]^+$ and different anions. This work has aided in the understanding of the nature of the phenomena surrounding LLT formation gives an insight into structure-property relationships governing LLT.

When an isotropic liquid is cooled below its melting point, it either crystallises, or enters a metastable supercooled state, which turns into a non-equilibrium amorphous phase (glass). However, it has been reported that a few single-component materials display another behaviour, undergoing a first-order liquid-liquid transition (LLT). Two or more liquid states may exist even for single-component substances, which is known as liquid polymorphism, and the transition between them is called LLT. Tanaka and co-workers[191] explained that the interplay of packing effects and particular symmetry-selective interactions typically results in cooperative medium-range ordering within any liquid and it is this bond ordering that is the origin of LLT. LLTs separate fluids of different local structures, density and thermodynamic properties. They have been identified in a few materials, from atomic elements (sulfur, phosphorus,[192] silicon,[193,194] carbon[195]) to molten oxides.[196,197,198] Only four molecular liquids exhibit LLT: water,[199,200] triphenyl phosphate,[201,202,203] *n*-butanol[201] and D-mannitol.[204] Even so, experimental evidence for the LLT formation in many systems is controversial, since it occurs in the supercooled state capable of cold crystallisation.[191] In addition, apart from a few cases,[205,206] very little is known about the effect of molecular packing on LLT. As a result, there is uncertainty surrounding the critical factor leading to such a transition. The first report of LLT in ILs was from Harris *et. al* in 2021 for the aprotic IL trihexyl(tetradecyl)phosphonium tetrahydroborate, $[P_{666,14}][BH_4]$.[207] Upon the transition, the IL was reported to undergo enhanced ordering of the alkyl chains in the nonpolar domains. This was seen from wide-angle X-ray scattering data which showed an extension and increased ordering of the polarity-alternation structure, with an increase in coordination number. This structural reorganisation was also supported by Raman and calorimetric studies, but it was seen as unique to this particular IL.

This work inspired the systematic investigation into LLTs in $[P_{666,14}]^+$ ionic liquids based on six anions: $[BF_4]^-$, $[SCN]^-$, $[TAU]^-$, $[NTf_2]^-$ $[BOB]^-$ and $[TCM]^-$ (Figure 39) as reported by Wojnarowska *et. al*.[181] $[P_{666,14}][BF_4]$ crystallised, $[P_{666,14}][BOB]$ underwent a glass transition, and the four remaining ILs exhibited LLT in a differential scanning calorimetry (DSC) experiment. Further to the calorimetric proof of LLT *via* DSC, the phase change was detected by the measurement of conductivity relaxation times, both under isobaric cooling and under isothermal compression. The effect of cation self-assembly and its influence on LLT was further highlighted in a recent publication by Wojnarowska *et. al*.,[182] which showed that the carbon-14 chain length of tetraalkylphopshonium ILs was necessary to induce the LLT. The nanostructure of $[P_{666,14}]^+$ ILs was found to be dependent on the size of the anion, and it was the nanostructure that controlled the charge transport mechanism.[183]

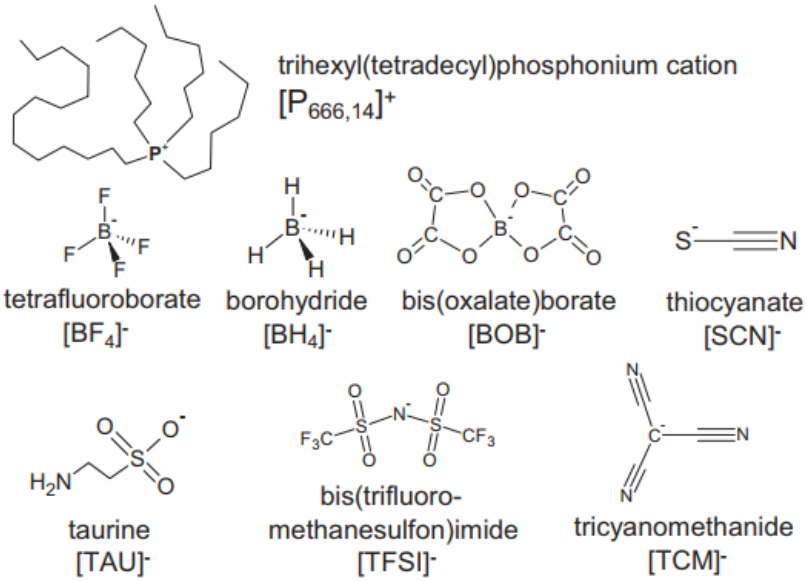

Figure 39. Structures of the trihexyl(tetradecyl)phosphonium cation $[P_{666,14}]^+$ and anions: tetrafluoroborate $[BF_4]^-$, borohydride $[BH_4]^-$, bis(oxalate)borate $[BOB]^-$, thiocyanate $[SCN]^-$, taurine $[TAU]^-$, bis(trifluoromethanesulfon)imide $[TFSI]^-$, tricyanomethanide $[TCM]^-$.

It is known that ionic liquids are highly structured media (considering their liquid state), which is driven by Coulombic interactions.[2,18,130,208–210] The presence of long alkyl chains induces microsegregation into polar and non-polar domains, which translates to differences in physicochemical properties.[22,211–213] It could therefore be expected that an experimental, neutron scattering study of the liquid structure of ILs with the same anion but three different cations: $[C_2mim][NTf_2]$, $[C_{10}mim][NTf_2]$ and $[P_{666,14}][NTf_2]$ (Figure 40), would add fundamental understanding to structure-property relationships. Until recently, such studies were prevented by the paucity of suitable software.

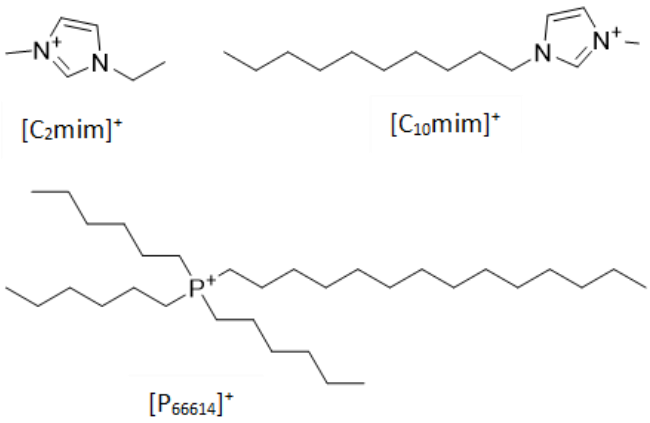

Figure 40. The structure of the three cations studied in this work: $[C_2mim]^+$, $[C_{10}mim]^+$ and $[P_{666,14}]^+$.

Over the past two decades, the use of Empirical Potential Structure Refinement (EPSR) package, developed by Soper,[6] to analyse neutron scattering data has been a valuable and indispensable tool. A new code, Dissolve,[94] builds on the success of EPSR but employs a full classical force field and has capability for million-atom simulations.[94] This fully flexible forcefield has now allowed for larger and more flexible structures, such as $[C_{10}mim][NTf_2]$ and $[P_{666,14}][NTf_2]$, to be treated more accurately. Dissolve was used in this work to analyse the structure of the three ILs and, at the time of writing, this is the first report of using Dissolve to study the liquid structure of ionic liquids. To demonstrate the robustness of Dissolve analysis, three different sets of cation charges were used for the three ILs, and the models were shown to converge on the same outcome. This demonstrated the relative insensitivity of the simulation to these reasonable charge models.

Neutron scattering data for $[C_2mim][NTf_2]$, $[C_{10}mim][NTf_2]$ and $[P_{666,14}][NTf_2]$ were recorded with full H/D isotopic substitution. Along with demonstrating the suitability of the Dissolve methodology for the analysis of IL data, an improved method for the synthesis of fully deuteriated D_{68}-$[P_{666,14}][NTf_2]$ is also described. This work successfully addresses challenges in both modelling and synthesis of ionic liquids with long alkyl chains, which will hopefully open up a new strand of neutron scattering studies.

3.2 Experimental

3.2.1 General

Trihexyl(tetradecyl)phosphonium chloride, $[P_{666,14}]Cl$, was kindly provided by Solvay. Perdeuteriated 1-hexanol and 1-tetradecanol as well as deuteriated $[C_2mim][NTf_2]$ and $[C_{10}mim][NTf_2]$ was provided from D-lab at ISIS

Neutron and Muon source. All other chemicals were purchased from Sigma-Aldrich and used as received. XRF analysis was performed on a Rigaku NEX QC+ QuantEZ High-Resolution Energy Dispersive X-ray Fluorescence (EDXRF) Spectrometer. NMR spectra were recorded on either a Bruker Avance III 400 MHz spectrometer or a Bruker Avance II DPX 600 MHz spectrometer. Quantitative ^{1}H NMR was recorded on a Bruker Avance III 400 MHz spectrometer, with benzene as an internal standard and CD_3OD as NMR solvent.

3.2.2 Synthesis of $[P_{666,14}][BOB]$

$[P_{666,14}][BOB]$ was synthesised in a two-step synthesis, following a recently-reported, improved procedure.[214]

Na[BOB]. Oxalic acid (0.030 mol eq.) and boric acid (0.010 mol eq.) were separately dissolved in water and then combined under constant stirring. Na_2CO_3 (0.5 mol eq.) was slowly added to the mixture with vigorous stirring. The turbid solution was heated to 120 °C and water collected by distillation until a dry white powder was obtained. The crude product was dispersed in hot acetonitrile at 60 °C and stirred for one hour. The white powder formed was isolated using vacuum filtration. The product was further washed with cold ethanol and the powder was dried overnight under high vacuum (12 h, 60 °C, 10^{-2} mbar). ^{13}C and ^{11}B NMR spectra of sodium bis(oxalate)borate, Na[BOB], were recorded in $CDCl_3$. ^{13}C NMR (600 MHz, $CDCl_3$) δ: 158.59. ^{11}B NMR (600 MHz, $CDCl_3$) δ: 7.35.

$[P_{666,14}][BOB]$. Trihexyl(tetradecyl)phosphonium chloride $[P_{666,14}]Cl$ (0.010 mol eq.) and sodium bis(oxalato)borate (0.010 mol eq.) were mixed in 150 ml of dichloromethane, DCM. The reaction mixture was stirred overnight at room temperature and then water was added under continuous stirring. The aqueous layer was separated, and the organic layer was collected and washed with 100 ml deionised water. Subsequent washes were performed with solution of Na[BOB] in deionised water. The final three washes were performed with deionised water until no chloride could be detected with silver nitrate solution. Subsequently, DCM was removed *via* rotary evaporation (30 min, 35 °C) and the ionic liquid was dried overnight under high vacuum (12 h, 60 °C, 10^{-2} mbar). XRF analysis of $[P_{666,14}][BOB]$ recorded a chloride content of 158 ppm with a lower detection limit (LDL) of 2.22 ppm. ^{1}H, ^{13}C and ^{31}P NMR spectra of the ionic liquid were recorded in $CDCl_3$. ^{1}H NMR (600 MHz, $CDCl_3$) δ 0.90 (m, 12H), 1.25-1.54 (m, 48H), 2.15 (m, 8H). ^{13}C NMR (600 MHz, $CDCl_3$) δ 13.98, 14.23, 18.99, 19.00, 21.63, 21.67, 21.71, 22.37, 22.80, 27.92, 28.35, 28.94, 29.47, 29.65, 29.75, 29.79, 30.44, 30.79, 31.01, 32.03, 159.03. ^{11}B NMR (600 MHz, $CDCl_3$) δ 7.66. ^{31}P NMR (600 MHz, $CDCl_3$) δ 33.18.

3.2.3 Synthesis of $[P_{666,14}][BH_4]$

Trihexyl(tetradecyl)phosphonium chloride $[P_{666,14}]Cl$ (0.010 mol eq.) and sodium borohydride, $Na[BH_4]$ (0.013 mol eq.) were separately added to 25 ml deionised water (total 50 ml) and then combined in a round-bottomed flask (250 ml), resulting in the formation of a biphasic liquid system; the mixture was left to react (1 h, room temperature, 600 rpm). The aqueous layer was separated, and the organic layer was collected and washed, firstly with deionised water (10 ml) and then dichloromethane, DCM (10 ml). Subsequent washes were performed with solution of $Na[BH_4]$ in deionised water. Final three washes were performed with deionised water until no chloride could be detected with silver nitrate solution. Subsequently, DCM was removed *via* rotary evaporation (30 min, 35 °C) and the ionic liquid was dried under high vacuum (overnight, 70 °C, 10^{-2} mbar). ^{1}H, ^{13}C, ^{11}B and ^{31}P NMR spectra were recorded in d_6-DMSO. XRF analysis confirmed chloride content was below the detectable limit. ^{1}H NMR (600 MHz, d_6-DMSO) δ -0.72 (q, 4H), 0.44-0.60 (m, 12H), 0.60-0.92 (m, 18H), 0.92-1.01 (m, 14H), 1.04-1.16 (m, 8H), 1.17-1.38 (m, 8H), 1.92-2.48 (m, 8H). ^{13}C NMR (600 MHz, d_6-DMSO) δ 13.15, 13.18, 18.07, 20.98, 21.06, 21.62, 21.75, 21.84, 27.54, 28.29, 28.57, 28.75, 28.87, 28.96, 29.64, 30.00, 30.17, 30.36, 31.11. ^{11}B NMR (600 MHz, d_6-DMSO) δ -36.98 ^{31}P NMR (600 MHz, d_6-DMSO) δ 32.72.

3.2.4 Synthesis of $[P_{666,14}][NTf_2]$

Trihexyl(tetradecyl)phosphonium chloride, $[P_{666,14}]Cl$ (0.010 mol eq.) and lithium bis(trifluoromethanesulfon)imide $Li[NTf_2]$ (0.013 mol eq.) were separately dissolved in 25 mL deionised water (total 50 mL) and then combined resulting in the formation of a biphasic liquid system; the mixture was left to stir for 1 h at room temperature, 600 rpm. The aqueous layer was separated, and the organic layer was collected and washed, firstly with deionised water (10 mL) and then dichloromethane, DCM (10 mL). Subsequent washes were performed with solution of $Li[NTf_2]$ in deionised water. Final three washes were performed with deionised water until no chloride could be detected with silver nitrate solution. Subsequently, DCM was removed *via* rotary evaporation and the ionic liquid was dried under high vacuum (12 h, 70 °C, 10^{-2} mbar). XRF analysis confirmed chloride content was below the detectable limit. ^{1}H, ^{13}C, ^{19}F and ^{31}P NMR spectra of the IL were recorded in $CDCl_3$. ^{1}H NMR (400 MHz, $CDCl_3$) δ 0.89 (m, 12H), 1.26-1.48 (m, 48H), 2.11 (m, 8H). ^{13}C NMR (400 MHz, $CDCl_3$) δ: 13.53, 13.64, 17.45, 17.52, 20.46, 20.50, 20.54, 21.75, 22.07, 28.81, 28.90, 29.04, 29.09, 29.70, 29.95, 30.34, 31.32, 119.50 (q, $^{1}J_{C\text{-}F}$ = 1280 Hz CF_3). ^{19}F NMR (400 MHz, $CDCl_3$) δ -79.00. ^{31}PNMR (400 MHz, $CDCl_3$) δ 32.94.

3.2.5 Direct deuteriation of $[P_{666,14}]^+$ cation in $[P_{666,14}]Cl$

The reaction was carried out in a 100 mL Parr high pressure reactor fitted with a mechanical stirrer. 5.08 g of $[P_{666,14}]Cl$, 0.50 g NaOH, 0.25 g Pt/C and 50 ml D_2O were added to the 100 mL Parr reactor body (made of Hastelloy c276). After the reactor was sealed, the reactor was pressurised with nitrogen (40-50 bar). The reactor was then heated to 180 ^oC using the heating mantle and stirred at 600 RPM for 3 days. After cooling, the reaction mixture was diluted with dichloromethane, filtered through Celite, washed with dichloromethane and then the aqueous phase was extracted with dichloromethane (3 x 50 mL). Dichloromethane was removed by rotary evaporation and four subsequent cycles were performed. $[P_{666,14}][OH]$ was formed and mass spec showed that 8 hydrogens (four P–CH_2 protons) of the 68 hydrogens were deuteriated. ^1H NMR (400 MHz, CD_3OD) δ 0.71 (m), 1.07-1.33 (m). ^{13}C NMR (400 MHz, CD_3OD) δ 12.74 (m), 21.12 (m), 26.94 (m), 29.73 (m). ^{31}P NMR (400 MHz, CD_3OD) δ 32.55.

3.2.6 Synthesis of D_{68}-trihexyltetradecylphosphonium bis(trifluoromethylsulfonyl)amide *via* Grignard reaction

Scheme 2 and Sections 3.2.6.1-3.2.6.4 describe the steps to synthesise perdeuteriated trihexylphosphine, D_{39}-P_{666}, via Grignard reaction, followed by alkylation with D_{29}-1-chlorotetradecane to yield D_{68}-$[P_{666,14}]Cl$. This would then be subjected to ion exchange with $Li[NTf_2]$ to generate D_{68}-$[P_{666,14}][NTf_2]$.

Scheme 2. The synthesis of perdeuteriated trihexylphosphine, D_{39}-P_{666}, via Grignard reaction, followed by alkylation with D_{29}-1-chlorotetradecane to yield D_{68}-[$P_{666,14}$]Cl. This was then subjected to ion exchange with Li[NTf_2] to generate D_{68}-[$P_{666,14}$][NTf_2]. Blue alkyl chains depict the deuteriated alkyl chains.

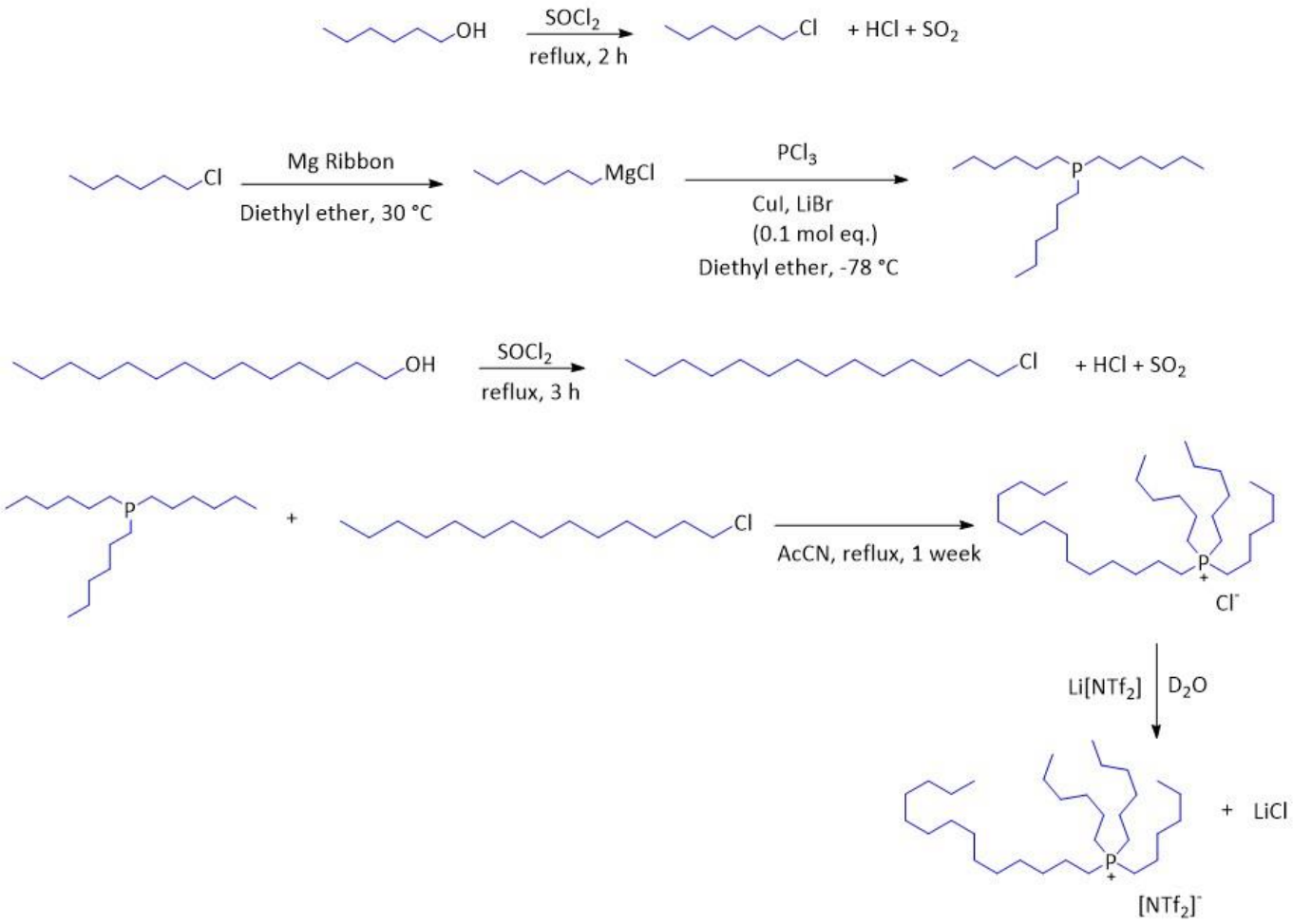

3.2.6.1 Synthesis of D_{13}-1-chlorohexane

Thionyl chloride (27.62 g, 0.232 mol) was added to a 2-necked round bottom flask equipped with a PTFE coated magnetic stirrer bar, condenser and pressure equalising dropping funnel, which were both fitted with calcium chloride guard tubes. D_{13}-hexanol (8.92 g, 0.0774 mol) was then added to the pressure equalising dropping funnel and added slowly to the thionyl chloride with stirring. As the reaction progressed, heat and SO_2 evolved. When all the alcohol was added, the mixture was heated at reflux for 2 hours. The excess of thionyl chloride was then separated from the product by distillation, (78-80 °C), with the crude D_{13}-1-chlorohexane at 132-133 °C. This was then washed with D_2O, 10% sodium carbonate solution and twice with D_2O. Then, dried with anhydrous calcium chloride and distilled again. Pure 1-chlorohexane-d_{13} passes over at 133-134 °C.^{13}C NMR (400 MHz, $CDCl_3$) δ 12.8 (m), 21.1 (m), 25.1 (m), 28.4 (m), 29.6 (m), 31.4 (m), 44.3 (m).

3.2.6.2 Synthesis of D_{29}-1-tetradecylchloride

Thionyl chloride (13.93 g, 0.117 mol) was added to a 2-necked round-bottomed flask equipped with a PTFE coated magnetic stirrer bar, condenser, and pressure equalising dropping funnel, which were both fitted with calcium chloride guard tubes. D_{29}-tetradecanol (9.50 g, 0.0390 mol) was then added to the pressure equalising dropping funnel and added slowly to the thionyl chloride with stirring. As the reaction progressed, both heat and SO_2 evolved. When all the alcohol was added, the mixture was heated at reflux for 3 hours. The excess of thionyl chloride was then separated from the product by distillation, (78-80 °C), with the crude 1-tetradecylchloride requiring 98 °C and 0.5 mbar. This was then washed with D_2O, 10% sodium carbonate solution and twice with D_2O. Then, dried with anhydrous calcium chloride and distilled again. (8.31 g, 81% yield, deuteriation level 99% calculated by quantitative ^{1}H NMR). ^{1}H NMR (400 MHz, $CDCl_3$) residual protons δ 0.82 (m), 1.19 (m), 1.36 (m), 1.54 (m), 1.72 (m), 3.58 (m). ^{2}H NMR (400 MHz, $CDCl_3$) δ 0.85-3.48 (m). ^{13}C NMR (400 MHz, $CDCl_3$) δ 13.1 (m), 21.4 (m), 25.8 (m), 28.2 (m), 30.4 (m), 31.6 (m). 44.2 (m).

3.2.6.3 Synthesis of D_{39}-trihexylphosphine

Magnesium turnings (0.54 g, 1.20 eq.) were transferred into an oven-dried two-necked round-bottomed flask (100 ml) equipped with a reflux condenser with argon gas inlet, a septum and a PTFE coated magnetic stirring bar. Anhydrous diethyl ether (10 ml) was then added, followed by a crystal of iodine, and the flask was heated to 30 °C, with stirring. Subsequently, a small portion of D_{13}-1-chlorohexane (2.51 g, 1.0 eq.) was added dropwise *via* a syringe. After approximately 50% was added, the yellow iodine colour disappeared, with the solution becoming a grey colour, and the commencement of gentle refluxing. The remainder of the solution was added and the reaction was allowed to proceed (35 °C, overnight), before being cooled back to room temperature.

In another oven-dried two-necked round-bottomed flask (100 ml), equipped with a stirring bar and connected to an argon filled Schlenk line, phosphorus trichloride (0.51 g, 12.35 mmol), lithium bromide (0.03 g, 1.24 mmol) and copper(I) iodide (0.07 g, 1.24 mmol) were added to degassed, dry diethyl ether (15 ml). The flask was placed in an acetone-dry ice bath (-78 °C), and the mixture was allowed to cool, with vigorous stirring.

The solution containing the Grignard reagent was transferred *via* a cannula filter into the PCl_3 solution, and stirred at -78 °C. The dry ice-acetone bath was then removed, and the reaction mixture was brought to ambient temperature and left to react for a further 2 h with vigorous stirring on reaching this temperature. The solvent was removed under reduced pressure (25 °C, 10^{-2} bar) and the product was dissolved in pentane

(25 ml). Degassed water (25 ml) was subsequently added, and the flask was vigorously shaken by hand, the organic layer was removed *via* cannula transfer into an oven dried flask (100 ml) and again washed with degassed water (25 ml). This was transferred *via* cannula into an oven dried flask (100 ml). Finally, the organic phase was dried using sodium sulfate and the liquid phase was transferred *via* cannula filtration into an oven dried flask (100 ml). The solvent was removed under reduced pressure in an ice bath (0 °C, 10^{-2} bar), to give a colourless liquid. ^{31}P NMR showed that multiple phosphorus environments were present.

3.2.6.4 Synthesis of D_{68}-trihexyltetradecylphosphonium chloride

D_{39}-P_{666} (1.0 eq.) and D_{29}-1-tetradecylchloride (1.3 eq.) were added to a flask in acetonitrile and heated to reflux (60 °C) under argon for 1 week. ^{31}P NMR showed that multiple phosphorus environments were present.

3.2.7 Synthesis of D_{68}-trihexyltetradecylphosphonium bis(trifluoromethylsulfonyl)amide

The steps to form D_{68}-trihexyltetradecylphosphonium bis(trifluoromethylsulfonyl)amide are outlined in Scheme 3, and described in Sections 3.2.7.1-3.2.7.4.

Scheme 3. Synthesis of D_{68}-trihexyltetradecylphosphonium bis(trifluoromethylsulfonyl)amide. Black alkyl chains show the protonated chains and the blue alkyl chains depict the deuteriated alkyl chains.

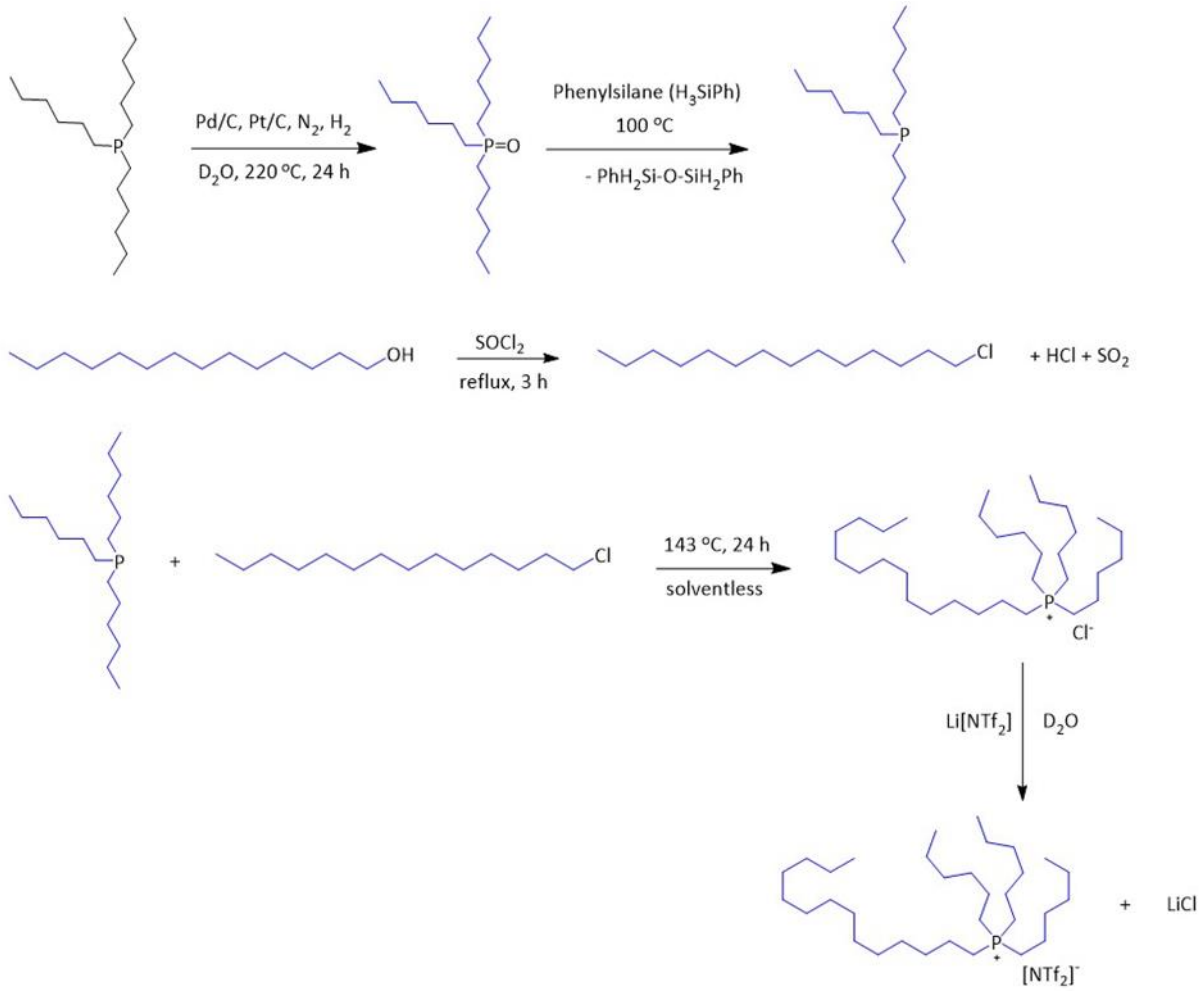

3.2.7.1 Synthesis of D_{39}-trihexylphosphine oxide

The reaction was carried out in a 100 mL Parr high pressure reactor fitted with a mechanical stirrer. A mixture of trihexylphosphine (3.48 g, 0.0121 mol), 10 wt. % Pt/C catalyst (0.75 g), and 10 wt.% Pd/C catalyst (0.75 g) in D_2O (65 mL) were added to the 100 mL Parr reactor body (made of Hastelloy c276), followed by N_2 bubbling for 2 min and then H_2 bubbling for 2 min at room temperature. After the reactor was sealed, the reactor was pressurised with nitrogen (40-50 bar). The reactor was then heated to 220 °C using the heating mantle and stirred at 600 RPM for 24 h. After cooling, dichloromethane was added to the reaction mixture, filtered through Celite, washed with dichloromethane and then the aqueous phase was extracted with dichloromethane (3 x 50 mL). The combined extracts were dried over $MgSO_4$ and then evaporated to give

deuteriated D_{39}-trihexylphosphine oxide as a white solid (1.72 g, 41% yield, deuteriation level of 96%, calculated by quantitative ^{1}H NMR). ^{1}H NMR (400 MHz, $CDCl_3$) residual protons δ 0.87 (m), 1.27 (m), 1.35 (m), 1.53 (m), 1.63 (m). ^{2}H NMR (400 MHz, $CDCl_3$) δ 0.8 (m), 1.20-1.62 (m). ^{13}C NMR (400 MHz, $CDCl_3$) δ 13.1 (m), 20.7 (m), 27.14 (m), 29.45 (m). ^{31}P NMR (400 MHz, $CDCl_3$) δ 48.7

3.2.7.2 Synthesis of D_{39}-trihexylphosphine

In a 25 mL round bottom flask fitted with a condenser, D_{39}-trihexylphosphine oxide (4.49 g, 0.0148 mmol) was dissolved in phenylsilane (6 mL) under an atmosphere of argon and then heated to 100 °C overnight with stirring. The reaction was monitored by ^{31}P NMR, by taking a sample from the reaction mixture and dissolving degassed $CDCl_3$. The disappearance of the starting material peak at 50.8 ppm and the appearance of D_{39}-trihexylphosphine peak at -33.65 ppm confirmed that the reaction was complete. Phenylsilane was removed under reduced pressure to give a pale yellow residue, which is used in the next step without further purification.

3.2.7.3 Synthesis of D_{68}-trihexyltetradecylphosphonium chloride

D_{39}-trihexylphosphine (4.50 g, 0.0127 mol) and D_{29}-tetradecylchloride (4.32 g, 0.0165 mol) were mixed together and heated to 143 °C in a sealed tube in an argon filled glovebox for 24 h. A white solid was present in the tube along with the ionic liquid. The liquid was decanted and ^{31}P NMR of the liquid in $CDCl_3$ showed that the ^{31}P NMR peak of D_{39}-trihexylphosphine at -33.65 ppm had disappeared to give a peak at 32 ppm, indicating the formation of D_{68}-[P_{66614}]Cl. The white solid was not fully soluble in common NMR solvents and this was attributed to the formation of 1,3-diphenyl-disiloxane (PhH_2Si-O-SiH_2Ph) that would have formed in the previous step. This was further verified by XRF analysis, which confirmed the presence of silicon, reporting a value of 82,000 ppm. This was not a high precision calibration but an internal calibration. XRF analysis of the ionic liquid did not detect any silicon. The solid was extracted with chloroform and filtered. Chloroform and excess alkylating agent were removed under vacuum. ^{1}H NMR (400 MHz, $CDCl_3$) residual protons δ 0.89 (m), 1.29 (m), 1.49 (m), 2.45 (m). ^{2}H NMR (400 MHz, $CDCl_3$) 0.78 (m), 1.16-2.46 (m). ^{13}C NMR (400 MHz, $CDCl_3$) δ 13.0 (m), 21.0 (m), 27.0 (m), 29.8 (m). ^{31}P NMR (400 MHz, $CDCl_3$) δ 32.21.

3.2.7.4 Synthesis of D_{68}-trihexyltetradecylphosphonium bis(trifluoromethylsulfonyl)amide

D_{68}-[$P_{666,14}$]Cl (0.010 mol eq.) was dissolved in hexane and Li[NTf_2] (0.012 mol eq.) was dissolved in D_2O, combined in a round-bottomed flask, and left to stir for 3 h at room temperature, 600 rpm. The organic layer was separated and washed multiple times with D_2O. Hexane was removed and the ionic liquid was dried under high vacuum (12 h, 70 °C, 10^{-2} mbar) to give a colourless liquid (5.67 g, 94% yield, deuteriation level 97% by ^{1}H qNMR). XRF analysis confirmed chloride content was below the detectable limit. ^{1}H NMR (400 MHz, $CDCl_3$) residual protons δ 0.90 (m), 1.30 (m), 1.34 (m), 1.48 (m), 2.08 (m). ^{2}H NMR (400 MHz, $CDCl_3$) δ 0.88 (m), 1.27-2.62 (m). ^{13}C NMR (400 MHz, $CDCl_3$) δ 12.7 (m), 21.1 (m), 26.9 (m), 29.7 (m). ^{31}P NMR (400 MHz, $CDCl_3$) δ 32.23. ^{19}F NMR (400 MHz, $CDCl_3$) δ -79.12

3.2.8 Synthesis of [C_2mim][NTf_2]

[C_2mim]Cl (0.0272 mol, 4.00 g) and Li[NTf_2] (0.0299 mol, 8.59 g) were separately dissolved in water (total 30 ml) and then combined, resulting in the formation of a separate liquid phase. This was left to stir for 1 hour at room temperature. The aqueous layer was separated out and the organic layer was collected and washed. The first wash was with 10 ml of water and 10 ml of dichloromethane (DCM). Subsequent washes (7) were performed with deionised water. Two subsequent negative tests for chloride with $AgNO_3$ were required to ensure removal of LiCl. DCM was removed *via* reduced pressure at 35 °C, and the product was a colourless viscous ionic liquid. The ionic liquid was dried overnight on the Schlenk line at a temperature of 100 °C. ^{1}H NMR: (400 MHz, d_6 -DMSO) δ 1.43 (t, 3H), 3.84 (s, 3H), 4.18 (t, 2H), 7.68 (t, 1H), 7.76 (t, 1H), 9.09 (s, 1H). ^{13}C NMR (400 MHz, d_6 -DMSO) δ 14.98, 35.66, 44.20, 119.94 (q, $^1J_{C-F}$ = 1280 Hz CF_3), 121.97, 123.58, 136.28. 19F NMR (400 MHz, d_6-DMSO) δ -79.82

3.2.9 Synthesis of [C_{10}mim][NTf_2]

[C_{10}mim]Br (0.073 mol, 22.114 g) and Li[NTf_2] (0.080 mol, 23.027 g) were separately dissolved in water (total 30 ml) and then combined, resulting in the formation of a separate liquid phase. This was left to stir for 1 h at room temperature. The aqueous layer was separated out and the organic layer was collected and washed. The first wash was with 10 ml of water and 10 ml of dichloromethane (DCM). Subsequent washes (7) were performed with deionised water. Two subsequent negative tests for chloride with $AgNO_3$ were required to ensure removal of LiCl. DCM was removed *via* reduced pressure at 35 °C, and the product was a colourless

viscous liquid. The ionic liquid was dried overnight on the Schlenk line at a temperature of 100 °C. ^{1}H NMR (400 MHz, d_6 -DMSO): 8.72 (s, 1H), 7.58 (t, 1H), 7.50 (t, 1H), 4.28 (m, 2H), 4.00 (s, 3H), 1.99 (m, 2H), 1.39 (m, 14H), 0.98 (t, 3H). ^{13}C NMR (400 MHz, d_6-DMSO) δ 136.94, 122.65, 124.75, 119.35 (q, $^{1}J_{C\text{-}F}$ = 1276 Hz CF_3), 49.27, 36.09, 31.73, 29.84, 29.34, 29.25, 29.11, 28.81, 25.93, 22.51, 14.19. ^{19}F NMR (400 MHz, d_6 -DMSO) δ -80.12.

3.2.10 Neutron scattering experiments

Neutron scattering data for $[P_{666,14}][NTf_2]$ were recorded using the NIMROD diffractometer and $[C_2mim][NTf_2]$ and $[C_{10}mim][NTf_2]$ on the SANDALS diffractometer at the ISIS Pulsed Neutron and Muon Source at Rutherford Appleton Laboratory, Oxfordshire, UK. The neutron diffraction data was analysed using Dissolve software. For each IL, isotopologues containing protiated (H), deuteriated (D) or equimolar mixture of protiated and deuteriated components (H/D) were prepared. Simulation box size contained 500 ion pairs for $[C_2mim][NTf_2]$ and $[C_{10}mim][NTf_2]$ and 250 ion pairs for $[P_{666,14}][NTf_2]$. The forcefield parameters were taken from the Canongia Lopes & Padua (CL&P) force field.[215]

3.2.11 Differential Scanning Calorimetry Measurements

DSC samples were prepared in a glove box (MBraun Lap Master dp, <0.6 ppm O_2 and H_2O) using Tzero aluminium pans, Tzero aluminium hermetic lids and sealed using a Tzero sample press. DSC measurements were performed using a TA instruments Q2000 DSC equipped with an RCS 90 refrigerated cooling accessory under nitrogen flow (50 mL min^{-1}). Sample temperature was ramped between -90 °C and 30 °C using a 2 °C min^{-1} ramp rate and three cycles were recorded.

3.3 Results and discussion

3.3.1 Synthesis of D_{68}-trihexyltetradecylphosphonium bis(trifluoromethylsulfonyl)amide

Three approaches to the synthesis of perdeuteriated $[P_{666,14}][NTf_2]$ were attempted. When synthesising deuteriated compounds, there are certain factors which must be taken into consideration. The majority of synthetic procedures in the literature are optimised for protiated materials and a direct comparison cannot

always be made when synthesising deuteriated compounds. This is mostly due to the deuterium kinetic isotope effect,[216,217] leading to longer reactions times and often - decreased yields. There are also challenges associated with limited availability and high cost of deuteriated starting materials or reagents, when compared to their protiated counterparts.[217]

In the literature, most of the synthesis of deuteriated ionic liquids cover $[C_n\text{mim}]^+$ ILs. The deuteriation procedure typically involves starting from the protiated versions and use D_2O as the deuterium source and applying high temperatures and pressures in the presence of a catalyst.[218,219] Sometimes, basic conditions are also used.[220] These conditions are typical of deuteriations for a variety of compounds.

The first attempted method was the direct deuteriation of $[P_{666,14}]^+$ cation of $[P_{666,14}]Cl$, which yielded a hydroxide IL, followed by acid/base neutralisation with $HNTf_2$ (Scheme 4). This method was provided by the deuteriation lab at the ISIS Pulsed Neutron and Muon Source at Rutherford Appleton Laboratory, who used the procedure to successfully deuterate the $[P_{4444}]^+$ cation using three cycles with fresh D_2O. As $[P_{666,14}]Cl$ has longer alkyl chains it was proposed that the same method could be attempted, but with more cycles.

Scheme 4. Direct deuteriation of $[P_{666,14}]^+$ cation of $[P_{666,14}]Cl$, yielding a hydroxide IL, followed by acid/base neutralization with $HNTf_2$. Black alkyl chains show the protonated chains and the blue alkyl chains depict the deuteriated alkyl chains.

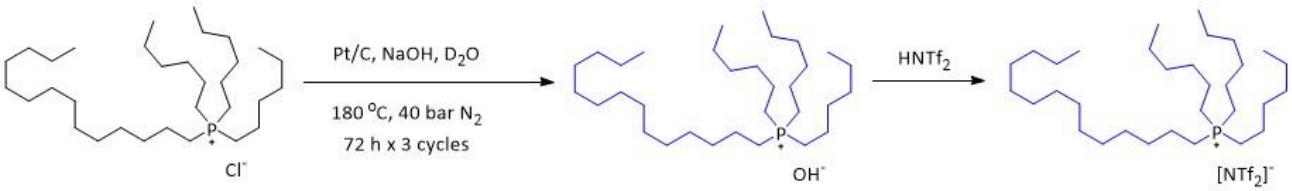

The first step was carried out by subjecting $[P_{666,14}]Cl$ to multiple cycles of hydrothermal H/D exchange in D_2O, under basic conditions, catalysed with Pt/C, which yielded $[P_{666,14}][OH]$ solution in D_2O. This solution, after filtration, was neutralised with $HNTf_2$ to generate $[P_{666,14}][NTf_2]$. The product gave one strong NMR signal at δ_{31P} = 32 ppm (Figure 41a). However, despite multiple cycles only the eight protons in the alpha position with respect to the phosphorus atom (H-C-P) were deuteriated. This was confirmed by ^1H NMR spectroscopy (Figure 41b) and mass spectrometry (Figure 42), where an average m/z value of 492 was reported in the positive spectrum, corresponding to D_8-$[P_{666,14}]^+$.

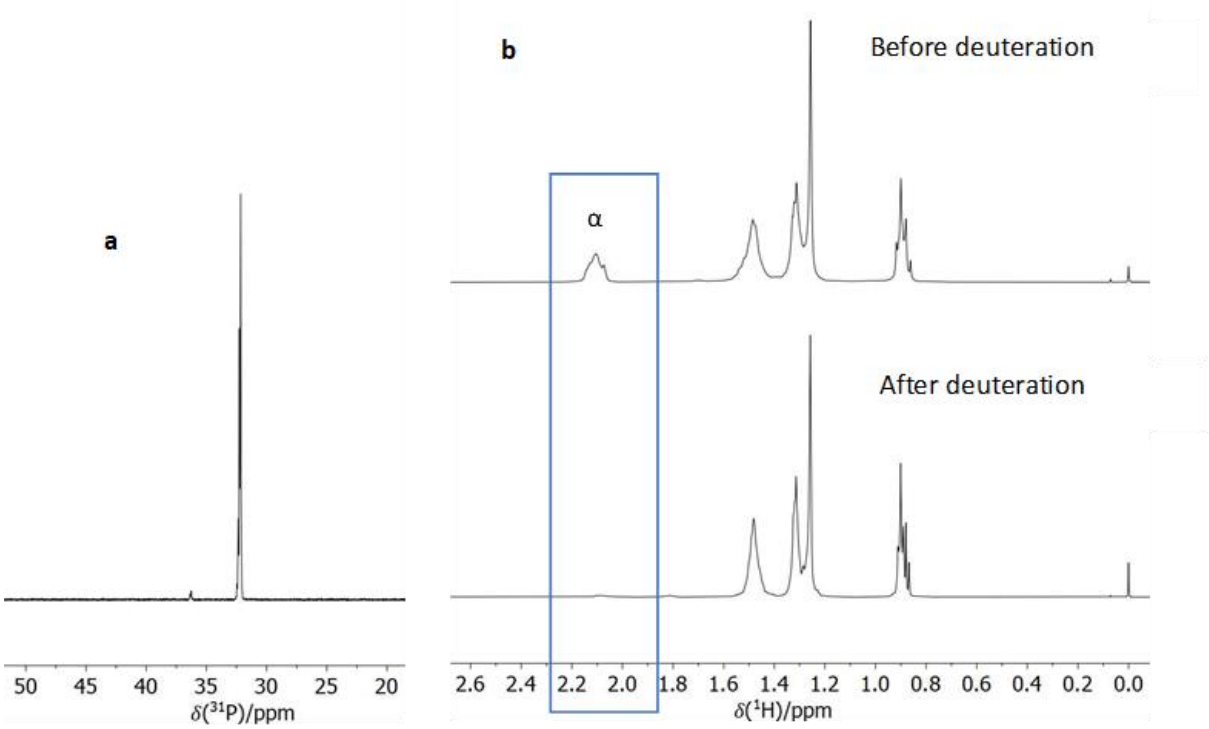

Figure 41. a) ^{31}P NMR spectrum of D_8-[$P_{666,14}$][NTf_2] and b) ^{1}H NMR spectrum showing disappearance of the peak corresponding to the 8 α protons to the phosphorus after deuteration.

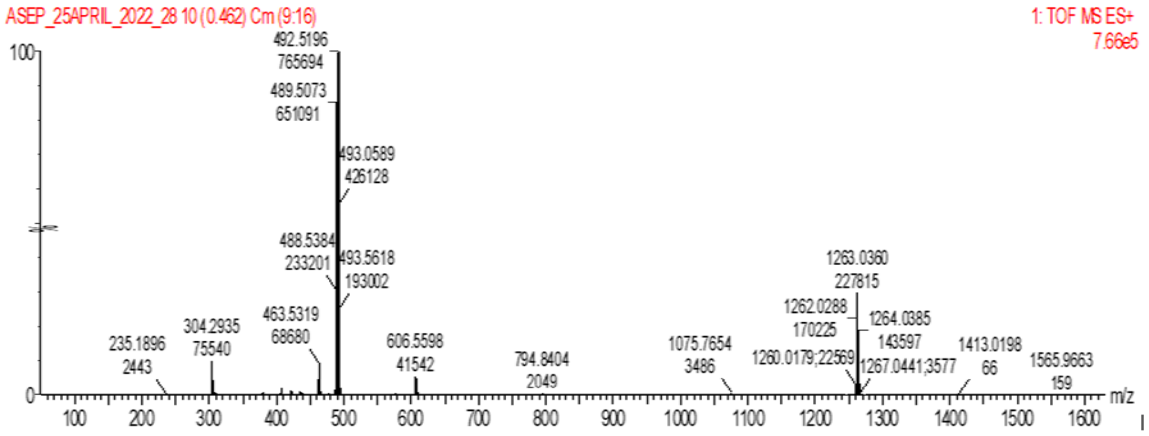

Figure 42. ESI-MS of D_8-[$P_{666,14}$][NTf_2] in positive mode.

An attempt to optimise the method was undertaken. Firstly, it was noted that poor H/D exchange could be due to [$P_{666,14}$]Cl having very poor solubility in D_2O. Therefore, deuterated methanol (CD_3OD) was chosen as a solvent for the screening. From the literature, it has been seen that some deuteriation procedures use a slight positive pressure of H_2 gas to activate the catalyst.[218,221] Therefore, the effect of purging the reaction mixture was tested, firstly with N_2 gas to degas the solution, followed by H_2 gas for 2 minutes. N_2 gas only was used as

a control experiment. Pt/activated carbon *vs.* Pd/activated carbon were also tested, as well as the addition of a base (NaOH). A screening experiment was set up to optimise the reaction conditions (Table 8). $[P_{666,14}]Cl$ was treated either with D_2O or a 50/50 mix of D_2O/CD_3OD and stirred for 3 days at 60 °C. To test a number of solutions quickly as an initial screening procedure, Biotage reaction vessels (glass vials sealed with caps, able to withstand 30 bar pressure) were used instead of a Parr reactor as used previously. 10 wt% of Pt/C or Pd/C catalyst were used and 10 wt% of NaOH was used as the base, with an additional screening run without the base.

Deuterium content was determined by ^1H NMR and the results showed that a key element was the presence of base as mixtures **5-8** which had no base showed no H/D exchange. For the rest of the mixtures, ^1H NMR spectroscopy showed that the eight protons in the alpha position with respect to the phosphorus atom (H-C-P) were deuteriated. Therefore, D_2O vs. D_2O/CD_3OD mix, Pt/C vs. Pd/C or the presence of a H_2 atmosphere did not provide any increase in deuterium content. It was concluded that the direct deuteriation of $[P_{666,14}]Cl$ was not possible to the degree needed for neutron scattering experiments. This was an ambitious approach given the long alkyl chains. H/D exchange occurs on the surface of Pt/C and Pd/C catalysts and the probability of H/D exchange decreases for the terminal end of the alkyl protons as they are less likely to get sufficient contact with the catalyst during the reaction. This has already been observed by Darwish and co-workers,[218] who reported that the deuteriation ratio of $[C_n mim]Cl$ decreased with increasing length of the alkyl chain.

Table 8. Screening conditions in an attempt to deuteriate $[P_{666,14}]^+$ cation of $[P_{666,14}]Cl$.

Entry	Solvent	t / h	T / °C	Catalyst	Base	Gas
1	D_2O	72	60	Pt/C	Y	H_2
2	D_2O	72	60	Pt/C	Y	N_2
3	D_2O	72	60	Pd/C	Y	H_2
4	D_2O	72	60	Pd/C	Y	N_2
5	D_2O/CD_3OD	72	60	Pt/C	N	H_2
6	D_2O	72	60	Pt/C	N	H_2
7	D_2O/CD_3OD	72	60	Pd/C	N	H_2
8	D_2O	72	60	Pd/C	N	H_2
9	D_2O/CD_3OD	72	60	Pd/C	Y	H_2
10	D_2O	72	60	Pd/C	Y	H_2

The second method involved the synthesis of D_{13}-1-chlorohexane and D_{29}-1-chlorotetradecane by the chlorination of the corresponding alcohols with thionyl chloride. Then, the synthesis of perdeuteriated

trihexylphosphine, D_{39}-P_{666}, from D_{13}-1-chlorohexane *via* Grignard reaction, followed by alkylation with D_{29}-1-chlorotetradecane to yield D_{68}-[$P_{666,14}$]Cl. This would then be subjected to ion exchange with Li[NTf_2] to generate D_{68}-[$P_{666,14}$][NTf_2] (Scheme 5).

Scheme 5. The synthesis of perdeuteriated trihexylphosphine, D_{39}-P_{666}, via Grignard reaction, followed by alkylation with D_{29}-1-chlorotetradecane to yield D_{68}-[$P_{666,14}$]Cl. This was then subjected to ion exchange with Li[NTf_2] to generate D_{68}-[$P_{666,14}$][NTf_2]. Blue alkyl chains depict the deuterated alkyl chains.

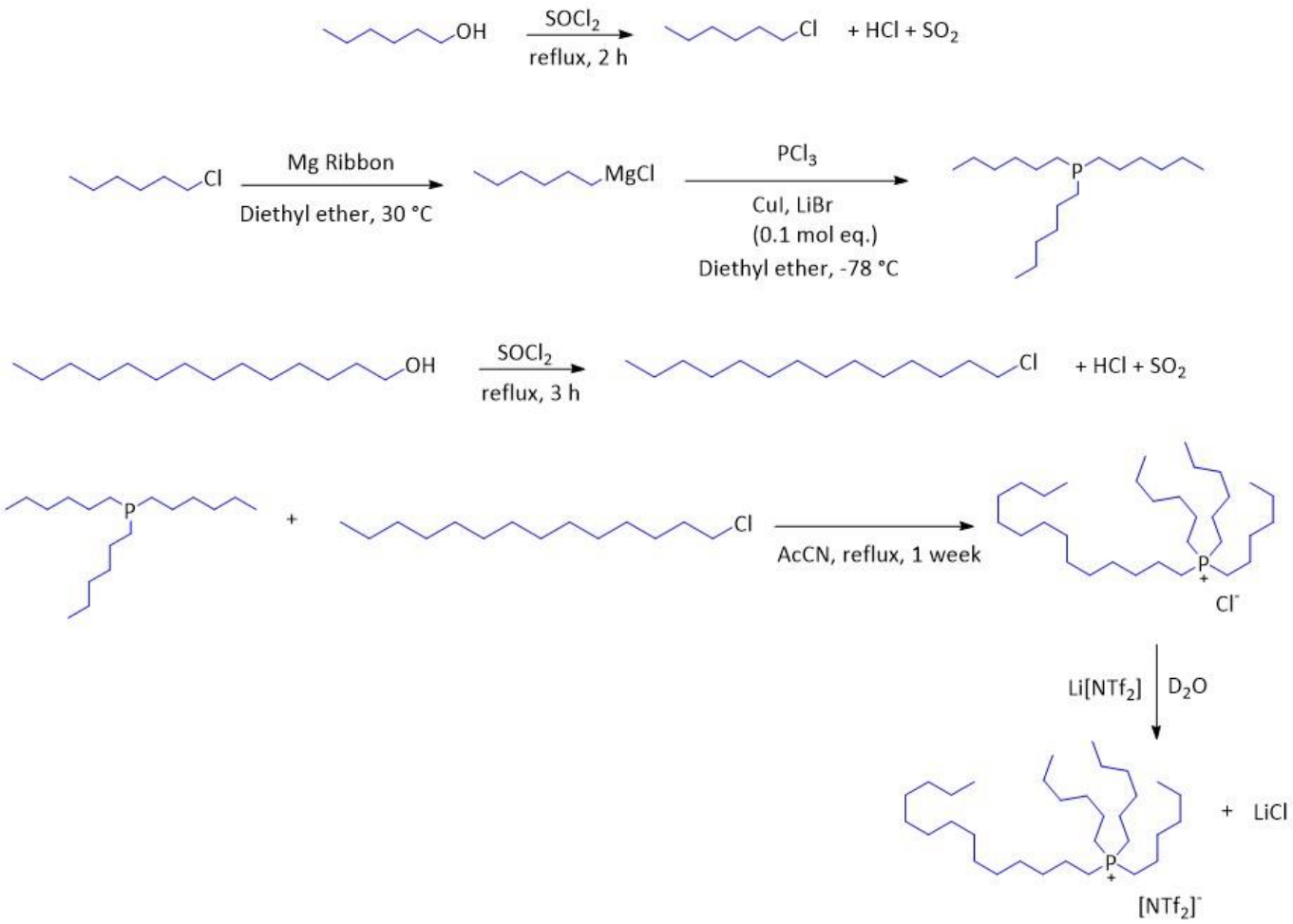

The method to synthesise the perdeuteriated trihexylphosphine has been adapted from a synthetic procedure for perdeuteriated tri-*tert*-butylphosphine, developed jointly by the Swadźba-Kwaśny group and the ISIS D-lab.[222] The challenge in this synthesis was the air sensitive nature of the phosphine. Therefore, it was vital to prevent any contact or contamination with air and to ensure all solvents were fully degassed to prevent the rapid formation of oxidation products. The first step of the reaction was the formation of a Grignard reagent. This was encouraged by crushing magnesium turnings with a mortar and pestle and stirred overnight under an inert atmosphere, to increase the available exposed magnesium sites. The Grignard formation was very exothermic and achieving the balance between heating and cooling was key. Enough heat must be applied to

overcome activation energy and initiate the reaction. Once initiated, however the reaction required cooling to prevent loss of reactants with the volatile diethyl ether. The generation of the Grignard intermediate is also promoted by the addition of a crystal of iodine. Lithium bromide and copper(I) iodide were added to the PCl_3 solution before the Grignard reagent was added. This step was taken from the synthetic procedure for perdeuteriated tri-*tert*-butylphosphine ($P^tBu)_3$,[222] where they showed that without the addition of these reagents radical reaction pathways were not prevented, resulting in multiple products being formed. The addition of the Grignard reagent to the solution of PCl_3 was also performed *via* cannula filtration to avoid any contamination with remaining traces of magnesium flakes. Magnesium is the main source of reducing agent which can promote side reactions and the formation of the phosphorus-phosphorus bond which was seen in the synthesis of P^tBu_3. However, P^tBu_3 is more sterically bulky, and the formation of P-P bonds is more favoured, compared to P_{666}.

After the synthesis, purification involved removing the reaction solvents, dissolving the products in dry pentane and washing with degassed water. The organic phase was then dried and, upon removal of solvent, a colourless, crystalline solid was obtained. ^{31}P NMR spectroscopy showed the formation of D_{39}-P_{666} at -27.9 ppm but other peaks were present (Figure 43a). The peak at 50 ppm corresponds to D_{39}-$P_{666}O$ and the other peaks are likely to be other oxide species due to the high propensity for trialkylphosphines to oxidise. When trialkylphosphines oxidise, there are several species which can form in addition to $R_3P=O$. The additional insertion of oxygen atoms into P-C bonds is commonly observed generating phosphinic ($R_2(OR)P=O$) and phosphonic ($R(OR)_2P=O$) and sometimes phosphoric acid esters ($(OR)(OH)_2P=O$)) and ($(OR)_2(OH)P=O$)). Furthermore, phosphinites ($R_2(OR)P$), phosphonites ($R(OR)_2P$) and phosphites ($(OR)_3P$) can be created.[223–225]

Despite the existence of oxide species, it has been decided to continue the subsequent step, *i.e*. the alkylation with D_{29}-1-tetradecylchloride. After 1 week, there was no D_{39}-P_{666} remaining and some conversion to the D_{68}-$[P_{666,14}]Cl$, with a signal at 32 ppm. However, the other peaks remained, with an increase in intensity of the D_{39}-$P_{666}O$ signal (Figure 43b).

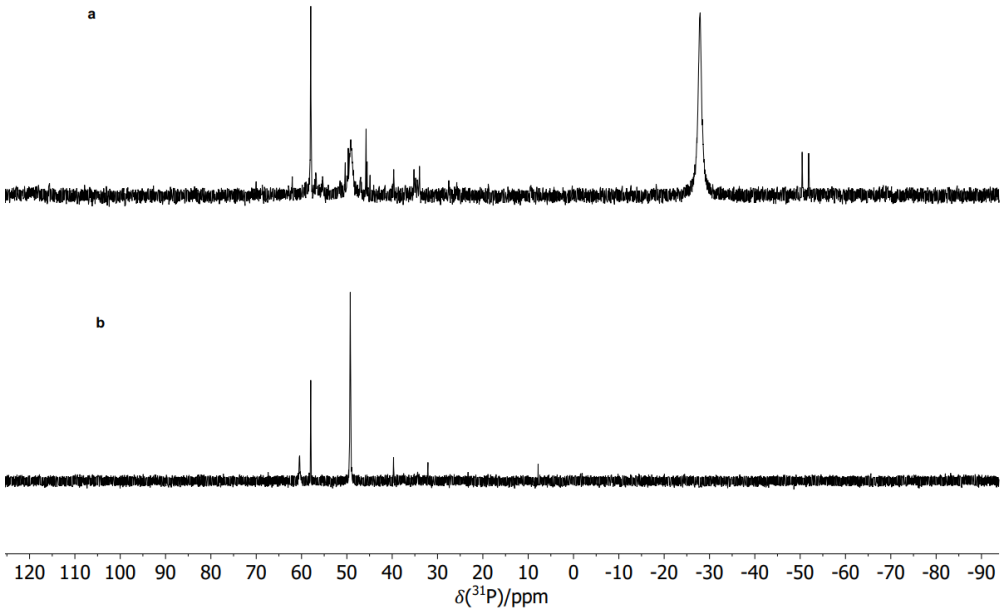

Figure 43. ^{31}P NMR spectra of a) attempted synthesis of D_{39}-P_{666} showing the presence of multiple species and b) alkylation with D_{29}-1-chlorotetradecane after one week.

Method three was the catalytic deuteriation of trihexylphosphine in D_2O, with perdeuteriated trihexylphosphine oxide as the product. The phosphine oxide was subsequently reduced, and then alkylated with D_{29}-1-chlorotetradecane, followed by anion exchange with Li[NTf_2], as shown in Scheme 6. The procedure was based on the method reported by Atkin *et. al.*,[226] with several key modifications. Firstly, D_{29}-1-chlorotetradecane was synthesised by the chlorination of the corresponding alcohol with thionyl chloride, rather than using *n*-chlorosuccinimide and triphenylphosphine. This may be a safer option, but purification using column chromatography could be avoided. Secondly, whereas Atkin *et. al* used column chromatography to purify D_{68}-[$P_{666,14}$]Cl, here it has been possible to convert the crude D_{68}-[$P_{666,14}$]Cl directly into pure D_{68}-[$P_{666,14}$][NTf_2], leaving all side products in the aqueous phase, again avoiding column chromatography.

Scheme 6. Synthesis of D_{68}-trihexyltetradecylphosphonium bis(trifluoromethylsulfonyl)amide. Black alkyl chains show the protonated chains and the blue alkyl chains depict the deuterated alkyl chains.

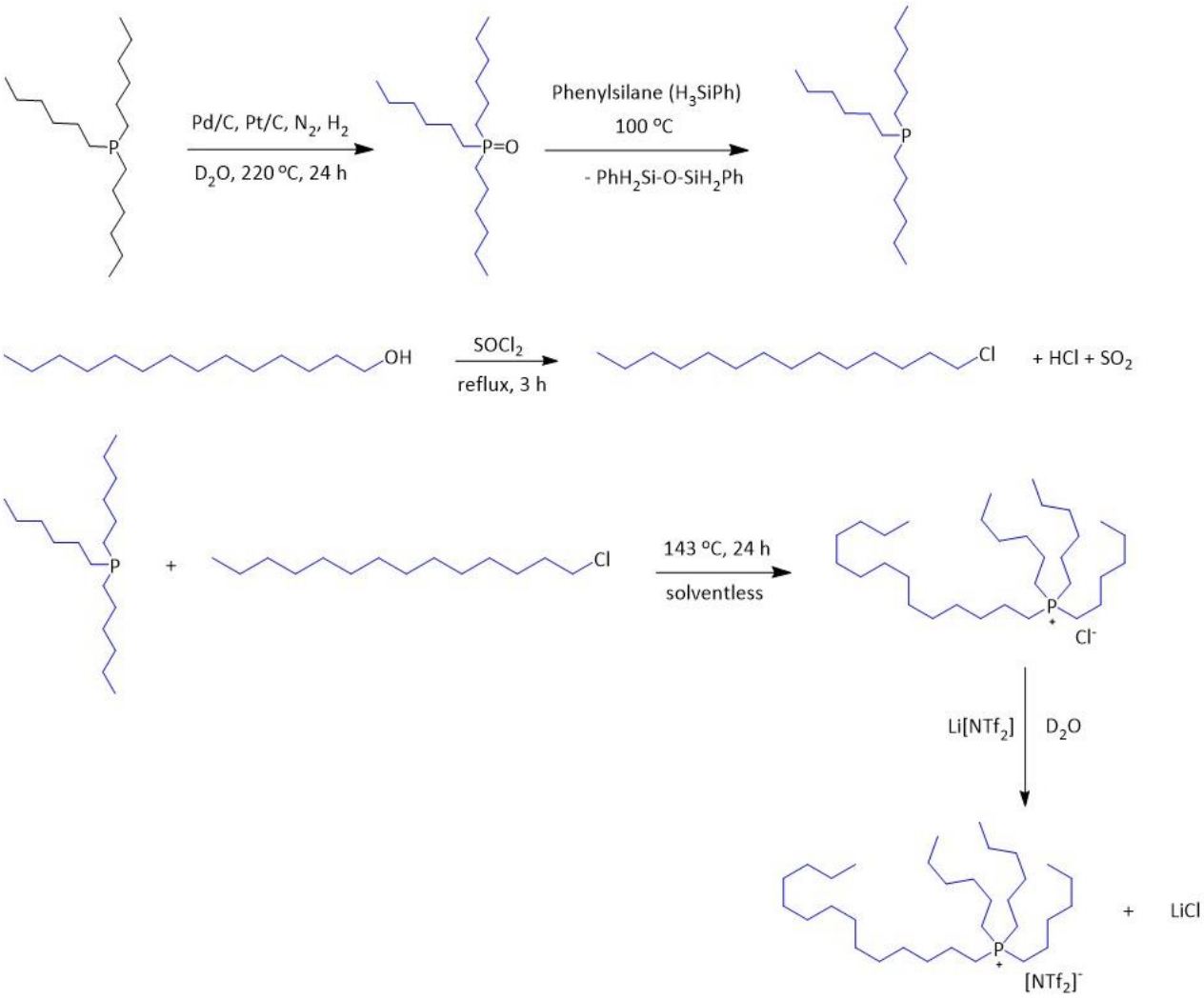

Deuteriation of P_{666} was carried out using a combination of Pt/C and Pd/C catalysts in D_2O, with the reaction carried out at 220 °C for 24 h in a pressurised reactor vessel. It has previously been reported that this catalyst system is effective for the deuteriation of other substrates.[227] Prior to the reaction, N_2 was bubbled through the mixture to degas it, followed by H_2 bubbling to activate the catalyst. The product was a white solid that gave one strong NMR signal at δ_{31P} = 48.8 ppm (Figure 44a), with deuterium content of 96%, as calculated by quantitative ^{1}H NMR spectroscopy. This was further confirmed by mass spectrometry (Figure 45), which gave an average m/z value of 341, which is consistent with deuteriation and oxidation to D_{39}-$P_{666}O$. D_{39}-$P_{666}O$ was then reduced using phenylsilane, and the reaction was monitored by ^{31}P NMR spectroscopy in degassed $CDCl_3$, following the disappearance of the starting material peak at δ_{31P} = 48.8 ppm and the appearance of D_{39}-P_{666} peak at δ_{31P} = -32.6 ppm (Figure 44b). A side-product formation (δ_{31P} = -70.9 ppm), accounting for *ca*. 11% of the product mixture, has been observed, in agreement with the report by Atkin *et. al.*[226] This was attributed

to dihexylphosphine, in agreement with the literature.[223] There was also a small peak at 48.4 ppm, corresponding to D_{39}-$P_{666}O$, accounting for about 6%. The small peak at 35.0 ppm (*ca*. 2% by integration) could be due to a small amount of dihexylphosphine oxide.

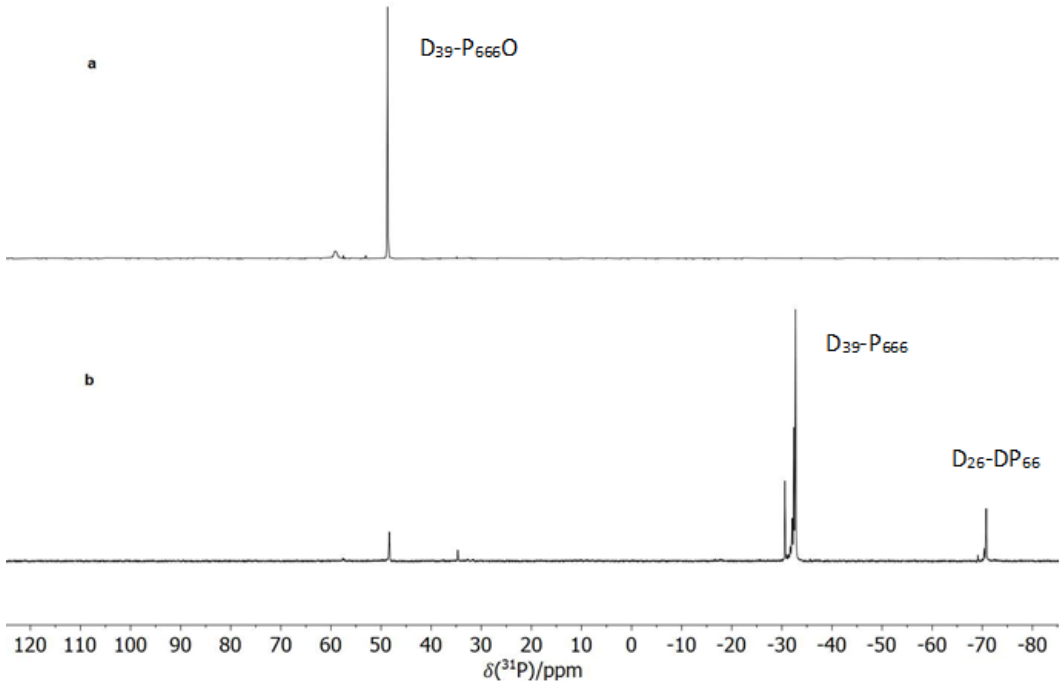

Figure 44. ^{31}P NMR spectra of a) D_{39}-$P_{666}O$ and b) D_{39}-P_{666}, with assignments of products and impurities.

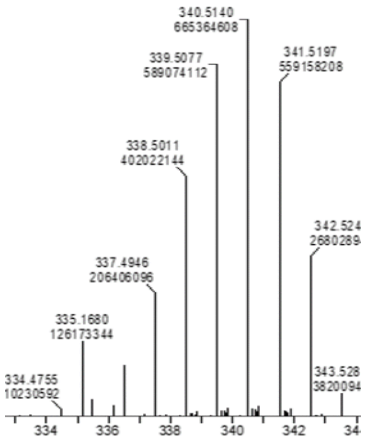

Figure 45. ESI-MS of D_{39}-$P_{666}O$

It was crucial to keep D_{39}-P_{666} protected from any air, as this would rapidly form D_{39}-$P_{666}O$ again. The next step was the alkylation of D_{39}-P_{666} with D_{29}-1-tetradecylchloride. Atkin and co-workers[226] reported that they firstly heated D_{39}-P_{666} to 143 °C and then added D_{29}-1-tetradecylchloride slowly in the glovebox. After that, the temperature was maintained at 143 °C for 24 h, followed by purification of the phosphine using column chromatography. In this work, the reagents were instead added together in degassed and dried acetonitrile and heated to reflux under argon on the Schlenk line, with the D_{29}-1-tetradecylchloride in 1.3 mol eq. excess. After 72 h, the progress of the reaction was checked by ^{31}P NMR in degassed $CDCl_3$. The disappearance of the D_{39}-P_{666} peak at -32.6 ppm and the appearance of D_{68}-$[P_{666,14}]Cl$ peak at 32 ppm would indicate completion of the reaction. The ^{31}P NMR showed the formation of D_{68}-$[P_{666,14}]Cl$ at 32.1 ppm (Figure 46). Formation of the oxide also occurred as indicated by the signal at 49 ppm, accounting for 48%. The peaks at -70 and 35 ppm, previously assigned to dihexylphosphine and the corresponding oxide, remained - integrating to 5 and 21%, respectively.

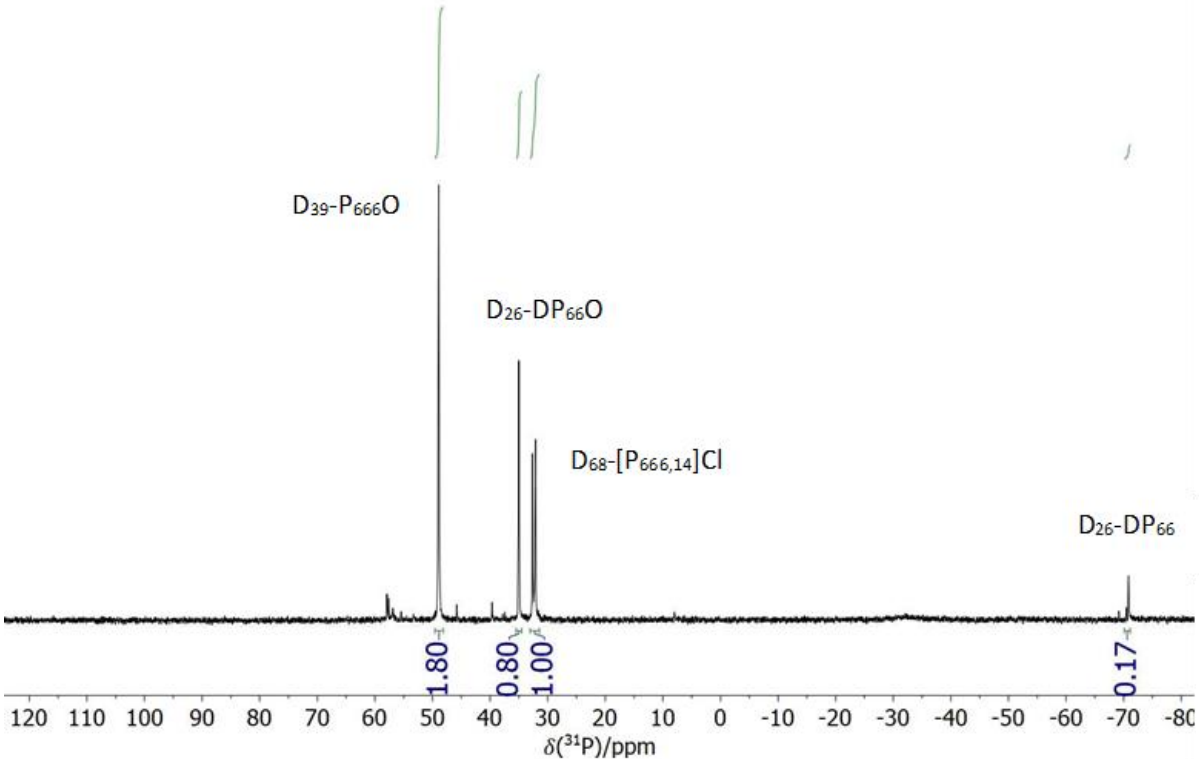

Figure 46. ^{31}P NMR showing formation of D_{68}-$[P_{666,14}]Cl$ along with other phosphorus species as discussed in the text.

This was significant oxide formation and so steps were taken to reduce the oxide back to the phosphine. First, the acetonitrile was distilled, followed by excess D_{29}-1-tetradecylchloride. Then phenylsilane was added and left to react under the same conditions as before and successfully reduced most of the oxide back to D_{39}-P_{666} (Figure 47).

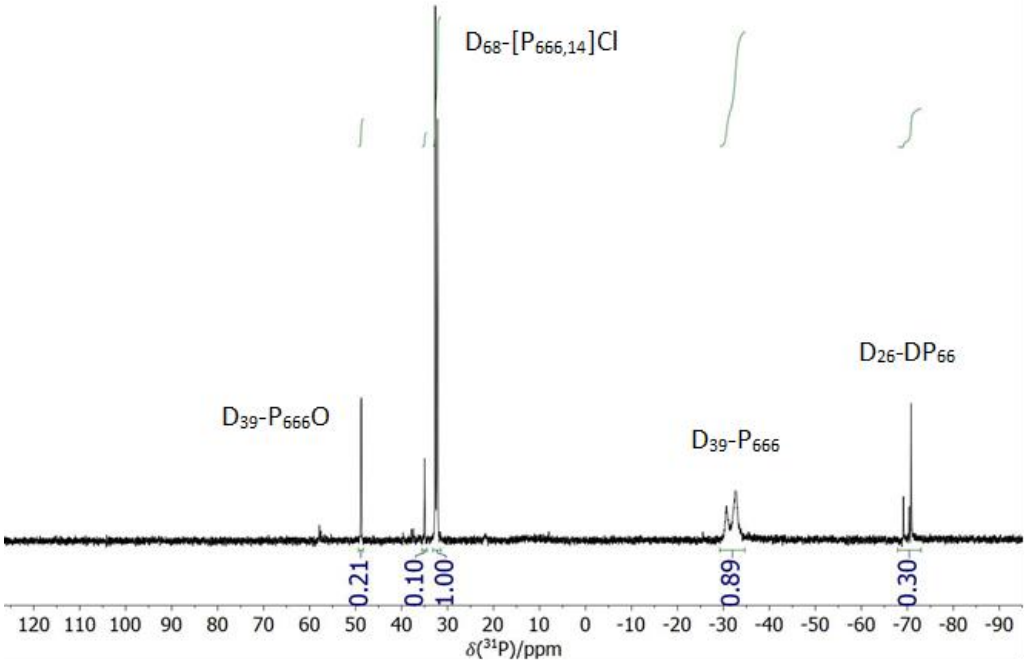

Figure 47. ^{31}P NMR showing the reduction of the majority of the phosphine oxides to the phosphines using phenylsilane.

Alkylation was attempted again, however, 31% of D_{39}-$P_{666}O$ remained (Figure 48a). This was an improvement compared to 48% of D_{39}-$P_{666}O$ in the first alkylation, but still too high. Another round of reduction brought the D_{39}-$P_{666}O$ formed to 16% (Figure 48b).

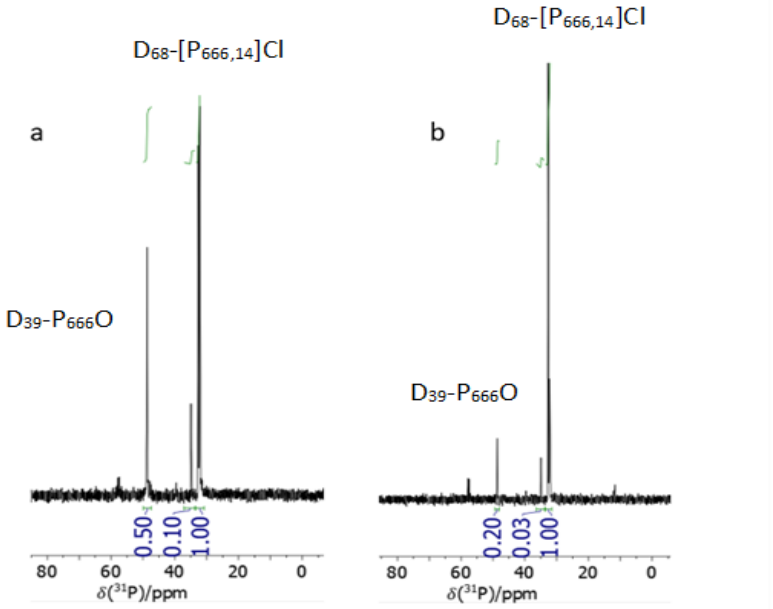

Figure 48. ^{31}P NMR showing formation of $[P_{666,14}]Cl$ at 32 ppm and 31% of D_{39}-$P_{666}O$ at 49 ppm (a) and 16% of D_{39}-$P_{666}O$ (b)

Despite progress, 16% of oxide was considered as too wasteful, therefore another (fourth) round of reduction (Figure 50) followed, with subsequent alkylation procedure as reported by Atkin and co-workers.[226] In this procedure, the reagents were added neat, therefore avoiding any potential O_2 contaminants from the solvent. Also, this reaction could be done in the glovebox, further reducing the possibility of contact with air. There was solid present in the flask along with the ionic liquid, which was initially thought to be D_{39}-P_{666}. In the procedure, Atkin and co-workers firstly heated D_{39}-P_{666} to 143 °C before addition of D_{29}-1-tetradecylchloride, which led to assumption that D_{39}-P_{666} did not melt until 143 °C. However, upon reaching this temperature, there was still solid in the reaction mixture, and remained present throughout the reaction.

After the reaction, the solid (not reported by Atkin and co-workers) was filtered and washed with chloroform, leaving the product in the organic phase. The unknown white powder was insoluble in common NMR solvents; analysing the synthetic procedure for the reduction of D_{39}-$P_{666}O$ using phenylsilane (Figure 49) it was assumed that it could be 1,3-diphenyl-disiloxane (PhH_2Si-O-SiH_2Ph), which forms in addition to D_{39}-P_{666}, and is likely poorly soluble in the organic phase. Indeed, XRF analysis confirmed the presence of silicon at 82,000 ppm, which corresponds to 8.2% of Si in the sample which is less than the theoretical 25% of Si content in PhH_2Si-O-SiH_2Ph.

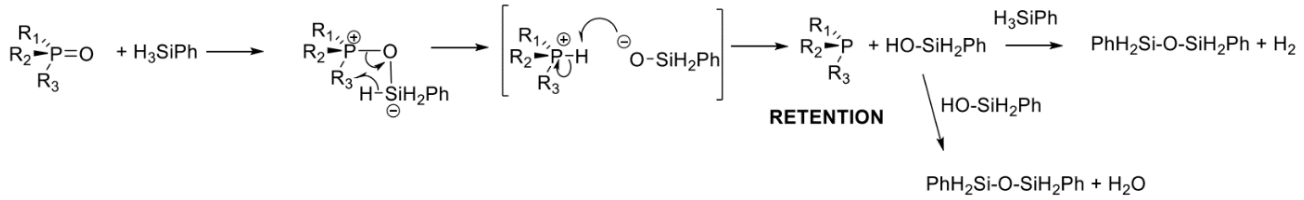

Figure 49. The mechanism for reduction of phosphine oxides with phenylsilane.[228]

^1H and ^{31}P NMR analysis of the filtrate liquid confirmed the formation of D_{68}-[$P_{666,14}$]Cl, at 90% purity. There was a small peak at 48.4 ppm corresponding to ~7% D_{39}-$P_{666}O$ and a small peak at -70 ppm corresponding to ~3% of another impurity (Figure 51a). It was then hypothesised that the impurities present could be washed out with the aqueous phase, in the next step during ion exchange.

Chloroform and excess D_{29}-1-tetradecylchloride were removed under vacuum, and neat IL was analysed by XRF to test for the presence of silicon impurities; fortunately, no silicon was detected. Li[NTf_2] in D_2O was then added to D_{68}-[$P_{666,14}$]Cl in hexane and left to stir for 3 h. After which the organic layer was washed multiple times with D_2O, separated and dried under vacuum. The ^{31}P NMR spectrum of the product showed a singlet at 32 ppm, indicating 95% pure D_{68}-[$P_{666,14}$][NTf_2] (Figure 51b). The impurities associated with D_{39}-$P_{666}O$ and

D_{26}-DP_{66} were removed with multiple aqueous washes upon the ion exchange step. ^{19}F NMR spectrum featured a single peak at -79 ppm, corresponding to the bistriflimide anion[229] (Figure 52). A deuterium content of 88%, calculated from quantitative ^{1}H NMR spectroscopy, was surprisingly lower than expected, given the high deuterium content of >95% of the starting materials (trihexylphosphine oxide and D_{29}-1-tetradecylchloride) both of which were calculated by quantitative ^{1}H NMR spectroscopy. It is suggested that the deuterium content of the IL must be underestimated. Mass spectrometry confirmed this suspicion, suggesting high deuterium incorporation (Figure 53) where 100% deuteriation level would give an m/z value of 552.

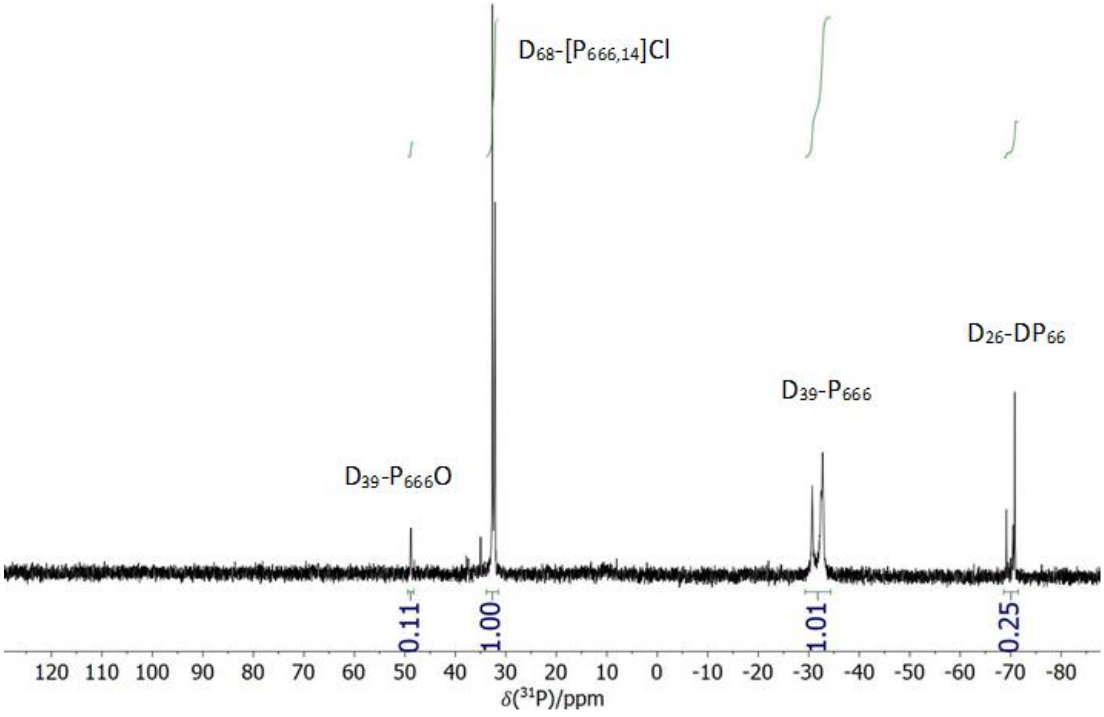

Figure 50. ^{31}P NMR after final reduction with phenylsilane before alkylation.

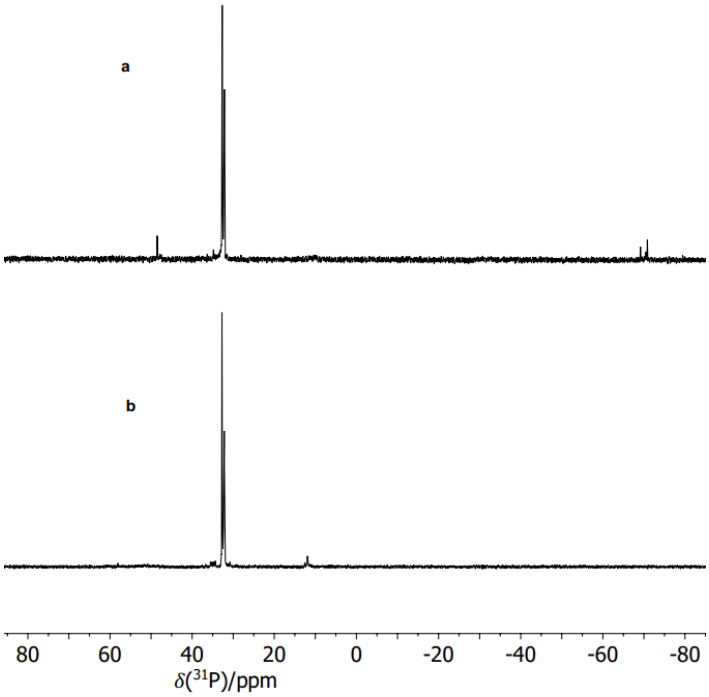

Figure 51. ^{31}P NMR of a) D_{68}-[$P_{666,14}$]Cl and b) D_{68}-[$P_{666,14}$][NTf_2]

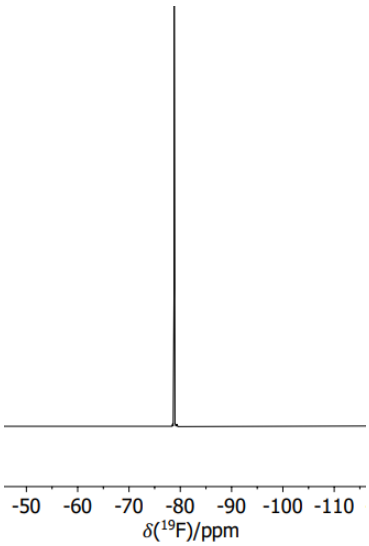

Figure 52. ^{19}F NMR of D_{68}-[$P_{666,14}$][NTf_2]

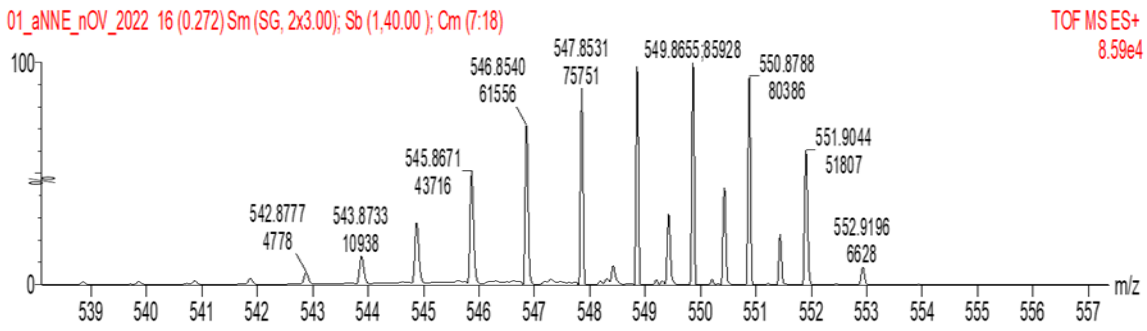

Figure 53. ESI-MS of D_{68}-[$P_{666,14}$][NTf_2]

3.3.2 Neutron scattering studies of phase transitions in [$P_{666,14}$][NTf_2]

[$P_{666,14}$][NTf_2] exhibits a clear liquid-liquid transition (LLT), and the initial aim of this neutron scattering experiment was to study its liquid structure above and below LLT, with H/D substitution on the cation to provide isotopic contrast. The goal was to get an insight, at a molecular level, into the changes in the nanostructure upon LLT, which would be instrumental in understanding of the factors triggering LLTs in ionic liquids, and broader – in organic materials. It would also be the first study of LLT in an ionic liquid using neutrons.

Neutron scattering data were collected using the Near and InterMediate Range Order Diffractometer (NIMROD) instrument at the ISIS Pulsed Neutron and Muon Source at Rutherford Appleton Laboratory, Oxfordshire, UK. As per the beamtime proposal, data was to be collected for three samples: [$P_{666,14}$][NTf_2], D_{68}-[$P_{666,14}$][NTf_2] and their equimolar mixture. The experimental plan was to measure each sample above and below LLT, that is at -43 and -93 °C, in TiZr cans. To record data at these temperatures, the experiment required the use of the closed cycle refrigerator (CCR). Prolonged isothermal run at -93 °C could result in spontaneous crystallisation, but from preliminary experiments of the protiated IL, it was known that samples could be held at this temperature for at least 1 h without crystallising. The plan was to record data for 3 h at -93 °C, with data sets collected over consecutive 10 min runs, as a precaution to minimise the risk of recording data of the crystalline phase. The data would also be recorded for 3 h at -43 °C, as well as upon heating.

Firstly, the protiated [$P_{666,14}$][NTf_2] sample was studied at -43 and -93 °C, and data were preliminarily analysed to make sure that crystallisation was not occurring (amorphous nature was verified by the absence of Bragg peaks). The sample remained amorphous, as shown in the plot of the averaged differential scattering cross section (Figure 54). Figure 55 shows the DSC trace for protiated [$P_{666,14}$][NTf_2]. Previous work[181] showed that

the peak observed indicates LLT as phase 2 observed below the endotherm is an optically transparent homogenous disordered phase, as confirmed by microscopic observations.

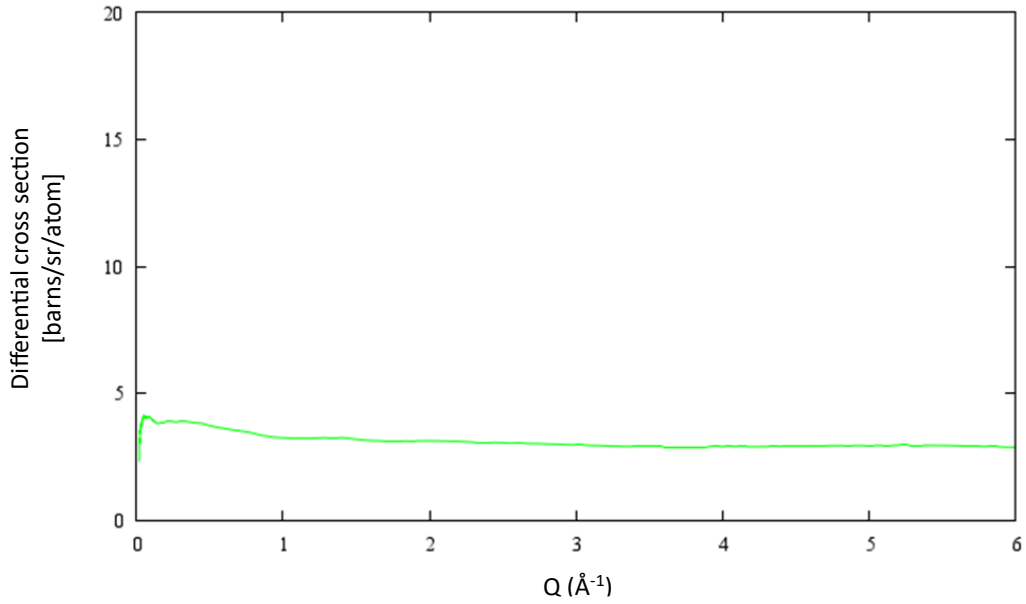

Figure 54. Plot of the averaged differential scattering cross section for $[P_{666,14}][NTf_2]$ at -43 °C.

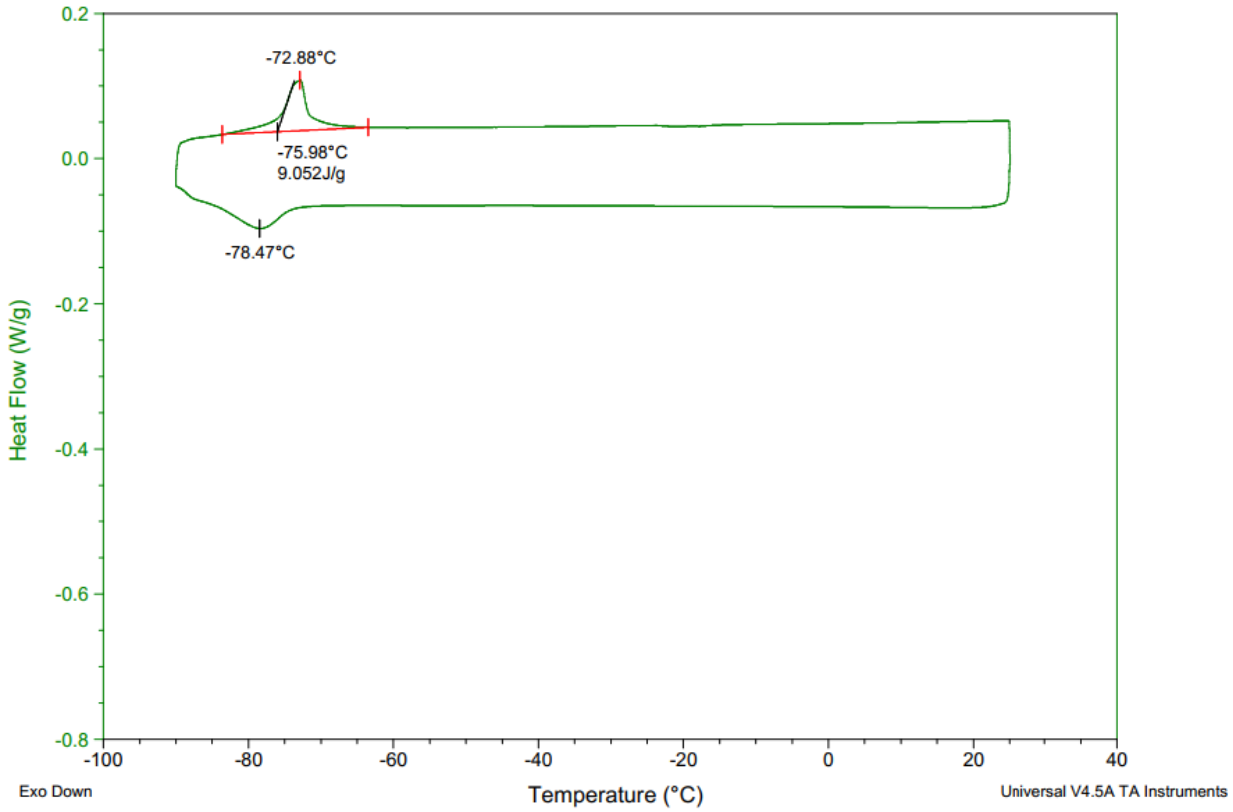

Figure 55. $[P_{666,14}][NTf_2]$ DSC trace. Temperature scan rate: 2 °C min^{-1}

Unfortunately, as the data was being collected at -43 °C for D_{68}-$[P_{666,14}][NTf_2]$, Bragg peaks were recorded (Figure 56). A DSC thermogram was then recorded (after beamtime), exhibiting a strong crystallisation event around -20 °C (Figure 57). Clearly, the deuteriated ionic liquid was more likely to crystallise. This could be attributed to deuterium being larger than hydrogen, creating more steric hindrance around the phosphorus centre. It is known that phosphonium ILs melt at lower temperatures than their ammonium analogues, because nitrogen ionic radius is smaller than phosphorus, therefore alkyl chains have more mobility around the phosphonium cationic centre. It is therefore possible, that swapping hydrogens for deuterium atoms counteracts this freedom of movement, promoting crystallisation.[230] The equimolar mixture also showed formation of Bragg peaks around -30 °C (Figure 58). Another mixture was tested, 75% $[P_{666,14}][NTf_2]$ and 25% D_{68}-$[P_{666,14}][NTf_2]$ which also showed similar behaviour, with crystallisation occurring around -30 °C as indicated by the formation of Bragg peaks (Figure 59). This was very surprising given the higher ratio of protiated versus deuteriated content. In addition, the DSC trace did not show evidence of crystallisation (Figure 60).

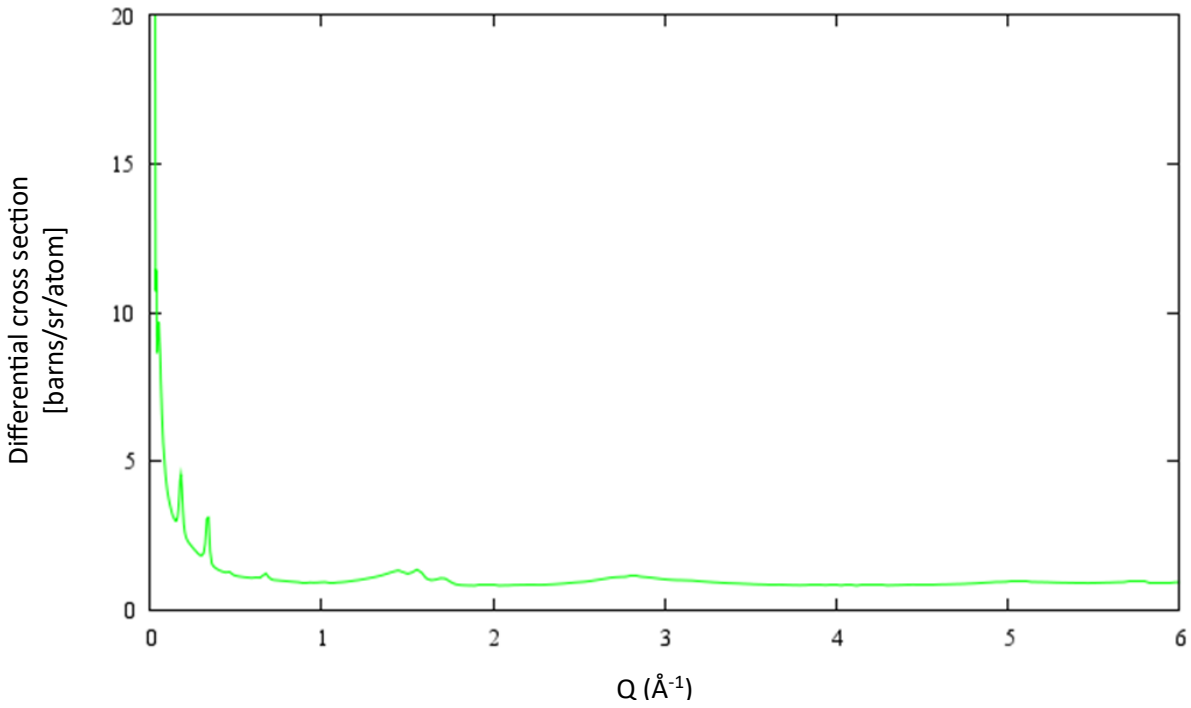

Figure 56. Plot of the averaged differential scattering cross section for D_{68}-[$P_{666,14}$][NTf_2] at -43 °C.

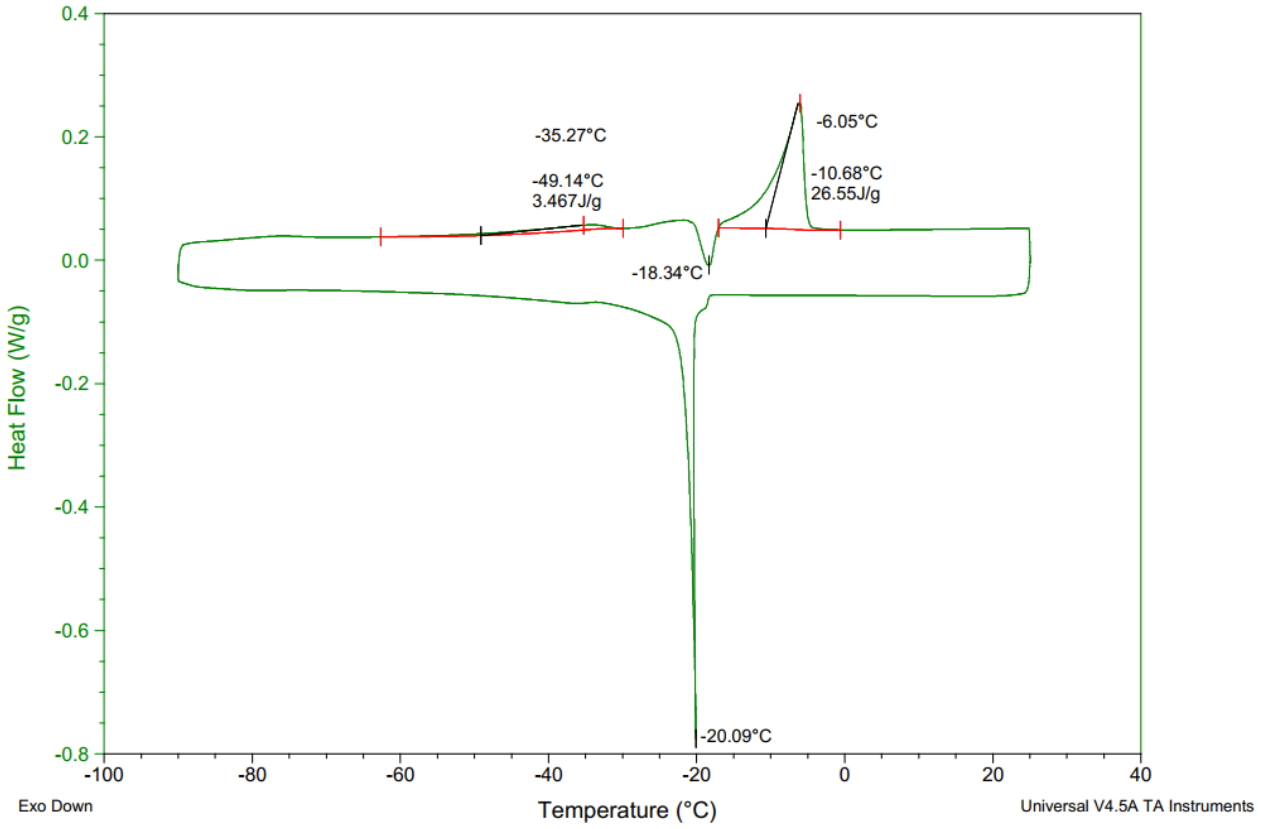

Figure 57. D_{68}-[$P_{666,14}$][NTf_2] DSC trace. Temperature scan rate: 2 °C min^{-1}.

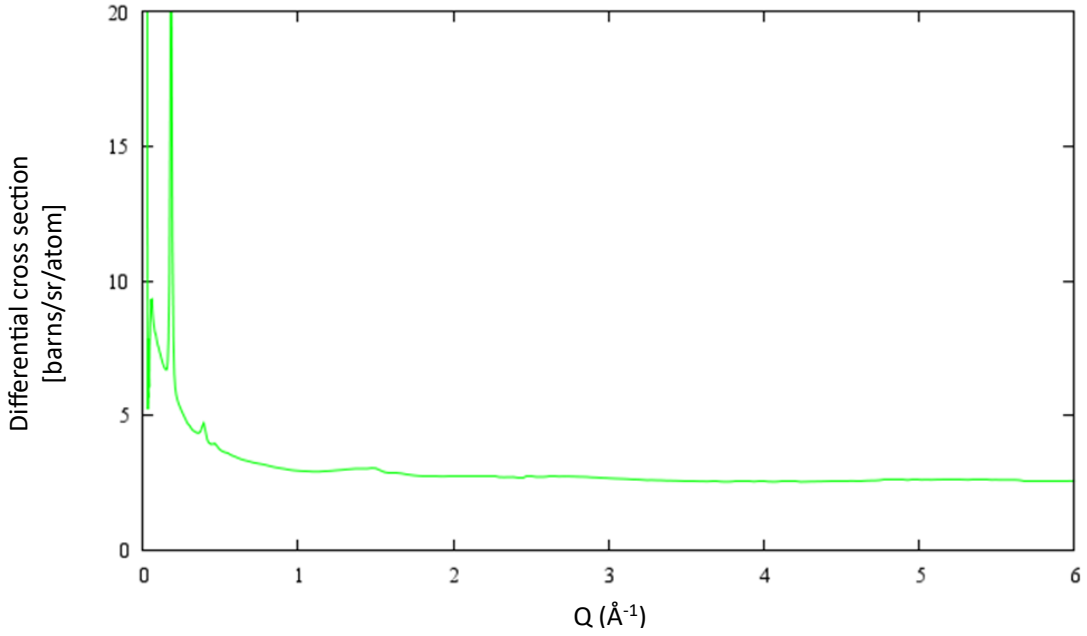

Figure 58. Plot of the averaged differential scattering cross section for the 50:50 mixture of $[P_{666,14}][NTf_2]$ and D_{68}-$[P_{666,14}][NTf_2]$ at -43 °C.

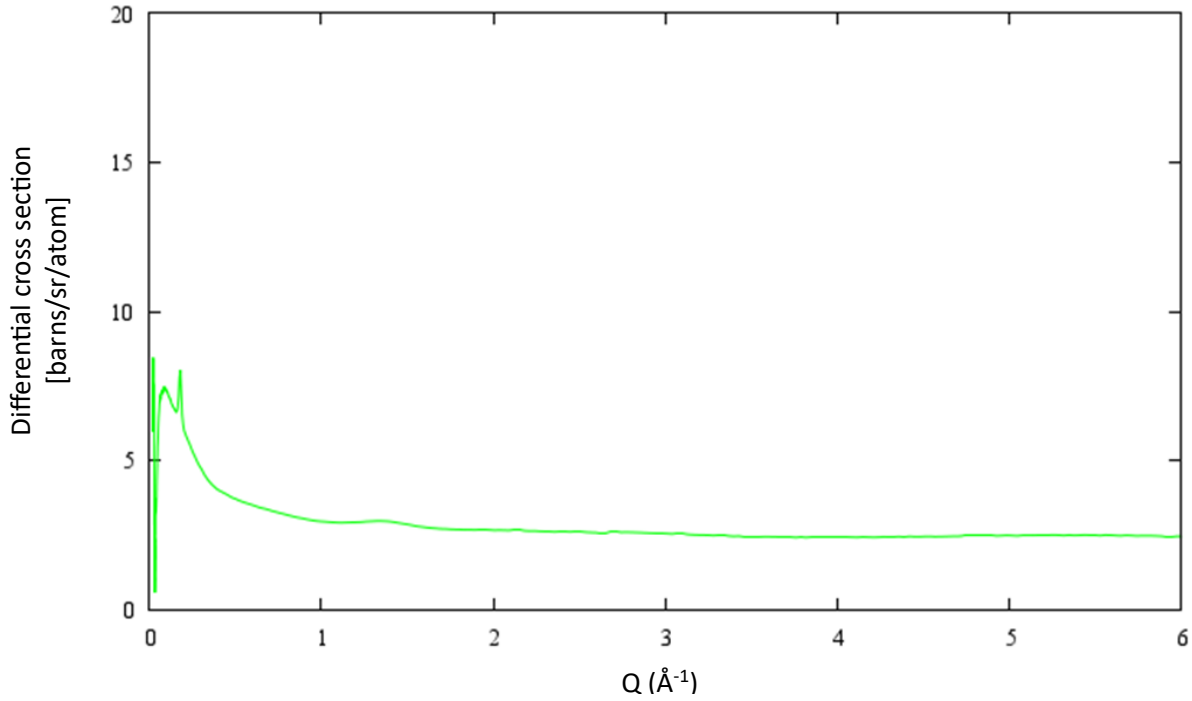

Figure 59. Plot of the averaged differential scattering cross section for the 75:25 mixture of $[P_{666,14}][NTf_2]$ and D_{68}-$[P_{666,14}][NTf_2]$ at -43 °C.

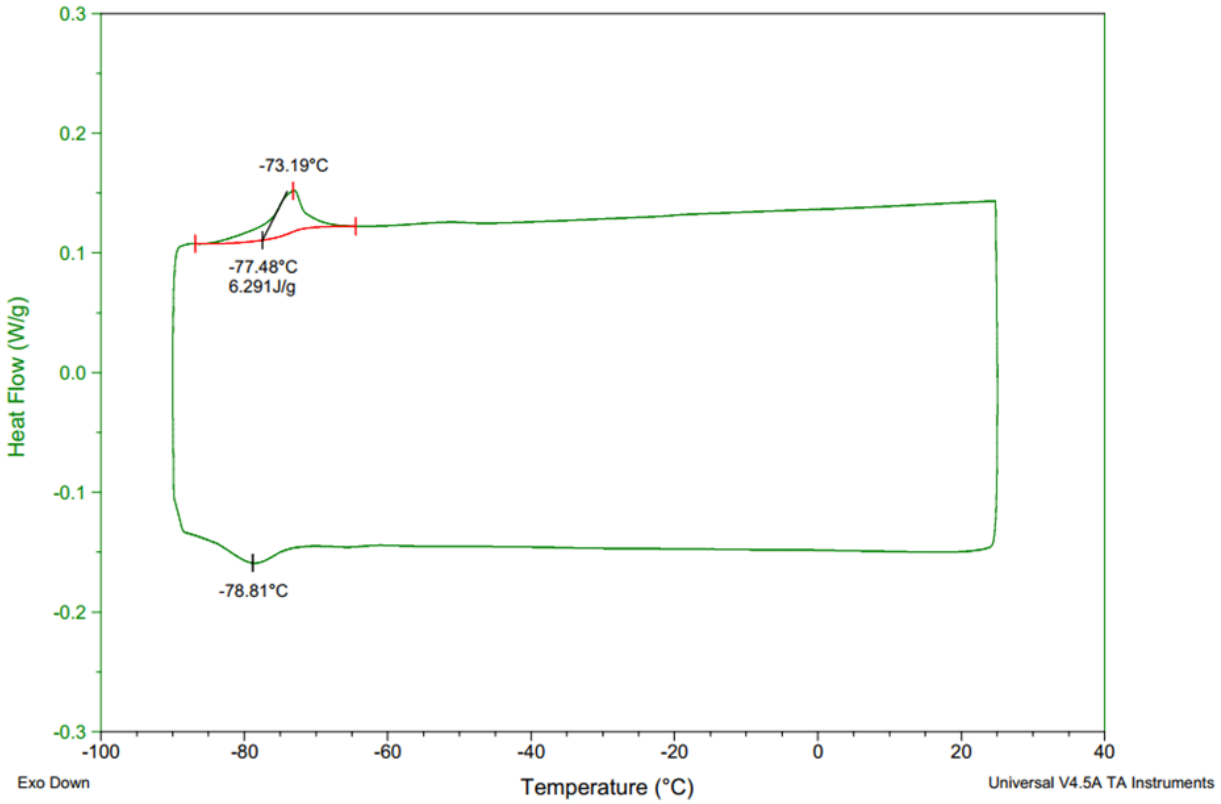

Figure 60. 75:25 mixture of $[P_{666,14}][NTf_2]$ and $[d_{68}\text{-}P_{666,14}][NTf_2]$ DSC trace. Temperature scan rate: 2 °C min^{-1}

It was then decided to record the neutron scattering data at room temperature for the three samples: $[P_{666,14}][NTf_2]$, $D_{68}\text{-}[P_{666,14}][NTf_2]$ and the 75:25 $[P_{666,14}][NTf_2]$:$D_{68}\text{-}[P_{666,14}][NTf_2]$ mixture. The study would pivot to study the structure of $[P_{666,14}][NTf_2]$, which has never been studied before using neutron scattering, and compare it with the structure of two 1,3-dialkylimidazolium ILs, also containing the $[NTf_2]^-$ anion.

3.3.3 The structure of $[NTf_2]^-$ ionic liquids by neutron scattering

Neutron scattering data for the three ILs were recorded using the Near and InterMediate Range Order Diffractometer (NIMROD) and the Small Angle Neutron Diffractometer for Amorphous and Liquid Samples (SANDALS) instruments at the ISIS Pulsed Neutron and Muon Source at Rutherford Appleton Laboratory, Oxfordshire, UK. Data reduction encompassing removal of container and instrument backgrounds, corrections for multiple scattering and attenuation, and the removal of inelasticity effects was performed with the Gudrun software.[93] For each IL, isotopologues containing protiated (H), deuteriated (D) or equimolar mixture of protiated and deuteriated components (H/D) were prepared. The neutron diffraction data was analysed using Dissolve software for the three ILs. Simulation box size contained 500 ion pairs for $[C_2mim][NTf_2]$ and $[C_{10}mim][NTf_2]$ and 250 ion pairs for $[P_{666,14}][NTf_2]$. The forcefield parameters were taken from the Canongia

Lopes & Padua (CL&P) force field.[215,231,232] To test the methodology, three different sets of cation charges were used, for each of the three ILs. The atom types used in the Dissolve model are shown in Figure 61 and the simulation box size parameters are shown in Table 9.

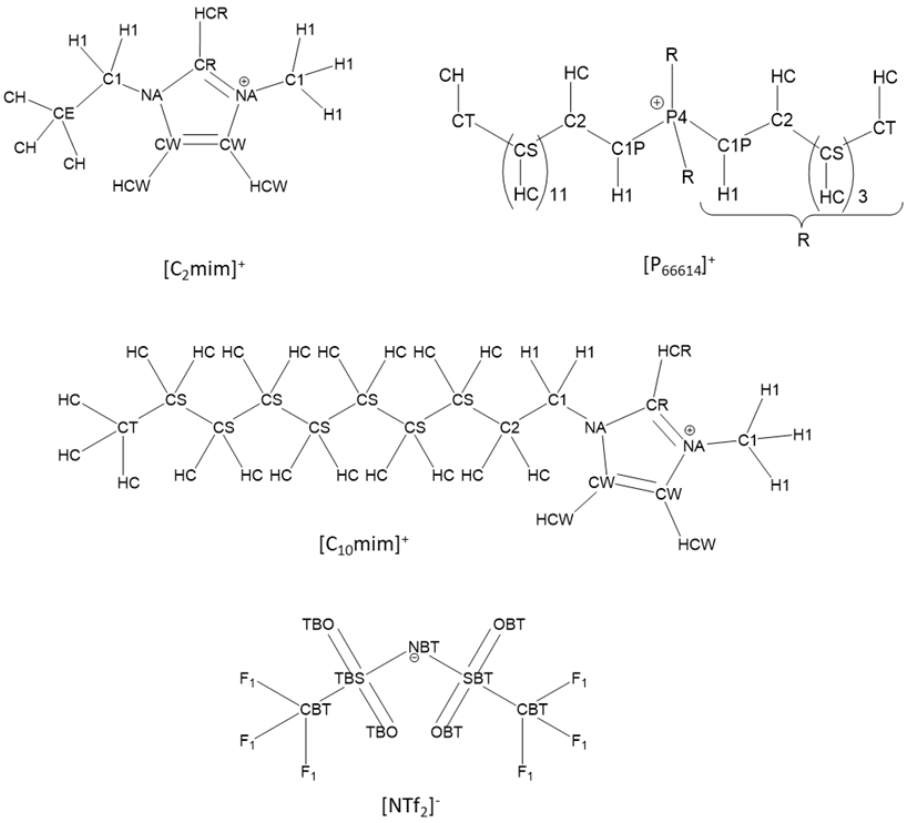

Figure 61. Molecular structures and atom types for $[C_2mim]^+$, $[C_{10}mim]^+$ and $[P_{666,14}]^+$ cation and $[NTf_2]^-$ anion.

Table 9. Simulation box size parameters.

Ionic liquid	Number of molecules (cation:anion)	Box size, n/ Å	Number density / atoms Å^{-3}
$[C_2mim][NTf_2]$	1000 (500:500)	59.66	0.080
$[C_{10}mim][NTf_2]$	1000 (500:500)	68.86	0.089
$[P_{666,14}][NTf_2]$	500 (250:250)	66.68	0.098

3.3.3.1 EPSR modelling using Dissolve and fit to experimental data

Total neutron scattering data for $[C_2mim][NTf_2]$, $[C_{10}mim][NTf_2]$ and $[P_{666,14}][NTf_2]$, each measured at three levels of isotopic substitutions (H, D, H/D) were reduced using the GUDRUN[93] package and modelled using Dissolve.[94] The experimental sample densities and scattering levels were consistent with the correct isotopic compositions of the samples. Comparisons of experimental and simulated total structure factors, *F(R),* and the corresponding Fourier transforms to real space, *G(r),* for the three ILs at three substitution levels, measured at ambient temperature, are shown in Figure 62. Apart from the region at $Q \leq 1$ Å$^{-1,}$ which is most susceptible to inconsistencies due to inelastic scattering contributions from hydrogen in the data, the fitted data aligns well with experiment.

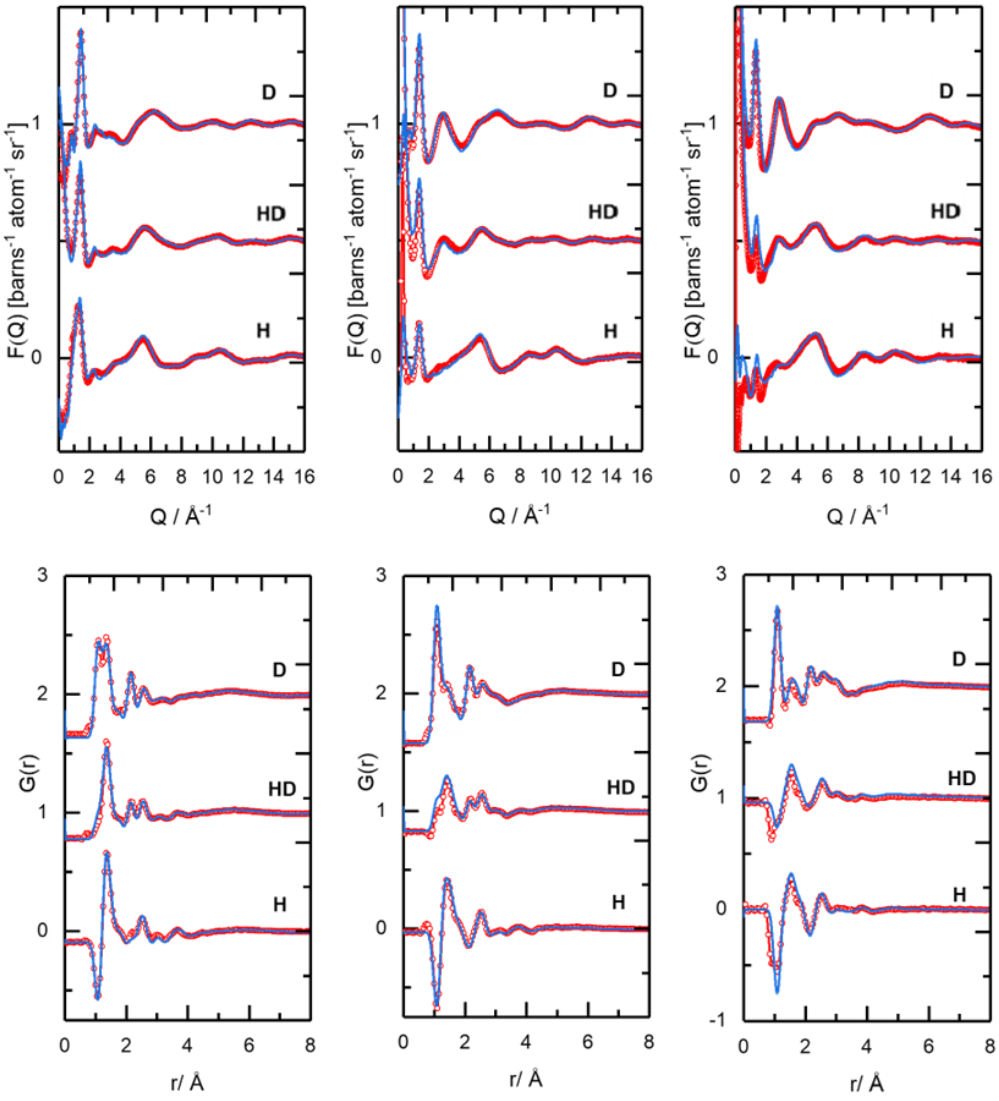

Figure 62. Total structure factors F(Q) (top), and the corresponding Fourier transform to real space G(r) radial distribution functions (bottom) showing experimental data (red symbols) and Dissolve modelled (blue solid line) for left: $[C_2mim][NTf_2]$, middle: $[C_{10}mim][NTf_2]$ and right: $[P_{666,14}][NTf_2]$.

Neutron and X-ray scattering experiments and MD studies have shown that the structure of ionic liquids is dominated by strong cation-anion interactions through Coulombic forces, as well as heterogeneity at microscopic level: segregation of polar (*e. g*. the cation polar head and the anion) and non-polar regions (alkyl chains).[19,20,22,233,234] This comparative study was deemed interesting, as modelling and X-ray[19,22,30–32,40,186] scattering experiments indicate that long chained ILs such as $[C_{10}mim][NTf_2]$ and $[P_{666,14}][NTf_2]$ will exhibit substantial nanosegregation compared to shorter chain ILs such as $[C_2mim][NTf_2]$. Furthermore, protons on the imidazolium ring in $[C_2mim][NTf_2]$ and $[C_{10}mim][NTf_2]$, as well as H-C-P protons in $[P_{666,14}][NTf_2]$ are expected to participate in hydrogen bonding, with oxygen and nitrogen atoms in the $[NTf_2]^-$ anion acting as hydrogen bond acceptors; these interactions can be quantified through a neutron scattering study.

3.3.3.2 Centre of mass radial distribution functions

The most important information about the IL structure – the ordering of cations and anions with respect to one another - can be extracted from the radial distribution functions (RDF), describing the distribution of atoms and species around a central point. In ionic liquids, these tend to be the nominal centres of charge. Following the convention, the central points selected in this work were: the phosphorus of $[P_{666,14}]^+$, the centre of mass taken from the mid-point of the two nitrogen atoms of the imidazolium ring in $[C_2mim]^+$ and $[C_{10}mim]^+$, and the nitrogen of $[NTf_2]^-$. RDFs describing the cation-anion distribution for the three $[NTf_2]^-$ ionic liquids are shown in Figure 63.

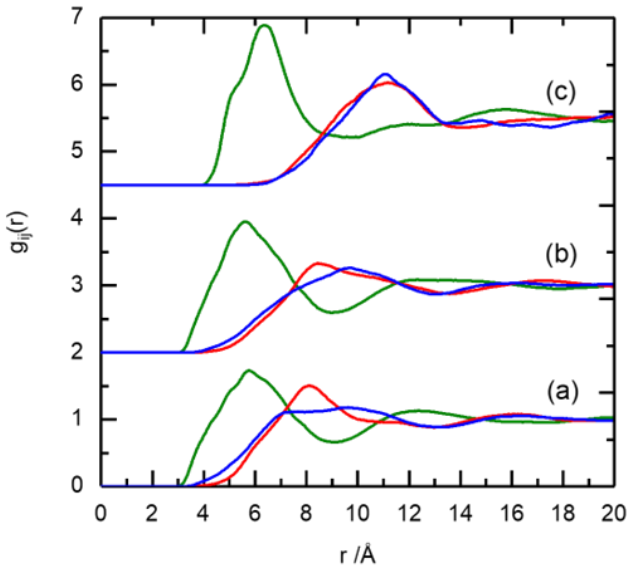

Figure 63. Comparison of the radial distribution functions for the cation-anion distribution (green line), the cation-cation distribution (blue line), and the anion-anion distribution (red line) for (a) $[C_2mim][NTf_2]$, (b) $[C_{10}mim][NTf_2]$ and c) $[P_{666,14}][NTf_2]$.

The cation-anion contact distance (green curves in Figure 63) is centred at ~6 Å for all three ILs, similarly to the distances reported for other ILs,[7,29,235,40] and irrespective of the size difference between $[C_2mim]^+$, $[C_{10}mim]^+$ and $[P_{666,14}]^+$. Computational studies have been published on all three ionic liquids: $[P_{666,14}][NTf_2]$ was modelled by Parker *et. al,*[188] $[C_2mim][NTf_2]$ was studied by the groups of Fujii (MD)[185] and Boero (DFT),[190] $[C_{10}mim][NTf_2]$ - by Lopes *et. al.*[186] In all cases, the models were broadly similar to the neutron scattering results, but computational methods suggested the presence of a double peak for the first-shell correlation of the cation-anion: around 5 and 6 Å, attributed to *cis* and *trans* $[NTf_2]^-$ conformers. In neutron scattering data, these features were significantly less resolved: in $[P_{666,14}][NTf_2]$, there was a slight shoulder at ~5 Å, and a single, albeit broader, peak was recorded for $[C_2mim][NTf_2]$ and $[C_{10}mim][NTf_2]$. Finally, several authors describe a low-intensity peak at 3.5 Å in calculated pRDFs for $[C_2mim][NTf_2]$ and $[C_{10}mim][NTf_2]$, which manifests itself in the neutron scattering data in the form of a broadening of the main feature at 6 Å (green curves in Figure 63a and b), which is absent from the analogous $[P_{666,14}][NTf_2]$ curve (green curves in Figure 63c). This broad peak is from the shortest contact of anion to centre of mass of the imidazolium ring cation where anion distribution is located above/below the ring. This distribution is due to the large size and charge delocalisation of the $[NTf_2]^-$ anion which has the effect of reducing the hydrogen bonding accepting ability of the anion, and thus the interaction with the ring hydrogens reduces, in contrast to smaller anions like chloride.[16] This first cation-anion contact distance centred ~6 Å which presents as a broad peak in the RDF, has also been observed in neutron scattering studies of several ILs; $[C_1mim][NTf_2]$,[46] $[C_4mim][NTf_2]$[235] and in a series of $[C_nmim][PF_6]$ ILs, where n = 4, 6, and 8.[40] The latter publication showed retention of the cation-anion first shell with changing cation alkyl chain length.

The cation-anion coordination numbers (CN), calculated from the integration of the cation-anion RDFs up to the first minimum at 9 Å (green curves in Figure 63) were found to increase with decreasing cation size. In $[P_{666,14}][NTf_2]$, there were three anions in the first shell of each cation, in agreement with MD studies by Liu and co-workers.[61] Coordination numbers increased to 5 for $[C_{10}mim][NTf_2]$ and further to 7 for $[C_2mim][NTf_2]$, which is again comparable with the literature data.[190]

The cation-cation distance and coordination numbers (P···P distribution), as well as anion-anion distance and coordination numbers (N···N distribution) are nearly identical for $[P_{666,14}][NTf_2]$, with maxima ~11 Å and coordination numbers of 9 (to a distance of 14 Å). It is evident from blue and red curves in Figure 63c, and remains in agreement with MD studies by Liu and co-workers.[61] In $[C_2mim][NTf_2]$ and $[C_{10}mim][NTf_2]$, the peaks describing the anion-anion distances (red curves in Figure 63a and b) have maxima at much shorter distance (~8.0 and 8.5 Å , respectively), but are much broader than the corresponding feature in $[P_{666,14}][NTf_2]$. In consequence, when integrated, they give coordination numbers of 25 and 17, respectively. The peaks corresponding to cation-cation interactions for $[C_2mim][NTf_2]$ and $[C_{10}mim][NTf_2]$, (blue curves in Figure 63a

and b) also have maxima at a shorter distance of ~9 Å but again, are much broader then the corresponding feature in $[P_{666,14}][NTf_2]$.

Conformational flexibility and low basicity of $[NTf_2]^-$,[16] combined with rotational freedom of the relatively small $[C_2mim]^+$ cation, resulted in very little long-range structure, aside from that imposed by the ordering of alternating charges. In particular, the nearly featureless blue curve in Figure 63a indicated a close to random orientation of $[C_2mim]^+$ cations. This is in agreement with a number of computational, Raman, IR and UV-VIS spectroscopic studies, which point to a large number of cation/anion orientations existing within a very small energy difference (<0.5 kcal/mol).[236,237] In $[C_{10}mim][NTf_2]$, the cation-anion distance is the same as in $[C_2mim][NTf_2]$, despite larger cation size. This suggests that the anion is positioned around the ring, and the long alkyl chain protrudes away from the charged region (does not contribute to cation-anion separation). While ring-anion interactions are analogous to $[C_2mim][NTf_2]$, the decyl chain restricts partially the rotational freedom of the cation, enforcing more cationic ordering (blue curve in Figure 63b). The structure of in $[P_{666,14}][NTf_2]$ can be envisaged as phosphonium point charges, arranged every 11 Å in all directions (coordination number 9), with alkyl chains that protrude from these cationic centres and overlap, attracted by van der Waals forces. Anions sit in holes between the alkyl chains, at 6 Å from the nearest cation (green curve in Figure 63c), the distance resulting from the interplay between Coulombic attraction and steric hindrance. For the weakly coordinating $[NTf_2]^-$ anion, long alkyl chains decrease electrostatic attraction, thus increasing attraction between the ion pairs. Ion pairing in phosphonium ionic liquids, studied by pulse field gradient NMR spectroscopy, has been shown to increase with increasing alkyl chain length, which points to the high degree of ion pairing in $[P_{666,14}][NTf_2]$.[238] This, in turn, explains the existence of identical, well-pronounced cation-cation and anion-anion corelations, as the direct consequence of ion pairing.

3.3.3.3 Aggregate analysis

To investigate the aggregation of the alkyl chains in $[C_{10}mim][NTf_2]$ and $[P_{666,14}][NTf_2]$, often described as hydrophobic domains, a comparison of the RDFs for carbon atoms in the beginning (C_2/C_{1P}), middle (C_{S4}) and terminal (C_T) parts of the alkyl chain were plotted (Figure 64). For codes of atom types, refer to Figure 61.

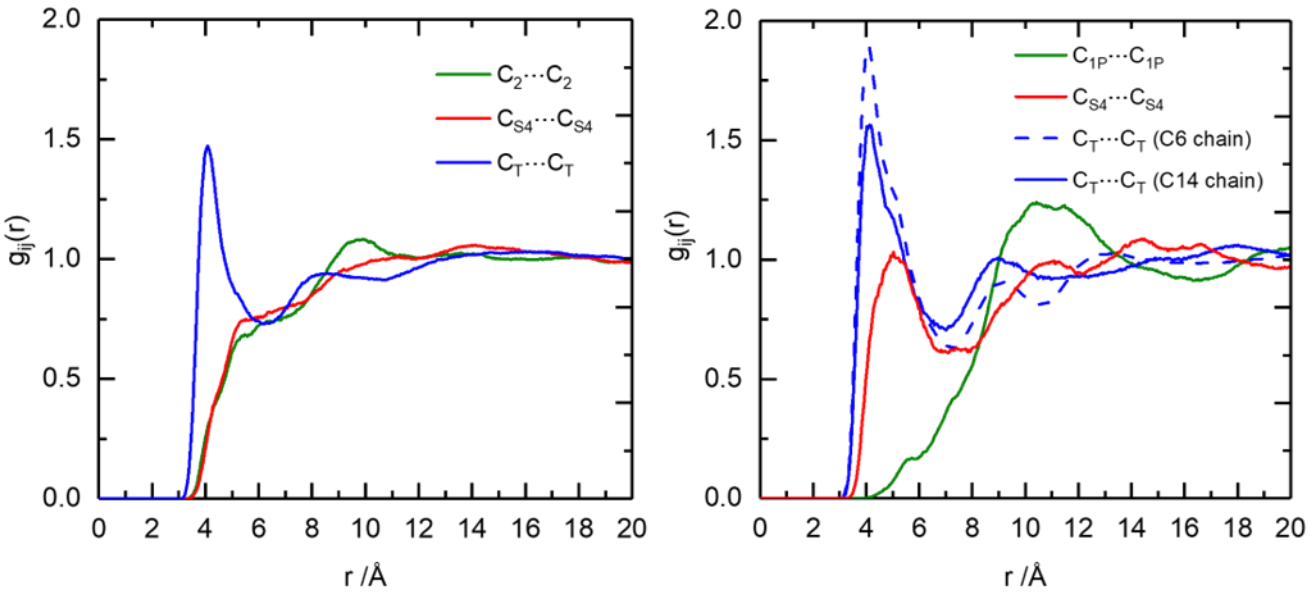

Figure 64. Radial distribution functions of carbon atoms along the alkyl chain in: left - $[C_{10}mim][NTf_2]$, C_2 (green), C_{S4} (red) and C_T (blue) and right: $[P_{666,14}][NTf_2]$ - C_{1P} (green), C_{S4} (red), C_T of the C6 chain (blue-dashed) and C_T of the C14 chain (blue-solid).

The highest and the most intense peaks occurred for the terminal carbons (C_T), demonstrating strong spatial correlation between the nonpolar parts of hydrocarbon chains. All three C_T first shell peaks have maxima at a very short distance of 4 Å, and CN = 2 for C_T in $[C_{10}mim][NTf_2]$, and CN = 1 for both C_T(C6) and C_T(C14) of $[P_{666,14}][NTf_2]$ (up to a distance of 7 Å) . There is also evidence for longer-range order, with pronounced second shell correlation peaks at 8-9 Å, which maps to typical cation-cation separation distance, and shows evidence of longer length scale oscillation in the structure. These findings correspond to a MD simulation study on $[C_{10}mim]^+$ ionic liquids with amino acid-derived anions.[239] On the other hand, carbons adjacent to charge centres showed features at 10 Å for C_2 in $[C_{10}mim][NTf_2]$, and 11 Å for C_{1P} in $[P_{666,14}][NTf_2]$, in both cases perfectly aligned with the corresponding cation-cation correlation (Figure 63). Finally, the RDF middle-of-the-chain carbon for $[C_{10}mim][NTf_2]$, showed no distinct peak, as this position is a function of the interplay between Coulombic and van der Waals forces, shaping the polar and non-polar regions. In contrast, the RDF middle-of-the-chain carbon of the C14 chain of $[P_{666,14}][NTf_2]$ did show a peak around 5 Å, and demonstrated a similar correlation pattern to the terminal carbons, with a small shift in the peaks and significantly less intense first shell correlation.

It is known from the literature, that $[C_{10}mim]Cl$ and its many hydrates have very ordered structures, with crystal packing containing double rows of charged imidazolium rings and chloride anions, and nonpolar domains of overlapping alkyl chains (close contacts for both $C_T \cdots C_T$ and $C_{4S} \cdots C_{4S}$).[240] In contrast, lack of order

in the polar domain of $[C_{10}mim][NTf_2]$, appears to result in alkyl chains protruding different directions, therefore no ordering in $C_{4S}\cdots C_{4S}$. Only the ends of decyl chains appear to assemble into nonpolar domains due to van der Waals forces, as shown by close $C_T\cdots C_T$ contacts (4 Å, CN = 2, Figure 64 left). In contrast, the RDF middle-of-the-chain carbon of the C14 chain of $[P_{666,14}][NTf_2]$ does show a peak around 5 Å. This is aligned with the image previously proposed, in which alkyl chains protrude from phosphonium point charges, arranged every 11 Å, resulting in necessary overlap of these alkyl chains. Unsurprisingly, this suggests that the size of nonpolar domains in $[P_{666,14}][NTf_2]$ is much larger than in $[C_{10}mim][NTf_2]$; not only due to increased volume of the alkyl chains, but also due to their much better overlap.

3.3.3.4 Hydrogen bond analysis

To understand atom-specific interactions in the cation-anion association for the three ILs, which can inform about their chemistry and solvating properties, atom-specific pRDFs were derived. Correlations between the cation ring hydrogens (H_{CR} and H_{CW}) of $[C_nmim]^+$, or the H_1 protons of $[P_{666,14}]^+$, and the O, F and N atoms of the $[NTf_2]^-$ anion, are shown in Figure 65.

At first glance, the distributions are similar for each interaction, demonstrating the presence of strong hydrogen bonds. The $H_{cation}\cdots O_{anion}$ interactions feature first-shell close contacts at ~2.7 Å, with weaker and broader peaks at ~5.5 Å. The $H_{cation}\cdots N_{anion}$ interactions feature a slight shoulder at ~2.7 Å, which is much less pronounced compared to the $H_{cation}\cdots O_{anion}$ interaction. The main peak for $H_{cation}\cdots N_{anion}$ is centered around 5 Å which is the distance associated with the anion interacting *via* its oxygens. This corresponds to reports by Boero *et. al* and Liu and co-workers.[61,190] In summary, the acidic hydrogens interact with the anion mainly through O atoms, much less through N atoms, and there is virtually no interaction *via* F atoms in the first coordination sphere. The imidazolium cation and $[NTf_2]^-$ anion preferentially interact through the H_{CR} atom in $[C_nmim]^+$, which is more acidic than H_{CW} (again, this is consistent with MD studies).[185,190] Coordination numbers for $H_{cation}\cdots O_{anion}$ contacts have reached CN = 0.4 - 0.5 for the $[C_nmim]^+$ ILs, and only CN = 0.2 for the H_1 protons in $[P_{666,14}]^+$. The latter value is smaller as interaction of each $[NTf_2]^-$ anion is averaged across eight H_1 hydrogens. The relative distances and coordination numbers of the key correlations for the three ILs are shown in Table 10 and Table 11.

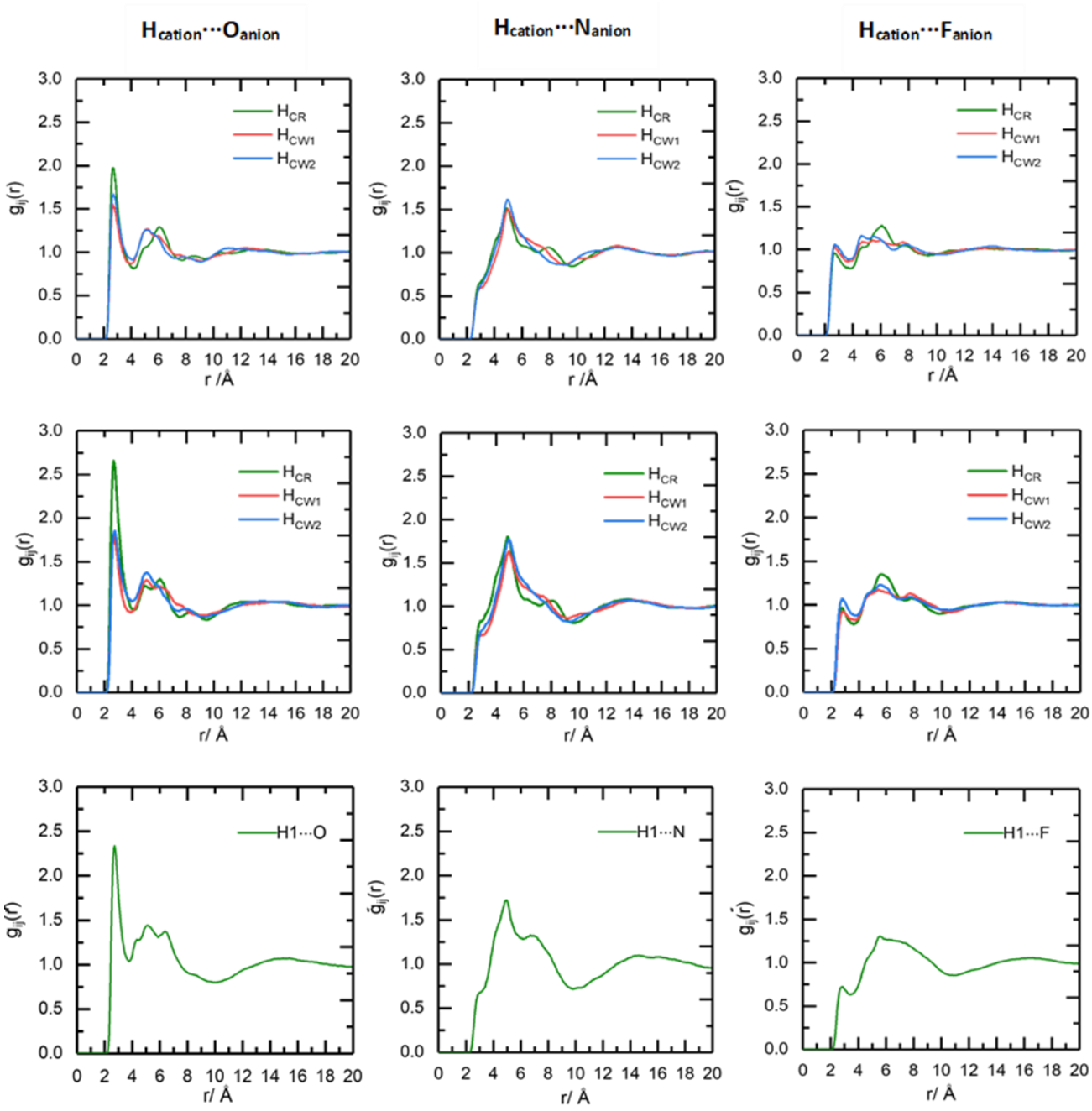

Figure 65. Radial distribution functions for top: [C_2mim][NTf_2], middle: [C_{10}mim][NTf_2] and bottom: [$P_{666,14}$][NTf_2] for interactions between the cation ring hydrogens/H_1 and oxygen (left), nitrogen (middle) and fluorine atoms (right) of the anion. H_{CW1} refers to H_{CW} beside the alkyl chain and H_{CW2} refers to H_{CW} beside the methyl group.

Table 10. Interatomic distances (taken from the first peak maximum in the site-site radial distribution functions) and relative coordination numbers (CN, calculated to the minimum after the first peak in the radial distribution functions) between different atom types for $[C_2mim][NTf_2]$ and $[C_{10}mim][NTf_2]$. H_{CW1} refers to H_{CW} beside the alkyl chain and H_{CW2} refers to H_{CW} beside the methyl group.

	$[C_2mim][NTf_2]$		$[C_{10}mim][NTf_2]$	
Interaction	**Peak (minima)**	**CN**	**Peak (minima)**	**CN**
$H_{CR}\cdots O_{BT}$	2.7 (4.0)	0.63	2.7 (4.0)	0.51
$H_{CW1}\cdots O_{BT}$	2.7 (4.0)	0.55	2.7 (4.0)	0.42
$H_{CW2}\cdots O_{BT}$	2.7 (4.0)	0.59	2.7 (4.0)	0.46
$H_{1(met)\cdots}O_{BT}$	2.7 (4.0)	0.48	2.8 (4.0)	0.38
$H_{1(C2\ chain)}\cdots O_{BT}$	2.7 (4.0)	0.44		
$H_C\cdots O_{BT}$	2.8 (4.0)	0.36		
$H_{CR}\cdots N_{BT}$	3.0		3.1	
$H_{CW1}\cdots N_{BT}$	3.0		3.1	
$H_{CW2}\cdots N_{BT}$	3.0		3.1	
$O_{BT}\cdots H_{CR}$	2.7 (4.0)	0.63	2.7 (4.0)	0.51
$O_{BT}\cdots H_{CW1}$	2.7 (4.0)	0.55	2.7 (4.0)	0.42
$O_{BT}\cdots H_{CW2}$	2.7 (4.0)	0.59	2.7 (4.0)	0.46
$N_{BT}\cdots H_{CR}$	3.01		3.1	
$N_{BT}\cdots H_{CW1}$	3.01		3.1	
$N_{BT}\cdots H_{CW2}$	3.01		3.1	

Table 11. Interatomic distances (taken from the first peak maximum in the site-site radial distribution functions) and relative coordination numbers (CN, calculated to the minimum after the first peak in the radial distribution functions) between different atom types for $[P_{666,14}][NTf_2]$.

Interaction	Peak	CN
$H_1 \cdots O_{BT}$	2.7 (3.7)	0.20
$H_1 \cdots N_{BT}$	3.1	
$O_{BT} \cdots H_1$	2.7 (3.7)	0.20
$N_{BT} \cdots H_1$	3.1	

Dissolve provides a new capability to depict distance and angle analysis as heat maps. Of particular interest in this work is the analysis of distances and angles in C_R-$H_{CR} \cdots O_{BT}$ and C_{1P}-$H_1 \cdots O_{BT}$, as well as C_R-$H_{CR} \cdots N_{BT}$ and C_{1P}-$H_1 \cdots N_{BT}$, as it gives further insight into cation-anion interactions. The maps of $[NTf_2]^-$ hydrogen bonding motifs *via* oxygen, for all three ILs, are shown in Figure 66, and the maps of $[NTf_2]^-$ hydrogen bonding motifs *via* nitrogen – in Figure 67. In Figure 66, maps on the left show the C-H bond length (∼1.09 Å) on the *x* axis, and the angle between this bond and the H···O hydrogen bond on the *y* axis. Maps on the right show the reverse: the H···O hydrogen bond length (∼2.7 Å) on the *x* axis, and the angle between this bond and the C-H bond on the *y* axis. Analogous representations for nitrogen hydrogen bonding are shown in Figure 67.

Despite very similar results from numerical analysis presented above, the heat maps show marked differences in the interaction of $[NTf_2]^-$ anion with H_{CR} in $[C_n mim]^+$, when compared to its interaction with H_1 in $[P_{666,14}]^+$; whereas all C-H distances are narrowly distributed around ∼1.09 Å, the angles of hydrogen bonding differ. The angles in C_R-$H_{CR} \cdots O_{BT}$ (in imidazolium ILs) vary between 60 and 180°, with a well-defined maximum around 130°. In contrast, the range of C_{1P}-$H_1 \cdots O_{BT}$ angles is much more diffuse, values starting from about 80°, but the highest probability values stretching from 140 to 180°, suggesting that the C_{1P}-$H_1 \cdots O_{BT}$ interaction is much more linear than C_R-$H_{CR} \cdots O_{BT}$. Hydrogen bonds to the nitrogen of $[NTf_2]^-$ increase in linearity as the bulk of the cation increases, which probably results from steric hindrance around the hydrogen bond donor sites (Figure 67). Comparing heat maps for H···O distances (Figure 66, right) and H···N distances (Figure 67, right), the interactions with nitrogen are less directional, with distance distribution further diffused along the *x* axis. Conventionally, more linear hydrogen bonds are stronger;[241] these results raise an interesting question, whether hydrogen bonding between $[NTf_2]^-$ and H_1 protons in $[P_{666,14}]^+$ is indeed stronger than that with the ring protons in $[C_n mim]^+$.

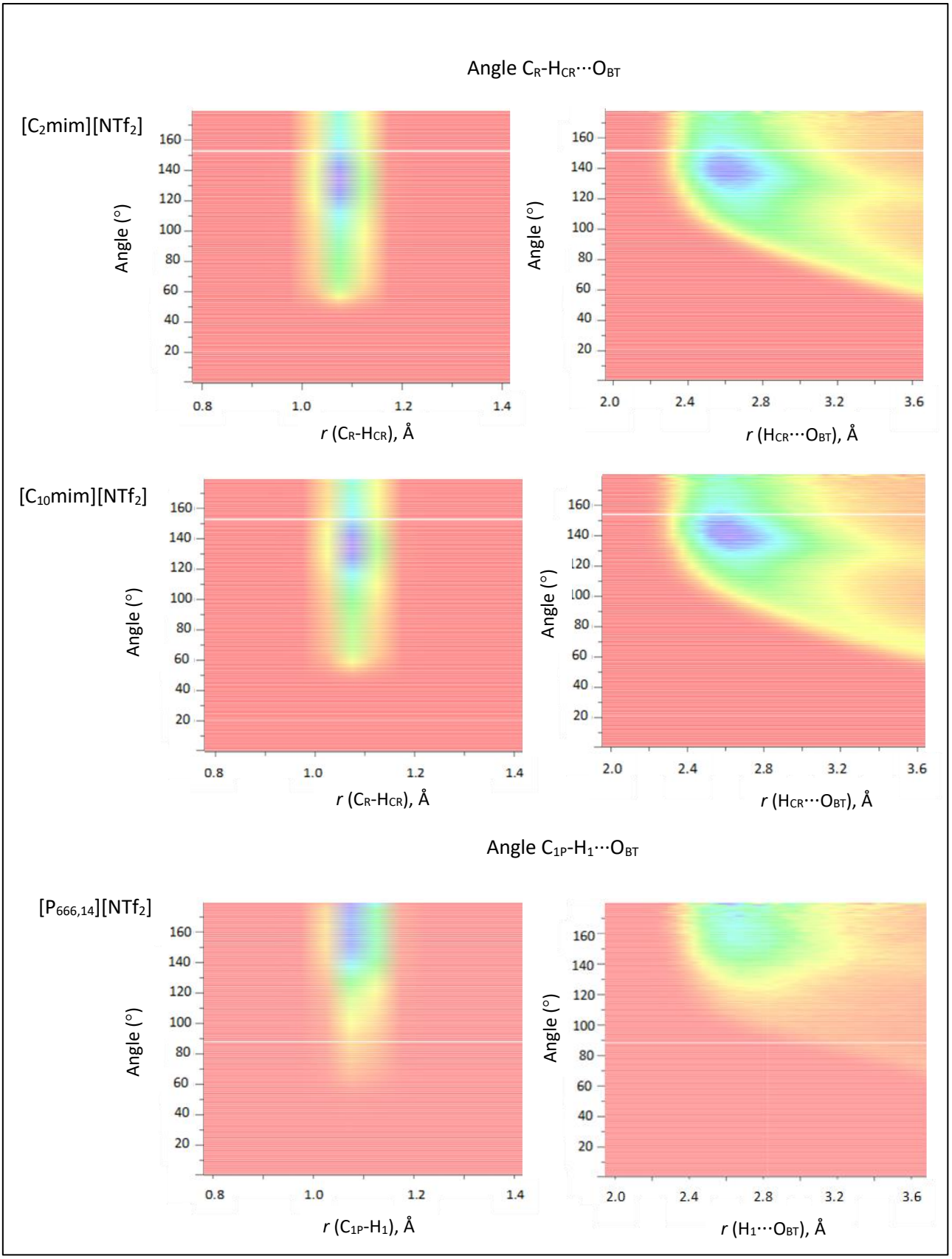

Figure 66. Distance and angle analysis of hydrogen bonds between atom types C_R-H_{CR}···O_{BT} for [C_2mim][NTf_2] and [C_{10}mim][NTf_2] and C_{1P}-H_1···O_{BT} for [$P_{666,14}$][NTf_2].

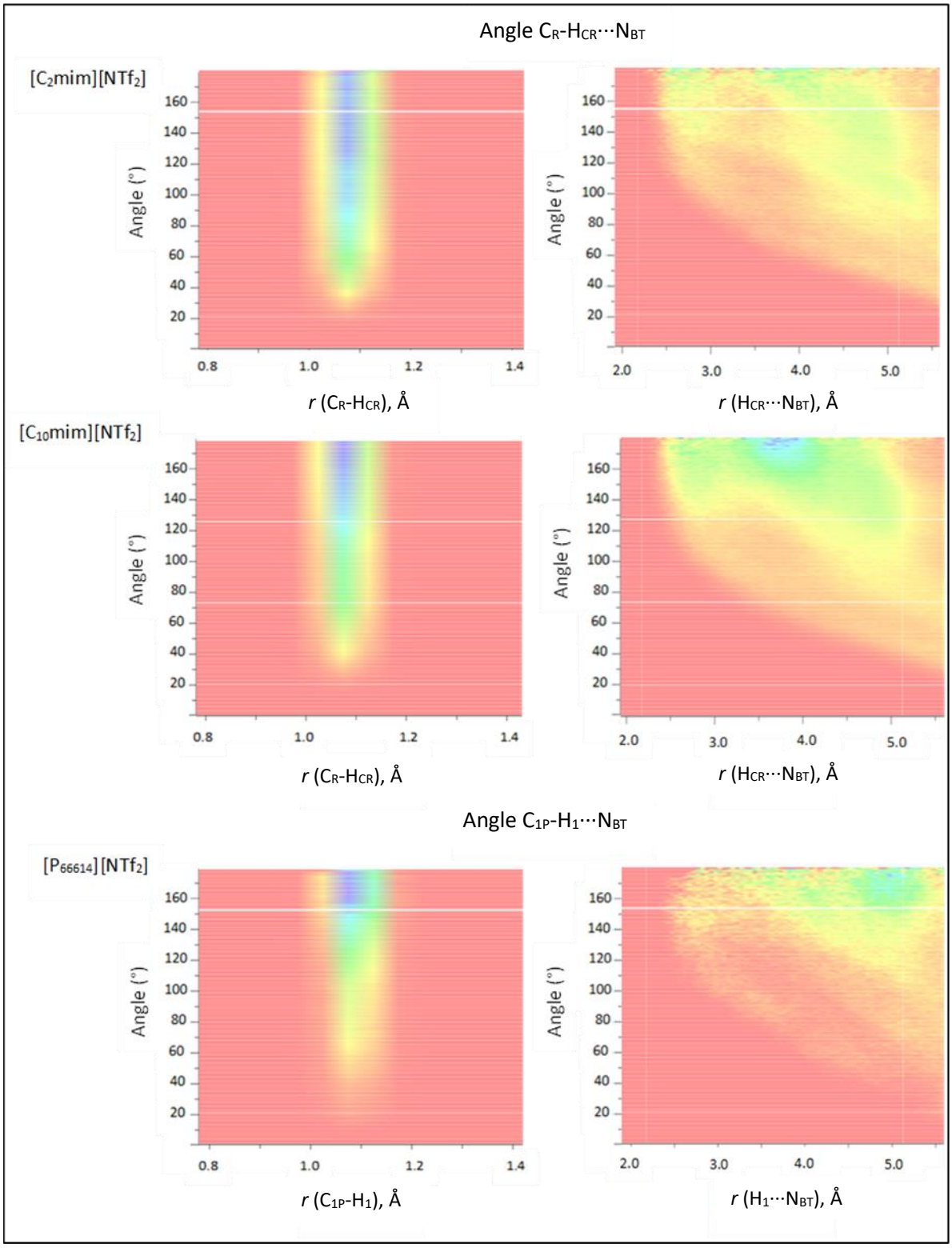

Figure 67. Distance and angle analysis of hydrogen bonds between atom types C_R-H_{CR}···N_{BT} for [C_2mim][NTf_2] and [C_{10}mim][NTf_2] and C_{1P}-H_1···N_{BT} for [$P_{666,14}$][NTf_2].

3.3.3.5 Model robustness

The robustness of Dissolve analysis was verified by comparative simulations using three different sets of atomic charges on the cation, sourced from ESP, LPG and CLP forcefields (Table 12-Table 14). Set 1 was from the CL&P forcefield. Set 2 was electrostatic potential (ESP) charges calculated with the NWChem software (v7.0.2). Geometry optimisations were performed on all ions at increasing basis sets up to HF/6-31+G(d), at which point the ESP charges were calculated using the standard module defaults. Resulting charges were averaged across symmetry-related and/or chemically equivalent sites on the molecules, and significant figures truncated to three in order to provide manageable charges for the simulation, always ensuring that the total charge remained at +/-1. Set 3 charges were generated from the LigParGen service offered by the Jorgensen group.[178–180]

Table 12. Three sets of charges used for the Dissolve model for $[C_2mim][NTf_2]$.

Atom type	Charge CLP	Charge ESP	Charge LPG
C_W	-0.094	-0.191	-0.058
N_A	0.108	0.159	-0.195
C_R	-0.080	-0.123	0.106
C_1	-0.123	0.050	-0.019
C_E	-0.036	-0.090	-0.236
H_1	0.094	0.106	0.131
H_{CW}	0.152	0.231	0.227
H_{CR}	0.152	0.237	0.241
H_1	0.094	0.014	0.128
H_C	0.043	0.044	0.111

Table 13. Three sets of charges used for the Dissolve model for $[C_{10}mim][NTf_2]$.

Atom type	Charge CLP	Charge ESP	Charge LPG
C_W	-0.094	-0.199	-0.059
N_A	0.108	0.180	-0.192
C_R	-0.080	-0.155	0.104
C_1	-0.123	0.036	-0.022
C_2	0.007	0.136	-0.175
C_S	-0.087	0.096	-0.151
C_T	-0.130	-0.137	-0.207
H_{CR}	0.152	0.244	0.241
H_{CW}	0.152	0.232	0.227
H_1	0.094	0.076	0.130
H_C	0.043	-0.038	0.082

Table 14. Three sets of charges used for the Dissolve model for $[P_{666,14}][NTf_2]$.

Atom type	Charge CLP	Charge ESP	Charge LPG
P_4	0.491	0.485	1.944
C_{1P}	-0.224	-0.111	-0.624
C_S	-0.087	0.089	-0.153
C_T	-0.13	-0.107	-0.208
C_2	0.007	0.171	-0.136
H_C	0.043	-0.028	0.08
H_1	0.094	0.045	0.138

Figure 68-Figure 70 show the comparisons of experimental and simulated total structure factors, *F(R),* and the corresponding Fourier transforms to real space, *G(r),* for the three ionic liquids, with the three sets of potential charges applied. The quality of fit to the experimental data and the comparisons of fits between the three sets of charges are very similar. The residual *R*-factors are also very close, and at least of the order of 10^{-4}, which represents an excellent agreement between the three models and the experiment.

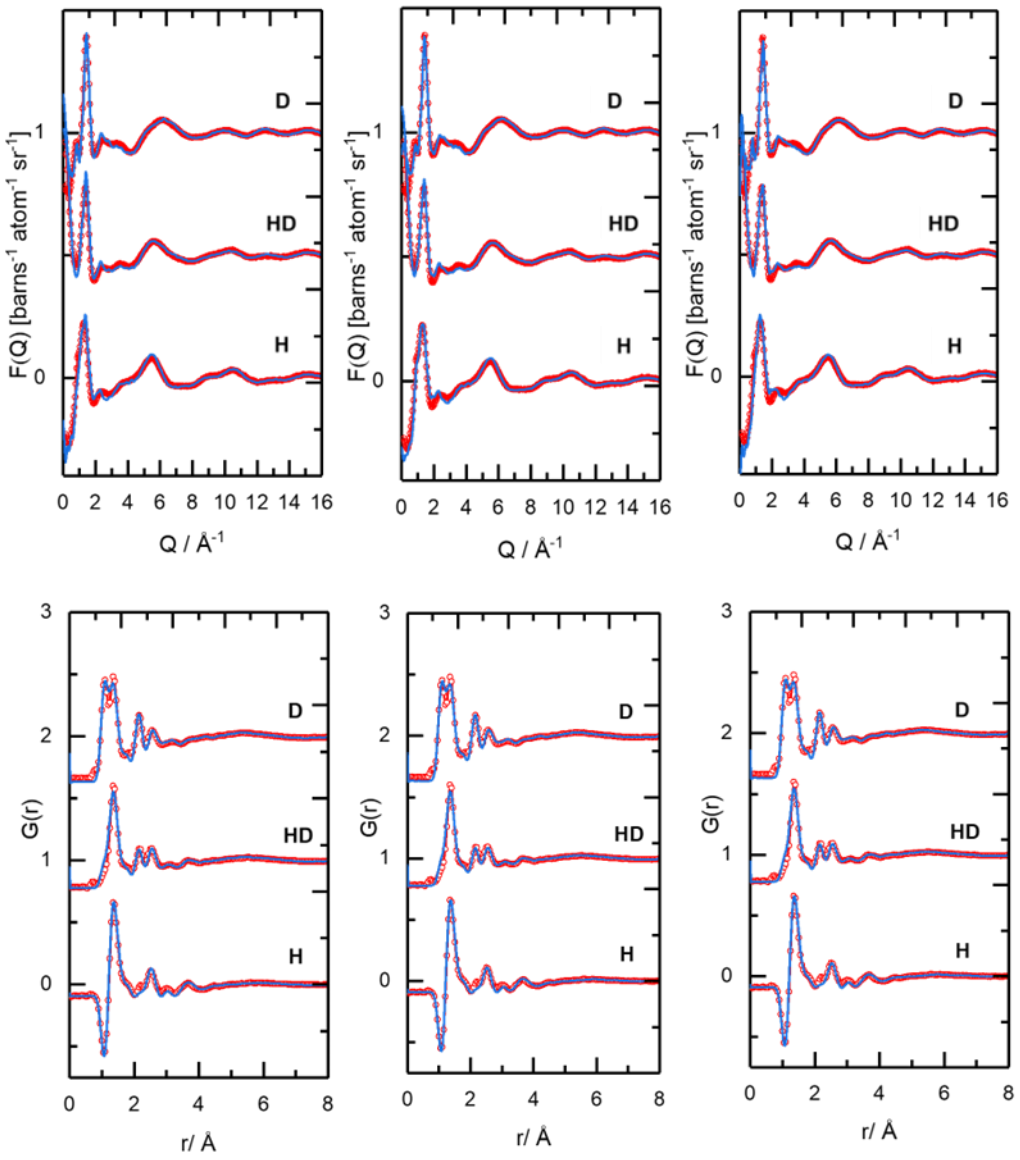

Figure 68. Total structure factors F(Q) (top), and the corresponding Fourier transform to real space G(r) radial distribution functions (bottom) showing experimental data (red symbols) and Dissolve modelled (blue solid line) for [C_2mim][NTf_2] for left: CLP charges, middle: ESP charges and right: LPG charges sets.

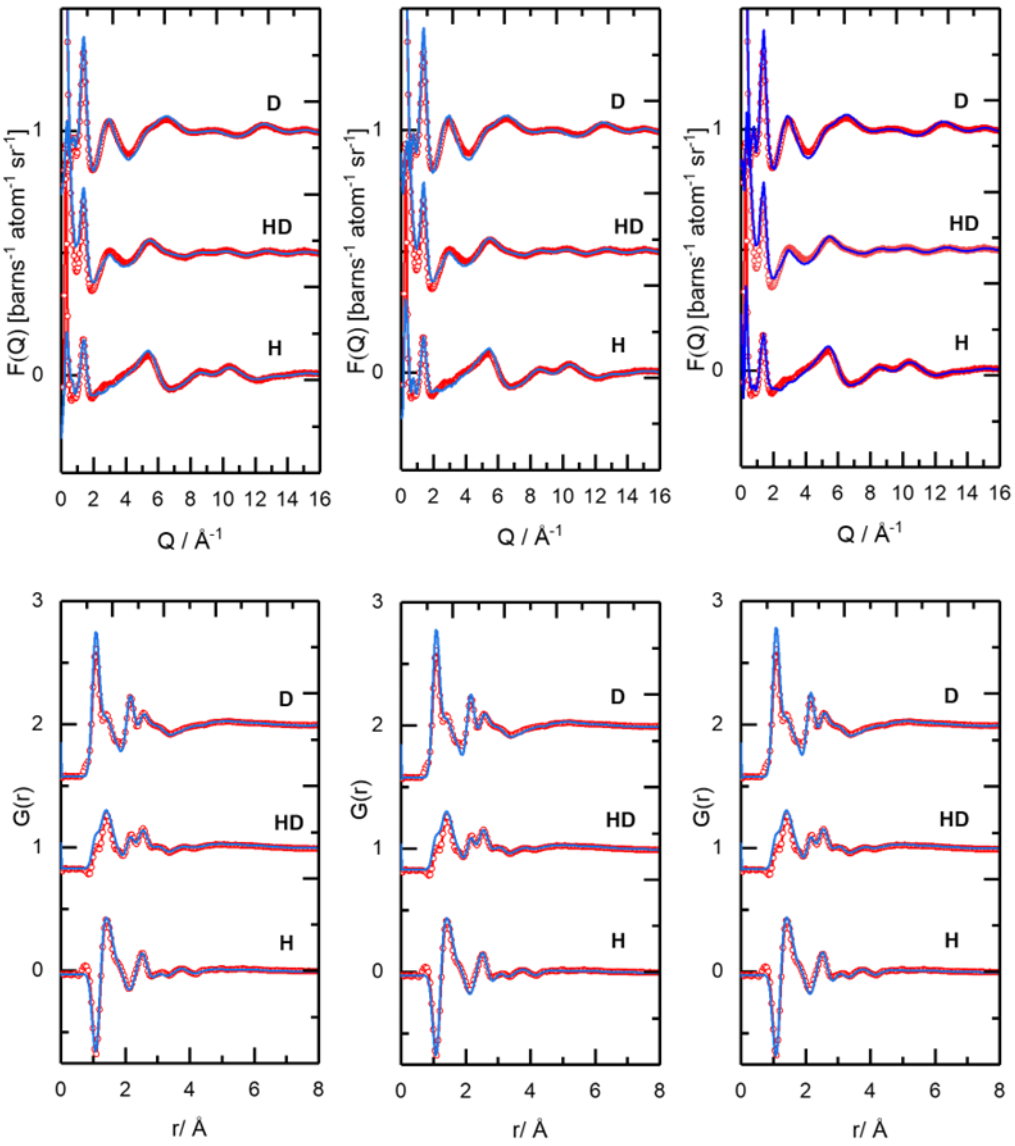

Figure 69. Total structure factors F(Q) (top), and the corresponding Fourier transform to real space G(r) radial distribution functions (bottom) showing experimental data (red symbols) and Dissolve modelled (blue solid line) for $[C_{10}mim][NTf_2]$ for left: CLP charges, middle: ESP charges and right: LPG charges sets.

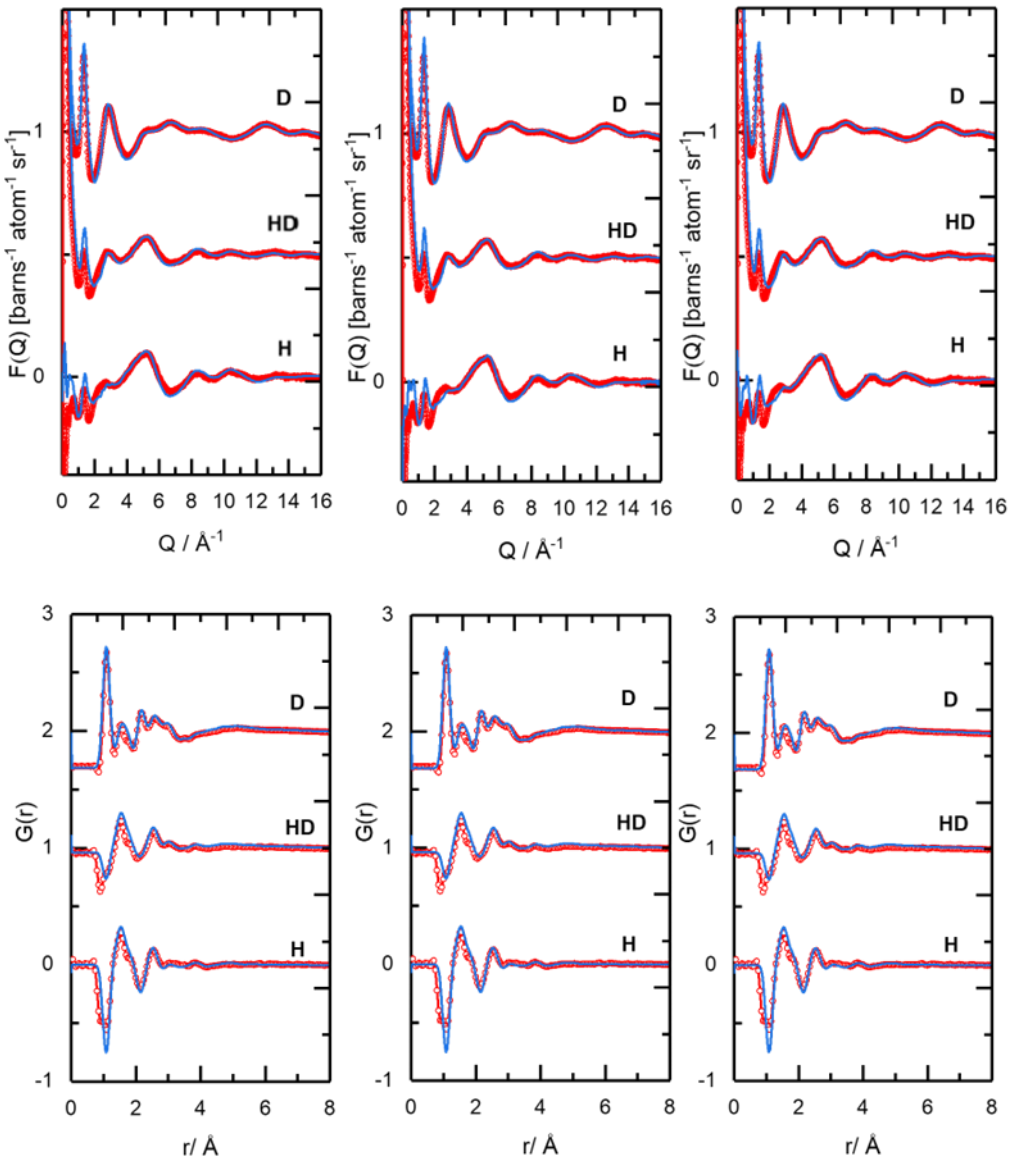

Figure 70. Total structure factors F(Q) (top), and the corresponding Fourier transform to real space G(r) radial distribution functions (bottom) showing experimental data (red symbols) and Dissolve modelled (blue solid line) for $[P_{666,14}][NTf_2]$ for left: CLP charges, middle: ESP charges and right: LPG charges sets.

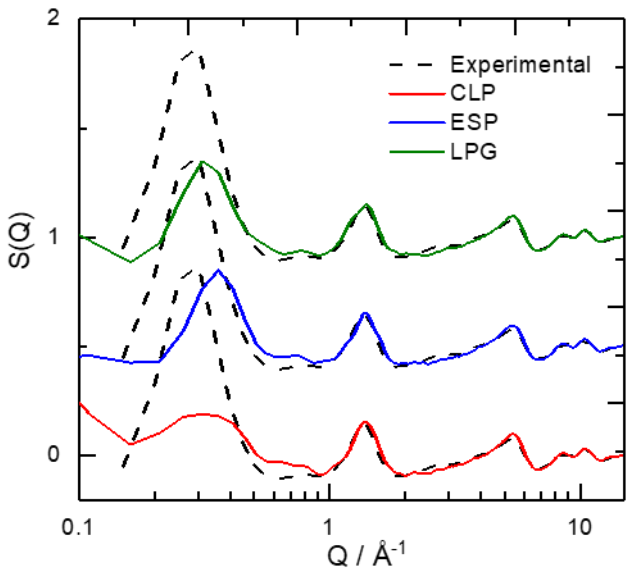

Figure 71. Comparisons between experiment and simulations of the neutron scattering structure function S(Q) for the fully protiated $[C_{10}mim][NTf_2]$ for the three charges sets. CLP charges (red line), ESP charges (blue line) and LPG charges (green line) with the experimental (dashed line). Differences occur between experimental and calculated values for each of the three charges sets at $Q < 1$ Å^{-1}.

Figure 71 shows the neutron scattering structure function S(Q) for the fully protiated $[C_{10}mim][NTf_2]$, taken from the refinement of the three data sets used in the simulation, and shows comparisons between experiment and simulated data using the three charges sets. The first peak at $Q < 1$ Å^{-1} is the "pre-peak" which corresponds to polar-apolar alternation in long chain ionic liquids. The simulation tries to capture this peak but does not match the intensity of the experimental peak and the position in *Q* is wrong. This is more evident for the ESP and LPG charges, although this is probably due to the broader peak observed for CLP charges. The current methodology doesn't match up well for the pre-peak, which has also been observed with EPSR,[40] and it might be beyond the capability of the empirical potential to do it within the constraints of the forcefield. Figure 71 highlights small differences between the charges sets. The pre-peak observed in the experimental is quite intense. It has been shown the intensity of the pre-peak increases with increasing alkyl chain length.[40] This pre-peak is not observed for $[C_2mim][NTf_2]$ which is as expected given its short alkyl chain. The peak was also not observed experimentally for $[C_2mim][OAc]$ by neutron diffraction.[45] For $[P_{666,14}][NTf_2]$, one would expect to observe the pre-peak due to the long alkyl chains. However, another situation can occur which is the cancellation of peaks and anti-peaks at the same *Q* value. In this case, polar-polar and apolar-apolar densities contribute to the pre-peak and polar-apolar densities contribute to the anti-peak.[37] The symmetry of $[P_{666,14}][NTf_2]$ has probably led to the cancellation of these peaks. It is worth noting that the pre-peak has been observed in X-ray scattering studies of $[P_{666,14}][NTf_2]$.[31,60,66] This could be due to the different atomic scattering contrasts in X-ray diffraction.

3.3.3.6 Centre of mass radial distribution functions using different cation charges

The RDFs for the three main interactions of cation-anion, anion-anion and cation-cation are shown in Figure 72 for each of the three sets of charges, for the three ILs. The cation-anion RDFs are similar across the three sets of charges, with a peak centred on 6 Å and a first minimum at 9 Å. The only difference, which is consistent across all three ILs, arises from the double peak for the first-shell correlation around 5 and 6 Å, which has been attributed earlier to *cis* and *trans* $[NTf_2]^-$ conformers.[188,185,190,186] The peak at 5 Å is more pronounced with ESP (blue line in Figure 72) and LPG charges (red line in Figure 72) for all three ILs. The first shell cation-anion coordination numbers are in good agreement across the three charges sets for all ILs.

The anion-anion RDFs are similar upon changing cation atomic charges for both $[C_2mim][NTf_2]$ and $[P_{666,14}][NTf_2]$. They are also very similar for $[C_{10}mim][NTf_2]$, but the use of LPG charges resulted in a slight shift in the peak maximum from 9 to 10 Å, and a shoulder preceding the peak, which is not observed with the two other charge sets.

The cation-cation RDFs for $[C_2mim][NTf_2]$ are also very similar, all three models returning broad peaks between 7 and 10 Å, and a minimum at 13 Å. The most obvious difference is the shoulder at 4 Å for LPG charges. Again, the profiles are very similar for $[C_{10}mim][NTf_2]$, with just a slight shift in the peak maximum with the CLP charges. For $[P_{666,14}][NTf_2]$, the peak maximum is consistent across the three charges sets, but a more defined shoulder preceding this peak is observed with the ESP and LPG charges compared to CLP charges. Upon changing the cation atomic charges, similar profiles are generated across the three interactions for all the ILs. Despite minor differences, all three potential charges gave convergent results, which confirms robustness of the Dissolve analysis.

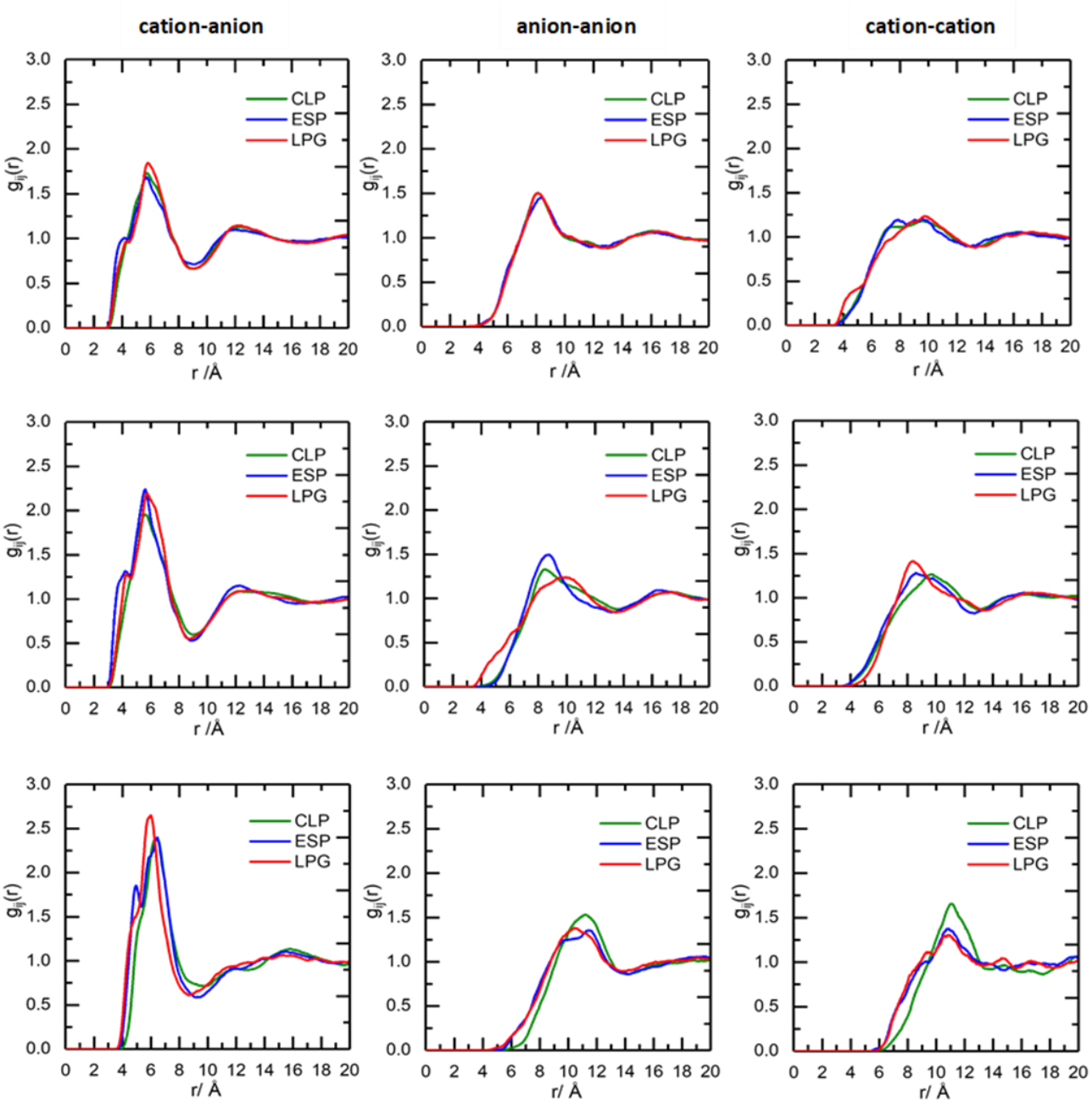

Figure 72. Radial distribution functions for top: $[C_2mim][NTf_2]$ middle: $[C_{10}mim][NTf_2]$ and bottom: $[P_{666,14}][NTf_2]$ for interactions between cation-anion (left), anion-anion (middle) and cation-cation (right) for CLP charges (green line), ESP (blue line) and LPG (red line).

3.3.3.7 *Cis*/*trans* behaviour of $[NTf_2]^-$ anion using different cation charges

The $[NTf_2]^-$ anion can adopt both *cis* and *trans* orientations in the liquid state (Figure 38). The *cis*/trans ratio is commonly obtained from the distribution of $CF_3\cdots CF_3$ distance, which was determined for each IL across the

three different charges sets (Figure 73). An intramolecular $CF_3\cdots CF_3$ distance is 4.2 Å for the *cis* orientation, and 5.2 Å for the *trans* orientation. It has been found that there is greater distribution of the *trans* conformer, in all three ILs, in agreement with both computational and experimental studies on $[NTf_2]^-$ ILs.[237,190,46] The preference for the *trans* conformer can be explained due to the greater availability of this orientation to form hydrogen bonds and the reduction of steric repulsion.

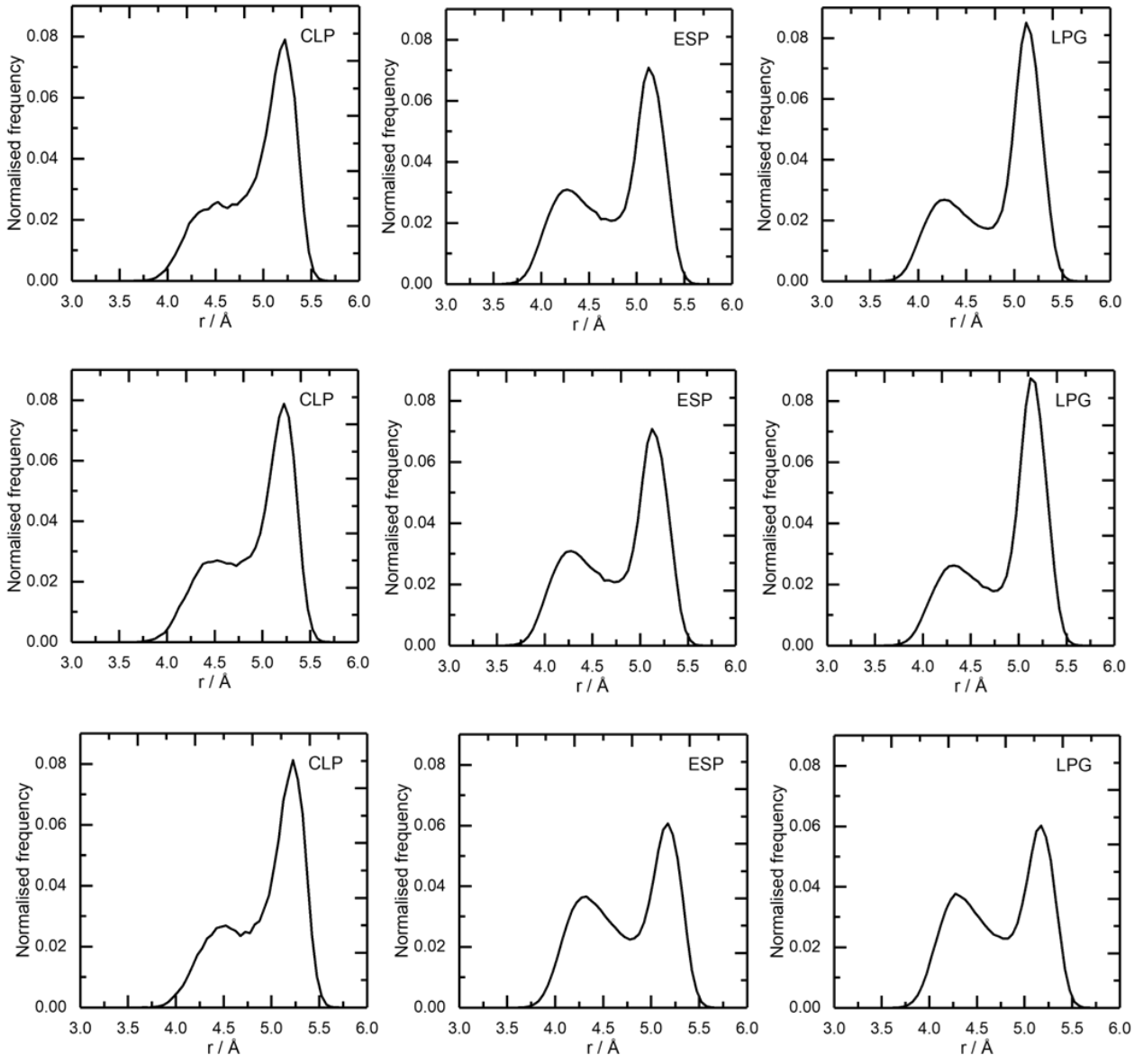

Figure 73. Distribution of the $CF_3\cdots CF_3$ distances in the bis(trifluoromethanesulfonyl)amide anion, showing the *cis* and *trans* configurations in $[C_2mim][NTf_2]$ (top), $[C_{10}mim][NTf_2]$ (middle) and $[P_{666,14}][NTf_2]$ (bottom) for the three sets of charges.

3.4 Conclusions and Outlook

The goal of this work was to facilitate the study of ionic liquids with long alkyl chains, in particular quaternary phosphonium systems, by neutron scattering. To overcome the first experimental barrier, that of availability of perdeuteriated ILs, a detailed procedure for the synthesis of fully deuteriated $[P_{666,14}][NTf_2]$ is reported. This will hopefully enable enhanced neutron scattering studies of tetraalkylphosphonium ionic liquids. It can be expanded very easily to other anions, and easily adopted to many different phosphonium cations. In addition to $[C_2mim][NTf_2]$, the structure of two ionic liquids with long alkyl chains, $[C_{10}mim][NTf_2]$ and $[P_{666,14}][NTf_2]$, has been resolved for the first time using neutron scattering, enabled by the new Dissolve data analysis package. Finally, robustness of the Dissolve approach has been demonstrated by generating three independent models for each of the three ionic liquids, starting from three different potential sets for cations, and reaching convergent results for each IL, across the three models.

Analysis of the neutron scattering data showed that $[C_{10}mim][NTf_2]$ and $[P_{666,14}][NTf_2]$ exhibit substantial nanosegregation compared to $[C_2mim][NTf_2]$, induced by the presence of long alkyl chains. It has been demonstrated that protons on the imidazolium ring in $[C_2mim][NTf_2]$ and $[C_{10}mim][NTf_2]$, as well as H-C-P protons in $[P_{666,14}][NTf_2]$ participate in hydrogen bonding, with oxygen and nitrogen atoms in the $[NTf_2]^-$ anion acting as hydrogen bond acceptors, with the dominant interaction to the oxygen. From bond distance and angle analysis, it was evident that bulkier cations promote more linear hydrogen bonds, and that hydrogen bonding to oxygen is more directional that that to nitrogen.

In the future, it is hoped that this work will open up the study of ILs with long alkyl chains by neutron scattering. It would be most valuable to accomplish the study of liquid-liquid phase transitions in phosphonium ILs, omitting the problem of enhanced propensity to crystallise. Such study would give unique insight into less common phase changes, not only in IL but in the broader field of soft matter studies.

Chapter 4

Structure of frustrated Lewis pairs in ionic liquids

4 Structure of frustrated Lewis pairs in ionic liquids

The work presented in this chapter builds on the earlier work in the Swadźba-Kwaśny group, which reported experimental evidence for the FLP weakly associated encounter complex, formed by tri(tert-butyl)phosphine ($P(^tBu)_3$ and tris(pentafluorophenyl)borane (BCF) in benzene.[184] The structure of this encounter complex was studied using neutron scattering, although it has been found too transient to be observable by NMR spectroscopy. Furthermore, the group found that the same encounter complex (association of the Lewis acid and the Lewis base through weak forces) was more robust in an ionic liquid, $[C_{10}mim][NTf_2]$, and could be observed by NMR spectroscopy. Unfortunately, neutron scattering data recorded for $P(^tBu)_3$/BCF in $[C_{10}mim][NTf_2]$ could not then be processed, due to EPSR modelling limitations.

In this work, neutron scattering data of the FLP in $[C_{10}mim][NTf_2]$ was modelled using Dissolve. The same FLP has been also studied in $[C_2mim][NTf_2]$, to investigate the effect of alkyl chain length on encounter complex formation. This was inspired by computational studies reporting that FLP encounter complexes are most stable in ionic liquids with long alkyl chains (*i.e*. large non-polar domains). The extracted data is discussed, and the challenges of modelling this data, as well as limitations of available analytical tools, are outlined.

Neutron scattering data for the FLP in benzene and in $[C_{10}mim][NTf_2]$ were recorded by Dr Lucy Brown. Neutron scattering data for the FLP in $[C_2mim][NTf_2]$, and Dissolve analysis of all three systems, were conducted as part of the work for this thesis.

4.1 Introduction to frustrated Lewis pairs

Early studies of sterically hindered Lewis acids and bases by Brown and Wittig (1940s and 1950s) revealed that steric interference can prevent the Lewis adduct formation.[242] However, it was not until 2006 that Stephan and co-workers uncovered the exceptional reactivity of these resulting complexes and later named them '*Frustrated Lewis Pairs'*. They demonstrated that a metal-free system consisting of an unquenched phosphorus Lewis base and boron Lewis acid could reversibly activate H_2 (Scheme 7).[243]

Scheme 7. The first FLP activation of H_2 reported by Stephan *et. al* in 2006.[243]

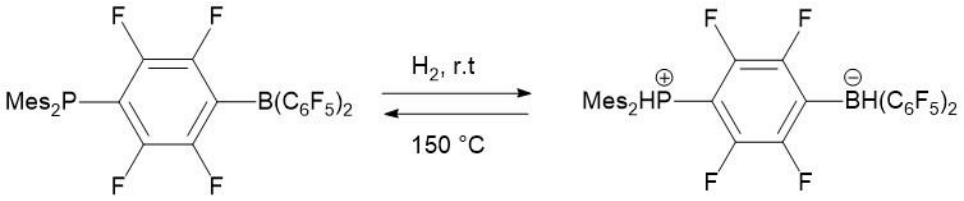

Stephan and co-workers then went on to show that this reactivity could be extended to combinations of sterically bulky phosphines and BCF which gave an intermolecular FLP system.[244] The intermolecular FLPs studied were tri-tert-butyl phosphine and tri-mesityl phosphine with BCF which are still very widely used today. These intermolecular FLPs allowed Stephan to show the lack of adduct formation with NMR spectroscopy, even at temperatures as low as -50 °C. On exposure of these mixtures to H_2, the formation of the salt could be observed by ^{1}H NMR. These publications marked the rapid development of FLP chemistry and inspired metal free approaches to catalytic reactions that were once only sustained by transition metals. These reactions include the capture of small molecules such as CO_2,[245] SO_2[246] and N_2O,[247] as well as the hydrogenation of several unsaturated organic substrates,[248–250] and activation of C-H bonds.[251]

4.1.1 Mechanism of FLP reactivity

The mechanism by which FLPs activate hydrogen has been widely discussed. By analogy to transition metal chemistry, Stephan and co-workers first proposed in 2006 that H_2 could react with the Lewis acid in a side-on fashion.[243] However, in a subsequent study they did not observe the formation of $(C_6F_5)B\cdots H_2$ species by NMR and later Papai and co-workers[252] used calculations to show that this interaction is unfavourable due to Pauli repulsion. Another scenario, where H_2 interacts with $P(^tBu)_3$ was also explored but this was also computed to be repulsive. Therefore, it was suggested that pre-organised acid–base encounter complexes must be present in solution, with a reactive pocket that can accommodate a small molecule such as H_2 and subsequently activate it. Papai then went on to identify a weakly associated $[(^tBu)_3P]\cdots[B(C_6F_5)_3]$ complex as a minimum on the potential energy surface, using DFT calculations.[252] The association energy was predicted to be ΔE = 4.18 kJ mol^{-1}, stabilised by weak dispersion interactions. From this work, the electron transfer (ET) model was proposed as the mechanism for activation of dihydrogen by FLPs (Figure 74). This cooperative action of the Lewis acid and base is not dissimilar to the reactivity of transition metals, which can simultaneously donate and accept electron density to and from a substrate. In FLPs, the Lewis base donates into the σ^* orbital of the H_2 molecule, while the Lewis acid accepts electron density from the σ orbital. An alternative electric field (EF)

model was also proposed by Grimme *et. al.,*[253] who suggested a simpler approach to H_2 activation (Figure 74). Like the ET model, they also assumed a pre-organised encounter complex, held together by weak dispersion interactions but that the role of the encounter complex was to generate an electric field which causes polarisation of the H-H bond, which was then cleaved, without overcoming additional energy barriers. However, in 2013, Rokob and colleagues explored these two mechanisms further using a set of six inter- and intramolecular FLP systems and DFT calculations.[254] They concluded that electron transfer *via* orbital overlap contributes more significantly to the cleavage of the dihydrogen bond compared to electric field effects. Since that publication, the electron transfer model has been widely accepted over the electric field model.

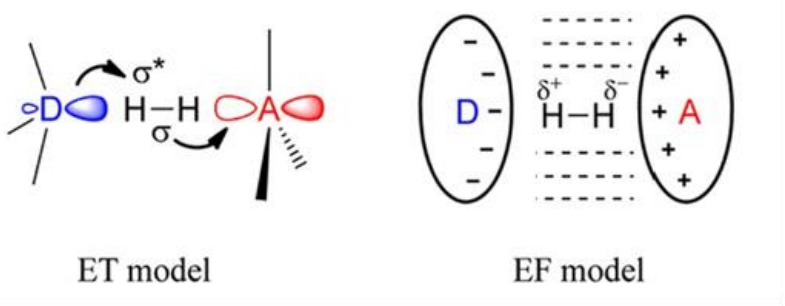

Figure 74. Electron transfer model (left) and electric field model (right) for hydrogen activation by frustrated Lewis pairs.[254]

Vankova *et. al.*[255] further provided evidence of the encounter complex in a computational study that estimated the average energy of formation across a range of systems studied to be ΔE_{form} = -42 kJ mol^{-1}, with the addition of solvent not contributing any significant changes. However, the favourable electronic interactions in the FLP are opposed by the decrease in entropy, and the formation of the encounter complex is slightly endergonic which agrees with the difficulty in observing these FLP encounter complexes experimentally at ambient conditions.

Papai and colleagues then moved on from static computational models and investigated the encounter complex of P(^{t}Bu)$_3$/BCF in toluene using molecular dynamics (MD) simulations.[256] They constructed a Helmholtz free energy curve (Figure 75) which showed that association through partial P–B dative bonding of distances less than 4.2 Å were unfavoured due to decreased conformational freedom. The energy of configurations with P···B distances in the region of 4.2-5.6 Å, were found at around 1.2 kcal mol^{-1} above the dissociation limit. Only a very low concentration, about 2% of the total amount of phosphine and borane in the system were found in the associated state, with distances less than 6 Å. Instead, it is more likely to find B···P correlations at larger distances, for example around 6.5 Å which correspond to solvated B/P pairs and around 8 Å which corresponds to solvent separated B/P pairs.

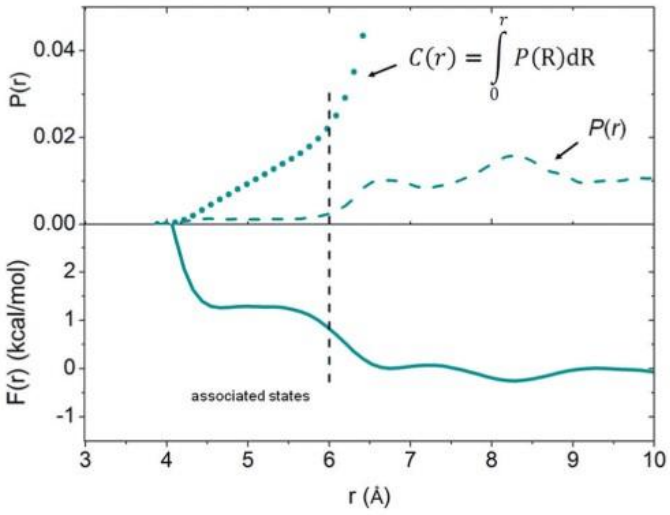

Figure 75. Free energy curve, F(r) and probability distribution, P(r), from MD simulations of $P(^tBu)_3$ and BCF in toluene.[256]

4.1.2 Experimental evidence of the encounter complex

Interactions between FLP components, dissolved in organic solvents, have not been observed by conventional 1D NMR spectroscopy, probably due to the weak stabilisation of the encounter complex and low concentrations in solution.[244,257] The first experimental evidence of the encounter complex in FLP solutions came from Rocchigiani *et. al.*[257] who used $^{19}F,^{1}H$ HOESY (Heteronuclear Overhauser Enhancement Spectroscopy) NMR to probe the association of $P(^tBu)_3$/BCF and $PMes_3$/BCF in toluene or benzene and observed clear cross-peaks corresponding to H/F interactions (Figure 76). They describe small shifts of the ^{19}F NMR resonances in comparison to the free borane when an excess of the phosphine is used, and no changes in the ^{1}H or ^{31}P NMR spectra. They also showed that the phosphine and borane had no preferred orientation, which is consistent with the association being driven *via* weak H/F intermolecular interactions. They also used diffusion ^{1}H and ^{19}F NMR spectroscopy to quantify the tendency of the phosphine and borane to associate and reported that the process is slightly endergonic (ΔG° = +0.4 ± 0.2 kcal mol^{-1}), consistent with previously discussed computational data.[256]

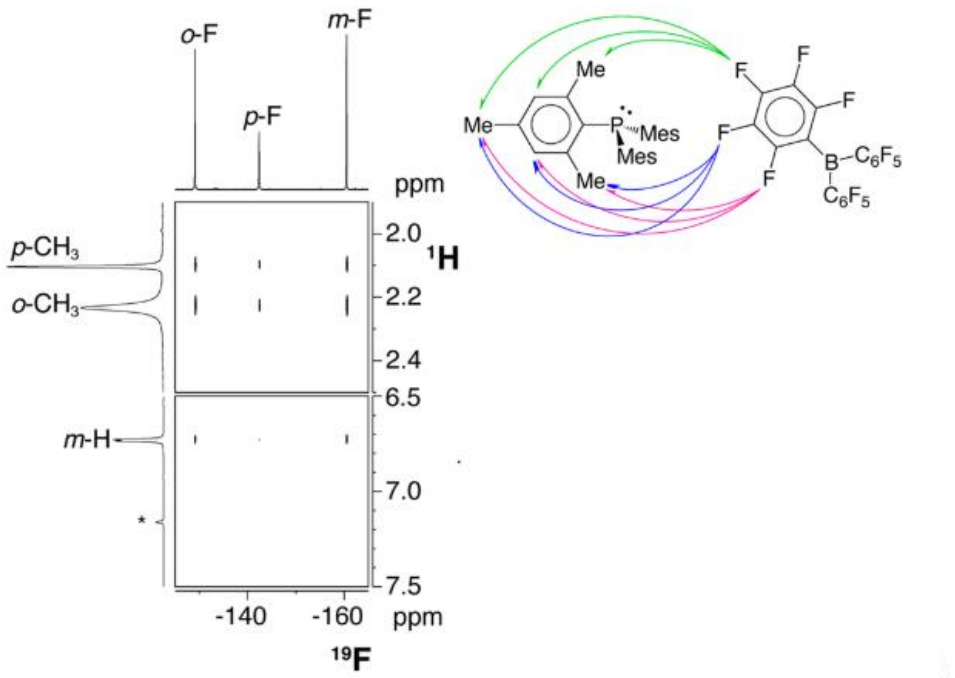

Figure 76. $^{19}F,^{1}H$ HOESY NMR spectrum of $PMes_3$/BCF in benzene-d_6, showing cross-peaks arising from H/F interactions.[257]

The work presented in this thesis was motivated by and is a continuation of previous work in the Swadźba-Kwaśny group which showed experimental evidence of the encounter complex, $P(^tBu)_3$/BCF in benzene by neutron scattering and in an ionic liquid, $[C_{10}mim][NTf_2]$ by NMR spectroscopy. The presence of new peaks in the ^{19}F and ^{31}P NMR spectra when the FLP is dissolved in the ionic liquid, compared to when the individual components are dissolved was reported, which strongly suggest interaction between the FLP components. Importantly, this was not observed for the FLP in benzene. It was reported that approximately 24% of the BCF is in a new environment upon contact with $P(^tBu)_3$ in the ionic liquid and 78% of the phosphine also experienced a change in the electronic environment. While it is difficult to make definitive assignments of these new signals, they could suggest interaction between the FLP components, which are greater stabilised in the ionic liquid compared to benzene.

Evidence of the encounter complex in benzene was verified by neutron scattering experiments, by extracting the P···B pair distribution function (Figure 77).[184] Equimolar solutions in benzene at 160 mmol concentration were studied, which is equivalent to a 1 : 1 : 70 molar ratio of $P(^tBu)_3$: BCF : benzene. This was at the maximum possible borane concentration and while higher than catalytic concentrations of FLP, this is still quite a low concentration for neutron scattering detection. This accounts for the poor resolution for the P···B interaction. Despite this, valuable data could be extracted which showed that at P···B separation distances of 5.7 Å, there

was less than 1% chance of correlation, suggesting that there is no interaction between the FLP components at this distance. This value then increased to ~5% when the distance was extended out to 8 Å. These findings support the weak interactions and low concentrations of the encounter complex in solution and is consistent with the previous studies discussed. Combining the NMR and neutron scattering study, it seems that the concentration of effective FLPs is enhanced substantially in the ionic liquid compared to benzene. In contrast to benzene, the encounter complex in an ionic liquid, $[C_{10}mim][NTf_2]$, could be detected by NMR, suggesting greater stabilisation of the complex, leading to higher concentration and longer lifetime. Indeed, NMR signals showed that over 20% of the FLP components were associated at any one time compared to 5% in benzene from neutron scattering. Importantly, this work also showed that neutron scattering can be used as a technique for directly observing the encounter complex. Further work needs to be done to explicitly verify the presence of the encounter complex. In this thesis, the focus is on interpretation of neutron scattering data recorded for the FLP in $[C_{10}mim][NTf_2]$ which the release of Dissolve[94] had allowed to be modelled. The FLP in $[C_2mim][NTf_2]$ is also modelled to further investigate the formation of the encounter complex and investigate the effect of alkyl chain length.

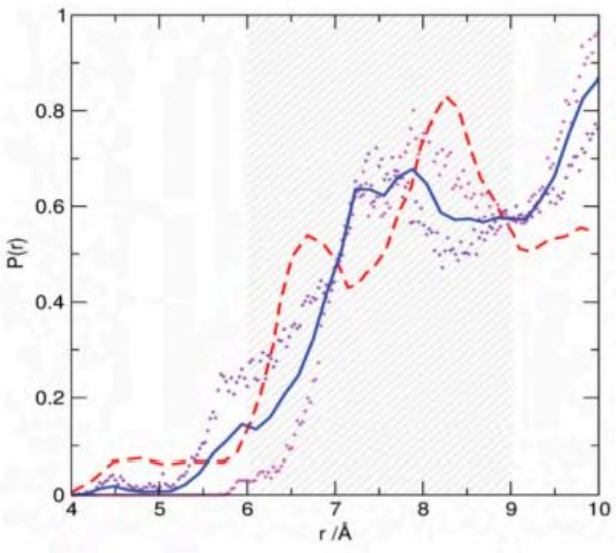

Figure 77. The plot of the P···B pair distribution function (blue) between $P(^tBu)_3$ and BCF in benzene (1:1:70), averaged from two independent data-driven simulation models (purple and magenta data points), and compared to the equivalent correlation from DFT simulation[256] of $P(^tBu)_3$ and BCF in toluene (red line). Correlation distances corresponding to the range of 'solvent separated' pairs (6–9 Å) are indicated by the shaded region.

Following on from the publication from our group, Liu and co-workers explored computationally the $P(^tBu)_3$/BCF FLP in toluene and in range of ionic liquids, including $[C_{10}mim][NTf_2]$.[258] The results confirmed that the concentration of encounter complexes is low in all the studied solvents but did increase with ionic liquids

compared to toluene. Approximately 2% of the FLPs were found in the associated state at distances below 6 Å in toluene versus 5% in $[C_{10}mim][NTf_2]$, which increased to 20% when the distance range was extended to 7 Å, in line with our previous study. They also found that with increasing the alkyl chain length of the ILs, the higher the concentration of the encounter complex. The authors proposed that the encounter complex can sit in the large cavities formed by the ionic liquid, whereas toluene molecules can come in between and separate the acid and base.

The increase in direct evidence of the encounter complex formation came from the recent discovery of frustrated radical pairs.[259–262] Certain FLPs such as $P(Mes)_3$/BCF can absorb a photon to promote single-electron transfer (SET) and generate a radical pair, confirmed by electron paramagnetic resonance (EPR) spectroscopy, by Stephan and co-workers in 2017.[262] A mixture of $P(Mes)_3$ and BCF in toluene gives rise to a violet solution, which was attributed to the formation of the $[P(Mes)_3]^{\bullet+}$ radical cation.[262] However, in 2020 Slootweg and colleagues[263] stated that the colour was more likely due to a charge-transfer band, where the P/B encounter complex can absorb a photon in the visible region and promote the electronic transition, rather than internal electronic transitions of the $[P(Mes)_3]^{\bullet+}$ radical. This was supported by DFT studies and the appearance of a new band in the UV-Vis spectra of the solution at 534 nm (Figure 78a). Confirmation that absorption of this band led to radical formation came from both EPR and transient absorption spectroscopy (Figure 78b and Figure 78c). Irradiation of the complex with visible light verified SET, with the presence of strong signals in the EPR spectrum corresponding to radical formation. These signals were not present when the experiment was performed in the dark. Transient absorption spectroscopy showed that the radical pair was short-lived, with a lifetime of 237 ps. They were also able to confirm the existence of a charge-transfer band for the FLP $P(^tBu)_3$/BCF. Upon irradiation of the new absorption band, characteristic signals of radical pair formation were present in the EPR spectrum and transient absorption spectroscopy recorded a lifetime of only 6 ps. These findings motivated Ando and co-workers[264] to use resonance Raman spectroscopy to further study the charge transfer in $P(Mes)_3$/BCF. They showed that multiple vibrational modes were enhanced in the spectrum of the FLP in dichloromethane. These modes belonged to both the phosphine and borane, which further confirms the association of the two components and the charge transfer. This discovery of frustrated radical pairs, verified by EPR and transient absorption spectroscopy, has enabled the encounter complex formation to be studied by UV-Vis and resonance Raman spectroscopy.

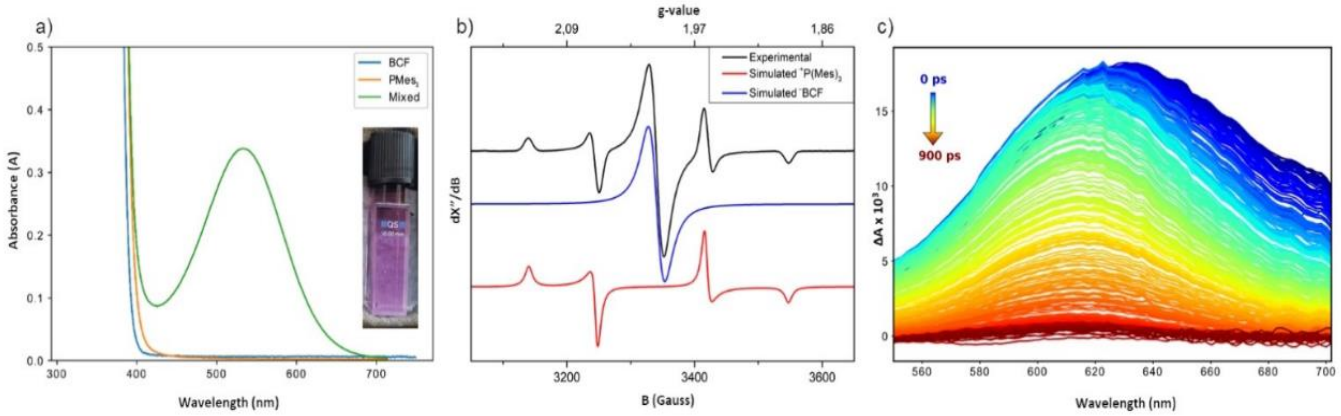

Figure 78. SET processes showing evidence of encounter complex formation of $P(Mes)_3$/BCF: (a) UV-Vis spectrum of $P(Mes)_3$/BCF in toluene compared to spectra of the separate components; (b) experimental EPR spectrum of $P(Mes)_3$/BCF in toluene measured at 30 K during irradiation with visible light (390–500 nm) and simulated spectra of $[P(Mes)_3]^{\bullet+}$ and $[BCF]^{\bullet-}$; (c) transient absorption spectra measured after pulsed excitation of $P(Mes)_3$/BCF with 530 nm light.[263]

In this work, the $P(^tBu)_3$/BCF encounter complex in benzene and two ILs was investigated by neutron scattering studies and modelled using Dissolve. The aim was to find corroborating experimental proof that IL environments promote the formation of encounter complexes. The extracted data is discussed, and the challenges of modelling this data, as well as limitations of available analytical tools, are outlined.

4.2 Experimental

4.2.1 General

All manipulations were performed in a nitrogen-filled MBraun glovebox with a high capacity recirculator (< 1 ppm of O_2 and H_2O). Tris(tert-butyl)phosphine was purchased from Sigma-Aldrich and used as received. The synthesis of deuteriated tris(tert-butyl)phosphine can be found from a recent publication.[222] $B(C_6F_5)_3$ was obtained from Fluorochem and purified by vacuum sublimation. $[C_{10}mim][NTf_2]$ and $[C_2mim][NTf_2]$ were dried in vacuo at 65 °C, and moisture content by Karl-Fisher was under the detection limit. Deuteriated $[C_2mim][NTf_2]$ and $[C_{10}mim][NTf_2]$ were provided from D-lab at ISIS Neutron and Muon source. NMR spectra were recorded on a Bruker Avance DPX 400 MHz spectrometer.

4.2.2 BCF and tris(tert-butyl)phosphine in [C_2mim][NTf_2]

In a nitrogen filled MBraun glovebox a mixture of BCF and tris(tert-butyl)phosphine in [C_2mim][NTf_2] at a concentration of 160 mmol was transferred into a flame dried Norell IPV valved NMR sample tube for intermediate pressure with a DMSO-d_6 filled, sealed capillary as an external lock.

4.2.3 Neutron scattering experiments

Neutron scattering data were collected from equimolar solutions of P(^{t}Bu)$_3$/BCF in benzene, [C_2mim][NTf_2] and [C_{10}mim][NTf_2] at 160 mmol concentration, using the SANDALS spectrometer at the ISIS Pulsed Neutron and Muon Source at Rutherford Appleton Laboratory, Oxfordshire, UK. Table 15 lists the 25 samples that data was collected for and analysed using Dissolve software. The forcefield parameters for the ionic liquids were taken from the Canongia Lopes & Padua (CL&P) force field.[215] For benzene, the OPLS-AA forcefield[95] was used. Parameters for P(^{t}Bu)$_3$ were generated from the LigParGen service offered by the Jorgensen group.[178–180] For BCF, the universal forcefield (UFF)[265] was applied with electrostatic potential (ESP) charges calculated with the NWChem software. The simulation box sizes and the corresponding experimentally determined molecular densities of the mixtures are shown in Table 16.

Table 15. Samples of FLP solutions in selected solvents, with levels of H/D substitution.

Sample number	Solution	P(^{t}Bu)$_3$	Solvent
1	BCF:benzene	-	H
2		-	H/D
3		-	D
4	P(^{t}Bu)$_3$:benzene	H	H
5		H	H/D
6		H	D
7	BCF:[C_2mim][NTf_2]	-	H
8		-	H/D
9		-	D
10	P(^{t}Bu)$_3$:[C_2mim][NTf_2]	H	H

11		H	H/D
12		H	D
13	$P(^tBu)_3$:BCF:benzene	H	H
14		H	H/D
15		H	D
16	$P(^tBu)_3$:BCF:$[C_2mim][NTf_2]$	H	H
17		H	D
18		H	H/D
19		H/D	H
20		H/D	H/D
21		H/D	D
22	$P(^tBu)_3$:BCF:$[C_{10}mim][NTf_2]$	H	H
23		H	H/D
24		H	D
25		D	D

Table 16. Simulation box size parameters.

Solutions	N_i^a	**Box size, n/ Å**	**Number density / atoms Å^{-3}**
BCF:benzene	710 (10:700)	48.21	0.078
$P(^tBu)_3$:benzene	730 (30:700)	48.21	0.076
BCF:$[C_2mim][NTf_2]$	520 (20:500)	48.95	0.078
$P(^tBu)_3$:$[C_2mim][NTf_2]$	520 (20:500)	48.95	0.084
$P(^tBu)_3$:BCF:benzene	720 (10:10:700)	47.81	0.084
$P(^tBu)_3$:BCF:$[C_2mim][NTf_2]$	540 (20:20:500)	49.55	0.082
$P(^tBu)_3$:BCF:$[C_{10}mim][NTf_2]$	560 (30:30:500)	57.45	0.088

4.3 Results and discussion

The experimental design included the study of the FLP P(^{t}Bu)$_3$/BCF in three solvents: benzene, [C_2mim][NTf_2] and [C_{10}mim][NTf_2]. NMR studies reported by Brown *et. al*[266] for the FLP in [C_{10}mim][NTf_2] and benzene showed that were was no evidence of strong interactions between the FLP components and either [C_{10}mim][NTf_2], or benzene. The presence of new peaks in the ^{19}F and ^{31}P NMR spectra when the FLP is dissolved in the ionic liquid, compared to when the individual components are dissolved was reported, which strongly suggest interaction between the FLP components. Importantly, these additional signals were not observed for the FLP solution in benzene, which was in agreement with the literature on FLP chemistry. While it was difficult to make definitive assignments of these new signals, they were understood to report on the interaction between the FLP components, which are greater stabilised in the ionic liquid compared to benzene.

In this work, it was decided to study the FLP encounter complex structure in benzene, [C_2mim][NTf_2] and [C_{10}mim][NTf_2]. For the sake of completeness, NMR studies of the FLP in [C_2mim][NTf_2] were recorded. Firstly, to ensure that there was no interaction between [C_2mim][NTf_2] and the FLP components and secondly, to see if the encounter complex could be observed by NMR spectroscopy in this ionic liquid.

The individual FLP components were separately dissolved in the IL at a concentration of 160 mmol (matching the concentrations used for neutron scattering experiments). The solution of both FLP components in [C_2mim][NTf_2] featured an additional upfield peak at 54 ppm (Δ^{31}P = 9 ppm) in the ^{31}P NMR spectra (Figure 79d). Brown *et. al*.[184] also observed this peak for the FLP in [C_{10}mim][NTf_2] and it was noted that when phosphines form adducts with strong Lewis acids, their ^{31}P NMR signal usually shifts downfield by about Δ^{31}P = +20 ppm.[266] Therefore, in this case where the ^{31}P environment is slightly shielded, rather than deshielded, does not suggest adduct formation, but a different interaction mode. For the ^{19}F NMR spectra of the FLP in [C_{10}mim][NTf_2], Brown *et. al*.[184] showed that in addition to the three peaks corresponding to the *ortho, meta* and *para* environments of BCF, six additional peaks upfield of the three major peaks were also observed. These additional signals may be explained as the BCF entering a weak, but relatively long-lasting interaction with P(^{t}Bu)$_3$, as would be expected for an encounter complex. Surprisingly, the ^{19}F NMR spectra of BCF in [C_2mim][NTf_2] suggests the presence of two different environments of BCF (Figure 79a), which was a reproducible result. Upon addition of P(^{t}Bu)$_3$, only one environment of BCF is observed, and there are no additional peaks (Figure 79c).

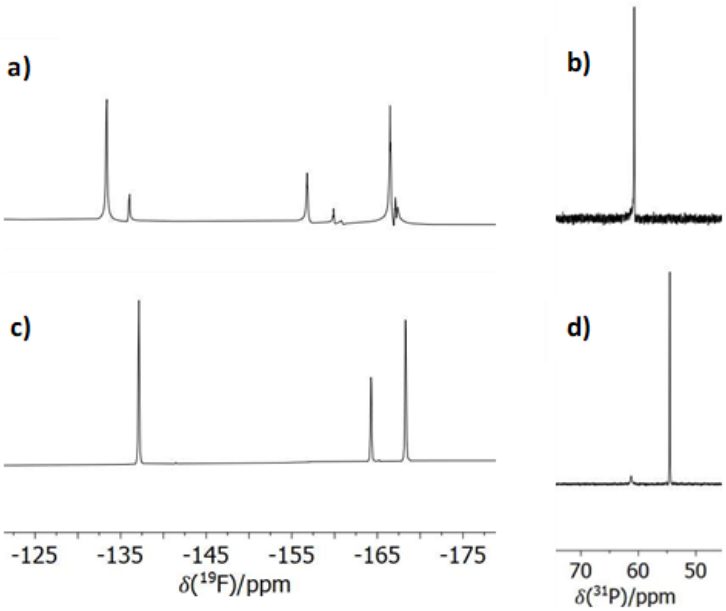

Figure 79. Spectra of the FLP, BCF/P(^{t}Bu)$_3$, and its components, in [C_2mim][NTf_2] (a) ^{19}F NMR spectrum of BCF, (b) ^{31}P NMR spectrum of P(^{t}Bu)$_3$, (c) ^{19}F NMR spectrum of BCF/P(^{t}Bu)$_3$ and (d) ^{31}P NMR spectrum of BCF/P(^{t}Bu)$_3$.

It is recognised that the NMR study of the FLP in the three solvents itself does not provide conclusive evidence for the encounter complex formation. However, the additional peaks featured in the NMR spectra when the FLP mixture is dissolved in the IL, but not when the individual components are dissolved, provide strong evidence for enhanced interaction between FLP components. Interestingly, this is only observed in [C_{10}mim][NTf_2] and in the ^{31}P NMR of [C_2mim][NTf_2], but not in benzene.

Motivated by the NMR spectroscopic study, Dissolve was employed to model the neutron scattering results of the FLP in the three solvents to gain further insight into the encounter complex formation.

4.3.1 Neutron scattering study

The FLP in benzene had been modelled previously in the group[184] using EPSR. In this work, the same system has been modelled using Dissolve for validation purposes, to ensure coherent outcomes from both models. This was followed by Dissolve simulations of neutron scattering data recorded for the FLP solutions in the two ILs. The concentration of the FLP was 160 mmol, aligned to that used previously in the benzene studies.

Data sets of the FLP BCF/P(^{t}Bu)$_3$ in benzene, [C_2mim][NTf_2] and [C_{10}mim][NTf_2] were recorded. As well as the individual FLP components in benzene and [C_2mim][NTf_2] (Table 15). Ideally, more experimental data sets with the deuteriated phosphine would have been collected (in particular for the FLP in the three solvents), but due

to the difficult synthesis with low yields, even combined efforts of our group and ISIS deuteriation lab gave insufficient quantity for the ideal data set. Notably, a batch of the phosphine perished in the fire of the D-lab, which enforced a decision to proceed with the quantity of phosphine available to the team at allocated beamtime.

Nevertheless, the samples listed in Table 15 give sufficient isotopic contrast for the experiment. The atom types used in the Dissolve simulation model are shown in Figure 80.

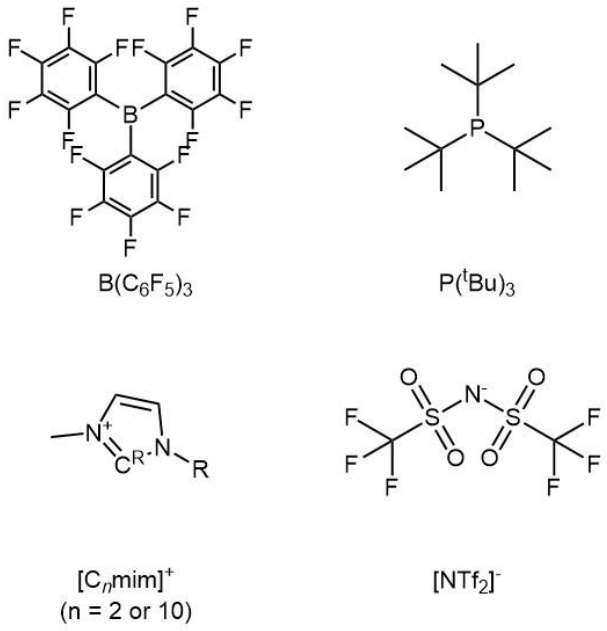

Figure 80. Atom types used in the Dissolve simulation model.

4.3.1.1 EPSR modelling and fit to experimental data

Firstly, the interactions between the individual FLP components in benzene and $[C_2mim][NTf_2]$ were studied (Table 15 - samples 1-12); this also allowed for comparisons to be made upon the formation of FLP. 160 mmol of the FLP components were dissolved apart from the solution of the phosphine in benzene were 500 mmol of the phosphine was dissolved. Figure 81-Figure 82 shows the comparisons of experimental and simulated total structure factors, *F(R)*, and the corresponding Fourier transforms to real space G*(r)* for each of the isotopically distinct experimental mixtures (Table 15 – samples 1-12) for the individual FLP components in benzene and $[C_2mim][NTf_2]$. The quality of fit to the experimental data is shown, with the exception of the region at $Q \leq 1$ Å^{-1}, which is most susceptible to inconsistencies due to inelastic scattering contributions from hydrogen in the data, the fitted data aligns well with experiment.

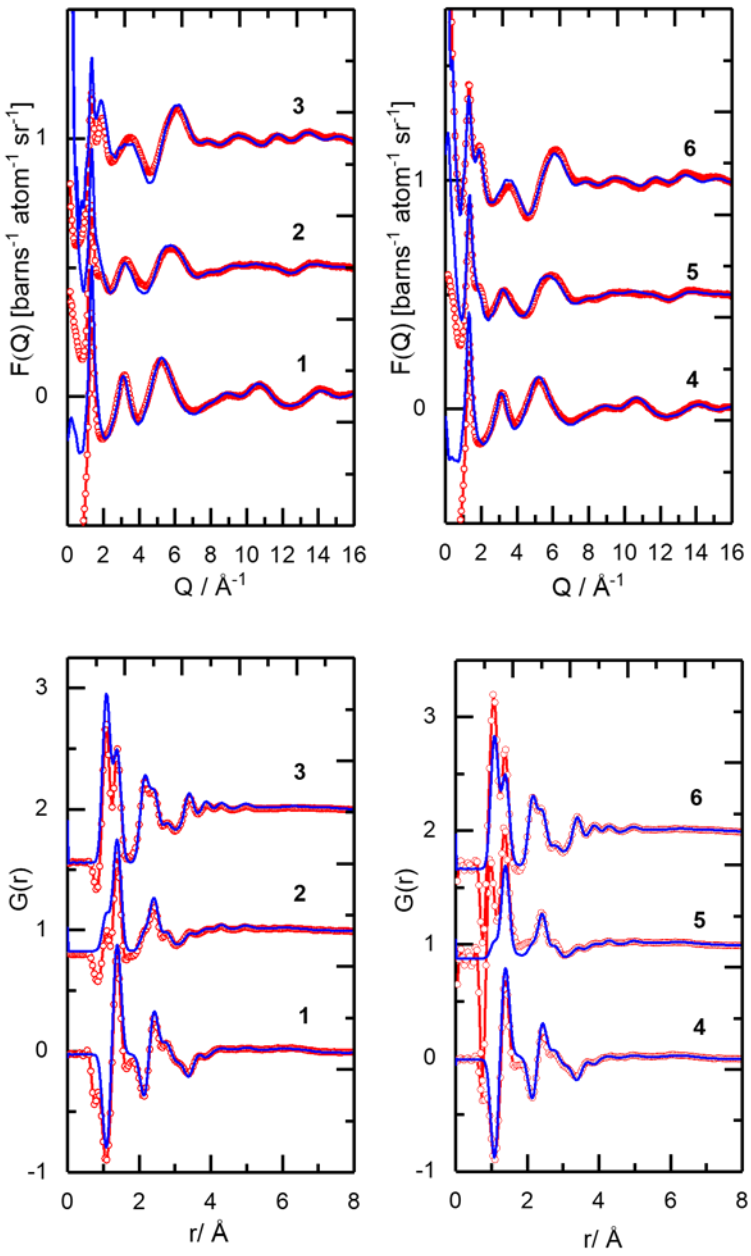

Figure 81. Total structure factors F(Q) (top), and the corresponding Fourier transform to real space G(r) radial distribution functions (bottom) showing experimental data (red symbols) and Dissolve modelled (blue solid line) for left: BCF in benzene and right: P(^{t}Bu)$_3$ in benzene.

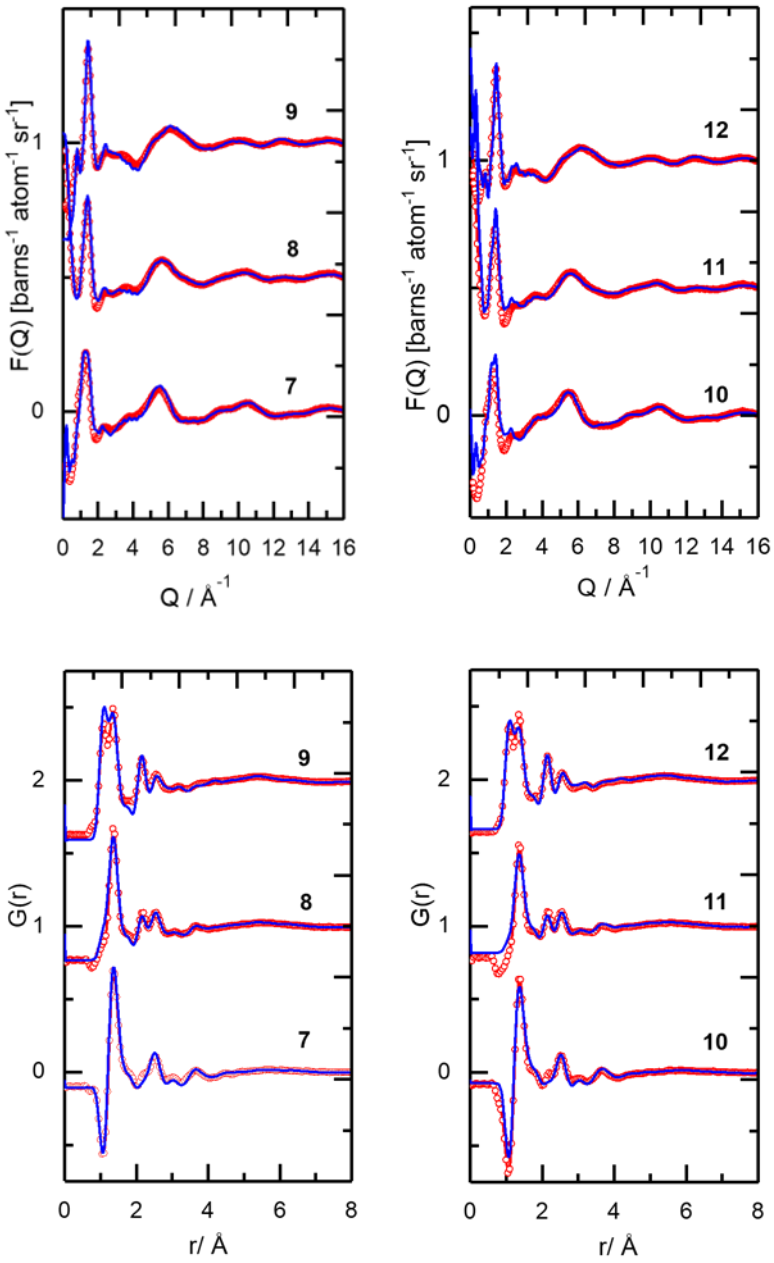

Figure 82. Total structure factors F(Q) (top), and the corresponding Fourier transform to real space G(r) radial distribution functions (bottom) showing experimental data (red symbols) and Dissolve modelled (blue solid line) for left: BCF in $[C_2mim][NTf_2]$ and right: $P(^tBu)_3$ in $[C_2mim][NTf_2]$.

The FLP mixtures were then modelled (Table 15 - samples 16-25). Figure 83 shows the comparisons of experimental and simulated total structure factors, *F(R)*, and the corresponding Fourier transforms to real space *G(r)*, for each of the isotopically distinct samples, across the three systems. There is a very good fit of the model to the experimental data, except for the region at $Q \leq 1$ Å^{-1}, which is most susceptible to inconsistencies due to inelastic scattering contributions from hydrogen in the data.

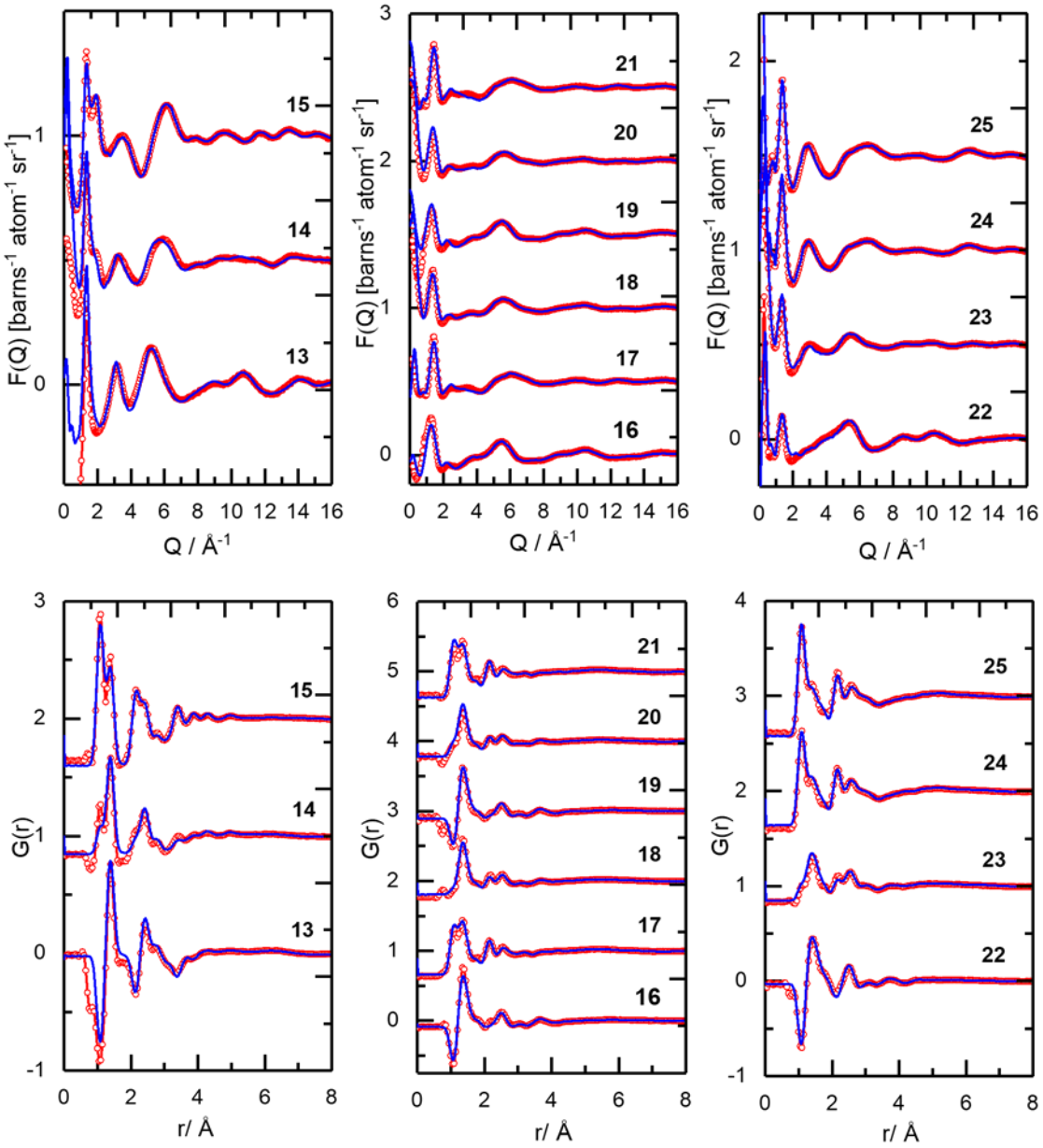

Figure 83. Total structure factors F(Q) (top), and the corresponding Fourier transform to real space G(r) radial distribution functions (bottom) showing experimental data (red symbols) and Dissolve modelled (blue solid line) for P(^{t}Bu)$_3$/BCF in left: benzene, middle: [C_2mim][NTf_2] and right: [C_{10}mim][NTf_2].

4.3.1.2 Comparing models of FLP in benzene: EPSR *vs.* Dissolve

The comparisons of radial distribution functions (RDFs) of the key interactions of the FLP in benzene modelled using EPSR and Dissolve are shown in Figure 84. The correlations are taken from the centre of mass of each component: the P atom for P(^{t}Bu)$_3$, the B atom for BCF and the centre of the ring for benzene. Broadly the profiles are similar between the two codes, with slight differences reflecting the different forcefield

parameters used to describe each component. It is evident that interactions between benzene and phosphine (Figure 84, blue line) and between benzene and borane (Figure 84, black line) are more probable than the interactions between phosphine and borane (Figure 84, green line). This is not surprising, as one would expect these FLP components to be solvated by benzene. This has also been seen in an MD study of the same FLP in toluene.[258] The peak for the benzene-borane correlation (Figure 84, black line) comes at *ca.* 4 Å, which is likely due to the interaction between the empty p-orbital on the boron centre and the aromatic system of the benzene which is capable of π-donation. A peak *ca.* 7 Å is observed for interactions between benzene and phosphine (Figure 84, blue line). This larger distance compared to benzene-borane interactions is due to the bulky tert-butyl ligands surrounding the phosphorus centre, preventing closer contact. The benzene-benzene correlation (Figure 84, red line) demonstrates first shell packing with a maximum at *ca.* 6.0 Å, which is consistent with packing of bulk neat benzene.[9]

The phosphine-borane (P···B) correlations (Figure 84, green line) for the FLP in benzene show a first shell correlation peak at *ca.* 8 Å, with a second peak at *ca.* 10.5 Å, which is consistent with the FLP in toluene studies.[258] The phosphine-borane P···B first shell correlation is more intense in Dissolve compared to EPSR, and the benzene-benzene and benzene-borane correlations are less intense. This suggests that Dissolve might be picking up on less solvation of the borane component by benzene, which would allow it to interact more closely with the phosphine. This is also reflected in the coordination numbers calculated from the two codes which show that *ca.* 4.9% of the total amount of phosphine and borane are found at distances to 8 Å in EPSR, compared to 7.5% in the Dissolve model. The poor resolution seen for the P···B correlation is due to the concentration of the FLP components at 160 mmol, which is low for neutron scattering detection. Nevertheless, both codes clearly show peaks at *ca.* 8 and 10.5 Å, with differences between EPSR and Dissolve attributed to the different starting forcefield parameters.

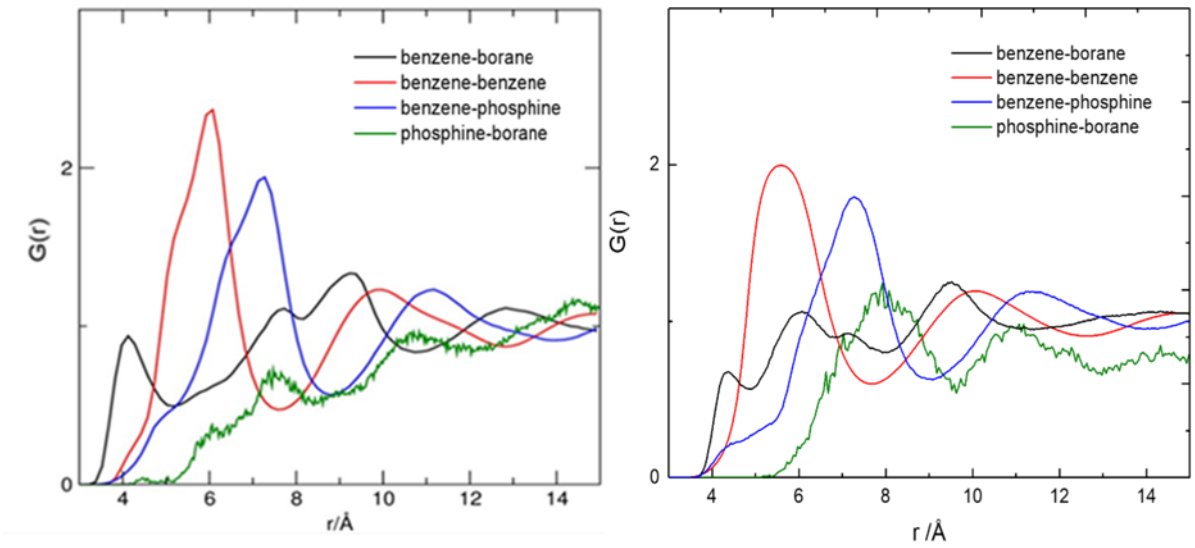

Figure 84. Radial distribution functions (RDFs) of the FLP, $P(^tBu)_3/B(C_6F_5)_3$ in benzene modelled using EPSR and Dissolve. Left: EPSR model and right: Dissolve model, showing correlations between benzene and borane (black), benzene-benzene self-correlation (red), benzene and phosphine (blue) and phosphine and borane (green).

4.3.1.3 FLP in benzene correlations

RDFs showing the benzene-borane (Figure 85, left) and benzene-phosphine correlations (Figure 85, right) were examined for two data sets: one where only one of the FLP components is dissolved in benzene (blue line) and the other when both FLP components are present in the mixture (black line). This was to identify any changes in these correlations upon the formation of FLP. Observably, very similar profiles were generated, showing benzene-solvated borane and benzene-solvated phosphine, irrespective whether these were individual component solutions, or both FLP components were present.

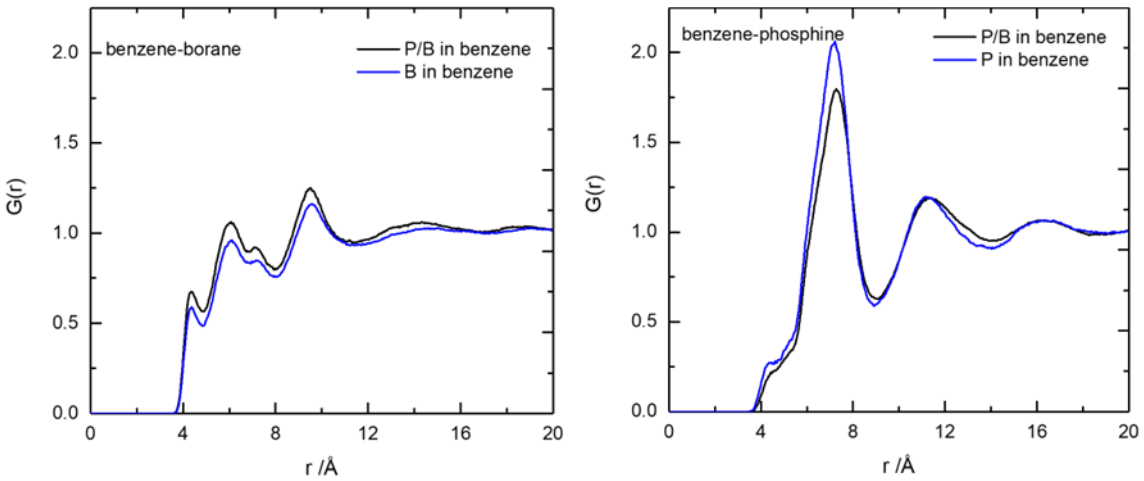

Figure 85. Radial distribution functions of benzene-borane and benzene-phosphine correlations in solutions of the isolated FLP components and mixtures of FLP in benzene. Benzene-borane correlations (left) and benzene-phosphine correlations (right) when only one FLP component is present (blue) and when both FLP components are present (black).

The correlations between the FLP components (P···P and B···B) in benzene are shown in Figure 86. Both the individual FLP components in benzene (blue line) and the FLP mixtures (black line) are plotted to see if there are any differences in the correlations upon FLP formation. For the phosphine in benzene simulation, 500 mmol of the phosphine was dissolved compared to 160 mmol for the FLP mixture. Therefore, differences in magnitudes of the peak correlations and coordination numbers are expected. The profiles for the P···P correlations (Figure 86, left) were similar, with a first small contact peak *ca.* 6.5 Å and the main peak *ca.* 8.4 Å. The difference in intensity of the peaks is due to the different concentrations of phosphine. The B···B correlations (Figure 86, right) give the impression of a very structured system, with an unresolved correlation spanning *ca.* 6-12 Å. This does not reflect a homogeneous distribution of components, and a possible interpretation was that there was clustering of the BCF molecules in the simulation box. The coordination numbers were calculated to the minimum after the first peak in the RDFs (Table 17); all give very low values, as expected given the low concentration of FLP components dissolved in benzene.

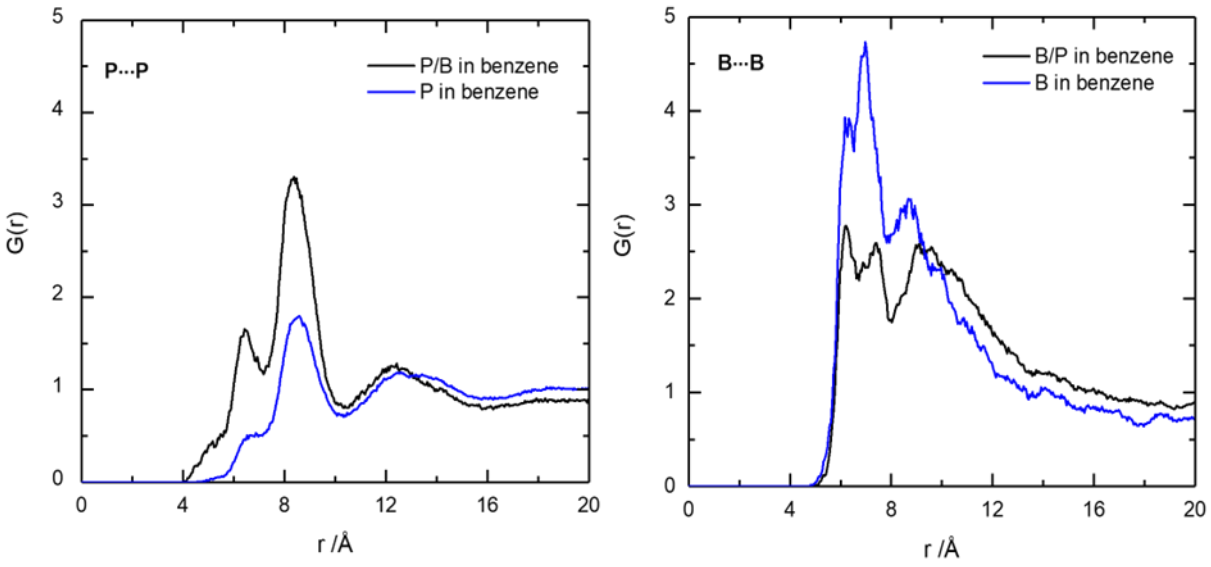

Figure 86. Radial distribution functions of the P(^{t}Bu)$_3$/BCF FLP components in benzene showing phosphine-phosphine correlations (left) and borane-borane correlations (right) when only one FLP component is present (blue) and when both FLP components are present (black).

Table 17. Coordination numbers (CN, calculated to the minimum after the first peak in the radial distribution functions) between FLP components (B···B and P···P) in benzene, when both the individual FLP components are dissolved in benzene and for the FLP mixtures.

Interaction	CN (minima)	CN (minima)
B···B (FLP mixture)	0.00 (6.6)	0.061 (8.0)
B···B	0.14 (6.6)	0.32 (8.0)
P···P (FLP mixture)	0.012 (7.1)	0.25 (10.4)
P···P	0.065 (7.1)	0.86 (10.4)

The B···B RDF (Figure 86, right) shows much greater 'structural correlation' than anticipated for a homogeneous distribution of components in the Dissolve simulation box, suggesting that some form of clustering is present. To examine this, the configuration box was plotted to see how the FLP components were distributed in a single step in the simulation. Figure 87 depicts the distribution of BCF and P(^{t}Bu)$_3$ molecules in the simulation box from the FLP in benzene data, where the benzene solvent molecules have been omitted for clarity. BCF molecules show a marked degree of self-association, consistent with the correlations in the B···B RDF (Figure 86, right). Likewise, there are localised, although less extensive clustering of P(^{t}Bu)$_3$ molecules with at least two pairs evident in the snapshot in Figure 87.

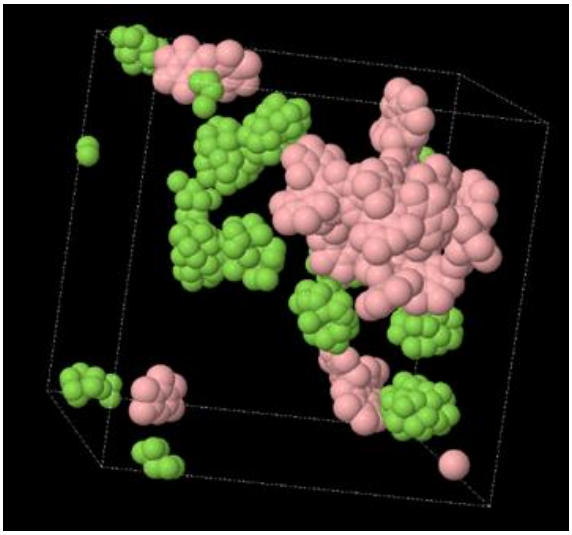

Figure 87. Simulation box of the FLP $P(^tBu)_3$/BCF in benzene with the benzene molecules omitted. BCF molecules are shown in pink and $P(^tBu)_3$ molecules in green.

There are two plausible and reasonable explanations for this observed clustering in the Dissolve refinement of the experimental data: either the FLP components, particularly BCF molecules, are self-aggregating in the benzene solution, possibly due to their high concentrations, or this is an artifact of the computational methodology.

Segregation of BCF molecules from benzene molecules in the solution, resulting in microphase separation, could be caused by the presence of the perfluorinated aromatic substituents on boron, driving separation based on the differences in electronegativity of the fluorinated and hydrogenous aromatic rings. This would also reflect the limiting solubility of BCF in benzene. It has been reported in mixtures of benzene and chlorobenzene, that chlorobenzene aggregates into clusters containing between 2-5 chlorobenzene molecules.[267] Although, in contrast, equimolar mixtures of benzene and hexafluorobenzene (C_6H_6/C_6F_6) were found to be completely miscible and form a stabilised ordered structure that crystalises at 24 °C with alternate layers of fluorinated and nonfluorinated aromatic molecules.[268] Alternatively, although not mutually exclusive, the outcome could demonstrate limitations with the Monte Carlo (MC) approach to sampling and refining the model against experimental data.

A cubic simulation box with sides of length 48 Å was used, which is typical for neutron scattering simulations.[12,40,107,157,166] This contains 10 molecules each of BCF and $P(^tBu)_3$ and 700 molecules of benzene, however both the BCF and $P(^tBu)_3$ molecules are large compared to benzene as the solvent. BCF contains three aromatic rings, and $P(^tBu)_3$ has three tertiary butyl groups, reducing the solvent contribution to approximately 10 solvent molecules per 'functional group' appended to either boron or phosphorus and, as

can be seen in Figure 87, they take up a significant proportion of the space in the simulation box. This high effective density of FLP components, and their bulky shapes is likely to limit diffusion and mobility of these components.

Larger simulation boxes could be generated, however this would be computationally intensive. Ideally, one could run multiple boxes, for example 50-100 simulations in parallel, and then average them instead of having a single box. However, this approach hasn't currently been implemented in the software. Therefore, the interpretation of this data needs to be treated carefully. Corroboration with another experimental technique, such as NMR or Raman spectroscopy, would be a good strategy to derive more robust conclusions.

4.3.1.4 FLP in ionic liquid correlations

Simulating ionic liquids is more challenging than simulating benzene, considering slow rates of diffusion and reduced mobility, resulting from strong Coulombic interactions. In consequence, simulating mixtures of bulky solutes dissolved in ionic liquids, such as BCF and $P(^tBu)_3$, is even more challenging, considering further reduced mobility of the FLP components in the ionic liquids, when compared to benzene.

Figure 88 show the distribution of BCF and $P(^tBu)_3$ molecules in the simulation box, when dissolved in $[C_2mim][NTf_2]$ (Figure 88, left) and in $[C_{10}mim][NTf_2]$ (Figure 88, right), where the ionic liquid molecules have been omitted for clarity. The cubic simulation boxes had sides of length 50 Å for $[C_2mim][NTf_2]$ and 57 Å for $[C_{10}mim][NTf_2]$. Demonstrably, both BCF and $P(^tBu)_3$ molecules are associating with each other, although to a lesser extent in the case of the phosphine. It must be recognised that the movement of all these components was limited within the simulation box, and since they aren't homogenously distributed, the interpretation of the data needs to be treated carefully.

Again, it is unsurprising that there was partial association, or weak clustering of these components, especially given the fluorinated nature of BCF and the FLP components are likely to sit excluded from the charged regions of the ionic liquids. Therefore, it is possible that this did not leave much room in the box and - given the size of the FLP components - they might have been artificially forced to sit closer together. It is also worth noting that the data was collected on SANDALS, which has the maximum length scale of *ca.* 30 Å. To study the degree of aggregation seen here, a lower Q range would be required, such as that provided by NIMROD instrument. Therefore, it is possible that there is limited information that SANDALS provides to drive the refinement from a simulation like this.

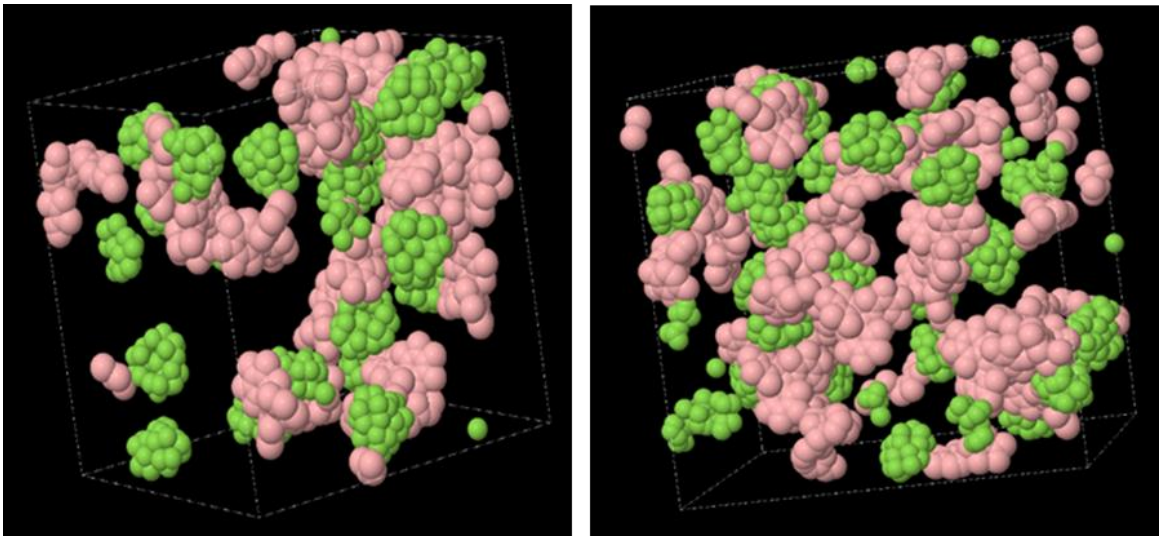

Figure 88. Simulation boxes of the FLP $P(^tBu)_3$/BCF in the ionic liquids $[C_2mim][NTf_2]$ (left) and $[C_{10}mim][NTf_2]$ (right), with the ionic liquid molecules omitted. BCF molecules are shown in pink and $P(^tBu)_3$ molecules in green.

Figure 89 shows the interactions between $P(^tBu)_3$ and BCF with the charged regions of the ILs for $[C_2mim][NTf_2]$ (left) and $[C_{10}mim][NTf_2]$ (right). The correlations are calculated from the P and B of $P(^tBu)_3$ and BCF as before and from the O atom of the anion and the C atom between the two nitrogens on the cation imidazolium ring (C^R). It is evident that the strongest interaction is from BCF interacting with $[NTf_2]^-$ (Figure 89, red line). Interactions of BCF and $P(^tBu)_3$ with $[C_nmim]^+$ (Figure 89, black and blue lines) are mainly centred around 8 Å, which is a typical separation seen in ILs and ILs plus solutes. Generally, the RDFs are similar for both ILs, showing that the components dissolve in the same way and the IL solvates the phosphine and borane.

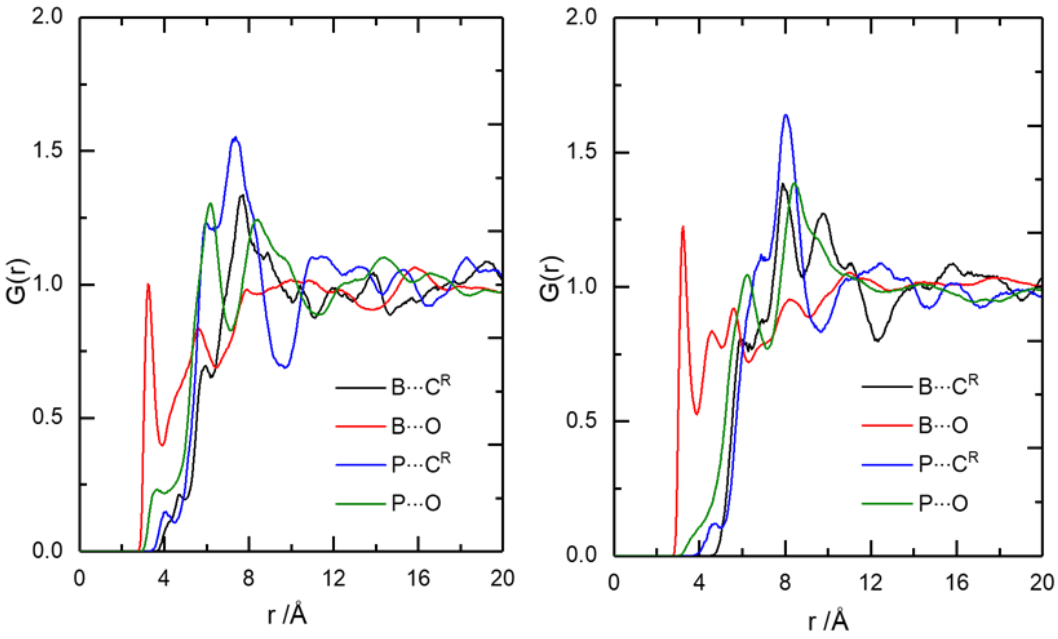

Figure 89. Partial radial distribution functions for the FLP, BCF/P(^{t}Bu)$_3$ in [C_2mim][NTf_2] and [C_{10}mim][NTf_2], showing the interactions between P(^{t}Bu)$_3$ (P) and BCF (B) with C^R of the cation and O of the anion for left: [C_2mim][NTf_2] and right: [C_{10}mim][NTf_2].

An MD study by Liu and co-workers[258] postulated that the FLP components sit in cavities formed in the hydrophobic domains of the long alkyl chains of [C_{10}mim][NTf_2]. To explore the association of the FLP components with the alkyl chain, Figure 90 shows pRDF profiles reflecting the correlations of both phosphine and borane with the middle of the alkyl chain (C6) of [C_{10}mim][NTf_2]. This indicates strong correlations of both FLP components with the alkyl chain, supporting the hypothesis that FLP components reside in non-polar domains.

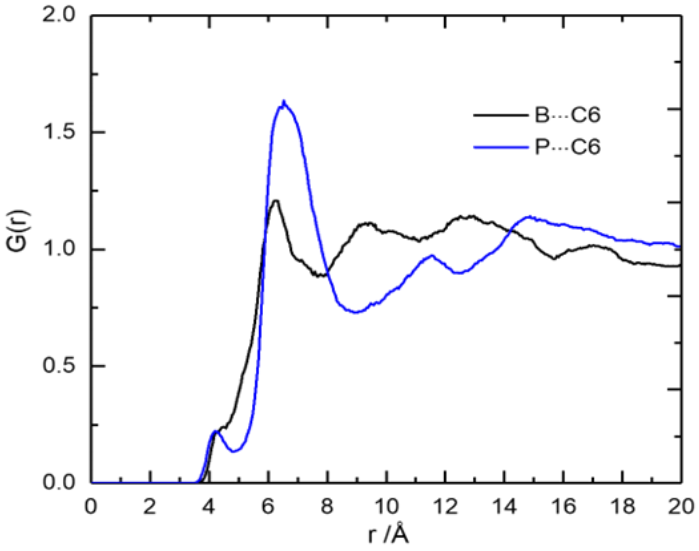

Figure 90. Partial radial distribution functions for the FLP, BCF/P(^{t}Bu)$_3$ in [C_{10}mim][NTf_2] showing interactions between P(^{t}Bu)$_3$ and BCF with the alkyl chain of [C_{10}mim][NTf_2]. C6 was chosen as a carbon in the middle of the alkyl chain and correlations to BCF (black line) and to P(^{t}Bu)$_3$ (blue line).

Considering lack of long alkyl chains in [C_2mim][NTf_2], it was assumed that FLP components must be situated in the proximity of charged moieties. The interactions between the FLP components with the cation and anion of [C_2mim][NTf_2] were investigated further to determine whether any change occurred when only the individual FLP components were dissolved in the IL and upon FLP formation. Similar profiles are generated for P···O and B···C^R correlations. However, notable distinctions are evident in the B···O correlation, with a more pronounced first shell peak in the FLP mixture compared to BCF in [C_2mim][NTf_2]. This implies a stronger interaction between boron and the anion in the FLP mixture. Further variations are observed in the P···C^R correlation of the FLP mixture in [C_2mim][NTf_2]. The pRDF indicates the existence of two distinct environments, as mirrored peaks for the phosphine in [C_2mim][NTf_2] are accompanied by two new peaks at *ca.* 7.5 and 15 Å. These new peaks, exhibiting a counter-phase relationship, suggest a distinct solvation environment for the FLP.

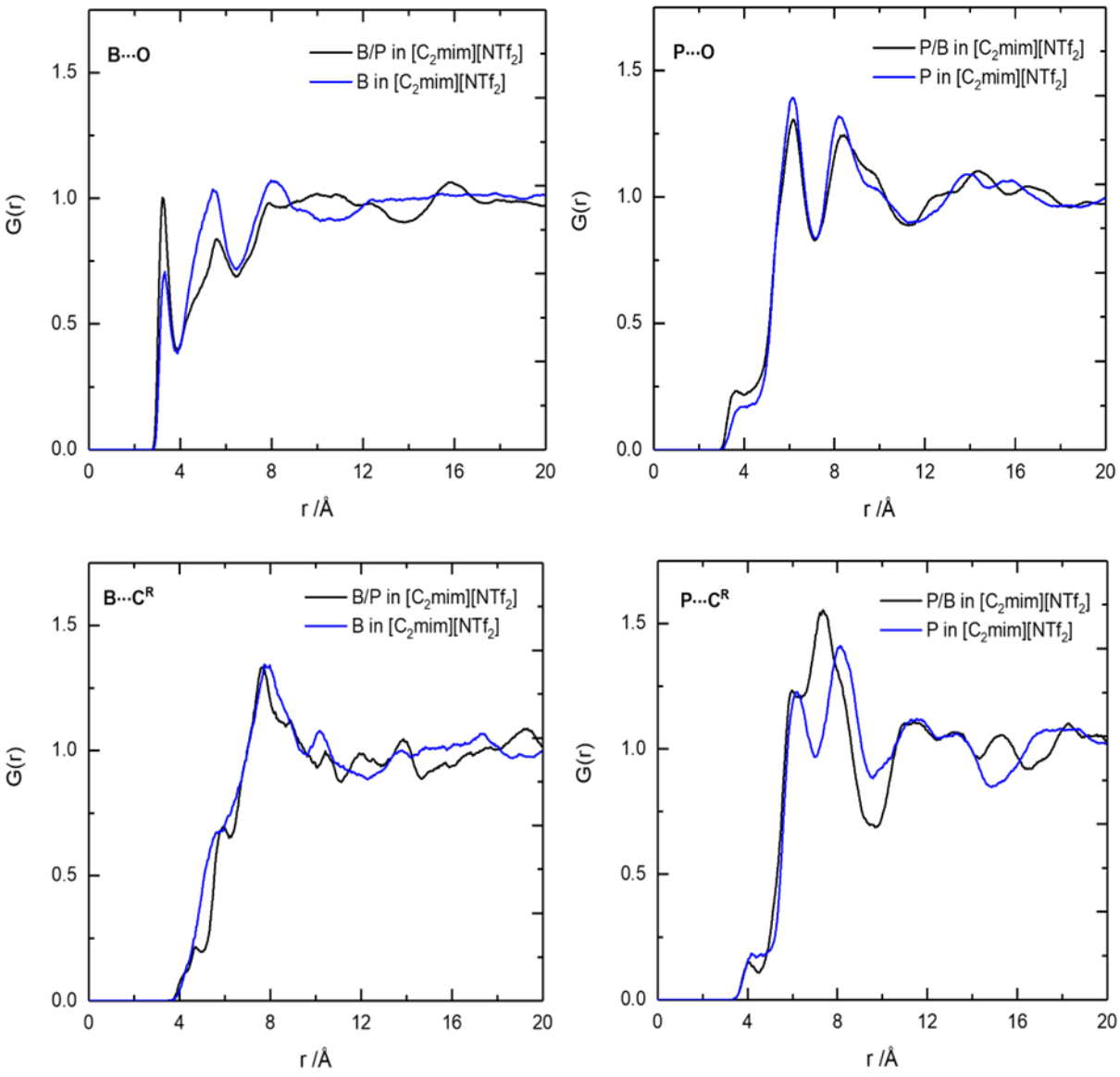

Figure 91. Partial radial distribution functions for the isolated FLP components and mixtures of the FLP, BCF/P(^{t}Bu)$_3$ in [C_2mim][NTf_2] showing the interactions between P(^{t}Bu)$_3$ (P) and BCF (B) with C^R of the cation and O of the anion for individual FLP components (blue) and FLP mixtures (black).

4.3.1.5 B···P pair distribution functions

B···P RDFs were generated for each of the three systems; FLP in benzene, [C_2mim][NTf_2] and [C_{10}mim][NTf_2] (Figure 92). The distance between the B···P centres is the main interest in this work, providing the most direct information about the encounter complex. In all three systems, a common peak at *ca.* 8.0 Å is observed, which corresponds to "solvent-separated" pairs. This is the first peak that appears for benzene (Figure 92, black line), indicating that the phosphine and borane are solvated by benzene. For the ILs, shorter separation distances are observed. For [C_2mim][NTf_2] (Figure 92, red line), there is a first peak at *ca.* 6.3 Å and a shoulder preceding

the peak at 8.0 Å which comes *ca.* 7.3 Å. For [C_{10}mim][NTf_2] (Figure 92, blue line), the first B···P correlation distance comes *ca.* 5.2 Å, followed by a broader peak *ca.* 6 Å and the peak *ca.* 7.3 Å is also seen. This would indicate the formation of more reactive FLP pairs in the ILs, with no solvent separation, at distances below 7 Å. These findings are consistent to the MD study of P(^{t}Bu)$_3$/BCF in [C_{10}mim][NTf_2], which report peaks at *ca.* 5.5, 6.5 and 8.0 Å.[258] There is more long-range order in the ILs, compared to benzene, as can be seen from the peaks after 10 Å. However, as mentioned before, it is difficult to draw hard conclusions from the present data. It is evident that there is contact between BCF and P(^{t}Bu)$_3$, however how much of this is from FLP association or how much of it is due to constricted aggregation of the FLP components as seen in the simulation box, is up for discussion.

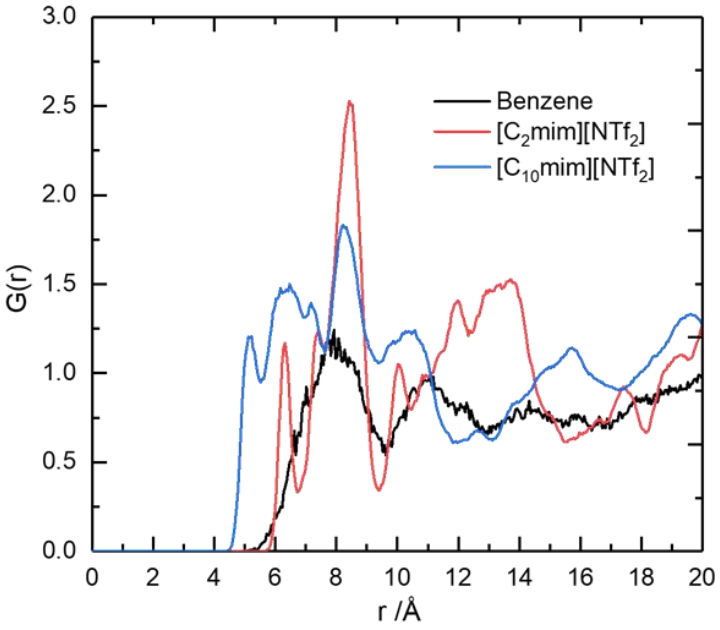

Figure 92. B···P pair partial radial distribution function for each of the three FLP systems studied showing correlations between P(^{t}Bu)$_3$ and BCF in benzene (black), [C_2mim][NTf_2] (red) and [C_{10}mim][NTf_2] (blue).

Analysis of coordination number for B···P correlation lengths, *G(r),* in benzene, show that only 0.7% of all phosphine and borane molecules are in contact at distances ≤7.0 Å. At 8 Å, this increases to 7.5% of all FLP components existing as solvent separated pairs. In contrast, for [C_{10}mim][NTf_2], B···P correlation lengths at ≤6.0 Å, account for 4.59% of the total FLP components forming close contact encounter complexes; at distances between 6.0 and 7.0 Å, there is another 13.88% (total of 18.47%). These values are very similar to those obtained in the MD study, reporting the values of 4.80% and 13.29%, respectively (total of 18.09%).[258] These results also corroborate with the NMR study done by the group, reporting an overall value of 20% of the FLP pairs having B···P interactions.[184]

In $[C_2mim][NTf_2]$, there is negligible correlation at distances of ≤6.0 Å, indicating lack of close contact encounter complexes. At ≤7.0 Å, 6.05% of FLP components are associated as solvent separated pairs. This is much lower than for $[C_{10}mim][NTf_2]$ (18.47%), but much higher than in benzene (0.7%). This is in agreement with previous findings that there is greater association of FLP components in ILs compared to molecular solvents such as benzene or toluene.[184,258] Comparing the two ILs, there is markedly higher concentration in the long chain IL, $[C_{10}mim][NTf_2]$, which is the only medium of the three supporting very close association (≤6.0 Å), with $P(^tBu)_3$/BCF pairs situated in the cavities formed by the long alkyl chains. Again, this is in agreement with the MD study, where the concentration of the encounter complex was reported to increase with increasing alkyl chain length of $[C_nmim][NTf_2]$ ionic liquids.[258]

4.3.1.6 Comparison of the interactions between FLP components for the three systems

Interactions between the FLP components (B···B, P···P and B···P) in the two ILs and benzene are shown in Figure 93. These super-structured RDFs show that all the FLP components sit close to each other and there is a lot more long-range order in the ILs compared to benzene. Again, like in the case of aggregation of the BCF molecules, this could be a consequence of how the components are distributed in the simulation box, and potentially attributable to the high concentrations of the FLP components or to an artifact of the computational methodology. The longer-range order observed for $[C_{10}mim][NTf_2]$ could be due to the FLP components arranging themselves in among the long alkyl chains and sitting in close proximity in these cavities (enforced ordering by forming channels in non-polar domains). Benzene is a much less structured solvent; therefore, it is expected that the FLP components solvated by benzene would generate broader correlations in the RDF.

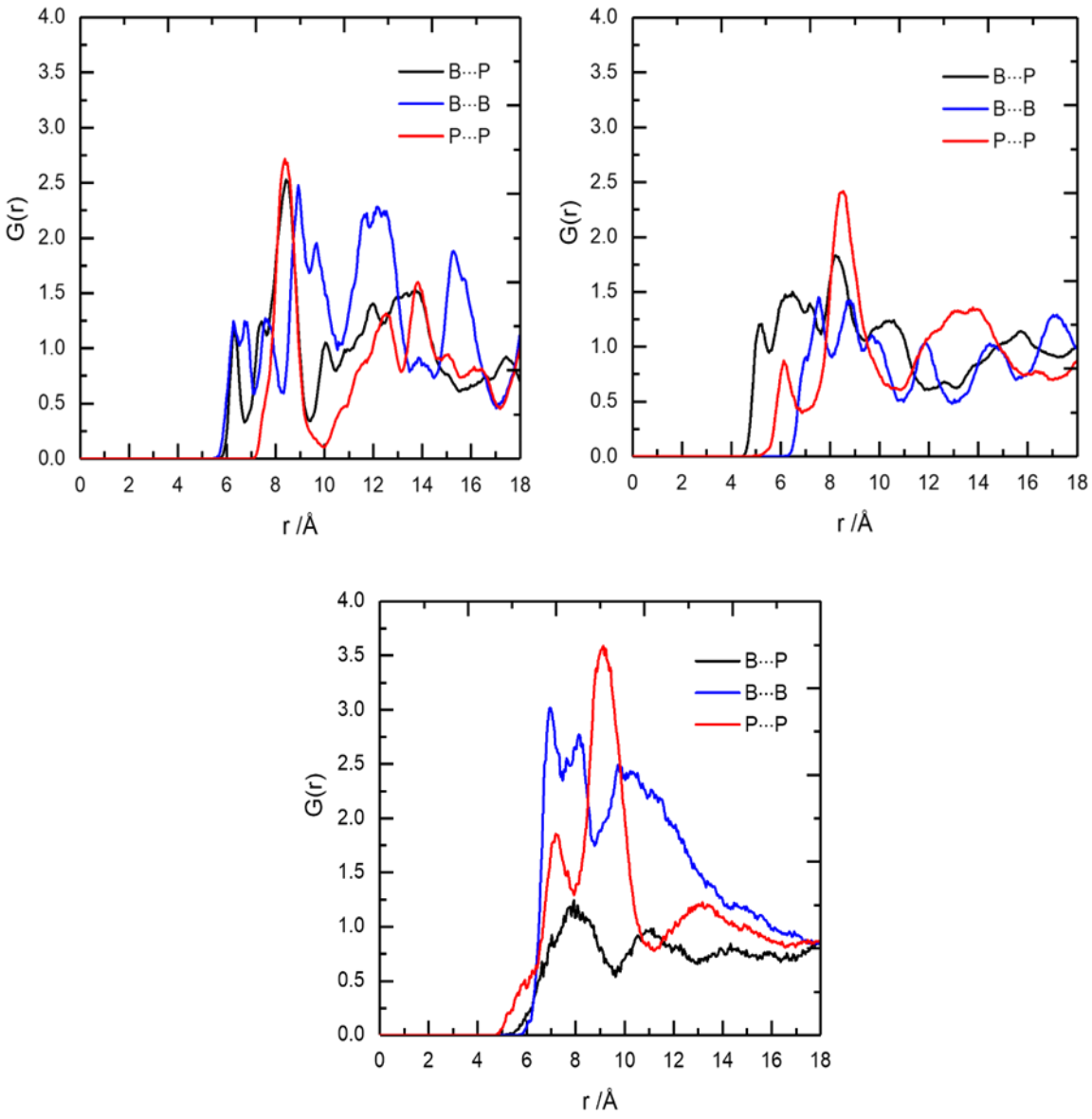

Figure 93. Radial distribution functions of FLP, BCF/P(^{t}Bu)$_3$ in the three systems studied showing the interactions of the FLP components P(^{t}Bu)$_3$ (P) and BCF (B) in [C_2mim][NTf_2] (top left), [C_{10}mim][NTf_2] (top right) and benzene (bottom middle).

The B···B and P···P correlations could also be compared when only one of the FLP components were dissolved in [C_2mim][NTf_2] and upon FLP formation. Correlations between BCF molecules (Figure 94, left) occur at a shorter distance in the FLP mixture (Figure 94, black line) compared to when only BCF is dissolved in the IL (Figure 94, blue line). The RDF also shows a more ordered structure upon the FLP formation. The opposite trend is seen with the P···P correlations (Figure 94, right), where shorter distances are observed for phosphine dissolved in the IL, than in the FLP solution. The RDF profiles show a common main peak at *ca.* 8 Å, which is

the same main contact distance for the B···P correlations. Finally, it is evident that there is noise in the simulation data, and there are limitations on how to simulate these systems with the current methodology.

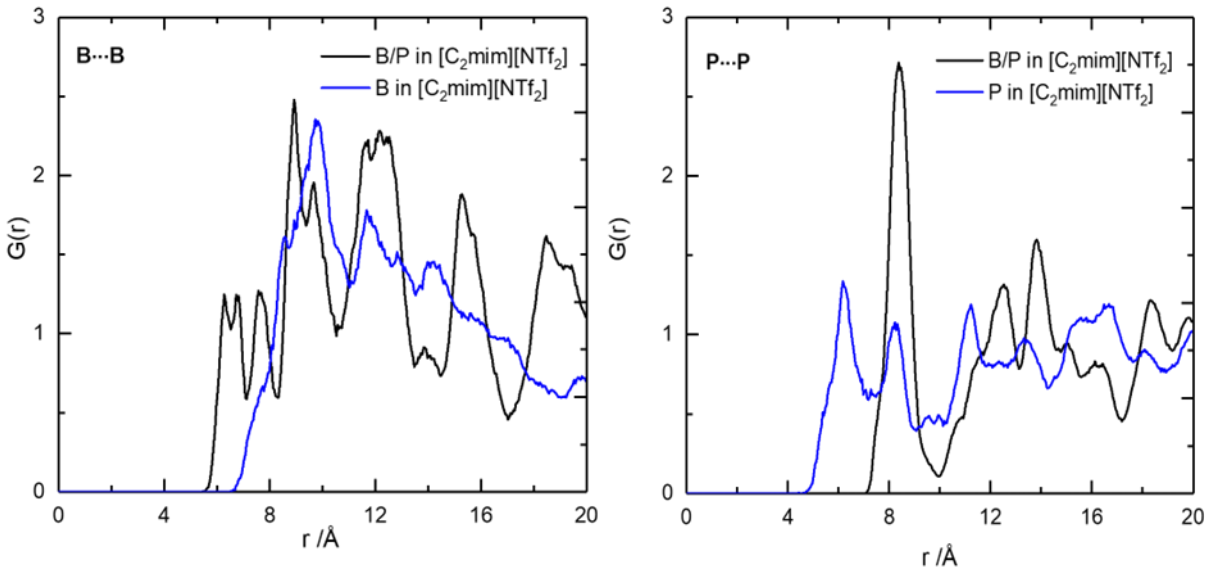

Figure 94. Radial distribution functions of the isolated FLP components and FLP, BCF/P(^{t}Bu)$_3$ in [C_2mim][NTf_2]. The interactions are shown between BCF molecules (B) and P(^{t}Bu)$_3$ (P) molecules in [C_2mim][NTf_2] when only one FLP component is dissolved (blue) and in the FLP mixture (black).

4.3.1.7 Centre of mass radial distribution functions of the ionic liquids

There is no significant change in the cation-anion interactions or anion-anion and cation-cation interactions of the ILs upon the addition of FLP components (Figure 95); the strong cation-anion correlations remain the core structural feature of the bulk liquid. This also supports the finding of increased concentration of associated FLPs in ILs compared to molecular solvents, as it is facilitated by the strong cation-anion interactions and the cavities generated in bulk phases created by the long alkyl chains of the cation where the FLP components can accommodate themselves.

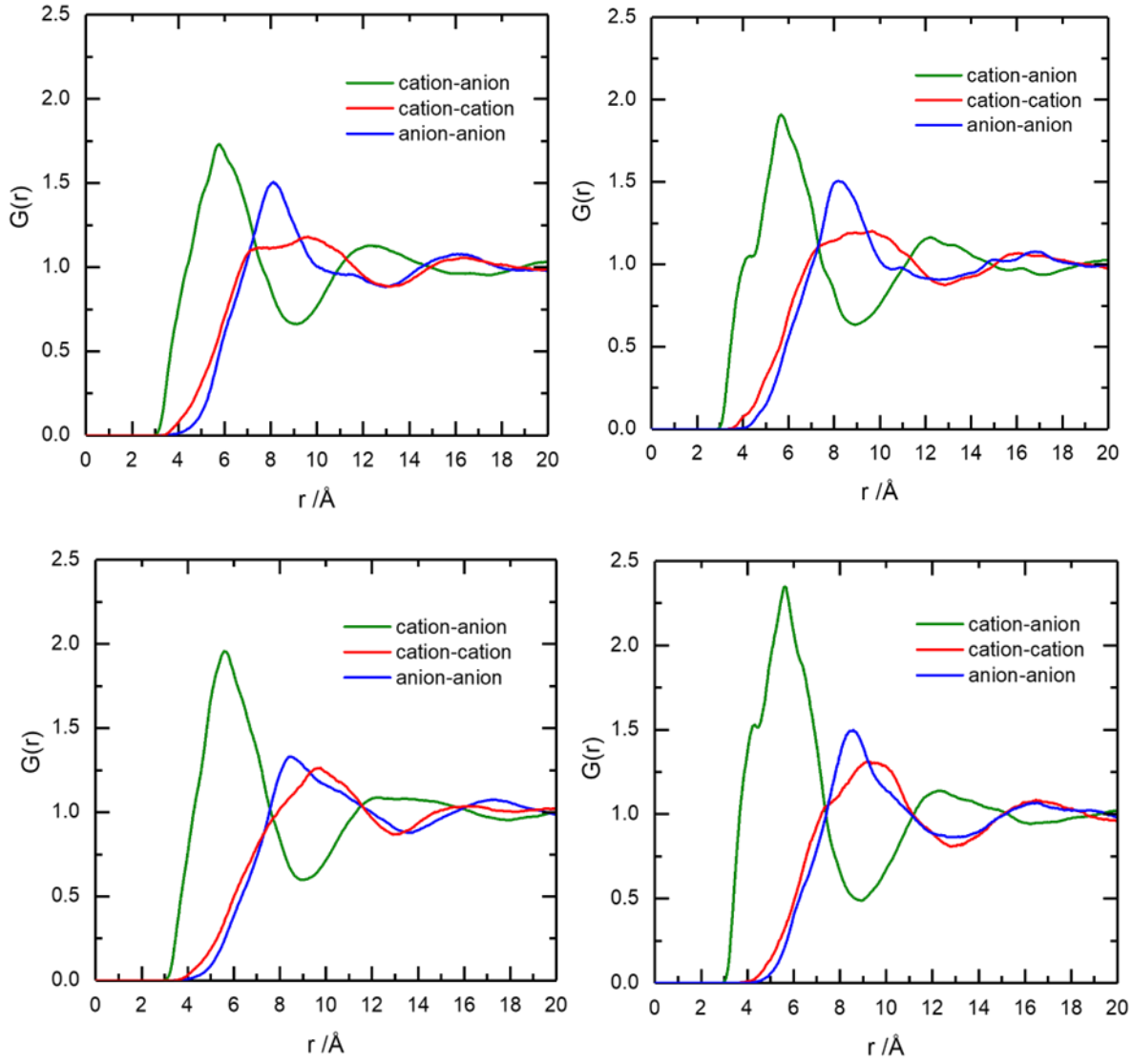

Figure 95. Radial distribution functions showing interactions between ionic liquid components in the neat ILs (left) and in the FLP, BCF/P(^{t}Bu)$_3$ in ionic liquid mixtures (right) for [C_2mim][NTf_2] (top) and [C_{10}mim][NTf_2] (bottom).

4.3.1.8 Investigating cluster formation

To investigate the origin of the clustering observed in the simulation boxes, the configuration was compared to that from the initial randomised configuration. Analysis of the component distributions in the initial starting configuration was aimed to determine whether clustering is present, and remains, from the beginning of the refinement, or if it genuinely formed as part of the refinement process. The configuration boxes were plotted for each of the three systems: FLP in benzene (Figure 96a), in [C_2mim][NTf_2] (Figure 96b), and in [C_{10}mim][NTf_2] (Figure 96c). Benzene and ionic liquid components have been removed for clarity, the BCF molecules are

shown in pink, and the $P(^tBu)_3$ molecules are in green. The left column shows the boxes plotted from the initial randomised configuration and shows that the components are distributed evenly in each of the boxes, with minimal clustering evident. This suggests that the clustering observed in the final Dissolve refinements forms as part of the refinement process. The subsequent question to address was whether the forcefield or the experimental data drove the cluster formation. To explore this, the Dissolve simulation was run with refinement against energy minimum, not against the data ($E_{req} = 0$). The configuration boxes plotted for each system (Figure 96, middle) show only limited clustering. Finally, the boxes in the right column are the same as those in Figure 87-Figure 88, plotted for the simulation refined to the data sets ($E_{req} > 0$), and show significant cluster formation.

This analysis points to the conclusion that clustering is not a result of the initial distribution of species in the randomised starting configurations. Furthermore, without fitting to the data sets, the clustering is limited and increases significantly in the full refinement, suggesting that this is a genuine observation. It is well understood that mobility (diffusion) of species in IL environments is slow due to the charge driven constriction in the systems, both the phosphine and borane are large, and boranes are fluorinated leading to potential self-aggregation. Therefore, it is highly likely that the entire configuration space of the simulation has not been sampled. Achieving this in a single Dissolve refinement, regardless of how many iterations are performed, would be challenging due to the fact that, once favourable associations are established between components (leading to a good correlation between simulated and experimental structure factors), they become "fixed" and persist as "good configurations" during the Monte Carlo simulation.

In the future, a possible approach to address this challenge would be to perform a large number of parallel refinements starting from different random starting configurations (parallelising computations) and then merging results together to give a greater statistical sampling of the configuration space.

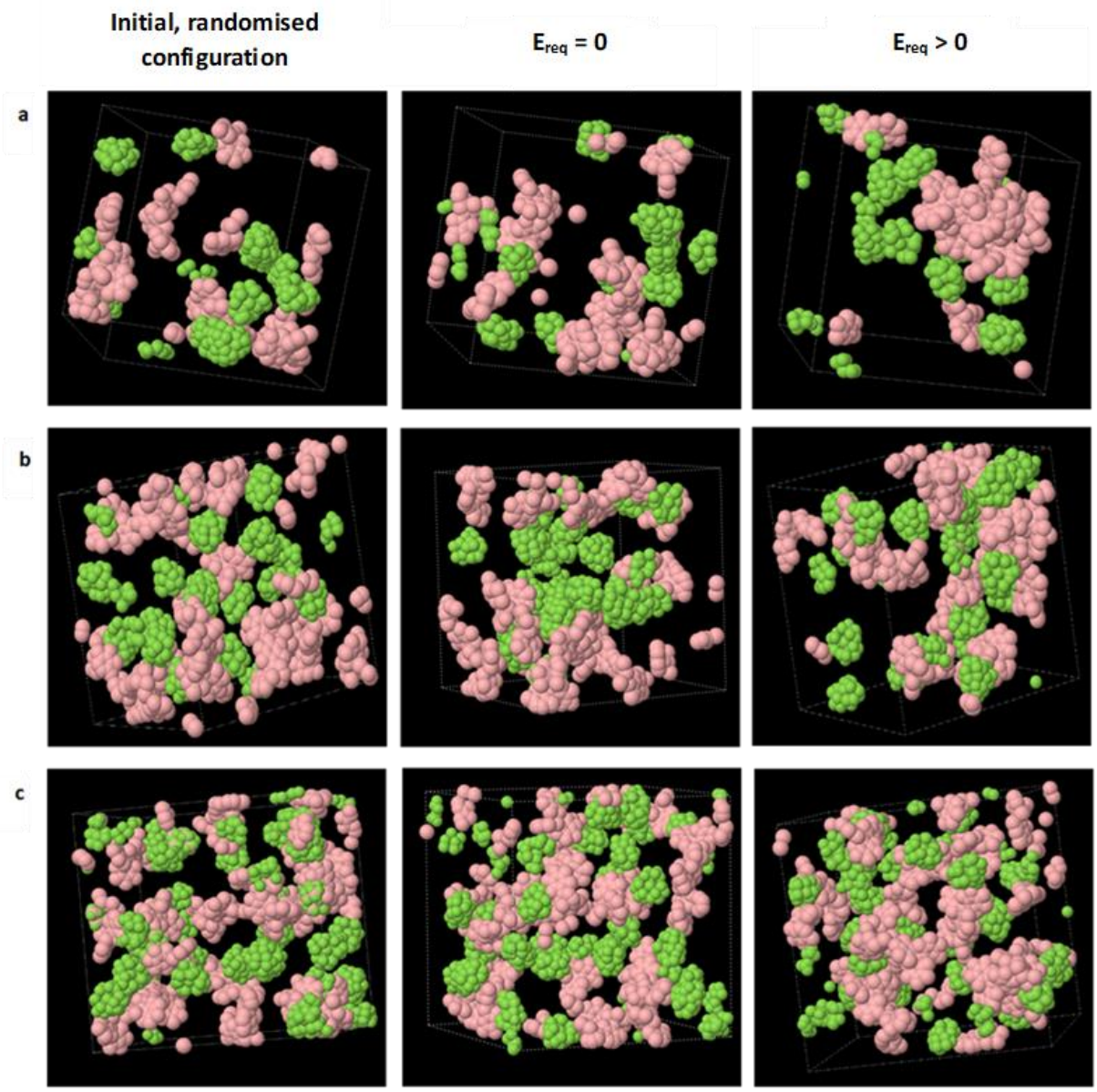

Figure 96. Simulation boxes of the three systems at different stages of the simulation process: FLP in benzene (a), FLP in $[C_2mim][NTf_2]$ (b) and FLP in $[C_{10}mim][NTf_2]$ (c) with the benzene/ionic liquid molecules omitted. BCF molecules are shown in pink and $P(^tBu)_3$ molecules in green. Left: initial randomised configurations, middle: E_{req}= 0 and right: E_{req} >0.

4.4 Conclusions and Outlook

The main aim of the study was to investigate the FLP encounter complex in benzene and two ILs by neutron scattering studies. In particular, it was aimed to find a corroborating experimental proof that IL environments promote the formation of encounter complexes, beyond our preliminary NMR spectroscopic study[184] and the MD work.[258]

In all solvents, most of the B···P distances are >7 Å, indicating separated molecules of $P(^tBu)_3$ and BCF; the concentration of encounter complexes is low, consistent with weak interactions of the two components, and previous studies. However, there was a marked difference between the three solvents. In benzene, only 0.7% of FLP molecules were associated at distances $\leq$ 7.0 Å. In $[C_2mim][NTf_2]$, this number increased to 6.05%, and in $[C_{10}mim][NTf_2]$, it reached 18.47% - more than twenty times the benzene concentration! Previous MD simulations have suggested that the FLP components sit in the cavities formed by the long alkyl chains of the ILs, which results in greater concentration of the encounter complex in $[C_{10}mim][NTf_2]$. Here, we have found that this IL was the only medium that featured encounter complexes with a very short B···P separation of ≤6.0 Å, accounting for 4.59% of the total FLP components forming close contact encounter complexes, as opposed to solvent-separated pairs.

The most surprising outcome of this study was the long-range ordering of the FLPs in ionic liquids. It has been recognised that large species, dissolved in viscous solvent with strong Coulombic interactions, would be slow to diffuse. However, it has not been clear whether this clustering was a real feature of the system, or a modelling artefact. To answer this question, FLPs in all three solvents were modelled with ($E_{req} > 0$) and without ($E_{req} = 0$) neutron scattering data driving the model and compared to initial configuration. It has been found that the initial configuration featured no clustering, and simulation driven by energy minimisation had little clustering compared to data-driven simulations in ionic liquids. In conclusion, at least to some extent this clustering was found to be a feature of the actual system. Having said this, it is highly likely that the entire configuration space of the simulation has not been sampled. In as a single Dissolve refinement, once favourable associations are established between components (finding a “local minimum” in discrepancy between simulated and experimental structure factors), they become persistent throughout the entire Monte Carlo simulation. This could be addressed by averaging over multiple parallel simulations, but this option is currently not available in the software, and such study was beyond the scope of this thesis.

In conclusion, there were two types of insights from this study: firstly, persistence of encounter complexes in ILs was demonstrated, with some quantitative data available; secondly, both capabilities and limitations of Dissolve in a very challenging model have been explored. In the future, such data could be recorded at NIMROD, to better access long-range structural data, and parallel modelling across a hundred simulation boxes could be attempted to gain a robust picture of long-range order in these solutions.

Chapter 5

Quantification of Lewis acidity of boron compounds

5 Quantification of Lewis acidity of boron compounds

The focus of this work was the application of two X-ray spectroscopies: X-ray photoelectron spectroscopy (XPS) and X-ray absorption spectroscopy (XAS) for the study of boron-based Lewis acids, with an outlook to develop a probe of Lewis acidity that is independent of a molecular (spectroscopic) probe. Boron 1s X-ray spectroscopy, especially in the liquid phase, is not very commonly studied due to extensive experimental challenges arising from the requirement for ultra-high vacuum conditions. This is unfortunate, as most boron-involving chemical reactions (borylations, hydroboration, FLP chemistry *etc*.) occur in solutions, and it would be of great interest to study electronic structure of boron Lewis acids in solvents, paving way to future *operando* studies. It is only with the introduction of the liquid micro-jet technique, on synchrotron source XPS instruments, that liquid-phase photoelectron spectroscopy has advanced.[99–106] By understanding how the electronic structure relates to chemical reactivity and probe-based Lewis acidity measurements, the aim was to elucidate different factors that influence Lewis acidity, and understand how each impacts the catalytic performance of boron Lewis acids.

The first part of this work involved the synthesis of tricoordinate boron compounds. The second part was the first study of liquid jet XPS measurements of boron Lewis acids. The experiments were conducted at the BESSY II synchrotron, Berlin, followed by data analysis, in collaboration with Dr Lovelocks group at Reading University. XPS is being processed by the Lovelock group, and here the XAS data in relation to NMR spectroscopic measurements is reported. DFT calculations were performed using ORCA by Tom Penfold, University of Newcastle.

This work was originally intended as the main focus of my PhD studies, but with COVID-19 pandemic, it has been side-lined in favour of neutron scattering studies, in particular modelling using the Dissolve package.

5.1 Introduction

5.1.1 Lewis acidity

In 1923, G.N. Lewis defined acids as chemical species which can accept an electron-pair from a base to complete its octet.[269] Many boron compounds are Lewis acidic, either due to the presence of a free *p* orbital in species with sp^2-hybridised boron, or due to labile ligands attached to sp^3-hybridised boron that can be readily replaced by a nucleophile.[270] Lewis acidic boranes are widely used as catalysts in organic synthesis[271–273] and as Lewis acidic components in frustrated Lewis pairs.[248,274–276] Quantifying Lewis acidity (of boron compounds, and in general) is very challenging, which to a certain extent hinders understanding of their

reactivity. It is well known that a universal Lewis acidity scale is prohibited as the strength of the acid-base interaction is inherently dependent on the Lewis base, as well as the Lewis acid.[277,278] However, since Lewis first proposed his theory of electron pair acceptors,[269] there have been numerous attempts of quantifying Lewis acidity in a meaningful way, that could guide the experiment. The most frequently used scaling methods rely on the use of a probe molecule or ion (which "fixes" the nature of the base) and quantifying the strength of the interactions between the probe and acid. Some of the most relevant scales in this work will be reviewed in the following section.

The theory of hard and soft acids and bases (HSAB) was introduced in the 1960s by Pearson[279] and is the most common qualitative approach to describe the acid-base interactions. A hard species would be typically small, with low polarisability and high electronegativity, in contrast a soft species would be larger with high polarisability and low electronegativity. It was then noted that a soft Lewis acid would bind preferentially to a soft Lewis base while hard acids prefer to associate with hard bases. These descriptions describe the formation of covalent *vs.* ionic bonds, respectively. This approach is useful in quickly rationalising a large number of Lewis acid-base reactions in a qualitative manner but lacks quantitative information.

The relative Lewis acidity of boron trihalides increases along the series $BF_3 < BCl_3 < BBr_3$. However, on the basis of electronegativity, one might predict BF_3 to be the strongest Lewis acid, owing to the increased removal of electron density from the boron centre. The most accepted explanation is that the charge donation from the fluorine lone-pair into the vacant *p* orbital of boron (π-back donation) is more efficient due to increased overlap of the orbitals given the similar size (especially in comparison to the larger p-orbitals of Cl and Br).[280] A stronger π-back bonding effect will decrease the availability of boron to accept an electron pair. During the formation of an adduct, the BX_3 moiety (X = F, Cl, Br) must change from its trigonal planar to a pyramidal geometry which is more difficult with stronger π-back donation. However, calculations have shown that the p(π)-p(π) overlap is actually larger for BCl_3 than for BF_3, in contrast to the π-back-bonding explanation.[281] It appears that the best explanation has been given by Bessac and Frenking,[282] who calculated the energy of the lowest unoccupied molecular orbital (LUMO) and found that BCl_3 has a lower LUMO energy compared to BF_3 resulting in more stable adduct formation.

It is evident that the factors determining the Lewis acidity of boron compounds are complex and many aspects of Lewis acidity need to be taken into account. These include three main factors: electrostatic interactions, frontier molecular orbital (FMO) interactions and the energy required for pyramidalization of boron geometry from trigonal planar (sp^2) to tetrahedral (sp^3) upon the adduct formation. The most common scales for determining Lewis acidity of boron compounds are discussed in the next section.

5.1.2 Quantification methods of Lewis acidity

5.1.2.1 Gutmann-acceptor number and Childs method

The Gutmann-acceptor number (AN) and Childs method are the most popular methods for scaling Lewis acidity, probably due to their experimental ease. Gutmann first used this approach to assign acceptor numbers to a variety of solvents to describe their electrophilic behaviour.[283] It has since expanded to Lewis acidic solutions and has been widely used for measuring the acidity of boron reagents and ionic liquids.[284–287] The method relies on the induced shift of the ^{31}P NMR signal of triethylphosphine oxide, $P_{222}O$ upon binding to a Lewis acid (Figure 97).

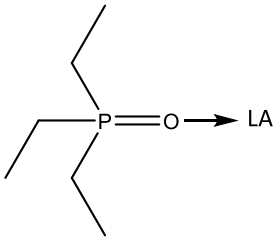

Figure 97. Adduct formation of $P_{222}O$ with a Lewis acid.

This chemical shift is measured at three known concentrations of the probe and subsequently extrapolated to infinite dilution. The ^{31}P NMR chemical shift of $P_{222}O$ in hexane is used as a reference and the AN value is calculated as per Equation 16 .

$$AN = 2.348 \cdot \Delta\delta_{inf}$$

Equation 16

Triethylphosphine oxide was selected as the probe molecule as the ^{31}P nucleus is naturally 100% abundant and has spin ½ producing clear NMR spectra. The ^{31}P chemical shift is sensitive to its environment, as its short ethyl chains prevent steric hindrance and make the molecule strongly donating. The molecule is stable even in highly acidic environments, as the ethyl chains provide protection to the oxygen atom and has good solubility in a wide variety of solvents. The AN scale was arbitrarily defined, based upon the ^{31}P NMR chemical shift of $P_{222}O$ in hexane (AN = 0) and in 2 molar solution of $SbCl_5$ in 1,2-dichloroethane (AN = 100).[288] A larger value indicates a greater shift in electron density from the oxygen atom to the acidic species, reducing the electron density around the phosphorus atom and deshielding the signal. ANs greater than 100 are classed as superacids.

Childs method uses trans-crotonaldehyde as the probe molecule and records the downfield shift of the H3 proton by ^{1}H NMR spectroscopy upon complexation to a Lewis acid (Figure 98).[289]

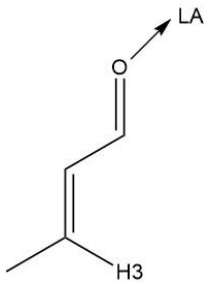

Figure 98. Crotonaldehyde probe molecule developed by Childs *et. al,* showing the position of H3 proton.

Lewis acidity in this scale is measured in comparison to 0.3 M solutions of boron tribromide and hexane in dichloromethane. The relative acidity of the strong Lewis acid, BBr_3, was assigned a value of 1.00 (δ^1H of H^3 = 8.47 ppm), whereas hexane was assigned a value of 0.00 (δ^1H of H^3 = 6.89 ppm). The calculation of relative acidity is given in Equation 17.

$$Relative\ acidity = \frac{\Delta^1 H\ LA\ crotonaldehyde\ adduct}{\Delta^1 H\ BBr_3\ crotonaldehyde\ adduct}$$

Equation 17

Both methods are strongly dependent on Pearson's HSAB principle.[279] $P_{222}O$ is a hard donor which will preferentially bind to hard Lewis acids, whereas the opposite is true for the softer Lewis base, crotonaldehyde. This effect is seen in the Lewis acidity order of a series of boron acids: $B(C_6F_5)_3$, $B(C_6F_5)_2(OC_6F_5)$, $B(C_6F_5)(OC_6F_5)_2$, $B(OC_6F_5)_3$, where the two methods suggest a completely opposite ordering.[290] The softer, largely covalent C=O pπ-pπ bond in crotonaldehyde has a higher affinity for $B(C_6F_5)_3$, while the harder, more ionic pπ-dπ P=O bond of $P_{222}O$ has a higher affinity for $B(OC_6F_5)_3$. Tilley and co-workers[291] also highlighted the HSAB effects with the AN method when they reported a larger difference in the ^{31}P NMR chemical shift of hard bis(catecholato)silane ($\Delta\delta$ = 33 ppm) compared to the powerful soft Lewis acid, $B(C_6F_5)_3$ ($\Delta\delta$ = 27 ppm). These methods are also limited by sterics, as exemplified for the series of $B(C_6F_5)_{3-n}(C_6Cl_5)_n$ (where n = 0-2).[292] With increasing n, one might expect, an increase in Lewis acidity as the C_6Cl_5 groups are more strongly electron withdrawing. However, the dominant effect is the increased steric shielding that these groups provide, and the Lewis acidity decreases as demonstrated with the $P_{222}O$ probe. Demonstrably, the scale of Lewis acidity is both probe dependent and affected by sterics, which makes it very difficult to make meaningful comparisons, especially between different classes of Lewis acids. Most importantly, neither method gives insight into different factors

influencing Lewis acidity: electrostatic interactions (hard Lewis acidity), FMO interactions (soft Lewis acidity) and the energy required for pyramidalization of boron geometry from trigonal planar (sp^2) to tetrahedral (sp^3) upon the adduct formation.

5.1.2.2 Fluoride and hydride ion affinity

Fluoride and hydride ion affinities (FIA/HIA) are based upon the thermodynamics of adduct formation of a Lewis acid with a fluoride or hydride ion.[293] As the fluoride anion is a hard Lewis base, it reflects better hard Lewis acidity, whilst the soft hydride anion better reflects soft Lewis acidity. The small size of both F^- and H^- means they can react with Lewis acids with minimal interference from the probe, with limited to no influence of steric or π-interactions. An effective quantitative scale of Lewis acidity using the most commonly applied FIAs was first presented by Dixon and colleagues in 1996 and 2000.[294,295] As the electron affinity of the F^- anion was then difficult to calculate, it was necessary to determine FIA values *via* isodesmic reactions and corelate it to the experimentally known FIA of compound COF_2 (Equation 18-Equation 20).[293]

$$CF_3O^- + LA \overset{\Delta H}{\rightarrow} COF_2 + [LA{-}F]^-$$

Equation 18

$$CF_3O^- \overset{\Delta H}{\rightarrow} COF_2 + F^-$$

Equation 19

$$LA + F^- \overset{FIA}{\longrightarrow} [LA - F]^-$$

Equation 20

Experimental determination of FIA and HIA is challenging, therefore currently these are derived exclusively through computational means. The limitation of FIA and HIA methods is that they require computational calculations, which may not be available to the experimental chemists. What is more problematic, when computational methods are available, a wide range of models tend to be applied which affects comparability, which has been outlined by Greb and co-workers.[293] They highlight that calculations are often performed at low levels, and in vacuum. Furthermore, the lack of experimental data detracts the reliability of the theoretical results.

FIA and HIA methods are also, of course, dependent on HSAB effects, which results in different order of Lewis acidity returned by each probe. Like the NMR spectroscopic methods, they return one number, which is affected by all three factors: electrostatic interactions, FMO interactions and the energy required for pyramidalization of boron geometry from trigonal planar (sp^2) to tetrahedral (sp^3) upon the adduct formation.

5.1.2.3 A general classification of scaling methods

Besides NMR spectroscopy and computational FIA/HIA approaches, there are other methods of scaling Lewis acidity, which involve the correlation of acid strengths with chemical reactivity,[296–298] spectroscopy (NMR, IR, UV-vis),[246,275,300] or thermochemistry.[301–303] Greb grouped the different scaling methods into three distinct categories of determining Lewis acidity (effective, global, and intrinsic, Figure 99).[304] The first class uses optical (*e.g.*, IR/UV/Vis/ fluorescence) or NMR spectroscopy to measure the interaction between the Lewis acid with a probe molecule, most common examples being the Gutmann AN method and Childs method. Global Lewis acidity considers the thermodynamics of the whole process of adduct formation (*ΔH/ΔG).* It incorporates factors such as deformation energies (E_{def}) and the immediate interaction energy (E_{inter}). The most common scale for this class is FIA. The final class is intrinsic metrics which examine the electronic structure of the uncoordinated, free Lewis acid through quantum theoretical computation or spectroscopy. Properties of the Lewis acid such as the LUMO energy and global electrophilicity index (GEI), based on the propensity of a molecule to take up electrons, and as such, the ranking of Lewis acidities is not defined with respect to a specific base. However, this method does not consider effects that arise from the interaction with a Lewis base, such as deformation energy or repulsion.

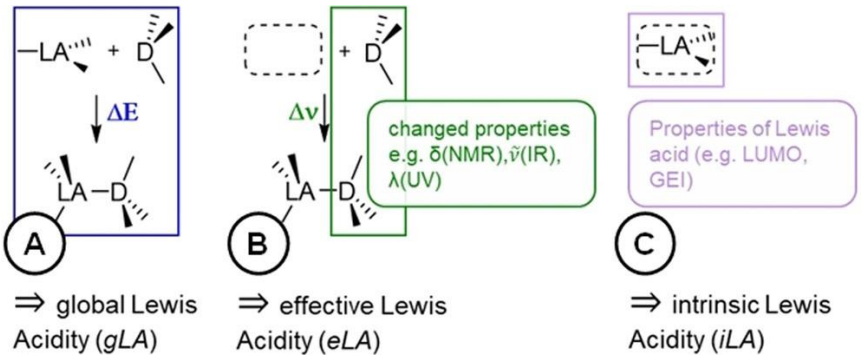

Figure 99: Three classifications of Lewis acidity scaling methods a) global metrics b) effective metrics and c) intrinsic metrics.[304]

Each class has their own advantages and disadvantages. Quantitative comparisons of these different scales often yield poor correlation. Melen and co-workers[305] reported discrepancies between computational (HIA, FIA, and GEI) and experimental (Gutmann AN and Childs) methods, when assessing the Lewis acidity of fluorinated triaryl borates. This was particularly highlighted when comparing FIA and Gutmann AN values. These are the two most common scales of Lewis acidity, and both demonstrate hard Lewis acidity but yet, have poor correlation, and the reasoning is not well understood. Greb *et. al*[304] evaluated the AN method through experiment and theory for a large set of Lewis acids to understand the offset between these scales. It was highlighted that for the AN method the reaction of the Lewis acid and $P_{222}O$ is an equilibrium reaction and therefore the reported ^{31}P NMR chemical shift of $P_{222}O$ represents the equilibrium constant-weighted average chemical shift of free $P_{222}O$ and coordinated $P_{222}O$. Therefore, the equilibrium shown in Figure 100 has a large influence on the reported chemical shift. This may lead to an underestimation of the Lewis acidity of weak Lewis acids due to incomplete adduct formation, especially at low concentrations or 1:1 ratio of Lewis acid:$P_{222}O$. Therefore, it is common to use an excess of Lewis acid to ensure complete adduct formation. Another point to keep in mind with this method is possible probe decomposition which can be seen from the presence of multiple phosphorus environments by NMR or in the case of unexpectedly large chemical shifts.

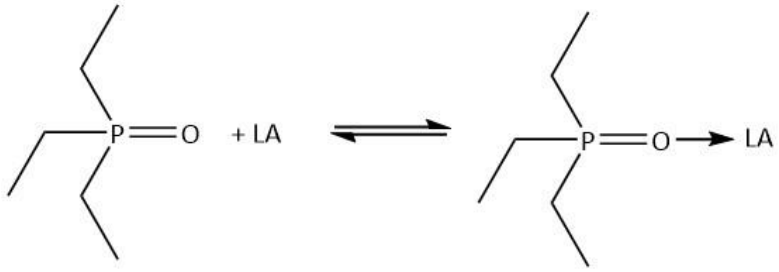

Figure 100. Equilibrium between free $P_{222}O$ and coordinated $P_{222}O$

When looking at links between effective Lewis acidity and global Lewis acidity, poor correlations between the induced NMR shift (eLA) and the $P_{222}O$ binding energy (gLA) were reported. The deformation energy (E_{def}) of the Lewis acid (Figure 101) was identified as the source of deviation between these two classes. This describes the energy required to change geometry of the Lewis acid from trigonal planar to pyramidal. gLA considers the whole process of adduct formation but eLA only sees the interaction energy (E_{inter}) of the two components. Therefore, eLA can be looked at as a type of intrinsic bond strength. It is evident that these two classes describe different properties of Lewis acidity and therefore a strong effective Lewis acid (high AN number) may not necessarily be strong in a thermodynamic or gLA sense. For example, $AlEt_3$ is a strong global Lewis acid as it has a small deformation energy but it is only a moderate effective Lewis acid, whereas tetrahedral Lewis acids

such as $SiCl_4$ are weak global Lewis acids due to their large deformation energy but show strong effective Lewis acidity.[304]

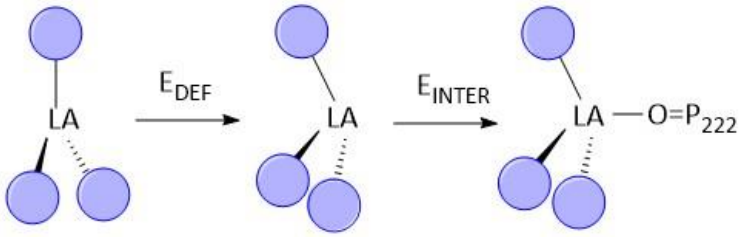

Figure 101. Deformation (E_{DEF}) and interaction energy (E_{INTER}) upon complexation of $P_{222}O$ to a Lewis acid.[304]

In this context, it is transparent how controversial is the use of term "Lewis superacid", which has been used by many authors, but its definition varies depending upon the scale with respect to which it has been defined. Olah suggested that superacids are those that are more acidic than anhydrous $AlCl_3$.[306] Krossing and co-workers suggested a definition based on the FIA-scale, stating that "molecular Lewis acids, which are stronger than monomeric SbF_5, in the gas phase, are Lewis superacids."[307] Corey *et. al* and Yamamoto *et. al* classed oxazaborinanes or trimethylsilyl derivatives as "superacid catalysts" for their effectiveness in promoting challenging Diels-Alder reactions.[308,309] Metal triflates and triflimides have also been defined as superacids as they are derived from the Brønsted superacids HOTf and $HNTf_2$.[310] For the Gutmann acceptor number, an acid reporting an AN greater than 100, is classed as a superacid.[288]

In conclusion, it is evident that the measured strength of a Lewis acid massively depends on what scale is used. While global and effective acidity methods are well established, there is a noticeable gap in experimental measurements for assessing intrinsic acidity. It is important to do this, especially considering the observed inconsistencies between computational methods for global Lewis acidity and experimental data.[293] The scattered range of computational results[293] further emphasises the critical need for more experimental measurements.

5.1.3 X-ray spectroscopy of boron species

Synchrotron radiation is electromagnetic radiation produced when a beam of high energy electrons are accelerated to relativistic speeds and forced to travel along a curved path by strong magnetic fields.[311] This enables high flux of monochromatic light that is required for high-resolution X-ray spectroscopic studies.

There are limited experimental measurements of electronic structure of boron compounds. A major challenge arises from the fact that boron 1s core orbital has an energy of ~200 eV, which is in the soft X-ray range. Conventionally, soft X-ray based techniques require high vacuum conditions because of strong scattering of the emitted electrons by gas molecules under ambient pressures. The vacuum requirement makes it challenging to directly measure volatile liquids and boron Lewis acids with low molecular weight.

Boron electronic structure measurements using XPS have been made since the 1970s for non-volatile solid samples;[312] in addition, a small number of resonant XPS (RXPS) experiments have been made on solid boron nitride.[313] However, the vast majority of chemical reactions, including boron catalysis, occurs in organic solvents; this results in disconnect between fundamental electronic structure data and applications in catalysis, preventing meaningful comparison. To date, the only boron electronic structure measurements in the liquid phase were X-ray absorption spectroscopy (XAS) studies of relatively simple boron-based species, $[BH_4]^-$ and boric acid, irrelevant for Lewis acid catalysis.[314,315]

It is only with the introduction of the liquid micro-jet technique, on synchrotron source XPS instruments, that liquid-phase photoelectron spectroscopy has advanced.[99–106] With the liquid jet sample delivery methodology, pure liquids and solutions are injected into the interaction chamber *via* a 10-20 µm glass capillary, forming free liquid surface in vacuum. Turbo pumps and liquid nitrogen cold-traps maintain the operational pressure around 10^{-4} mbar. The sample then gets ionised by soft X-ray radiation and the emitted photoelectrons are detected and their kinetic energy determined using the hemispherical electron analyser. The electron analyser is positioned about 0.5 mm from the jet, eliminating the effects of inelastic scattering. Jet velocity is typically 100 ms^{-1} and temperature is <10 °C. Under the described conditions, a fast-flowing laminar liquid stream is produced. These conditions, typically the liquid jet's relatively small diameter and high speed enables the study of liquids with high vapor pressure in vacuum conditions necessary for XPS experiments. Furthermore, the distance over which electrons travel is reduced and the effective pressure is reduced by several orders of magnitude over a very short distance. This creates a millimeter-long laminar-flow of liquid, providing a stable surface from which measurements can be performed. A free-flowing sample at high velocity also enables continuous renewal of the liquid surface.[99]

5.1.4 Scope of this work

The aim of this work was to explore the potential of X-ray spectroscopy to develop probe-free approaches to Lewis acidity, which would provide experimental data for intrinsic Lewis acidity (iLA). Originally, this work has been intended as the sole topic of this PhD thesis, and was planned to start from X-ray studies of simple boron

Lewis acids by a variety of X-ray spectroscopies, move on to borenium ionic liquids (that would also be amenable to high-vacuum techniques), and then to other Lewis acids, especially aluminium (organoaluminium compounds, aluminate ionic liquids, and aluminium-based liquid coordination complexes). However, it was interrupted by COVID-19, which shifted the work to neutron scattering studies, working with data collected just before the COVID-19 outbreak. As such, this chapter reports on the first study of six boron Lewis acids by liquid jet XAS, carried out at BESSY II. The continuation of this strand of work has now been taken up by a new PhD student, exploring the same compounds with complementary techniques of X-ray Raman spectroscopy (ESRF) and conventional XAS (Diamond).

5.2 Experimental

5.2.1 Materials and methods

Materials and synthesised products were stored in the glovebox. Unless stated otherwise all reagents were purchased from Sigma Aldrich and used as received. Catechol (99%) was purchased from Fluorochem, recrystallised from toluene and sublimed before use. NMR spectra were recorded on a Bruker Avance DPX 600 MHz spectrometer.

5.2.2 Purification of catechol

Catechol (16.58 g) was dissolved in toluene (100 cm^3, 80 °C, 1 h), cooled in a fridge (7 °C, 12 h) and a white precipitate formed. The precipitate was collected by Büchner filtration. The precipitate was sublimed (80 °C, 10^{-2} mbar, 12 h) to give a white crystalline product. Yield 14.73 g, 92%. ^{1}H NMR (600 MHz, DMSO) δ 6.78, 6.65 ^{13}C NMR (600 MHz, DMSO) δ 145.28, 119.60, 115.75.

5.2.3 Synthesis of tri-butyl borate

Boric acid (0.0809 mol, 5.00 g) and butanol (0.485 mol, 35.96 g) as well as 200 ml toluene, were placed in a 500 ml round-bottomed flask fitted with a Dean-Stark apparatus and heated to 150 °C for 4 h until 4.37 g of water was collected, indicating product formation. Toluene was removed on rotary evaporator and tri-butyl

borate is a colourless liquid, which was collected in quantitative yield. ^{1}H NMR, (400 MHz, $CDCl_3$) δ 3.65 (t, 6H), 1.56 (m, 6H), 1.39 (m, 6H), 0.94 (m, 9H). ^{13}C NMR (400 MHz, $CDCl_3$) δ 64.92, 34.56, 19.93, 12.34.

5.2.4 Synthesis of phenylboronic acid pinacol ester, B(pin)(Ph)

Phenylboronic acid (0.05 mol, 6.10 g) and pinacol (0.05 mol, 5.91 g) as well as 100 ml toluene, were placed in a 250 ml round-bottomed flask fitted with a Dean-Stark apparatus and heated to 150 °C for 4 h until 1.80 g of water was removed, indicating product formation. Toluene was removed on rotary evaporator, giving low viscosity yellow liquid in quantitative yield. ^{1}H NMR, (400 MHz, $CDCl_3$) δ 1.34 (s, 12H), 7.36 (m, 2H), 7.45 (m, 1H) 7.81 (m, 2H). ^{13}C NMR (400 MHz, $CDCl_3$) δ 134.75, 131.26, 127.72, 83.78, 24.89. ^{11}B NMR (400 MHz, $CDCl_3$) δ 31.42.

5.2.5 Synthesis of butyl borate catechol ester, B(cat)(OBu)

A mixture of catechol (0.0449 mol, 49.49 g) and tri-butyl borate (0.0449 mol, 103.44 g) was placed in a 250 ml round-bottomed flask, equipped with a water condenser and heated to reflux for 48 h. After, butanol was distilled at ambient pressure (119-121 °C). The product was purified by distillation under reduced pressure (107-109 °C, ca. 3 mbar) to give a colourless liquid, yield 60.29 g, 70%. ^{1}H NMR (600 MHz, $CDCl_3$) δ 7.11 (m, 2H), 7.02 (m, 2H), 4.16 (t, 2H), 1.71 (m, 2H) 1.47 (m ,2H), 0.98 (t, 3H). ^{13}C NMR (600 MHz, $CDCl_3$) δ 148.02, 122.21, 111.42, 66.09, 32.21, 19.02, 14.57. ^{11}B NMR (600 MHz, $CDCl_3$) δ 23.15.

5.2.6 Synthesis of butyl borate pinacol ester, B(pin)(OBu)

A mixture of pinacol (0.200 mol, 23.62 g) and tri-butyl borate (0.200 mol, 46.01 g) was placed in a 250 ml round-bottomed flask, equipped with a water condenser and was heated to reflux for 48 h. Butanol was distilled off at ambient pressure (118-121 °C) to give a colourless liquid, yield 29.72 g, 74%. ^{1}H NMR (600 MHz, $CDCl_3$) δ 3.84 (t, 2H), 1.55 (m, 2H), 1.38 (m, 2H), 1.25 (s, 12H) 0.91 (t, 3H). ^{13}C NMR (600 MHz, $CDCl_3$) δ 82.07, 64.15, 33.52, 24.55, 18.75, 13.74. ^{11}B NMR (600 MHz, $CDCl_3$) δ 22.98.

5.2.7 Synthesis of butyl boronic acid pinacol ester, B(pin)(Bu)

Pinacol (0.0626 mol, 7.40 g) and butyl boronic acid (0.0626 mol, 6.38 g) as well as 100 ml toluene, were placed in a 250 ml round-bottomed flask fitted with a Dean-Stark apparatus and heated to 150 °C for 4 h until 2.25 g of water was removed, indicating product formation. Toluene was removed on rotary evaporator, giving a slight yellow liquid in quantitative yield. ^{1}H NMR (600 MHz, $CDCl_3$) δ 1.37 (m, 2H), 1.28 (m, 2H), 1.23 (s, 12H), 0.86 (t, 3H) 0.76 (m, 2H). ^{13}C NMR (600 MHz, $CDCl_3$) δ 82.80, 26.20, 25.39, 24.79, 18.75, 13.86. ^{11}B NMR (600 MHz, $CDCl_3$) δ 33.24.

5.2.8 Synthesis of phenylboronic acid, 2-amino benzyl alcohol ester, B(C_7H_9NO)(Ph)

Phenylboronic acid (0.082 mol, 10.00 g) and 2-amino benzyl alcohol (0.082 mol, 10.10 g) as well as 100 ml toluene, were placed in a 250 ml round-bottomed flask fitted with a Dean-Stark apparatus and heated to 150 °C for 4 h until 2.95 g of water was removed, indicating product formation. Toluene was removed on rotary evaporator, giving a very pale orange solid in quantitative yield. ^{1}H NMR (600 MHz, $CDCl_3$) δ 5.21 (s, 2H), 5.80 (s, 1H), 6.71 (d, 1H), 6.88 (t, 1H), 7.14 (d, 1H), 6.95 (t, 1H) 7.39 (m, 2H), 7.44 (m, 1H), 7.74 (d, 2H). ^{13}C NMR (600 MHz, $CDCl_3$) δ 64.76, 115.35, 121.22, 122.71, 125.00, 127.95, 128.26, 130.68, 132.72, 138.98. ^{11}B NMR (600 MHz, $CDCl_3$) δ 29.68

5.2.9 Gutmann Acceptor Number Measurements

For each boron compound in the liquid state, three samples (*ca.* 0.5 g each) were weighed out accurately into sample vials. Triethylphosphine oxide ($P_{222}O$) was weighed accurately into each sample (*ca*. 1, 2 and 3 wt%) and mixed thoroughly. ^{31}P NMR spectra were recorded for the three concentrations, and the chemical shift value was extrapolated to the value of infinite dilution. The acceptor number was calculated according to Equation 16.

For each boron compound in the solid state, 1:1 adducts with $P_{222}O$ were prepared as described by Gutmann.[283] Solutions of accurately weighed boron compounds (*ca*. 0.58 mmol) in accurately known volumes of 1,2-dichloroethane (*ca*. 1.5 cm^3) were prepared to achieve concentrations of *ca.* 0.35 mol dm^{-3}. To each solution, 1 mol eq. of $P_{222}O$ (*ca*. 0.58 mmol) was added, and the mixture was stirred for 30 min. All solids dissolved readily upon the addition of $P_{222}O$. The ^{31}P NMR spectra of the solutions were recorded, and then

the solutions were diluted to *ca*. 0.25 mol dm^{-3}, and subsequently to *ca*. 0.20 mol dm^{-3}, with ^{31}P NMR spectra recorded for each concentration. The recorded ^{31}P NMR chemical shifts were plotted as a function of concentration and extrapolated to infinite dilution of $P_{222}O$ in the studied sample. The acceptor number was calculated according to Equation 16.

5.2.10 Child's method

Boron compound and trans-crotonaldehyde were mixed in a 1:1 ratio in dry CD_2Cl_2 and placed in a 5 mm borocilicate NMR tube. The ^1H NMR spectrum was then acquired, and the chemical shift of the H3 proton of crotonaldehyde was recorded. The relative acidity was calculated according to Equation 2.

5.2.11 XAS measurements

Experiments were performed at the U49/2 PGM-1 beamline at the BESSY II synchrotron facility (Helmholtz-Zentrum Berlin für Materialien und Energie), with SOL^3PES (Solid, Solution and Solar Photoelectron Spectroscopy) end-station,[316] using liquid-jet apparatus. Solutions of the boron compounds in anhydrous acetonitrile (0.5 M) were prepared in the glovebox. XAS spectra were collected by incrementing the photon energy (0.05 eV step size) across the boron adsorption edge, 190–215 eV.

5.3 Results and discussion

5.3.1 Sample selection

As boron 1s X-ray spectroscopy is not commonly measured, there is limited literature data for reference species to compare to our samples of interest. It was important to select samples that have importance in Lewis acid catalysis and that were structurally simple, for the ease of interpretation and comparison in the first liquid-jet XPS measurements of boron. Six tricoordinate boron compounds were studied (Figure 102), which dissolved in acetonitrile, were relatively stable towards moisture in the air, and had a good selection of B-C, B-N and B-O bonding, in addition to comparison between aliphatic and aromatic motifs.

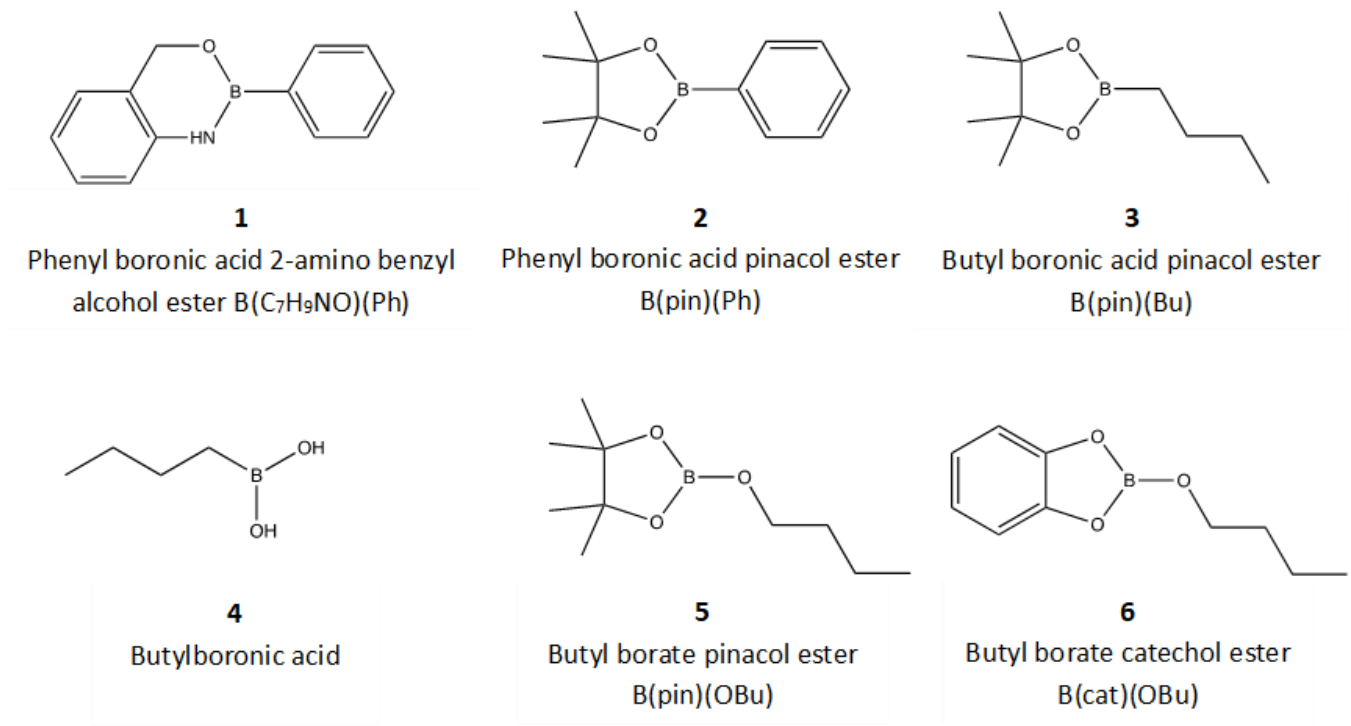

Figure 102. Boron compounds studied using XPS.

5.3.1.1 X-ray absorption spectroscopy

B 1s XAS was measured for the six boron compounds and the peak energies compared to DFT calculations (Figure 103). A single trigonal boron peak at *ca*. 194 eV is attributed to the transition of an electron from the B 1s state to the unoccupied B 2pz orbital. A lower peak energy means a lower boron LUMO energy which would translate into a greater Lewis acid as the boron would more readily accept electrons. Excellent correlation between the experimental (Figure 103, left) and DFT calculations (Figure 103, right) has been observed. The experimental B 1s XAS spectra for compound **1** is quite noisy, due to difficulties in getting the liquid-jet to stabilise.

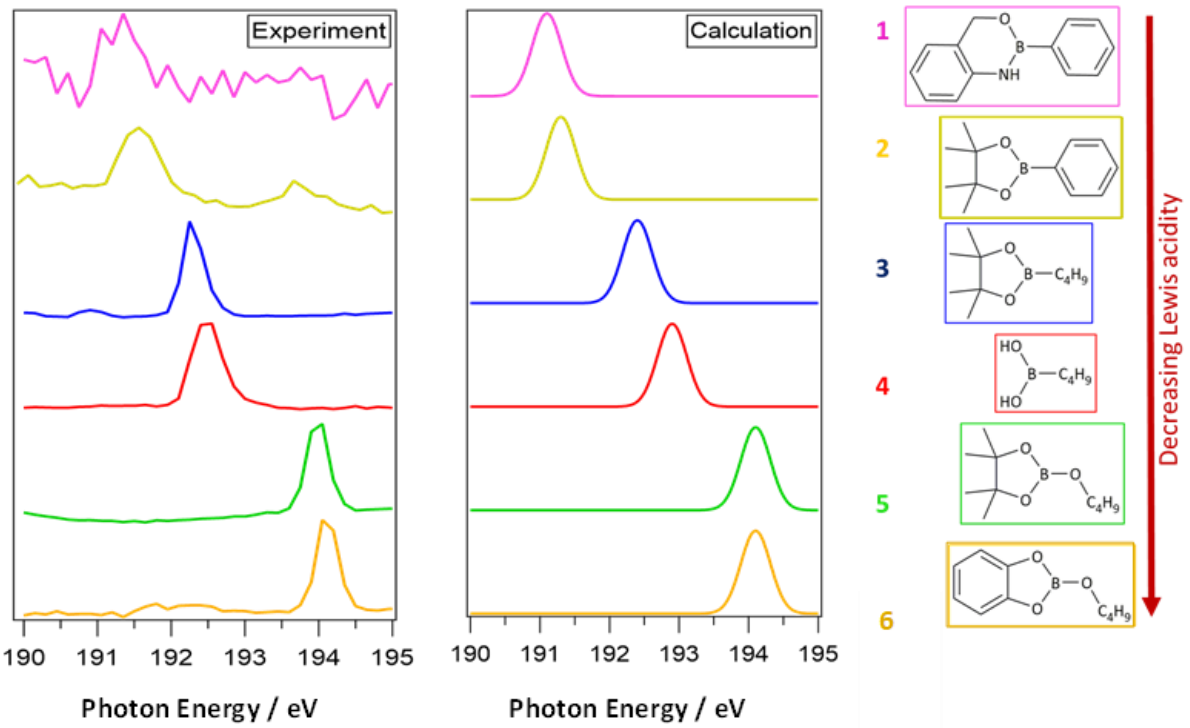

Figure 103. Experimental (left) and calculated (right) boron 1s XAS data for the six boron compounds studied.

It is evident that the peak energy varies greatly with structure, up to 3 eV (Table 18). This demonstrates that structure (electronic environment around the boron centre) has a large effect on the B 1s $\rightarrow \pi^*$ energy, even amongst charge-neutral tricoordinate boron compounds; in consequence, there is the potential to use this technique to rank a larger number of these compounds.

Table 18. Comparison of boron 1s XAS experimental and calculated peak energies as shown in Figure 103 for boron compounds **1-6**.

Compound number	Experimental peak energy (eV)	Calculated peak energy (eV)
1	191.3	191.1
2	191.6	191.3
3	192.3	192.4
4	192.5	192.9
5	194.0	194.1
6	194.1	194.1

The introduction of nitrogen or oxygen, adjacent to the boron centre often leads to a reduction in Lewis acidity. These heteroatoms can inductively withdraw electron density from boron, however, lone pairs on nitrogen and oxygen will donate electron density back into the empty p_z orbital on boron, reducing the Lewis acidity. Therefore, it was not surprising that the largest B 1s $\rightarrow \pi^*$ energy has been recorded for compounds **5** and **6**,

which both have three B-O bonds. Despite oxygen being a very electronegative element (3.44), which can withdraw electron density from the boron centre, the π-back-bonding from oxygen to empty p orbital of boron is the dominant factor, rendering these compounds least acidic. Butyl boronic acid (**4**) was more Lewis acidic (the B 1s → π* energy lower by 1.5 eV), because one oxygen has been replaced with carbon, which is only slightly more electronegative than boron (2.55 *vs*. 2.04) but has no capability for π-back-bonding. Quite remarkably, changing the two B-OH bonds in **4** to two B-O-C bonds in **3** further lowered the B 1s → π* energy by 0.2 eV. This could be due to carbon being slightly more electronegative than hydrogen (2.55 *vs.*2.20) leading to greater inductive withdrawal of electron density from boron in **3**. Furthermore, replacing the aliphatic butyl chain with an aromatic phenyl substituent lowered the B 1s → π* energy by 0.7 eV. It was initially thought that this substitution would have the opposite effect due to back donation from the aromatic π electron system to the boron p orbital, thereby lowering Lewis acidity. This expectation stemmed from the assumption that the aromatic ring, being in-plane with the pinacol ring, would facilitate this interaction. The crystal structure of 4-fluorophenyl boronic acid catechol ester supported this, revealing the alignment of the aromatic ring with the catechol ring (Figure 104).[317] Notably, if rotated, this configuration minimises the potential for effective back-bonding, and the dominant effect is the inductive withdrawal of electron density from boron. Considering the aliphatic chain, there is another effect which is hyperconjugation between the adjacent C-H σ bond and the empty boron p-orbital, which is not seen with the aromatic phenyl substituent. The delocalisation of σ electrons into the empty boron p-orbital will lower Lewis acidity. This could explain the higher acidity observed upon replacing the aliphatic chain with an aromatic phenyl substituent. Finally, compound **1** is the most Lewis acidic; it has one B-O bond and one B-N bond. Nitrogen is less electronegative than oxygen (3.04 *vs*. 3.44), therefore the electron withdrawing effect along the σ bond is lower; however, there is less effective π-backdonation from nitrogen to boron, due to the difference in the orientation of respective orbitals.

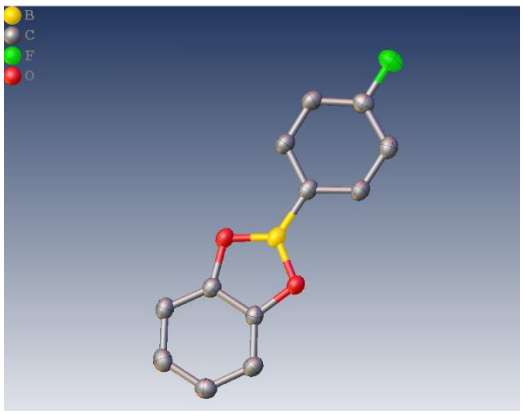

Figure 104. Crystal structure image of 4-fluorophenyl boronic acid catechol ester.

The difference in peak energy between experimental (192.5 eV) and DFT (192.9 eV) for compound **4** could be explained due to the DFT calculations being carried out in the gas phase *vs.* the liquid phase in the experimental. **4** is the only compound with hydroxyl groups that are available for hydrogen bonding. This hydrogen bonding is not considered in the gas phase DFT calculations.

These preliminary results have validated the new approach of using boron 1s X-ray spectroscopy to gain insight into Lewis acidity of tricoordinate compounds of boron. Such experimental XAS data can be used as a benchmark to validate a wider range of calculated B 1s XAS spectra, exploring the potential to use relatively simple calculations of LUMO energies as a complementary measure of Lewis acidity. It is important to keep in mind that this method provides experimental information about the LUMO energy of the Lewis acid (iLA), which is very valuable, but is only one aspect of Lewis acidity (Figure 99).

5.3.1.2 Comparison with Gutmann Acceptor Number and Child's method measurements

Gutmann AN is more commonly used than Child's method in the literature. Surprisingly, there were limited AN values reported for boron Lewis acids, and even when some AN values were measured, diverse methodologies were used,[318–322] preventing meaningful comparison between values given by different authors. Therefore, in this work, Lewis acidity of the six boron compounds measured by XAS was also quantified *via* the Gutmann acceptor number and Child's method (Table 19). Literature AN values for four common boron Lewis acids were added for comparison.

Table 19. AN values for all boron compounds at 300 K shown with the $\delta^{31}P$ resonances recorded (in ppm) measured for solutions of these liquids containing 1, 2 and 3 mol% $P_{222}O$ (referenced to $\delta^{31}P$, H_3PO_4 85% = 0 ppm).

Compound	**$\delta^{31}P$**			**AN**	**CA $\Delta\delta^{1}H$**
	1%	2%	3%		
B(cat)(OBu) **6**	82.89	82.88	82.89	93.7	0.03
B(pin)(OBu) **5**	48.29	48.35	48.35	12.4	0.02
Butylboronic acid **4**	54.83	54.83	54.83	27.8	0.00
B(pin)(Bu) **3**	47.64	47.48	47.61	10.9	0.01
B(pin)(Ph) **2**	46.65	46.65	46.65	8.6	0.00
$B(C_7H_9NO)(Ph)$ **1**	51.07	51.07	51.07	19.0	0.01
BCl_3				106[320]	

B(cat)(Ph)	65.4[319]
$B(C_6F_5)_3$	78.0[323]
$B(OBu)_3$	11.8[320]

The AN values for the six boron compounds were lower than expected (AN < 30), apart from compound **6,** B(cat)(OBu) which was significantly higher than expected (AN = 93.7). This was a confusing outcome, as the AN values measured in this work did not follow any conceivable trend in their order of the effective Lewis acidity (eLA), reported by the AN measurements. This is not an observation unique to this work; the same conclusions of ineffective complex formation and confusing AN values have also been reported by others, for example in a study of phenylboronates by Żukowska *et. al.*[318] What is more, in Child's method, only very slight shifts of the H3 atom of crotonaldehyde (CA) were recorded, $\Delta\delta$ = 0.01-0.03 ppm, suggesting the lack of adduct formation (Table 19). Melen and co-workers[305] also reported very small shifts using the Child's method ($\Delta\delta$ = 0.02-0.03 ppm), when assessing the Lewis acidity of fluorinated triaryl borates, which are generally considered stronger Lewis acids than the Lewis acids reported in this work.

There are multiple factors to consider, such as energy required to change the geometry, as well as steric hindrance, which have major influence on the reactions between a spectroscopic probe and a Lewis acid. First and foremost, however, it must be emphasised that AN method relies on an equilibrium reaction, and chemical exchange may be rapid at the NMR time scale. This means that the observed ^{31}P NMR signal represents the weighted average chemical shift of the coordinated and uncoordinated $P_{222}O$,[319] failing to report accurately on Lewis acidity for Lewis acids that are not very strong (see other factors affecting AN values, already discussed in Section 5.1.2.1). Again, it has been already reported in the literature that both AN and Childs method significantly underestimate the Lewis acidity of weak Lewis acids, which has been attributed to incomplete adduct formation.[304] Melen and co-workers investigated Lewis acidity for a series of fluorinated triaryl borates ($B(OAr^F)_3$), and the analogous boranes. They showed that the borates were stronger Lewis acids than the corresponding boranes according to the AN method, but the opposite was found when comparing the energy of their frontier orbitals by computational methods.[305]

Unsurprisingly, plotting of AN values against the B 1s $\rightarrow \pi^*$ energies (Figure 105) yields very poor corelation between the two measured values. In another example, Lewis acidity of chloroaluminate ionic liquids is consistently overestimated by the AN method, which returns very high values (AN >90) for ionic liquids containing the $[AlCl_4]^-$ anion, which is not an active Lewis acid under most conditions.[324,287] On the other hand, AN measurements have been used by our group in the past with success, reporting accurately on Lewis acidity of many chlorometallate families, in perfect correlation with speciation studied by a diverse range of spectroscopic techniques.[325,326] Furthermore, AN studies of Lewis superacidic borenium ionic liquids were very well correlated with their performance in catalytic reactions.[298] In conclusion, whereas AN method has its uses,

it must be treated with great caution. Currently, it is the method of choice for much of the Main Group community, but it appears that it can be very misleading, in particular for weaker boron Lewis acids. A more effective approach may involve the application of FIA or HIA calculations, which can be more robust when appropriate modelling standards are adhered to, as outlined by Greb and co-workers.[293] They emphasise the importance of high-level modelling using accurate computational models and methods and correcting for solvation effects.

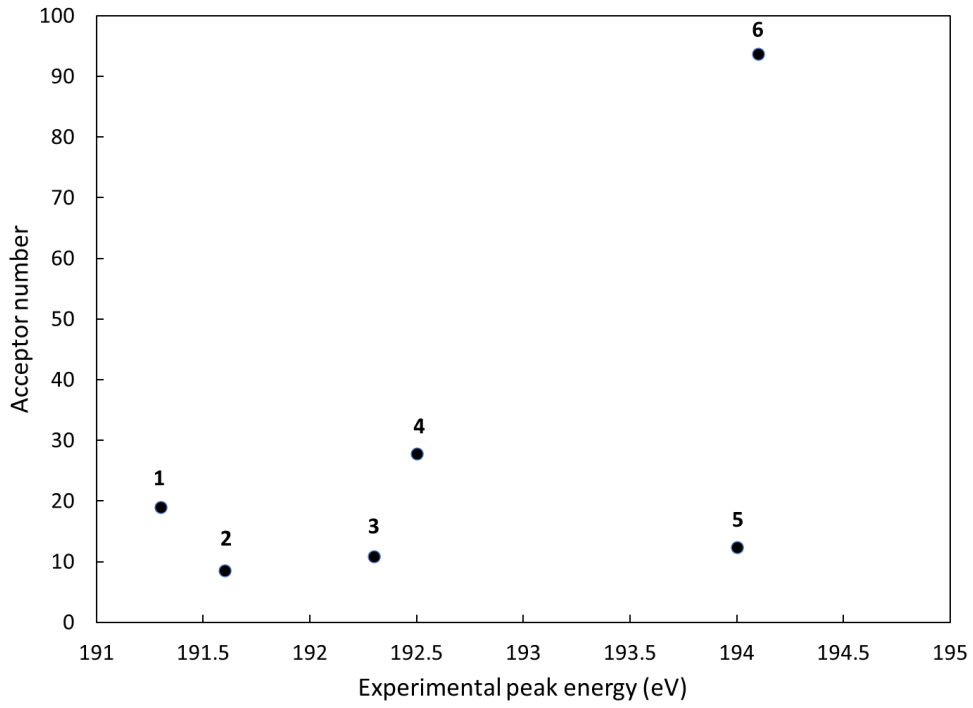

Figure 105. Plot of AN values against the boron 1s XAS experimental peak energies for compounds **1-6**, showing poor correlation between the two measured values.

It is evident that there are many factors that need to be considered when describing Lewis acidity such as electrostatic interactions, FMO interactions and the energy required for pyramidalization of boron geometry from trigonal planar (sp^2) to tetrahedral (sp^3) upon adduct formation. There are many scales which exist to determine Lewis acidity, each with their own advantages and disadvantages. However, it is unclear which aspect of Lewis acidity they report, and how gLA, eLA and iLA are related. As discussed, quantitative comparisons of different scales often lead to poor correlation and in some cases completely opposite trends are reported. The Gutmann acceptor number provides a quick and simple method of quantifying Lewis acidity but it uses a probe molecule which better describes hard Lewis acidity and it is also affected by sterics. This makes it very difficult to make meaningful comparisons, especially between different classes of Lewis acids. This method also relies on an equilibrium reaction, and chemical exchange may be rapid at the NMR time scale. This means that the observed ^{31}P NMR signal represents the weighted average chemical shift of the

coordinated and uncoordinated $P_{222}O$, failing to report accurately on weak Lewis acids. FIA calculations are also a popular scale due to the minimal influence of the Lewis base probe as the fluoride ion is small in size. There is also a significant amount of literature data available. The disadvantages to this method are the scattered range of computational methods which affects comparability and the lack of experimental data which affects reliability of the theoretical results. Additionally, it is common that solvation effects are not accounted for. While these global and effective acidity methods are well established, there is a noticeable gap in experimental measurements for assessing intrinsic acidity. It is important to do this, especially considering the observed inconsistencies between computational methods for global Lewis acidity and experimental data. The scattered range of computational results further emphasises the critical need for more experimental measurements. This is where B 1s XAS method fits in by providing experimental measurements of the LUMO energy of boron Lewis acids. The advantage of this technique is that it looks at the uncoordinated Lewis acid and doesn't require the use of a probe molecule. However, the disadvantage of that is that it misses some important information regarding how the Lewis acid interacts with a Lewis base. Furthermore, the use of a synchrotron is required, therefore this technique is expensive and not readily available. However, it is hoped that such experimental XAS data can be used as a benchmark to validate a wider range of calculated B 1s XAS spectra, exploring the potential to use relatively simple calculations of LUMO energies as a complementary measure of Lewis acidity. It is important to keep in mind that this method provides experimental information about the LUMO energy of the Lewis acid (iLA), which is very valuable, but is only one aspect of Lewis acidity. Therefore, there isn't one method that currently exists that looks at every aspect of Lewis acidity and there are advantages and disadvantages to each technique.

5.4 Conclusions and Outlook

In conclusion, it is evident that the measured strength of a Lewis acid massively depends on what scale is used. The aim of this work was to explore the potential of X-ray spectroscopy to develop probe-free approaches to Lewis acidity, which would provide experimental data for intrinsic Lewis acidity (iLA). B 1s XAS shows promise as a method to quantify Lewis acidity, distinguishing between weak Lewis acids, not quantifiable by AN. The experimental data shows excellent agreement with DFT calculations of B 1s XAS, with the goal being to explore the potential to use relatively simple calculations of LUMO energies as a complementary measure of Lewis acidity. However, the liquid jet technique has its drawbacks: (i) only low-viscosity solutions in a limited range of solvents could be studied, (ii) relatively large sample quantities were needed, (iii) exclusion of atmospheric moisture was impossible, which excluded the study of very strong Lewis acids, sensitive to moisture. This prevented us from investigating samples of key interest, such as borenium ionic liquids or Piers' borane (an archetypal Lewis acid in FLP chemistry). This work has discussed the problems of quantifying Lewis acidity and

has highlighted the many different components that can influence Lewis acidity. It has also outlined the most common methods of scaling Lewis acidity and their advantages and disadvantages. This work has opened up a new branch of study in the group which has been taken over by a new PhD student. The boron compounds synthesised in this work, along with Lewis acidic borenium ionic liquids were used for B 1s resonance Raman spectroscopy measurements at the European synchrotron radiation facility (ESRF), Grenoble, France. This technique allows the direct comparison of the electronic structure for neat boron Lewis acids irrespective of their physical state: crystal, molecular liquid, ionic liquid, as well as solution, without the need for vacuum experimental conditions or large quantities of sample. In addition to this, soft X-ray measurements were carried out on the boron containing samples using the B07 beamline at Diamond. Furthermore, the boron compounds in this work were also synthesised for a study exploring their use as lubricant additives (paper in preparation).

6. Summary and conclusions

A major theme in this thesis was elucidating the structure of the liquid phase, including both protic and aprotic ionic liquids, and solutes in these media. Neutron scattering studies were used to: understand the role of water in the phase behaviour of ionic liquids based on sulfuric acid, elucidate the liquid structure and hydrogen bonding motifs in $[NTf_2]^-$ ionic liquids, and to investigate the structure of FLP encounter complexes in ionic liquids and molecular solvents. A secondary theme was the study of Lewis acidity of boron compounds by an array of spectroscopic techniques. Notably, this work pioneered several new approaches, such as the first use of Dissolve for the analysis of ionic liquids by neutron scattering, as well as the first liquid-jet XPS measurements of boron compounds.

Chapter 2 reported on the neutron scattering structural studies of Brønsted acidic protic ILs based on sulfuric acid. The aim was to provide an insight into the relationship between the performance of PILs in esterification reactions and biomass pre-treatment processes and their liquid structure. The study showed that water doped into these Brønsted acidic protic ILs promotes phase separation of hydrophobic esters, and the dissolution of lignin, due to its incorporation into the $\{SO_4\}$ network. This essentially forms a new water-in-salt solvent system, with its own distinct structure and physicochemical properties. This finding allows for certain speculations in terms of the relationship between the phase behaviour and the liquid structure. In esterification reactions, the IL gradually binds the water that is generated upon the formation of an ester, and the resulting hydrated IL phase separates from the weakly hydrophilic ester product. In contrast, such a hydrated IL is excellent in hydrogen bonding to lignin and thereby more efficient in dissolving it.

Chapter 3 focused on the study of ionic liquids with long alkyl chains by neutron scattering using Dissolve. Firstly, a detailed approach to the synthesis of fully deuteriated $[P_{666,14}][NTf_2]$ is reported which can be expanded very easily to other anions, and easily adopted to many different phosphonium cations. Secondly, the structure of three ionic liquids based on the $[NTf_2]^-$ anion is reported for the first time using neutron scattering: $[C_2mim][NTf_2]$, $[C_{10}mim][NTf_2]$ and $[P_{666,14}][NTf_2]$. This study demonstrated the suitability of the Dissolve methodology for the analysis of long chained ionic liquids. The robustness of the Dissolve approach was demonstrated by generating three independent models for each of the three ionic liquids, starting from three different potential sets for cations, and reaching convergent results for each IL, across the three models. Analysis of the neutron scattering data showed that $[C_{10}mim][NTf_2]$ and $[P_{666,14}][NTf_2]$ exhibit substantial nanosegregation compared to $[C_2mim][NTf_2]$, induced by the presence of long alkyl chains. It has been demonstrated that protons on the imidazolium ring in $[C_2mim][NTf_2]$ and $[C_{10}mim][NTf_2]$, as well as H-C-P protons in $[P_{666,14}][NTf_2]$ participate in hydrogen bonding, with oxygen and nitrogen atoms in the $[NTf_2]^-$ anion acting as hydrogen bond acceptors, with the dominant interaction to the oxygen. From bond distance and

angle analysis, it was evident that bulkier cations promote more linear hydrogen bonds, and that hydrogen bonding to oxygen is more directional that that to nitrogen.

Chapter 4 covered neutron scattering structural studies of FLP encounter complexes in benzene and two ionic liquids – $[C_2mim][NTf_2]$ and $[C_{10}mim][NTf_2]$. This work showed persistence of encounter complexes in ILs compared to benzene, with only 0.7% of FLP molecules associated at distances $\leq$ 7.0 Å in benzene, compared to 6.05% in $[C_2mim][NTf_2]$ and 18.47% in $[C_{10}mim][NTf_2]$. Furthermore, 4.59% of the total FLP components formed close contact encounter complexes in $[C_{10}mim][NTf_2]$, with B···P separation of $\leq$6.0 Å. In addition, this work explored both the capabilities and limitations of Dissolve in a very challenging model.

Chapter 5 was inspired by the challenges of quantifying Lewis acidity and explored the different factors that influence Lewis acidity. This work highlighted that the measured strength of a Lewis acid massively depends on what scale is used. B 1s X-ray absorption spectroscopy was introduced as a probe-free approach to studying Lewis acidity, which provides experimental data for intrinsic Lewis acidity (iLA). The experimental data showed excellent agreement with DFT calculations of B 1s XAS. The challenges of liquid-jet X-ray spectroscopy were described, and future directions of the project were outlined. This included exploring the same boron compounds with complementary techniques of X-ray Raman spectroscopy (ESRF) and conventional XAS (Diamond).

In conclusion, the structure and behaviours of both protic and aprotic ionic liquids has been investigated, shedding light on their phase behaviour and interactions with solutes. Through the use of neutron scattering, the role of water in sulfuric acid-based ionic liquids, the liquid structure of $[NTf_2]^-$ ionic liquids, and the formation of FLP encounter complexes have been elucidated. Additionally, new approaches such as the application of Dissolve for neutron scattering analysis of ionic liquids and liquid-jet XPS measurements of boron compounds have been explored. Furthermore, the exploration of Lewis acidity not only highlights the importance of methodology in measurement but also presents avenues for future research.

7. Future work

Future work from chapter two would involve the study of these Bronsted acidic protic ionic liquid systems in the presence of water, and either lignocellulosic biomass or esters. Neutron scattering studies of these model compounds in both wet and dry protic ILs would enable a comparison of the extent of their solvation.

In chapter 3 hydrogen bonding was observed between protons on the imidazolium ring in $[C_2mim][NTf_2]$ and $[C_{10}mim][NTf_2]$, as well as H-C-P protons in $[P_{666,14}][NTf_2]$, with oxygen and nitrogen atoms in the $[NTf_2]^-$ anion acting as hydrogen bond acceptors. This was confirmed by bond distance and angle analysis, but further investigation could be carried out using other techniques such as Raman spectroscopy to observe the change

in polarisability of the S=O bond, to further confirm the findings. Additionally, it would be most valuable to accomplish the study of liquid-liquid phase transitions in phosphonium ILs, omitting the problem of enhanced propensity to crystallise. Such study would give unique insight into less common phase changes, not only in IL but in the broader field of soft matter studies.

Chapter four provided some evidence of persistence of encounter complexes in ionic liquids compared to organic solvents. However, there were questions raised surrounding the aggregation of BCF molecules, seen in the simulation and whether this was a real feature of the system or not. Future work could involve investigating this further such as using NIMROD instrument to record data on these systems to better access long-range structural data. Furthermore, parallel modelling across a hundred simulation boxes could be attempted to gain a robust picture of long-range order in these solutions.

Chapter five highlighted challenges involved in measuring Lewis acidity and introduced the use of B 1s X-ray absorption spectroscopy as a probe-free approach. Future work would involve the use of complementary techniques such as B 1s resonance Raman spectroscopy measurements at the European synchrotron radiation facility (ESRF), Grenoble, France. This technique allows the direct comparison of the electronic structure for neat boron Lewis acids irrespective of their physical state: crystal, molecular liquid, ionic liquid, as well as solution, without the need for vacuum experimental conditions or large quantities of sample. In addition to this, soft X-ray measurements could be carried out on boron containing samples using the B07 beamline at Diamond. This will allow comparisons of results between techniques and will allow for a wider range of boron compounds to be studied.

8. Bibliography

1 T. Welton, *Chem. Rev.*, 1999, **99**, 2071–2084.

2 R. Hayes, G. G. Warr and R. Atkin, *Chem. Rev.*, 2015, **115**, 6357–6426.

3 T. L. Greaves and C. J. Drummond, *Chem. Soc. Rev.*, 2008, **37**, 1709–1726.

4 H. Wang, G. Gurau and R. D. Rogers, *Chem. Soc. Rev.*, 2012, **41**, 1519–1537.

5 H. E. Fischer, A. C. Barnes and P. S. Salmon, *Reports Prog. Phys.*, 2006, **69**, 233–299.

6 A. K. Soper, *Chem. Phys.*, 1996, **202**, 295–306.

7 A. K. Soper, *Mol. Phys.*, 2001, **99**, 1503–1516.

8 A. K. Soper, *Chem. Phys.*, 2000, **258**, 121–137.

9 T. F. Headen, C. A. Howard, N. T. Skipper, M. A. Wilkinson, D. T. Bowron and A. K. Soper, *J. Am. Chem. Soc.*, 2010, **132**, 5735–5742.

10 S. Imberti and D. T. Bowron, *J. Phys. Consens. Matter*, 2010, **22**, 404212–404224.

11 M. Falkowska, D. T. Bowron, H. G. Manyar, C. Hardacre and T. G. A. Youngs, *ChemPhysChem*, 2016, **17**, 2043–2055.

12 J. A. Mccune, A. H. Turner, F. Coleman, C. M. White, S. K. Callear, T. G. A. Youngs, M. Swadźba-Kwäny and J. D. Holbrey, *Phys. Chem. Chem. Phys.*, 2015, **17**, 6767–6777.

13 A. H. Turner, S. Imberti, M. Swadźba-Kwaśny and J. D. Holbrey, *Faraday Discuss.*, 2018, **206**, 247–263.

14 R. Hayes, S. Imberti, G. G. Warr and R. Atkin, *Angew. Chem. Int. Ed.*, 2013, **52**, 4623–4627.

15 M. Deetlefs, C. Hardacre, M. Nieuwenhuyzen, O. Sheppard and A. K. Soper, *J. Phys. Chem. B*, 2005, **109**, 1593–1598.

16 C. Hardacre, J. D. Holbrey, M. Nieuwenhuyzen and T. G. A. Youngs, *Acc. Chem. Res.*, 2007, **40**, 1146–1155.

17 R. Atkin and G. G. Warr, *J. Phys. Chem. B*, 2008, **112**, 4164–4166.

18 O. Russina, A. Triolo, L. Gontrani and R. Caminiti, *J. Phys. Chem. Lett.*, 2012, **3**, 27–33.

19 A. Triolo, O. Russina, H. J. Bleif and E. Di Cola, *J. Phys. Chem. B*, 2007, **111**, 4641–4644.

20 Y. Wang, W. Jiang and G. A. Voth, *J. Am. Chem. Soc*, 2005, **127**, 12192–12193.

21 Y. Wang and G. A. Voth, *J. Phys. Chem. B*, 2006, **110**, 18601–18608.

22 J. N. A. Canongia Lopes and A. A. H. Pádua, *J. Phys. Chem. B*, 2006, **110**, 3330–3335.

23 J. D. Bernal, *Proc. R. Inst. G. Br.*, 1959, **37**, 355–393.

24 J. D. Bernal and R. H. Fowler, *J. Chem. Phys.*, 1933, **1**, 515–548.

25 J. S. Wilkes, J. A. Levisky, R. A. Wilson and C. L. Hussey, *Inorg. Chem.*, 1982, **21**, 1263–1264.

26 A. A. Fannin, D. A. Floreani, L. A. King, J. S. Landers, B. J. Piersma, D. J. Stech, R. L. Vaughn, J. S. Wilkes and J. L. Williams, *J. Phys. Chem.*, 1984, **88**, 2614–2621.

27 J. S. Wilkes and M. J. Zaworotko, *J. Chem. Soc. Chem. Commun.*, 1992, 965–967.

28 C. J. Margulis, *Mol. Phys.*, 2004, **102**, 829–838.

29 S. M. Urahata and M. C. C. Ribeiro, *J. Chem. Phys.*, 2004, **120**, 1855–1863.

30 L. Gontrani, O. Russina, F. Lo Celso, R. Caminiti, G. Annat and A. Triolo, *J. Phys. Chem. B*, 2009, **113**, 9235–9240.

31 H. K. Kashyap, C. S. Santos, H. V. R. Annapureddy, N. S. Murthy, C. J. Margulis and E. W. Castner, *Faraday Discuss.*, 2012, **154**, 133–143.

32 O. Russina, A. Triolo, L. Gontrani, R. Caminiti, D. Xiao, L. G. Hines, R. A. Bartsch, E. L. Quitevis, N. Plechkova and K. R. Seddon, *J. Phys. Condens. Matter*, 2009, **21**, 424121.

33 A. Triolo, O. Russina, B. Fazio, R. Triolo and E. Di Cola, *Chem. Phys. Lett.*, 2008, **457**, 362–365.

34 J. C. Araque, J. J. Hettige and C. J. Margulis, *J. Phys. Chem. B*, 2015, **119**, 12727–12740.

35 J. J. Hettige, H. K. Kashyap, H. V. R. Annapureddy and C. J. Margulis, *J. Phys. Chem. Lett.*, 2013, **4**, 105–110.

36 H. K. Kashyap, C. S. Santos, R. P. Daly, J. J. Hettige, N. S. Murthy, H. Shirota, E. W. Castner and C. J. Margulis, *J. Phys. Chem. B*, 2013, **117**, 1130–1135.

37 H. K. Kashyap, J. J. Hettige, H. V. R. Annapureddy and C. J. Margulis, *Chem. Commun.*, 2012, **48**, 5103–5105.

38 E. Bodo, L. Gontrani, A. Triolo and R. Caminiti, *J. Phys. Chem. Lett.*, 2010, **1**, 1095–1100.

39 A. Triolo, O. Russina, R. Caminiti, H. Shirota, H. Y. Lee, C. S. Santos, N. S. Murthy and E. W. Castner, *Chem. Commun.*, 2012, **48**, 4959–4961.

40 C. Hardacre, J. D. Holbrey, C. L. Mullan, T. G. A. Youngs and D. T. Bowron, *J. Chem. Phys.*, 2010, **133**, 4–11.

41 C. Hardacre, J. D. Holbrey, S. E. J. McMath, D. T. Bowron and A. K. Soper, *J. Chem. Phys.*, 2003, **118**, 273–278.

42 C. Hardacre, S. E. J. McMath, M. Nieuwenhuyzen, D. T. Bowron and A. K. Soper, *J. Phys. Condens. Matter*, 2003, **15**, S159–S166.

43 J. Dupont, *J. Braz. Chem. Soc.*, 2004, **15**, 341–350.

44 T. G. A. Youngs, J. D. Holbrey, M. Deetlefs, M. Nieuwenhuyzen, M. F. Costa Gomes and C. Hardacre, *ChemPhysChem*, 2006, **7**, 2279–2281.

45 D. T. Bowron, C. D'Agostino, L. F. Gladden, C. Hardacre, J. D. Holbrey, M. C. Lagunas, J. McGregor, M. D. Mantle, C. L. Mullan and T. G. A. Youngs, *J. Phys. Chem. B*, 2010, **114**, 7760–7768.

46 M. Deetlefs, C. Hardacre, M. Nieuwenhuyzen, A. A. H. Padua, O. Sheppard and A. K. Soper, *J. Phys. Chem. B*, 2006, **110**, 12055–12061.

47 A. M. Moschovi and V. Dracopoulos, *J. Mol. Liq.*, 2015, **210**, 189–199.

48 K. J. Fraser and D. R. MacFarlane, *Aust. J. Chem.*, 2009, **62**, 309–321.

49 A. Hofmann, D. Rauber, T. M. Wang, R. Hempelmann, C. W. M. Kay and T. Hanemann, *Molecules*, 2022, **27**, 4729.

50 S. Khazalpour, M. Yarie, E. Kianpour, A. Amani, S. Asadabadi, J. Y. Seyf, M. Rezaeivala, S. Azizian and M. A. Zolfigol, *J. Iran. Chem. Soc.*, 2020, **17**, 1775–1917.

51 B. H. R. Suryanto, K. Matuszek, J. Choi, R. Y. Hodgetts, H. L. Du, J. M. Bakker, C. S. M. Kang, P. V. Cherepanov, A. N. Simonov and D. R. MacFarlane, *Science (80-.).*, 2021, **372**, 1187–1191.

52 X. H. Liu, M. Rebroš, I. Dolejš and A. C. Marr, *ACS Sustain. Chem. Eng.*, 2017, **5**, 8260–8268.

53 K. Glińska, J. Gitalt, E. Torrens, N. Plechkova and C. Bengoa, *Process Saf. Environ. Prot.*, 2021, **147**, 181–191.

54 L. H. Perales, L. E. Hernández Cruz, F. L. García, B. M. García and M. Á. Rodríguez, *Adv. Mater. Res.*, 2014, **976**, 217–221.

55 A. C. Barsanti, C. Chiappe, T. Ghilardi and C. S. Pomelli, *RSC Adv.*, 2014, **4**, 38848–38854.

56 R. Leyma, S. Platzer, F. Jirsa, W. Kandioller, R. Krachler and B. K. Keppler, *J. Hazard. Mater.*, 2016, **314**, 164–171.

57 C. M. S. S. Neves, J. F. O. Granjo, M. G. Freire, A. Robertson, N. M. C. Oliveira and J. A. P. Coutinho, *Green Chem.*, 2011, **13**, 1517–1526.

58 J. Castillo, M. T. Coll, A. Fortuny, P. Navarro Donoso, R. Sepúlveda and A. M. Sastre, *Hydrometallurgy*, 2014, **141**, 89–96.

59 M. Panigrahi, M. Grabda, D. Kozak, A. Dorai, E. Shibata, J. Kawamura and T. Nakamura, *Sep. Purif. Technol.*, 2016, **171**, 263–269.

60 J. J. Hettige, J. C. Araque, H. K. Kashyap and C. J. Margulis, *J. Chem. Phys.*, 2016, **144**, 121102.

61 X. Liu, G. Zhou, S. Zhang and G. Yu, *Mol. Simul.*, 2010, **36**, 79–86.

62 A. Gupta, S. Sharma and H. K. Kashyap, *J. Chem. Phys.*, 2015, **142**, 134503.

63 M. Liang, S. Khatun and E. W. Castner, *J. Chem. Phys.*, 2015, **142**, 121101.

64 A. Mariani, M. Bonomo, X. Gao, B. Centrella, A. Nucara, R. Buscaino, A. Barge, N. Barbero, L. Gontrani and S. Passerini, *J. Mol. Liq.*, 2021, **324**, 115069.

65 K. J. Fraser, E. I. Izgorodina, M. Forsyth, J. L. Scott and D. R. MacFarlane, *Chem. Commun.*, 2007, 3817–3819.

66 J. J. Hettige, H. K. Kashyap and C. J. Margulis, *J. Chem. Phys.*, 2014, **140**, 1–5.

67 F. Nemoto, M. Kofu, M. Nagao, K. Ohishi, S. I. Takata, J. I. Suzuki, T. Yamada, K. Shibata, T. Ueki, Y. Kitazawa, M. Watanabe and O. Yamamuro, *J. Chem. Phys.*, 2018, **149**, 054502.

68 C. A. Angell, N. Byrne and J. P. Belieres, *Acc. Chem. Res.*, 2007, **40**, 1228–1236.

69 J. P. Belieres and C. A. Angell, *J. Phys. Chem. B*, 2007, **111**, 4926–4937.

70 M. Yoshizawa, W. Xu and C. A. Angell, *J. Am. Chem. Soc.*, 2003, **125**, 15411–15419.

71 M. S. Miran, H. Kinoshita, T. Yasuda, M. A. B. H. Susan and M. Watanabe, *Phys. Chem. Chem. Phys.*, 2012, **14**, 5178–5186.

72 J. Stoimenovski, E. I. Izgorodina and D. R. MacFarlane, *Phys. Chem. Chem. Phys.*, 2010, **12**, 10341–10347.

73 D. R. MacFarlane and K. R. Seddon, *Aust. J. Chem.*, 2007, **60**, 3–5.

74 D. F. Evans, S. H. Chen, G. W. Schriver and E. M. Arnett, *J. Am. Chem. Soc*, 1981, **103**, 481–482.

75 K. Fumino, A. Wulf and R. Ludwig, *Angew Chem. Int. Ed.*, 2009, **48**, 3184–3186.

76 R. Hayes, S. Imberti, G. G. Warr and R. Atkin, *Phys. Chem. Chem. Phys.*, 2011, **13**, 3237–3247.

77 R. Hayes, S. Imberti, G. G. Warr and R. Atkin, *Angew. Chem. Int. Ed.*, 2012, **51**, 7468–7471.

78 Y. Umebayashi, W. Chung, T. Mitsugi, S. Fukuda, M. Takeuchi, K. Fujii, T. Takamuku, R. Kanzaki and S. Ishiguro, *J. Comput. Chem. Jpn.*, 2008, **7**, 125–134.

79 J. W. Shuppert and C. A. Angell, *J. Chem. Phys.*, 1977, **67**, 3050–3056.

80 G. Driver and K. E. Johnson, *Green Chem.*, 2003, **5**, 163–169.

81 R. Hagiwara, K. Matsumoto, Y. Nakamori, T. Tsuda, Y. Ito, H. Matsumoto and K. Momota, *J. Electrochem. Soc.*, 2003, **150**, D195–D199.

82 R. Hagiwara and Y. Ito, *J. Fluor. Chem.*, 2000, **105**, 221–227.

83 K. Matsumoto and R. Hagiwara, *J. Fluor. Chem.*, 2007, **128**, 317–331.

84 R. Hagiwara, Y. Nakamori, K. Matsumoto and Y. Ito, *J. Phys. Chem.B*, 2005, **109**, 5445–5449.

85 R. Hagiwara, T. Hirashige, T. Tsuda and Y. Ito, *J. Fluor. Chem.*, 1999, **99**, 1–3.

86 Y. Saito, K. Hirai, K. Matsumoto, R. Hagiwara and Y. Minamizaki, *J. Phys. Chem. B*, 2005, **109**, 2942–2948.

87 K. M. Johansson, E. I. Izgorodina, M. Forsyth, D. R. MacFarlane and K. R. Seddon, *Phys. Chem. Chem. Phys.*, 2008, **10**, 2972–2978.

88 G. A. Olah, T. Mathew, A. Goeppert, B. Török, I. Bucsi, X.-Y. Li, Q. Wang, E. R. Marinez, P. Batamack, R. Aniszfeld and G. K. Surya Prakash, *J. Am. Chem. Soc*, 2005, **127**, 5964–5969.

89 K. Matuszek, A. Chrobok, F. Coleman, K. R. Seddon and M. Swadźba-Kwaśny, *Green Chem.*, 2014, **16**, 3463–3471.

90 S. Combet, *EPJ Web Conf.*, 2020, **236**, 01001.

91 T. G. A. Youngs, H. Manyar, D. T. Bowron, L. F. Gladden and C. Hardacre, *Chem. Sci.*, 2013, **4**, 3484–3489.

92 A. K. Soper, *GudrunN and GudrunX: Programs for correcting raw neutron and X-ray diffraction data to differential scattering cross section. Rutherford Appleton Laboratory Technical Report RAL-TR-2011-013, STFC,* 2011.

93 A. K. Soper, *GudrunN and GudrunX: programs for correcting raw neutron and X-ray diffraction data to differential scattering cross section*, 2011.

94 T. Youngs, *Mol. Phys.*, 2019, **117**, 3464–3477.

95 W. L. Jorgensen, D. S. Maxwell and J. Tirado-Rives, *J. Am. Chem. Soc.*, 1996, **118**, 11225–11236.

96 F. Nüsslin, *Phys. Medica*, 2020, **79**, 65–68.

97 F. A. Stevie and C. L. Donley, *J. Vac. Sci. Technol. A*, 2020, **38**, 063204.

98 G. Chen, S. Zhou, H. Liao and L. Wu, *J. Compos. Mater.*, 2005, **39**, 215–231.

99 B. Winter and M. Faubel, *Chem. Rev.*, 2006, **106**, 1176–1211.

100 B. Winter, *Nucl. Instruments Methods Phys. Res. A*, 2009, **601**, 139–150.

101 R. Seidel, S. Thürmer and B. Winter, *J. Phys. Chem. Lett.*, 2011, **2**, 633–641.

102 R. Seidel, B. Winter and S. E. Bradforth, *Annu. Rev. Phys. Chem.*, 2016, **67**, 283–305.

103 M. Faubel, B. Steiner and J. P. Toennies, *J. Electron Spectrosc. Relat. Phenom.*, 1998, **95**, 159–169.

104 M. Faubel, B. Steiner and J. P. Toennies, *J. Chem. Phys.*, 1997, **106**, 9013–9031.

105 K. R. Siefermann, Y. Liu, E. Lugovoy, O. Link, M. Faubel, U. Buck, B. Winter and B. Abel, *Nat. Chem.*, 2010, **2**, 274–279.

106 T. A. Pham, M. Govoni, R. Seidel, S. E. Bradforth, E. Schwegler and G. Galli, *Sci. Adv.*, 2017, **3**, 1–9.

107 A. Mcgrogan, E. L. Byrne, T. G. A. Youngs, A. Chrobok, R. Guiney, T. F. Headen and J. D. Holbrey, *Phys. Chem. Chem. Phys.*, 2023, **25**, 9785–9795.

108 C. Andreani, C. Petrillo and F. Sacchetti, *Mol. Phys.*, 1986, **58**, 299–306.

109 P. C. Pascard-Billy, *Acta Cryst.*, 1965, **18**, 827–829.

110 A. R. Moodenbaugh, J. E. Hartt, J. J. Hurst, W. Youngblood, D. E. Cox and B. C. Frazer, *Phys. Rev. B*, 1983, **28**, 3501–3505.

111 Y. Kameda, K. Hosoya, S. Sakamoto, H. Suzuki, T. Usuki and O. Uemura, *Stud. Phys. Theor. Chem.*, 1995, **83**, 305–308.

112 A. D. Fortes, I. G. Wood, L. Vočadlo, L. Chapon, K. S. Knight and R. I. Smith, *J. Chem. Phys.*, 2008, **128**, 054506.

113 A. D. Fortes, I. G. Wood and K. S. Knight, *J. Chem. Phys.*, 2006, **125**, 1–7.

114 H. E. Maynard-Casely, H. E. A. Brand and K. S. Wallwork, *J. Appl. Crystallogr.*, 2012, **45**, 1198–1207.

115 F. J. V Gschwend, L. M. Hennequin, A. Brandt-talbot, F. Bedoya-lora, G. H. Kelsall, K. Polizzi, P. S. Fennell and J. P. Hallett, *Green Chem.*, 2020, **22**, 5032–5041.

116 H. Baaqel, I. Díaz, V. Tulus, B. Chachuat, G. Guillén-gosálbez and J. P. Hallett, *Green Chem.*, 2020, **22**, 3132–3140.

117 L. Chen, M. Sharifzadeh, N. Mac Dowell, T. Welton, N. Shah and J. P. Hallett, *Green Chem.*, 2014, **16**, 3098–3106.

118 A. George, A. Brandt, K. Tran, S. M. S. N. S. Zahari, D. Klein-Marcuschamer, N. Sun, N. Sathitsuksanoh, J. Shi, V. Stavila, R. Parthasarathi, S. Singh, B. M. Holmes, T. Welton, B. A. Simmons and J. P. Hallett, *Green Chem.*, 2015, **17**, 1728–1734.

119 A. Brzęczek-Szafran, J. Więcławik, N. Barteczko, A. Szelwicka, E. Byrne, A. Kolanowska, M. Swadźba Kwaśny and A. Chrobok, *Green Chem.*, 2021, **23**, 4421–4429.

120 F. J. V. Gschwend, C. L. Chambon, M. Biedka, A. Brandt-Talbot, P. S. Fennell and J. P. Hallett, *Green Chem.*, 2019, **21**, 692–703.

121 M. P. Atkins, M. J. Earle, K. R. Seddon, M. Swadźba-Kwaśny and L. Vanoye, *Chem. Commun.*, 2010, **46**, 1745–1747.

122 M. Przypis, K. Matuszek, A. Chrobok, M. Swadźba-Kwaśny and D. Gillner, *J. Mol. Liq.*, 2020, **308**, 113166–113179.

123 K. Matuszek, A. Brzeczek-Szafran, D. Kobus, D. R. Macfarlane, M. Swadźba-Kwaśny and A. Chrobok, *Aust. J. Chem.*, 2019, **72**, 130–138.

124 A. Brandt-Talbot, F. J. V. Gschwend, P. S. Fennell, T. M. Lammens, B. Tan, J. Weale and J. P. Hallett, *Green Chem.*, 2017, **19**, 3078–3102.

125 P. Verdía, A. Brandt, J. P. Hallett, M. J. Ray and T. Welton, *Green Chem.*, 2014, **16**, 1617–1627.

126 A. Brandt, M. J. Ray, T. Q. To, D. J. Leak, R. J. Murphy and T. Welton, *Green Chem.*, 2011, **13**, 2489–2499.

127 D. R. MacFarlane, A. L. Chong, M. Forsyth, M. Kar, R. Vijayaraghavan, A. Somers and J. M. Pringle, *Faraday Discuss.*, 2018, **206**, 9–28.

128 S. Suriyakumar, M. Kathiresan and A. M. Stephan, *ACS Omega*, 2019, **4**, 3894–3903.

129 K. Fujita, D. R. MacFarlane and M. Forsyth, *Chem. Commun.*, 2005, **70**, 4804–4806.

130 T. L. Greaves and C. J. Drummond, *Chem. Rev.*, 2015, **115**, 11379–11448.

131 D. R. Macfarlane, A. L. Chong, M. Forsyth, M. Kar, R. Vijayaraghavan, A. Somers and J. M. Pringle, *Faraday Discuss.*, 2018, **206**, 9–28.

132 C. L. Chambon, M. Chen, P. S. Fennell and J. P. Hallett, *Front. Chem.*, 2019, **7**, 1–13.

133 F. J. V. Gschwend, F. Malaret, S. Shinde, A. Brandt-Talbot and J. P. Hallett, *Green Chem.*, 2018, **20**, 3486–3498.

134 M. Chen, F. Malaret, A. E. J. Firth, P. Verdía, A. R. Abouelela, Y. Chen and J. P. Hallett, *Green Chem.*, 2020, **22**, 5161–5178.

135 P. Y. S. Nakasu, P. Y. S. Nakasu, C. J. Clarke, S. C. Rabelo, A. C. Costa, A. Brandt-Talbot and J. P. Hallett, *ACS Sustain. Chem. Eng.*, 2020, **8**, 7952–7961.

136 W.-C. Tu, L. Weigand, M. Hummel, H. Sixta, A. Brandt-Talbot and J. P. Hallett, *Cellulose*, 2020, **27**, 4745–4761.

137 F. Malaret, F. J. V. Gschwend, J. M. Lopes, W. C. Tu and J. P. Hallett, *RSC Adv.*, 2020, **10**, 16050–16060.

138 C. L. Chambon, V. Fitriyanti, P. Verdía, S. M. Yang, S. Hérou, M. M. Titirici, A. Brandt-Talbot, P. S. Fennell and J. P. Hallett, *ACS Sustain. Chem. Eng.*, 2020, **8**, 3751–3761.

139 A. R. Abouelela, A. Al Ghatta, P. Verdía, M. Shan Koo, J. Lemus and J. P. Hallett, *ACS Sustain. Chem. Eng.*, 2021, **9**, 10524–10536.

140 P. Y. S. Nakasu, P. Verdía Barbará, A. E. J. Firth and J. P. Hallett, *Trends Chem.*, 2022, **4**, 175–178.

141 S. O. Anuchi, K. L. S. Campbell and J. P. Hallett, *Sci. Rep.*, 2022, **12**, 1–11.

142 C. L. Chambon, P. Verdía, P. S. Fennell and J. P. Hallett, *Sci. Rep.*, 2021, **11**, 1–15.

143 W. C. Tu and J. P. Hallett, *Curr. Opin. Green Sustain. Chem.*, 2019, **20**, 11–17.

144 A. R. Abouelela, F. V. Gschwend, F. Malaret and J. P. Hallett, in *Commercial applications of ionic liquids*, ed. M. B. Shiflett, Springer International Publishing, Switzerland, 2020, pp. 103–105.

145 M. G. Resch, J. O. Baker and S. R. Decker, *Low Solids Enzymatic Saccharification of Lignocellulosic Biomass. National Renewable Energy Laboratory Technical Report NREL/TP-510-42629*, 2015.

146 A. Sluiter, B. Hames, D. Hyman, C. Payne, R. Ruiz, C. Scarlata, J. Sluiter, D. Templeton and J. W. Nrel, *Determination of total solids in biomass and total dissolved solids in liquid process samples. National Renewable Energy Laboratory Technical Report NREL/TP-510-42621*, 2008.

147 T. G. A. Youngs, J. D. Holbrey, C. L. Mullan, S. E. Norman, M. C. Lagunas, C. D'Agostino, M. D. Mantle, L. F. Gladden, D. T. Bowron and C. Hardacre, *Chem. Sci.*, 2011, **2**, 1594–1605.

148 D. Bedrov, J.-P. Piquemal, O. Borodin, A. D. J. Mackerell, B. Roux and C. Schröder, *Chem. Rev.*, 2019, **119**, 7940–7995.

149 A. Brzęczek-Szafran, K. Erfurt, M. Swadźba-Kwaśny, T. Piotrowski and A. Chrobok, *ACS Sustain. Chem. Eng.*, 2022, **10**, 13568–13575.

150 W. C. Tu, L. Weigand, M. Hummel, H. Sixta, A. Brandt-Talbot and J. P. Hallett, *Cellulose*, 2020, **27**, 4745–4761.

151 I. Tankov, R. Yankova, S. Genieva, M. Mitkova and D. Stratiev, *J. Mol. Struct.*, 2017, **1139**, 400–406.

152 R. D. Rogers and C. B. Bauer, *J. Chem. Crystallogr.*, 1994, **24**, 285–287.

153 M. Canales and E. Guàrdia, *J. Mol. Liq.*, 2016, **224**, 1064–1073.

154 L. Saiz, J. A. Padro and E. Guardia, *Mol. Phys.*, 1999, **97**, 897–905.

155 J. J. Towey, A. K. Soper and L. Dougan, *Faraday Discuss.*, 2013, **167**, 159–176.

156 B. D. T. Bowron, J. L. Finney and A. K. Soper, *Mol. Phys.*, 1998, **93**, 531–543.

157 O. S. Hammond, D. T. Bowron and K. J. Edler, *Green Chem.*, 2016, **18**, 2736–2744.

158 O. S. Hammond, K. J. Edler, D. T. Bowron and L. Torrente-murciano, *Nat. Commun.*, 2017, **8**, 1–7.

159 A. K. Soper, *ISRN Phys. Chem.*, 2013, **2013**, 1–67.

160 A. K. Soper, *Mol. Phys.*, 2009, **107**, 1667–1684.

161 J. Curtius, K. D. Froyd and E. R. Lovejoy, *J. Phys. Chem. A*, 2001, **105**, 10867–10873.

162 T. K. Hirsch and L. Ojamae, *Acta Cryst.*, 2004, **B60**, 179–183.

163 D. Mootz and A. Merschenz-Quack, *Z. Naturforsch Tl. B*, 1987, **42**, 1231–1236.

164 T. F. Headen, P. L. Cullen, R. Patel, A. Taylor and N. T. Skipper, *Phys. Chem. Chem. Phys.*, 2018, **20**, 2704–2715.

165 A. H. Turner and J. D. Holbrey, *J. Solution Chem.*, 2015, **44**, 621–633.

166 A. H. Turner, E. L. Byrne, T. Pereira and J. D. Holbrey, *Phys. Chem. Chem. Phys.*, 2020, **22**, 10219–10226.

167 M. M. Seitkalieva, A. V. Vavina, A. V. Posvyatenko, K. S. Egorova, A. S. Kashin, E. G. Gordeev, E. N. Strukova, L. V. Romashov and V. P. Ananikov, *ACS Sustain. Chem. Eng.*, 2021, **9**, 3552–3570.

168 C. G. Ding, T. Taskila, K. Laasonen and A. Laaksonen, *Chem. Phys.*, 2003, **287**, 7–19.

169 G. F. King and M. Mobli, in *Comprehensive Natural Products II*, eds. H.-W. Liu and L. Mander, Elsevier Ltd, Amsterdam, 2010, vol. 9, pp. 279–325.

170 H. K. Stassen, R. Ludwig, A. Wulf and J. Dupont, *Chem. - A Eur. J.*, 2015, **21**, 8324–8335.

171 C. L. Chambon, T. Y. Mkhize, P. Reddy, A. Brandt-Talbot, N. Deenadayalu, P. S. Fennell and J. P. Hallett, *Biotechnol. Biofuels*, 2018, **11**, 1–16.

172 R. Muazzam, A. M. Asim, M. Uroos, N. Muhammad and J. P. Hallett, *RSC Adv.*, 2021, **11**, 19095–19105.

173 Y. Kohno and H. Ohno, *Chem. Commun.*, 2012, **48**, 7119–7130.

174 S. Zahn, K. Wendler, L. Delle Site and B. Kirchner, *Phys. Chem. Chem. Phys.*, 2011, **13**, 15083–15093.

175 R. Hayes, S. Imberti, G. G. Warr and R. Atkin, *Angew. Chemie - Int. Ed.*, 2012, **51**, 7468–7471.

176 V. Loukonen, T. Kurtén, I. K. Ortega, H. Vehkaḿaki, A. A. H. Ṕadua, K. Sellegri and M. Kulmala, *Atmos. Chem. Phys.*, 2010, **10**, 4961–4974.

177 Y. Wu, H. L. Tepper and G. A. Voth, *J. Chem. Phys.*, 2006, **124**, 024503.

178 L. S. Dodda, J. Z. Vilseck, J. Tirado-Rives and W. L. Jorgensen, *J. Phys. Chem. B*, 2017, **121**, 3864–3870.

179 L. S. Dodda, I. C. De Vaca, J. Tirado-Rives and W. L. Jorgensen, *Nucleic Acids Res.*, 2017, **45**, W331–W336.

180 W. L. Jorgensen and J. Tirado-Rives, *Proc. Natl. Acad. Sci. U. S. A.*, 2005, **102**, 6665–6670.

181 Z. Wojnarowska, S. Cheng, B. Yao, M. Swadzba-Kwasny, S. McLaughlin, A. McGrogan, Y. Delavoux and M. Paluch, *Nat. Commun.*, 2022, **13**, 1–10.

182 B. Yao, M. Paluch, M. Dulski, C. Quinn, S. McLaughlin, A. McGrogan, M. Swadzba-Kwasny and Z. Wojnarowska, *J. Phys. Chem. Lett.*, 2023, **14**, 2958–2964.

183 B. Yao, M. Paluch, J. Paturej, S. Mclaughlin, A. Mcgrogan, M. Swadzba-kwasny, J. Shen, B. Ruta, M. Rosenthal, J. Liu, D. Kruk and Z. Wojnarowska, *ACS Appl. Mater. Interfaces*, 2023, **15**, 39417−39425.

184 L. C. Brown, J. M. Hogg, M. Gilmore, L. Moura, S. Imberti, S. Gärtner, H. Q. N. Gunaratne, R. J. O'Donnell, N. Artioli, J. D. Holbrey and M. Swadźba-Kwaśny, *Chem. Commun.*, 2018, **54**, 8689–8692.

185 K. Fujii, Y. Soejima, Y. Kyoshoin, S. Fukuda, R. Kanzaki, Y. Umebayashi, T. Yamaguchi, S. Ishiguro and T. Takamuku, *J. Phys. Chem. B*, 2008, **112**, 4329–4336.

186 K. Shimizu, C. E. S. Bernardes and J. N. Canongia Lopes, *J. Phys. Chem. B*, 2014, **118**, 567–576.

187 Y. Shim, M. Y. Choi and H. J. Kim, *J. Chem. Phys.*, 2005, **122**, 1–48.

188 Q. Parker, R. G. Bell and N. H. de Leeuw, *Mol. Simul.*, 2021, **47**, 152–160.

189 J. D. Holbrey, W. M. Reichert and R. D. Rogers, *Dalt. Trans.*, 2004, 2267–2271.

190 K. Ishisone, G. Ori and M. Boero, *Phys. Chem. Chem. Phys.*, 2022, **24**, 9597–9607.

191 H. Tanaka, *Phys. Rev. E - Stat. Physics, Plasmas, Fluids, Relat. Interdiscip. Top.*, 2000, **62**, 6968–6976.

192 Y. Katayama, T. Mizutani, W. Utsumi and O. Shimomura, 2000, **403**, 1998–2001.

193 V. V. Vasisht and S. Sastry, *Adv. Chem. Phys.*, 2013, **152**, 463–517.

194 D. J. Superconductivity, R. D. M. Dekker, N. York, I. Saika-voivod, P. H. Poole and F. Sciortino, 2001, **412**, 1–4.

195 J. N. Glosli and F. H. Ree, *Phys. Rev. Lett.*, 1999, **82**, 4659–4662.

196 W. Xu, M. T. Sandor, Y. Yu, H. B. Ke, H. P. Zhang, M. Z. Li, W. H. Wang, L. Liu and Y. Wu, *Nat. Commun.*, 2015, **6**, 1–9.

197 G. N. Greaves, M. C. Wilding, S. Fearn, D. Langstaff, F. Kargl, S. Cox, Q. Vu Van, O. Majérus, C. J. Benmore, R. Weber, C. M. Martin and L. Hennet, *Science (80-.).*, 2008, **322**, 566–570.

198 S. Wei, F. Yang, J. Bednarcik, I. Kaban, O. Shuleshova, A. Meyer and R. Busch, *Nat. Commun.*, 2013, **4**, 2083.

199 C. A. Angell and P. D. Bennett, *J. Am. Chem. Soc.*, 1982, **104**, 6304–6309.

200 I. Kaori, M. CT and C. Angell, *Nature*, 1999, **398**, 492–495.

201 R. Kurita and H. Tanaka, *J. Phys. Condens. Matter*, 2005, **17**, L293–L302.

202 R. Kurita and H. Tanaka, *Science (80-.).*, 2004, **306**, 845–848.

203 M. Kobayashi and H. Tanaka, *Nat. Commun.*, 2016, **7**, 1–8.

204 M. Zhu, J. Q. Wang, J. H. Perepezko and L. Yu, *J. Chem. Phys.*, 2015, **142**, 244504.

205 Q. S. Zeng, Y. Ding, W. L. Mao, W. Yang, S. V. Sinogeikin, J. Shu, H. K. Mao and J. Z. Jiang, *Phys. Rev. Lett.*, 2010, **104**, 1–4.

206 L. Liu, S. H. Chen, A. Faraone, C. W. Yen and C. Y. Mou, *Phys. Rev. Lett.*, 2005, **95**, 1–4.

207 M. A. Harris, T. Kinsey, D. V. Wagle, G. A. Baker and J. Sangoro, *Proc. Natl. Acad. Sci. U. S. A.*, 2021, **118**, 1–6.

208 E. W. Castner, C. J. Margulis, M. Maroncelli and J. F. Wishart, *Annu. Rev. Phys. Chem.*, 2011, **62**, 85–105.

209 H. Weingärtner, *Angew. Chemie - Int. Ed.*, 2008, **47**, 654–670.

210 E. C. Wijaya, T. L. Greaves and C. J. Drummond, *Faraday Discuss.*, 2013, **167**, 191–215.

211 H. Tokuda, K. Hayamizu, K. Ishii, M. A. B. H. Susan and M. Watanabe, *J. Phys. Chem. B*, 2005, **109**, 6103–6110.

212 W. Zheng, A. Mohammed, L. G. Hines, D. Xiao, O. J. Martinez, R. A. Bartsch, S. L. Simon, O. Russina, A. Triolo and E. L. Quitevis, *J. Phys. Chem. B*, 2011, **115**, 6572–6584.

213 M. G. Montalbán, C. L. Bolívar, F. G. Díaz Baños and G. Víllora, *J. Chem. Eng. Data*, 2015, **60**, 1986–1996.

214 M. R. Shimpi, P. Rohlmann, F. U. Shah, S. Glavatskih and O. N. Antzutkin, *Phys. Chem. Chem. Phys.*, 2021, **23**, 6190–6203.

215 J. N. Canongia Lopes, J. Deschamps and A. A. H. Pádua, *J. Phys. Chem. B*, 2004, **108**, 2038–2047.

216 F. H. Westheimer, *Chem. Rev.*, 1961, **61**, 265–273.

217 K. Hiruma-Shimizu, H. Shimizu, G. S. Thompson, A. P. Kalverda and S. G. Patching, *Mol. Membr. Biol.*, 2015, **32**, 139–155.

218 K. Akutsu-Suyama, M. Cagnes, K. Tamura, T. Kanaya and T. A. Darwish, *Phys. Chem. Chem. Phys.*, 2019, **21**, 17512–17516.

219 C. Hardacre, J. D. Holbrey and S. E. J. McMath, *Chem. Commun.*, 2001, **1**, 367–368.

220 R. Giernoth and D. Bankmann, *European J. Org. Chem.*, 2008, 2881–2886.

221 H. Esaki, F. Aoki, M. Umemura, M. Kato, T. Maegawa, Y. Monguchi and H. Sajiki, *Chem. - A Eur. J.*, 2007, **13**, 4052–4063.

222 L. C. Brown, A. McGrogan, Y. Delavoux, J. M. Hogg, J. D. Holbrey, H. Q. N. Gunaratne, M. Swadźba-Kwaśny, J. P. Tellam and S. E. Youngs, *J. Label. Compd. Radiopharm.*, 2022, **65**, 338–342.

223 C. Deferm, A. Van Den Bossche, J. Luyten, H. Oosterhof, J. Fransaer and K. Binnemans, *Phys. Chem. Chem. Phys.*, 2018, **20**, 2444–2456.

224 B. S. A. Bucklerib, *J. Am. Chem. Soc.*, 1962, **84**, 3093–3097.

225 C. R. Hilliard, N. Bhuvanesh, J. A. Gladysz and J. Blümel, *Dalt. Trans.*, 2012, **41**, 1742–1754.

226 P. K. Cooper, H. Li, N. R. Yepuri, A. Nelson, G. B. Webber, A. P. Le Brun, T. A. Darwish, G. G. Warr and R. Atkin, *J. Phys. Chem. C*, 2018, **122**, 24077–24084.

227 T. Maegawa, N. Ito, K. Oono, Y. Monguchi and H. Sajiki, *Synthesis (Stuttg).*, 2009, **16**, 2674–2678.

228 E. Podyacheva, E. Kuchuk and D. Chusov, *Tetrahedron Lett.*, 2019, **60**, 575–582.

229 K. Stagel, A. Szpecht, D. Zielinski, M. Smiglak, M. Schnürch and K. Bica-Schröder, *ACS Sustain. Chem. Eng.*, 2022, **10**, 11215–11222.

230 P. J. Carvalho, S. P. M. Ventura, M. L. S. Batista, B. Schröder, F. Gonçalves, J. Esperança, F. Mutelet and J. A. P. Coutinho, *J. Chem. Phys.*, 2014, **140**, 064505.

231 J. N. Canongia Lopes and A. A. H. Pádua, *J. Phys. Chem. B*, 2006, **110**, 19586–19592.

232 J. N. C. Lopes and A. A. H. Pádua, *J. Phys. Chem. B*, 2004, **108**, 16893–16898.

233 B. L. Bhargava, R. Devane, M. L. Klein and S. Balasubramanian, *Soft Matter*, 2007, **3**, 1395–1400.

234 B. L. Bhargava and M. L. Klein, *J. Phys. Chem. A*, 2009, **113**, 1898–1904.

235 L. Moura, M. Gilmore, S. K. Callear, T. G. A. Youngs and J. D. Holbrey, *Mol. Phys.*, 2019, **117**, 3364–3375.

236 S. Vyas, C. Dreyer, J. Slingsby, D. Bicknase, J. M. Porter and C. M. Maupin, *J. Phys. Chem. A*, 2014, **118**, 6873–6882.

237 P. Lassegues, J.C. Grondin, J. Holomb, R. Johansson, *J. Raman Spectrosc.*, 2007, **38**, 551–558.

238 O. Nordness and J. F. Brennecke, *Chem. Rev.*, 2020, **120**, 12873–12902.

239 S. Shokri, O. Naderi, K. Moradi, R. Sadeghi and S. Ebrahimi, *J. Mol. Liq.*, 2019, **277**, 290–301.

240 S. Saouane and F. P. A. Fabbiani, *Cryst. Growth Des.*, 2015, **15**, 3875–3884.

241 P. A. Hunt, C. R. Ashworth and R. P. Matthews, *Chem. Soc. Rev.*, 2015, **44**, 1257–1288.

242 H. C. Brown and B. Kanner, *J. Am. Chem. Soc.*, 1966, **88**, 986–992.

243 G. C. Welch, R. R. San Juan, J. D. Masuda and D. W. Stephan, *Science*, 2006, **314**, 1124–6.

244 G. C. Welch and D. W. Stephan, *J. Am. Chem. Soc.*, 2007, **129**, 1880–1881.

245 C. M. Mömming, E. Otten, G. Kehr, R. Fröhlich, S. Grimme, D. W. Stephan and G. Erker, *Angew. Chemie - Int. Ed.*, 2009, **48**, 6643–6646.

246 M. Sajid, A. Klose, B. Birkmann, L. Liang, B. Schirmer, T. Wiegand, H. Eckert, A. J. Lough, R. Fröhlich, C. G. Daniliuc, S. Grimme, D. W. Stephan, G. Kehr and G. Erker, *Chem. Sci.*, 2013, **4**, 213–219.

247 E. Otten, R. C. Neu and D. W. Stephan, *J. Am. Chem. Soc.*, 2009, **141**, 9918–9919.

248 J. Lam, K. M. Szkop, E. Mosaferi and D. W. Stephan, *Chem. Soc. Rev.*, 2019, **48**, 3558–3570.

249 P. A. Chase, G. C. Welch, T. Jurca and D. W. Stephan, *Angew. Chemie - Int. Ed.*, 2007, **46**, 8050–8053.

250 D. W. Stephan, *J. Am. Chem. Soc.*, 2021, **143**, 20002–20014.

251 M. A. Légaré, M. A. Courtemanche, É. Rochette and F. G. Fontaine, *Science (80-.).*, 2015, **349**, 513–516.

252 T. A. Rokob, A. Hamza, A. Stirling, T. Soós and I. Pápai, *Angew. Chemie - Int. Ed.*, 2008, **47**, 2435–2438.

253 S. Grimme, H. Kruse, L. Goerigk and G. Erker, *Angew. Chemie - Int. Ed.*, 2010, **49**, 1402–1405.

254 T. A. Rokob, I. Bakó, A. Stirling, A. Hamza and I. Pápai, *J. Am. Chem. Soc.*, 2013, **135**, 4425–4437.

255 L. L. Zeonjuk, N. Vankova, A. Mavrandonakis, T. Heine, G. V. Röschenthaler and J. Eicher, *Chem. - A Eur. J.*, 2013, **19**, 17413–17424.

256 I. Bakó, A. Stirling, S. Bálint and I. Pápai, *Dalt. Trans.*, 2012, **41**, 9023–9025.

257 L. Rocchigiani, G. Ciancaleoni, C. Zuccaccia and A. MacChioni, *J. Am. Chem. Soc.*, 2014, **136**, 112–115.

258 X. Liu, X. Wang, Y. Li, T. Yu, W. Zhao and L. Liu, *Phys. Chem. Chem. Phys.*, 2021, **23**, 12541–12548.

259 A. Dasgupta, E. Richards and R. L. Melen, *Angew. Chemie - Int. Ed.*, 2021, **60**, 53–65.

260 F. Holtrop, A. R. Jupp and J. C. Slootweg, in *Frustrated Lewis Pairs*, eds. J. C. Slootweg and A. R. Jupp, Springer, Switzerland, 2021, pp. 361–387.

261 L. L. Liu and D. W. Stephan, *Chem. Soc. Rev.*, 2019, **48**, 3454–3463.

262 L. Liu, L. L. Cao, Y. Shao, G. Ménard and D. W. Stephan, *Chem*, 2017, **3**, 259–267.

263 F. Holtrop, A. R. Jupp, N. P. van Leest, M. Paradiz Dominguez, R. M. Williams, A. M. Brouwer, B. de Bruin, A. W. Ehlers and J. C. Slootweg, *Chem. - A Eur. J.*, 2020, **26**, 9005–9011.

264 L. R. Marques and R. A. Ando, *ChemPhysChem*, 2021, **22**, 522–525.

265 A. K. Rappé, C. J. Casewit, K. S. Colwell, W. A. Goddard and W. M. Skiff, *J. Am. Chem. Soc.*, 1992, **114**, 10024–10035.

266 J. M. Hogg, L. C. Brown, K. Matuszek, P. Latos, A. Chrobok and M. Swadźba-Kwaśny, *Dalt. Trans.*, 2017, **46**, 11561–11574.

267 T. V. Bogdan and E. S. Alekseev, *J. Struct. Chem.*, 2012, **53**, 93–99.

268 J. H. Williams, J. K. Cockcroft and A. N. Fitch, *Angew. Chemie Int. Ed. English*, 1992, **31**, 1655–1657.

269 G. N. Lewis, *Valence and the structure of atoms and molecules*, Chemical Catalog Company, Incorporated, 1923.

270 S. Coffie, J. M. Hogg, L. Cailler, A. Ferrer-Ugalde, R. W. Murphy, J. D. Holbrey, F. Coleman and M. Swadźba-Kwašny, *Angew. Chem. Int. Ed.*, 2015, **54**, 14970–14973.

271 J. W. B. Fyfe and A. J. B. Watson, *Chem. Rev.*, 2012, **41**, 3558–3570.

272 K. Ishihara and H. Yamamoto, *Eur. J. Org. Chem.*, 1999, 527–538.

273 J. Cid, H. Gulyâs, J. J. Carbó and E. Fernândez, *Chem. Soc. Rev.*, 2012, **41**, 3558–3570.

274 P. A. Chase, T. Jurca and D. W. Stephan, *Chem. Commun.*, 2008, **2**, 1701–1703.

275 J. B. Geri, J. P. Shanahan and N. K. Szymczak, *J. Am. Chem. Soc.*, 2017, **139**, 5952–5956.

276 A. Simonneau and M. Etienne, *Chem. Eur. J.*, 2018, **24**, 12458–12463.

277 R. S. Drago, in *Coordinative Interactions. Structure and bonding*, Springer Berlin Heidelberg, 2005, pp. 73–139.

278 D. P. N. Satchell and R. S. Satchell, *Q. Rev. Chem. Soc.*, 1971, **25**, 171–199.

279 R. G. Pearson, *J. Am. Chem. Soc.*, 1963, **85**, 3533–3539.

280 Cotton F. A., Wilkinson G., Murillo C. and Bochmann M., *Advanced inorganic chemistry*, Wiley, New York, 6th edn., 1999.

281 T. Brinck, J. S. Murray and P. Politzer, 1993, **32**, 2622–2625.

282 F. Bessac and G. Frenking, *Inorg. Chem.*, 2003, **42**, 7990–7994.

283 V. Gutmann, *Electrochim. Acta*, 1976, **21**, 661–670.

284 I. B. Sivaev and V. I. Bregadze, *Coord. Chem. Rev.*, 2013, **270**, 75–88.

285 T. A. Zawodzinski and R. A. Osteryoung, *Inorg. Chem.*, 1989, **28**, 1710–1715.

286 I. C. Quarmby and R. A. Osteryoung, *J. Am. Chem. Soc.*, 1994, **116**, 2649–2650.

287 J. Estager, A. A. Oliferenko, K. R. Seddon and M. Swadźba-Kwaśny, *Dalt. Trans.*, 2010, **39**, 11375–11382.

288 U. Mayer, V. Gutmann and W. Gerger, *Monatshefte für Chemie*, 1975, **106**, 1235–1257.

289 R. F. Childs, D. L. Mulholland and A. Nixon, *Can. J. Chem.*, 1982, **60**, 801–808.

290 G. J. P. Britovsek, J. Ugolotti and A. J. P. White, *Organometallics*, 2005, **24**, 1685–1691.

291 A. L. Liberman-Martin, R. G. Bergman and T. D. Tilley, *J. Am. Chem. Soc.*, 2015, **137**, 5328–5331.

292 A. E. Ashley, T. J. Herrington, G. G. Wildgoose, H. Zaher, A. L. Thompson, N. H. Rees, T. Krämer and D. Öhare, *J. Am. Chem. Soc.*, 2011, **133**, 14727–14740.

293 P. Erdmann, J. Leitner, J. Schwarz and L. Greb, *ChemPhysChem*, 2020, **21**, 987–994.

294 C. G. Krespan and D. A. Dixon, *J. Fluor. Chem.*, 1996, **77**, 117–126.

295 D. McLemore, K. O. Christe, W. W. Wilson, J. a Sheehy, D. a Dixon and J. a Boatz, *J. Fluor. Chem.*, 2000, **101**, 151–153.

296 G. A. Olah, S. Kobayashi and M. Tashiro, *J. Am. Chem. Soc.*, 1972, **94**, 7448–7461.

297 S. Kobayashi, T. Busujima and S. Nagayama, *Chem. - A Eur. J.*, 2000, **6**, 3491–3494.

298 K. Matuszek, S. Coffie, A. Chrobok and M. Swadźba-Kwaśny, *Catal. Sci. Technol.*, 2017, **7**, 1045–1049.

299 C. S. Branch, S. G. Bott and A. R. Barron, *J. Organomet. Chem.*, 2003, **666**, 23–34.

300 M. F. Lappert, *J. Chem. Soc*, 1962, 542–548.

301 L. Luo and T. J. Marks, *Top. Catal.*, 1999, **7**, 97–106.

302 J. T. F. Fenwick and J. W. Wilson, *Inorg. Chem.*, 1975, **14**, 1602–1604.

303 M. V. Metz, D. J. Schwartz, C. L. Stern, T. J. Marks and P. N. Nickias, *Organometallics*, 2002, **21**, 4159–4168.

304 P. Erdmann and L. Greb, *Angew. Chemie - Int. Ed.*, 2022, **61**, e202114550.

305 A. Roldan, *Dalt. Trans.*, 2023, **52**, 1820–1825.

306 G. A. Olah, G. K. S. Prakash and J. Sommer, *Science (80-.).*, 1979, **206**, 1299–1309.

307 L. O. Müller, D. Himmel, J. Stauffer, G. Steinfeld, J. Slattery, G. Santiso-Quiñones, V. Brecht and I. Krossing, *Angew. Chemie - Int. Ed.*, 2008, **47**, 7659–7663.

308 Y. Hayashi, J. J. Rohde, E. J. Corey and R. V March, 1996, **7863**, 5502–5503.

309 A. Hasegawa, K. Ishihara and H. Yamamoto, *Angew. Chemie - Int. Ed.*, 2003, **42**, 5731–5733.

310 S. Antoniotti, V. Dalla and E. Duñach, *Angew. Chemie - Int. Ed.*, 2010, **49**, 7860–7888.

311 B. D. Patterson, *Am. J. Phys.*, 2011, **79**, 1046–1052.

312 D. N. Hendrickson, J. M. Hollander and W. L. Jolly, *Inorg. Chem.*, 1970, **9**, 612–615.

313 A. B. Preobrajenski, A. S. Vinogradov and N. Mårtensson, *J. Electron Spectros. Relat. Phenomena*,

2005, **148**, 59–64.

314 A. M. Duffin, C. P. Schwartz, A. H. England, J. S. Uejio, D. Prendergast and R. J. Saykally, *J. Chem. Phys.*, 2011, **134**, 154503.

315 A. M. Duffin, A. H. England, C. P. Schwartz, J. S. Uejio, G. C. Dallinger, O. Shih, D. Prendergast and R. J. Saykally, *Phys. Chem. Chem. Phys.*, 2011, **13**, 17077–17083.

316 R. Seidel, M. N. Pohl, H. Ali, B. Winter and E. F. Aziz, *Rev. Sci. Instrum.*, 2017, **88**, 1–20.

317 I. D. Madura, K. Czerwińska, M. Jakubczyk, A. Pawełko, A. Adamczyk-Woźniak and A. Sporzyński, *Cryst. Growth Des.*, 2013, **13**, 5344–5352.

318 G. Zukowska, M. Szczechura, M. Marcinek, A. Zubrowska, A. Adamczyk-Woźniak, A. Sporzyński and W. Wieczorek, *ECS Trans.*, 2009, **16**, 105–114.

319 A. Adamczyk-Woźniak, M. Jakubczyk, A. Sporzyński and G. Zukowska, *Inorg. Chem. Commun.*, 2011, **14**, 1753–1755.

320 M. A. Beckett, G. C. Strickland, J. R. Holland and K. S. Varma, *Polym. Commun.*, 1996, **37**, 4629–4631.

321 M. Ullrich, A. J. Lough and D. W. Stephan, *J. Am. Chem. Soc.*, 2009, **131**, 52–53.

322 Y. Jiang, J. Hess, T. Fox and H. Berke, *J. Am. Chem. Soc.*, 2010, **132**, 18233–18247.

323 M. A. Beckett, D. S. Brassington, S. J. Coles and M. B. Hursthouse, *Inorg. Chem. Commun.*, 2000, **3**, 530–533.

324 R. A. Mantz, P. C. Trulove, R. T. Carlin, T. L. Theim and R. A. Osteryoung, *Inorg. Chem.*, 1997, **36**, 1227–1232.

325 M. Currie, J. Estager, P. Licence, S. Men, P. Nockemann, K. R. Seddon, M. Swadźba-Kwaśny and C. Terrade, *Inorg. Chem.*, 2013, **52**, 1710–1721.

326 J. Estager, P. Nockemann, K. R. Seddon, M. Swadźba-Kwaśny and S. Tyrrell, *Inorg. Chem.*, 2011, **50**, 5258–5271.